

University of Trento
University of Padova

Fabio Pietro Marchesini (Ph.D. Student)

FATIGUE VULNERABILITY ANALYSIS FOR EXISTING METALLIC STRUCTURES

Prof. Carlo Pellegrino (Tutor)
Prof. Claudio Modena (Co-Tutor)

2016

© Fabio P. Marchesini

UNIVERSITY OF TRENTO and UNIVERSITY OF PADOVA
Engineering of Civil and Mechanical Structural Systems – XXVIII Cycle

Prof. Paolo Scardi (Ph. D. Head's)

Final Examination 04/04/2016

Board of Examiners:

Prof. Claudia Battaino	(University of Trento, Italy)
Prof. Andrea Vignoli	(University of Firenze, Italia)
Prof. Herve Degee	(Hasselt University, Belgium)
Prof. Elizabeth Vintzileou	(National Technical University of Athens, Greece)

to Nicola

ACKNOWLEDGEMENTS

A special thanks to my father, my family and all my beloved ones
for their encouragements;
to prof. Carlo Pellegrino and Prof. Modena, my supervisors;
Prof. Francesca da Porto; Ph.D. Massimo Dalla Benetta;
Ph.D. Riccardo Morbin, Ph.D. Giulia Bettiol;
Eng. Elvis Cescatti, Ph.D Giovanni Giacomello;
Eng. Massimo Nicolosi (R.F.I.);
and all my colleagues and the DICEA technicians;
for their advice.

INDEX

1	SUMMARY	2
2	INTRODUCTION.....	6
3	THEORETICAL BACKGROUND	11
3.1	Overview	13
3.2	Micromechanical process.....	14
3.3	Fatigue design.....	17
3.3.1	<i>S-N curves and mean stress.....</i>	<i>17</i>
3.3.2	<i>Damage, surface roughness and statistical reflection</i>	<i>22</i>
3.3.3	<i>Stress concentration</i>	<i>25</i>
3.3.4	<i>Strain based design</i>	<i>28</i>
4	HISTORICAL BRIDGES	31
4.1	Steel	31
4.2	Fatigue design code.....	32
4.3	Riveted structures	34

4.4	Remaining life	36
5	RIVETS OVERVIEW.....	37
5.1	Historical considerations	40
5.2	Realization process and static behavior	42
5.3	Clamping force	43
5.4	Combined effect.....	47
5.5	Connections	50
5.5.1	<i>Slip coefficient.....</i>	<i>53</i>
5.5.2	<i>Failure mechanisms.....</i>	<i>59</i>
5.5.3	<i>Behaviour under repeated loading.....</i>	<i>62</i>
6	SAN STINO'S RAILWAY BRIDGE	64
6.1	Reticular structure	70
6.2	Steel characterization.....	78
6.3	Traction test	79
6.4	Impact test.....	82
6.5	Vickers test.....	83
6.6	Optical microscope analysis	85
6.7	Quantometer analysis	86
6.8	Material fatigue test.....	88
6.9	Final considerations	93
7	TORSIONAL CLAMPING TESTS (TCT).....	95
7.1	Original clamping force	95

7.2	Current clamping force	96
7.2.1	<i>TCT - Experimentation</i>	97
7.2.2	<i>TCT: Small displacement</i>	101
7.2.3	<i>TCT: Big displacement</i>	120
7.2.4	<i>TCT: Clamping force measured</i>	134
7.2.5	<i>Notes on frictional coefficient</i>	142
7.3	Final considerations	143
8	SAN STINO'S RAIL BEARER TESTS	145
8.1	Rail bearer "A" characteristics	145
8.1.1	<i>Rivets</i>	147
8.1.2	<i>Holes and rivets standard dimensions</i>	155
8.1.3	<i>Plates dimensions and rivets distribution</i>	156
8.2	Loads, remaining life and fatigue verifications	157
8.3	Experimental campaign: fatigue identification test	162
8.3.1	<i>Symmetric test</i>	166
8.3.2	<i>Asymmetric test and additional acquisition</i>	169
8.4	Elastic Fem simulation	177
8.5	Non-linear Fem simulation	187
8.6	Final considerations	199
9	LABORATORY EQUIPMENT AND FATIGUE TEST	201
9.1	Introduction	201
9.1.1	<i>Welded components: nominal stress</i>	201

9.1.2	<i>Structural (or geometric) stress: hot spot method</i>	204
9.2	Laboratory equipment	215
9.2.1	<i>Servo actuator</i>	219
9.2.2	<i>Design</i>	222
9.2.3	<i>Analysis</i>	227
9.3	Real scale fatigue test.....	255
9.4	Final considerations	260
10	CONCLUSIONS AND DEVELOPMENTS	262
10.1	Further development	265
11	ATTACHED TABLES	268
12	BIBLIOGRAPHY	277

LIST OF FIGURES

Figure 1. W. A. J. Albert.....	11
Figure 2. Example of fatigue damage in stringer-to-floor-beam connections: (a) at the junction between the rivet head and shank; (b) at the external leg of the connection angle [2].	14
Figure 3. Intrusions and extrusions [3].	15
Figure 4. S-N Curve.....	18
Figure 5. Sinusoidal waveform.	20
Figure 6. Life plots.	21
Figure 7. Haigh diagram.	21
Figure 8. EN 1993 -1-9: fatigue strength curves	33
Figure 9. EN 1993 -1-9: fatigue shear strength curves	33
Figure 10. Category C=71.	35
Figure 11. Rivet schematic realization.....	37
Figure 12 Rivet installation.	37
Figure 13 Hot rivet.	38
Figure 14. Manufactured Rivet.	38
Figure 15. Driven Rivet.	38
Figure 16. Driven Head imperfections.....	39
Figure 17. Driven Head misalignment.	39
Figure 18. Shank imperfection.....	39
Figure 19. Shank deformation.	39
Figure 20. Plate gap.	39
Figure 21. Plate curvature.	39
Figure 22. Hole imperfection.	39
Figure 23. Stress – Strain diagram.....	40
Figure 24. Historical rivets.	41
Figure 25. Schematic clamping forces.	44
Figure 26. Different clamping areas. Zone 1: Hoop tension (HT), Zone 2: Hoop compression (HC), zone 3: Rivet hole; RC = radial compression.....	45
Figure 27. Springs deformation.	46
Figure 28. Shear type.	48
Figure 29. Different shear to tension load ratios.	49
Figure 30. Connection types.....	51
Figure 31. In plane load.....	51
Figure 32. Load – elongation.....	52
Figure 33. Pretension effect.	54
Figure 34. Forces distribution.	55
Figure 35. Forces.....	57
Figure 36. Plates slip.	58
Figure 37. Double riveted lap joint.....	60
Figure 38. Double strap butt joint.	60
Figure 39. Plate tearing.	60
Figure 40. Tearing across the rivets.	61
Figure 41. Shearing off a rivet, lap and butt joint.....	61
Figure 42. Crushing.	62
Figure 43. Crack initiation.	63

Figure 44. San Stino di Livenza, Venice, Italy.....	64
Figure 45 Frontal view.....	64
Figure 46 Lateral view.....	65
Figure 47. Bridge support (Portugruaro side).....	65
Figure 48. Bridge support (Mestre side).....	65
Figure 49 Bridge Lateral View.....	67
Figure 50. Bridge Plan.....	68
Figure 51. Extracted elements.....	69
Figure 52 Lateral plates zone.....	70
Figure 53 Mid-span plates zone.....	70
Figure 54. Lateral view: diagonals detail.....	71
Figure 55. Plan view. 1) rail bearers, 2) principal diagonal, 3) cross girders 4) secondary diagonal.....	71
Figure 56. Blowpipe cut.....	71
Figure 57. Rail bearer: corrosion and damage.....	72
Figure 58. Cross girders and longitudinal intersections.....	72
Figure 59. Protective coating, Pb_3O_4	72
Figure 60. Longitudinal and cross girders (plan).....	73
Figure 61. Rail bearer (section).....	73
Figure 62. Rail bearer (plan).....	73
Figure 63. Cross girder: frontal view.....	74
Figure 64. Cross girders: plan.....	74
Figure 65. Schematic Fem model.....	75
Figure 66. 3D Fem model.....	75
Figure 67. Cross girders and rail bearers model.....	76
Figure 68. Mode 1: 4,33Hz.....	77
Figure 69. Mode 2: 5,45 Hz.....	77
Figure 70. Sample plate.....	78
Figure 71. Tensile test specimen.....	79
Figure 72. Galdabini machin.....	80
Figure 73. Tensile test.....	80
Figure 74. Some specimens after test.....	80
Figure 75. Constitutive law.....	81
Figure 76. V-notches sample.....	82
Figure 77. Charpy apparatus.....	83
Figure 78. Post-test sample.....	83
Figure 79. Vickers test.....	84
Figure 80. Specimen.....	85
Figure 81. 200x magnification.....	85
Figure 82. 500x magnification.....	85
Figure 83. Quantometer.....	86
Figure 84. Steel composition.....	87
Figure 85. Test set up: 1. Actuator and force transducer 2. Specimen 3. Supports.	89
Figure 86. Acquisition system.....	90
Figure 87. Non-linear model.....	90
Figure 88. Quadratic wave.....	90
Figure 89. Sample 1 crack.....	91
Figure 90. Sample 2 crack.....	91
Figure 91. S-N curves.....	92

Figure 92. Rivet 1. Frictional area 2. Clamping force.....	97
Figure 93. External moment.....	98
Figure 94. Resisting moment.....	98
Figure 95. Welded rod.....	98
Figure 96. Monolithic nut connection.....	98
Figure 97. Nut welding.....	99
Figure 98. Test set up: 1) instrumented wrench 2) force multiplier 3) rod 4) displacement transducer.....	99
Figure 99. Wrench.....	100
Figure 100. Rods.....	100
Figure 101. HBM controller.....	100
Figure 102. Top rivet.....	101
Figure 103. Force – Rod displacement.....	102
Figure 104. Force – Time.....	102
Figure 105. Rod displacement – Time.....	103
Figure 106. Tangent method (1a).....	103
Figure 107. Tangent method (3a).....	104
Figure 108. Tangent method (4a).....	104
Figure 109. Tangent method (5a).....	105
Figure 110. Tangent method (6a).....	105
Figure 111. Methods comparison.....	106
Figure 112. Shank deformation (Fem).....	107
Figure 113. Schematic union: 1. Ideal connection 2. Real connection.....	107
Figure 114. Schematic union: 1. Original position 2. Post-torsion position.....	108
Figure 115. Increment factor.....	108
Figure 116. Force – Wand rotation (“a” Rivet).....	109
Figure 117. Moment – Wand rotation (“a” Rivet).....	110
Figure 118. Activation torque.....	110
Figure 119. Hysteresis.....	111
Figure 120. Medium rivet.....	111
Figure 121. Force – Wand displacement (“m” Rivet).....	112
Figure 122. Force – Time (“m” Rivet).....	112
Figure 123. Wand displacement – Time (“m” Rivet).....	113
Figure 124. Increment factor.....	114
Figure 125. Moment – Wand rotation (“m” Rivet).....	114
Figure 126. Hysteresis.....	115
Figure 127. Activation torque.....	115
Figure 128. Bottom rivet.....	116
Figure 129. Force – Wand displacement (“b” Rivet).....	116
Figure 130. Force – Time (“b” rivet).....	117
Figure 131. Wand displacement – Time (“b” Rivet).....	117
Figure 132. Increment factor.....	118
Figure 133. Moment – Wand rotation (“b” Rivet).....	118
Figure 134. Hysteresis.....	119
Figure 135. Activation torque.....	119
Figure 136. Top rivet.....	120
Figure 137. Force – Wand displacement (“A” Rivet).....	121
Figure 138. Force – Time (“A” Rivet).....	121
Figure 139. Wand displacement – Time (“A” Rivet).....	122
Figure 140. Increment factor.....	122

Figure 141. Moment – Wand rotation (“A” Rivet).	123
Figure 142. Hysteresis.	123
Figure 143. Activation torque.	124
Figure 144. Medium rivet.	124
Figure 145. Force – Wand displacement (“M” Rivet).	125
Figure 146. Force – Time (“M” Rivet).	125
Figure 147. Wand displacement – Time (“M” Rivet).	126
Figure 148. Increment factor.	126
Figure 149. Moment – Wand rotation (“M” Rivet).	127
Figure 150. Hysteresis.	127
Figure 151. Activation torque.	128
Figure 152. Bottom rivet.	128
Figure 153. Force – Wand displacement (“B” Rivet).	129
Figure 154. Force – Time (“B” Rivet).	129
Figure 155. Wand displacement – Time (“B” Rivet).	130
Figure 156. Increment factor.	131
Figure 157. Moment – Wand rotation (“B Rivet).	131
Figure 158. Hysteresis.	132
Figure 159. Activation torque.	132
Figure 160. Post-test rivet.	133
Figure 161. Head rotation.	133
Figure 162. Protective coat slip.	133
Figure 163. Torsion.	134
Figure 164. Stress distribution.	134
Figure 165. M external.	136
Figure 166. M internal.	136
Figure 167. Rivet heads and plate.	137
Figure 168. Points contact and rigid links.	137
Figure 169. Fem non-linear analysis.	138
Figure 170. Non-linear Fem solutions.	138
Figure 171. Clamping: upper rivet.	141
Figure 172. Clamping: medium rivet.	141
Figure 173. Clamping: bottom rivet.	142
Figure 174. Distribution of slip condition: clean mill scale surfaces.	143
Figure 175. Rail bearer “A”.	145
Figure 176. Node detail.	146
Figure 177. Section.	146
Figure 178. Surface treatment.	146
Figure 179. Corrosion.	146
Figure 180. WWII damages + shielding material.	147
Figure 181. Exposed rivets.	147
Figure 182. Rivet dimension.	148
Figure 183. Rivet section (Girder “B”).	148
Figure 184. Rivets hole (Girder “B”).	148
Figure 185. Height measurement.	149
Figure 186. Diameter and shank gauge.	150
Figure 187. Rivets position.	150
Figure 188. Rivet section.	152
Figure 189. Rivets head diameter -side A-.	152
Figure 190. Variations -side A-.	153

Figure 191. Variations % -side A-.....	153
Figure 192. Rivets head diameter -side B-.....	154
Figure 193. Variations -side B-.....	154
Figure 194. Variations % -side B-.....	155
Figure 195. Typical hole.....	156
Figure 196. Riveted joint.....	157
Figure 197. Fatigue static scheme (rail bearer).....	159
Figure 198. Nominal stress ($F = 2 \times 100 \text{ kN}$).....	160
Figure 199. Static scheme.....	162
Figure 200. Plates for rivets gap.....	162
Figure 201. Aluminium bar.....	163
Figure 202. 8 channels acquisition.....	163
Figure 203. 1) DD1 transducer, 2) inductive transducer.....	164
Figure 204. Side B.....	164
Figure 205. Side A.....	165
Figure 206. Static scheme.....	166
Figure 207. $F - \delta$ (500kN Midspan).....	167
Figure 208. $F - \delta$ (500 kN Midspan).....	168
Figure 209. Force – deformation (500 kN Mid-span).....	169
Figure 210. Static scheme.....	170
Figure 211. Force position.....	170
Figure 212. Eccentric load configuration.....	170
Figure 213. 350 kN at 1/3 length.....	171
Figure 214. 350 kN at 1/3 length.....	172
Figure 215. Force – deformation, 350 kN at 1/3 length.....	173
Figure 216. Plate sensor (Side B).....	174
Figure 217. plate sensor (side A).....	174
Figure 218. 350 kN at 1/3 length (High accuracy).....	175
Figure 219. 350 kN at 1/3 length (Ha).....	176
Figure 220. 350 kN at 1/3 length (Ha).....	176
Figure 221. Side A.....	177
Figure 222. Side B.....	177
Figure 223. Elastic model.....	178
Figure 224. Symmetric static scheme.....	178
Figure 225. Asymmetric static scheme.....	179
Figure 226. Channel 2.....	180
Figure 227. Channel 3.....	180
Figure 228. Channel 5.....	181
Figure 229. Channel 6.....	181
Figure 230. Channel 4.....	182
Figure 231. Elastic deformation.....	182
Figure 232. Symmetric load.....	183
Figure 233. Asymmetric load.....	183
Figure 234. Channel 2.....	184
Figure 235. Channel 3.....	185
Figure 236. Channel 5.....	185
Figure 237. Channel 6.....	186
Figure 238. Channel 4.....	186
Figure 239. Elastic deformation.....	187
Figure 240. Plate composition.....	188

Figure 241. Non-linear model.....	188
Figure 242. Point contact.....	189
Figure 243. Symmetric static scheme (500kN)	189
Figure 244. Channel 2.....	190
Figure 245. channel 3.....	191
Figure 246. Channel 5.....	191
Figure 247. Channel 6.....	192
Figure 248. Channel 4.....	192
Figure 249. Iterations.....	193
Figure 250. Beam displacement (500 kN).....	193
Figure 251. Asymmetric static scheme (300kN).....	195
Figure 252. Channel 2.....	195
Figure 253. Channel 3.....	196
Figure 254. Channel 5.....	196
Figure 255. Channel 6.....	197
Figure 256. Channel 4.....	197
Figure 257. Up flange.....	198
Figure 258. Beam displacement (300 kN).....	198
Figure 259. Nominal stress: excluding micro-detail	202
Figure 260. Different mesh accuracy.....	203
Figure 261. Modified nominal stress.....	203
Figure 262. Structural stress at weld toe.....	204
Figure 263. Stress discontinuities and stress orientation.....	205
Figure 264. Hot spot types.....	205
Figure 265. 8-nodes element.....	206
Figure 266. Component modelling.....	206
Figure 267. Type a. (a): relatively fine mesh; (b): relatively coarse mesh.....	207
Figure 268. Toe distance.....	208
Figure 269. Thickness correction exponents.....	208
Figure 270. Type b. (c): relatively fine mesh; (d): relatively coarse mesh.....	209
Figure 271. Structural details.....	210
Figure 272 Structural details.....	211
Figure 273. Example of strain gauges.....	213
Figure 274. Non-linear stress distribution.....	214
Figure 275. Steel frame.....	216
Figure 276. High precision 3D model: 1-4. 3D design.....	218
Figure 277. High precision 3D model: 5-7. 3D design, 8. Calibrated assembly.....	219
Figure 278. Lateral view.....	221
Figure 279. Front view.....	221
Figure 280. Manifold.....	221
Figure 281. Test controller.....	221
Figure 282. Servo actuator.....	222
Figure 283. ¼ Fem model.....	223
Figure 284. Point contact.....	224
Figure 285. Profiles manufacturing.....	225
Figure 286. Full penetration weld.....	225
Figure 287. Rail bearer test. 1: Actuator 2. Frame 3. Connection element 4. Rail bearer 5. Fastening element.....	226
Figure 288. Plate displacement (DZ).....	227
Figure 289. Maximum displacement: 0,44 mm (displacement scale increased).....	227

Figure 290. Plate stress.....	228
Figure 291. Columns.....	229
Figure 292. Sandblasting.....	229
Figure 293. HEM360M + gusset plates.....	229
Figure 294. Deep beam (design).....	232
Figure 295. Section.....	232
Figure 296. Deep beam.....	233
Figure 297. Fem model.....	236
Figure 298. Removed corner.....	237
Figure 299. Opposed plate and gusset plates.....	237
Figure 300. Opposed plate during assembly phases.....	238
Figure 301. Bolted joints during the assembly phases.....	240
Figure 302. Fem model, y direction.....	240
Figure 303. Fem model, x direction.....	241
Figure 304. Fem model, z direction.....	243
Figure 305. Hot Spot detail.....	244
Figure 306. Type a Hot Spot.....	245
Figure 307. Detail: type a Hot Spot.....	245
Figure 308. Type b Hot Spot.....	246
Figure 309 Detail: type b Hot Spot.....	246
Figure 310. Bolted joint (design).....	247
Figure 311. Bolt forces.....	247
Figure 312. Bolted joint.....	248
Figure 313. Fem simulation.....	249
Figure 314. Fem simulation.....	250
Figure 315. Bolted joint (design).....	251
Figure 316. Joint.....	251
Figure 317. Floor bars.....	252
Figure 318. Connection plates.....	252
Figure 319. Brick model.....	253
Figure 320. Connection plates.....	253
Figure 321. Contact element.....	254
Figure 322. High configuration.....	255
Figure 323. Mid configuration.....	255
Figure 324. Test controller.....	256
Figure 325. Fatigue test.....	256
Figure 326. Different load waves.....	256
Figure 327. Stress wave.....	256
Figure 328. Laboratory stress distribution.....	257
Figure 329. Full scale tests: FAT 71.....	258
Figure 330. Fatigue cycles.....	259

NOMENCLATURE

σ_a	Constant amplitude fatigue
$\Delta\sigma$	Stress amplitude
σ_m	Mean stress
R	Stress ratio
N_f	Number of cycles to fatigue failure
σ_e	Effective stress (Von Mises)
$\Delta\varepsilon$	Total strain amplitude
$\Delta\sigma_c$	Stress range corresponding to a value of $N = 2$ million cycles
T_u	Rivet tensile capacity
F_{cl}	Magnitude of clamping force
ΔL_{riv}	Rivet elongation
τ_u	Rivet shear strength
E	Young modulus
σ	Stress (general)
ε	Deformation (general)
Subscript “y”	Yield point (material)
Subscript “u”	Ultimate point (material)
nEm	$n \cdot 10^m$
I_f	Increment factor (laboratory tests)
k_s	Frictional coefficient
d	Rivet shank diameter
D	Rivet head diameter
ϕ	Diameter
Ch	Channel (acquisition)
$\delta(x)$	Deflection
DD1	Compact strain transducer with high accuracy
Ind	Inductive transducer
Fem	Finite element method
a	Weld throat
σ_{hs}	Stress at hot spot
ε_{hs}	Deformation at hot spot
t	Thickness
FAT	Reference fatigue detail
SR	Safety factor
$\Delta\sigma_D$	Fatigue design stress
γ_{Mf}	Fatigue safety factor

1 SUMMARY

This thesis focuses on fatigue problem on riveted structures and the correlated experimental tests. The term “fatigue” denotes the cracking of metals under repeated loading. The technique of riveting structures is obsolete due to the low level of standardization in the construction process. Knowledge concerning riveted structure’s ability to withstand fatigue has not been investigated to the same extent as for modern structures assembled by welding. Nevertheless, many riveted structures are still in service after over 100 years. Clamping force originates when the hot rivet is placed into the hole of the plates and the rivet shorten in length due to cooling. In Europe, a large number of railway bridges are riveted. Moreover, all over the world, the rivet assembly technique has been largely used for different types of buildings. The riveted structures are subjected, evidently, to fatigue degradation as all the other steel structures. The riveted joint complexity and the non-uniform realization lead to a structure-specific consideration. In Europe, current regulations recognise only one fatigue class for riveted structures neglecting the clamping force effect. This approach is characterized by an elevated standard deviation for the assessed results. This research aims to improve the riveted structures fatigue comprehension and to propose appropriate tests. Some elements have been extracted from a dismantled railway bridge located near San Stino di Livenza (Venice). An innovative clamping test (TCT) has been conceived: applying a torsional moment to the rivets and evaluating the sliding friction, the clamping force has been estimated. Contrary to traditional clamping tests, this setup, at an affordable price, provides good precision. Moreover, the test is in-site and does not provoke damages to the examined structure. Fem models of rail bearer have been realized taking into account rivets, holes and multilayer plates section inertia. A specific laboratory set up has been designed with the intention to calibrate the fem models. Frictions and clamping force have been taken into account in the rail bearer models. There is a close correspondence between the non-linear models and the experimental tests. The clamping assumptions, derived from the TCT, have been verified. A full scale fatigue test has been prepared and the first cycles have been monitored. Full scale fatigue tests are sophisticated and involve many parameters. For this test, a specific metallic frame has been designed and realized using advanced fatigue models. An advanced analysis (hot spot method) has been

carried out, for the frame, in order to evaluate the stress into the welds. This frame will be used by the DICEA laboratory to test, principally, specimens extracted from bridges.

SOMMARIO

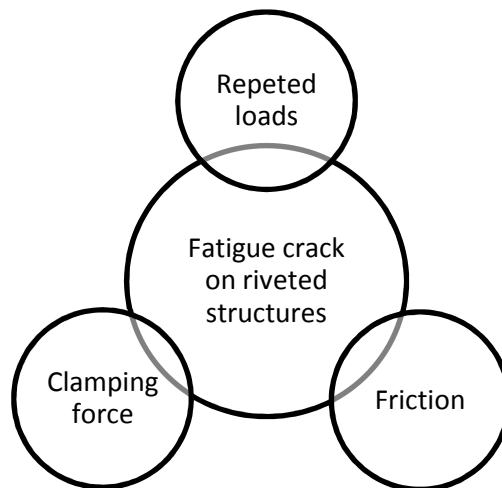
Questa tesi si concentra su problemi di fatica nelle strutture rivettate e sui test in laboratorio dedicati ad esse mirati a valutarne il grado di sicurezza. Il termine "fatica" denota la rottura del metallo a seguito di cicli ripetuti di carico. La tecnica di costruzione tramite giunzioni rivettate è obsoleta e la conoscenza riguardo queste strutture non è approfondita quanto per le moderne opere realizzate tramite saldature. Tuttavia molte strutture, nonostante abbiano più di 100 anni, sono ancora in servizio e diventa sempre più necessario valutarne la vita residua. La forza di serraggio nel rivetto si genera a seguito del raffreddamento dello stesso una volta posizionato in opera. In Europa un grande numero di ponti ferroviari sono rivettati. Inoltre, nel mondo, la tecnica di assemblaggio con rivetti è stata largamente utilizzata per varie tipologie di edifici che venivano eseguiti senza l'ausilio di norme specifiche. Le strutture rivettate sono soggette, evidentemente, a problemi di fatica come tutte le strutture in acciaio. La complessità dei giunti rivettati e la realizzazione non uniforme porta a considerazioni specifiche per ogni struttura. Le attuali norme introducono solo una classe di fatica per le strutture rivettate trascurando la forza di preserraggio. Questo approccio è caratterizzato però da un'alta deviazione standard nei risultati. La mia ricerca ha cercato di migliorare la comprensione del comportamento statico e a fatica dei giunti rivettati. Alcuni elementi sono stati prelevati da un ponte ferroviario dismesso presso San Stino di Livenza (Venezia). Un innovativo test di preserraggio (TCT) è stato concepito: applicando un momento torsionale al rivetto e, tenendo in considerazione l'attrito, è stata stimata la forza di preserraggio dei rivetti. A differenza dei tradizionali test di misura del preserraggio, questa prova permette, con buona precisione e ad un basso costo, di testare direttamente in opera la forza di preserraggio esistente senza provocare danni alle strutture. Sono stati realizzati modelli Fem delle longherine tenendo in conto l'effetto dei rivetti, dei fori e dell'inerzia delle sezioni composte da vari strati di piatti d'acciaio. Specifici set up di laboratorio sono stati progettati per calibrare i modelli Fem. In particolare l'attrito e la forza di preserraggio sono stati introdotti nei modelli delle longherine. I modelli non lineari hanno mostrato una buona correlazione con i dati sperimentali dei test, le assunzioni riguardanti la forza di preserraggio sono state quindi convalidate. È stato eseguito un test di fatica in scala 1:1 sulle longherine e ne sono stati monitorati i primi cicli. I test in scala 1:1 sono molto sofisticati e coinvolgono molti parametri. Per questo test a fatica è stato progettato e realizzato un apposito telaio in acciaio di contrasto. Nella progettazione sono stati utilizzati metodi avanzati quali il metodo Hot Spot per le saldature. Il telaio sarà

utilizzato dal laboratorio del Dipartimento ICEA (Università di Padova), principalmente, per test di fatica su campioni prelevati da ponti.

2 INTRODUCTION

Fatigue damage is caused by the simultaneous action of cyclic stress, tensile stress, and plastic strain. If any one of these three is not present, a fatigue crack will not initiate and propagate. The plastic strain resulting from cyclic stress initiates the crack; the tensile stress promotes crack growth. Chapter 0 introduces the theoretical considerations about the fatigue aspect. Predicting the fatigue life of a metal element is complicated because materials are sensitive to small changes in loading conditions, stress concentrations and other factors. The resistance of a metal structural member to fatigue is also affected by manufacturing procedures such as cold forming, welding, brazing, plating and by surface conditions such as surface roughness and residual stresses. Fatigue tests performed on small specimens are not sufficient for precisely establishing the fatigue life of element. These tests are useful for rating the relative resistance of a material and the baseline properties of the material to cyclic stress. Chapter 4 introduces the basis for the static and cyclic considerations about old riveted structures. The technique of riveting bridges is obsolete and knowledge concerning riveted structure's ability to withstand fatigue has not been investigated to the same extent as for modern structures assembled by welding. The proposed design code for fatigue in Europe is EN 1993-1-9. Fatigue tests are plotted in log scale diagrams with the number of cycles on the horizontal axis and the stress range on the vertical axis. All tests are compared to detail category $C = 71$. The endurance of tested elements has been evaluated statistically (5% fractile; 75% significance level). In order to understand the real structure behaviour, it is fundamental to analyse rivets connections and their clamping force. Chapter 5 synthesizes the rivets behaviour and their clamping force. The method of riveting, before the 1940's, was used to assemble especially civil structures. The method of riveting two plates together was carried out by producing a drilling or punching hole in the plates that were to be assembled. The plates were fastened by driving a hot rivet through the hole of the two plates and by hammering the shank to form a second rivet head. When the rivet cooled, it contracted both longitudinally and radially, thereby it provided a clamping force joining the plates. The size of the clamping force produced by rivets should transfer some shear by friction. In most cases shear forces are transferred as a mix of friction and shear of rivets. Initially the forces are transferred by friction at the ends

of the joints, but as the load increases the friction zone extends towards the centre of the connection until the friction resistance is exceeded. As the joint starts to slip, the rivets at the end of a connection come in contact with the surface of the rivet hole first: an adequate clamping force is then beneficial since the frictional resistance of the connection will prevent the connection plates to slip into bearing. Fatigue cracks often originate in the rivet holes at the end of connections due to the higher bearing stresses. The amount of clamping force in rivets differs and therefore the common engineering practice assessing riveted shear connections only as a pure shear connection. Fatigue crack initiation may start from micro-cracks around the rivet hole and the magnitude of stress concentration is dictated by the geometry of the detail and the fabrication process.



Conceptual scheme

Chapter 6 shows the case study. The vulnerability fatigue assessment is developed in a reticular disused railway bridge located near S. Stino di Livenza (Venice), in North Eastern part of Italy. The bridge belongs to the Italian State Railways and it was operational for about a century. The girders fatigue behaviour, taking into account clamping effect, is investigated in detail. The girders are riveted the profiles made up by multilayer plates and they are connected by rivets, similar to the other structures of that period. The static scheme is a simply supported girder bridge; moreover the rail bearers are 3360 mm long. Tensile tests on the samples, taken from the bridge case study, were carried out to characterize the material. Moreover, the study of the material was performed by the analysis with the optical microscope

and the spectrometer. Considering these first analyses, it is observed that the steel of San Stino Bridge is very similar to Mild Steel. A specific clamping test on San Stino's elements has been designed to evaluate the preload present in the rivets shank. The results are presented in Chapter 7. Rivets has two circular friction areas in correspondence of the heads. A torsional moment is applied using instrumented wrench to measure the force, and the correlate clamping force, activating the dynamic friction. In order to gauge the small rotations of rivets head a metallic wand is welded on the rivets and its displacements assessed by inductive transducers. The second step has been the static identifications 3 points bending test to identify the fatigue crack growth zone in San Stino's girders. Chapter 8 shows the methodology and the results of the tests. The tests provide some information regarding the inertia of the beam, the rivets efficiency and the global performance of the elements. In order to avoid imperfect measurements of girder's displacements, a secondary beam has been coupled and some sensors assess the deformation of the plates. During the service life, the girders, were subject to dynamic loads and the trains flowed changing the static scheme continuously. A second set up has been conceived to induce the shear behaviour and the force has been applied in correspondence of anti-winding joint. Subsequently, on the entire rail bearer, a specific fatigue test will be carried out with the intention to evaluate the crack propagations in real scale. For this reason, a 4 columns metal frame has been designed and realized to join the fatigue hydraulic actuator mounted vertically above the specimen. The frame design and specimen tests are shown in Chapter 9. The total mass of the anchored floor framework is about 16 tons while the actuator (1500 kN \pm 100 mm) mass is 4200 kg. The structure is composed by four box-section columns composed by commercial profiles closed with thick plates welded at the ends of the wings. This solution has allowed to optimize the weight (and therefore costs) obtaining a local buckling resistant section and, at the same time, to guarantee a sufficient area to limit the axial elongation. The columns, at the top, are joined together by two deep beams and at the centre of which it is installed the actuator support element: a thick plate with two ribs for housing the actuator. The columns/beams and beams/plate connections are made using friction bolted joints in order to avoid any type of shear effect that would be detrimental to the fatigue strength. All other connections are made by a full penetration weld and, the most critical ones, are modelled using hot spot method. Girders experimentations are only the first step of a more extensive tests campaign including primary beam and diagonal truss. Results from the fatigue investigations conducted on full scale structures and small scale details from bridges taken out of service will be evaluated.

The aim of the thesis is to investigate the fatigue resistance of riveted structures taken out of service and also to determine the influence of clamping force, corrosion, hole preparation and material on the fatigue performance. This thesis provides some useful tools to estimate the clamping force in rivets connections, to evaluate old metallic girder residual strength and to forecast the fatigue failure.

Tutor

Prof. Carlo Pellegrino

Co-Tutor

Prof. Claudio Modena

Ph. D Head's

Prof. Paolo Scardi

3 THEORETICAL BACKGROUND

In the first report, fatigue, is redefined as a change in properties that can occur in a metallic material due to repeated application of stress or strain, although this term usually applies specially to those changes that lead to cracking or failure. Fatigue failures occur in many different forms: fluctuations in externally applied load or deformation result in mechanical fatigue or, for example, when the temperature of the cyclically loaded component fluctuates as well (thermomechanical fatigue). Recurring loads imposed in the presence of an aggressive environment give rise to corrosion fatigue. The repeated application of loads in structural joint with sliding and rolling contact between materials produce sliding contact fatigue and rolling contact fatigue, respectively, while fretting fatigue occurs as a result of pulsating stresses along with oscillator relative motion and frictional sliding between surfaces. Such failures generally take place under the influence of cyclic loads whose peak values are considerably smaller than the ultimate static loads estimated.

Since the nineteenth century scores of engineers made pioneering contribution to the understanding of fatigue in a wide variety of metallic and non-metallic, brittle and ductile, monolithic and composite and natural and synthetic analysis. The expression “fatigue” has been in use for a very long time. The first study of a metal fatigue is believed to have been conducted around 1829 by W. A. J. Albert (Figure 1), a German mining engineer. Interest in the study of fatigue began to expand with the increasing use of ferrous structures, particularly bridges in railway systems.



Figure 1. W. A. J. Albert.

The first detailed research effort into metal fatigue was initiated in 1842 following the railway accident near Versailles (France) which resulted in the loss of human lives. The cause of this accident was traced to fatigue failure originating in the locomotive front axle. Moreover, few years later, in Britain, a research on fatigue fracture was documented in Braithwaite's work who employed the term "fatigue" to denote exclusively the cracking of metals under repeated loading. A. Wohler conducted systematic investigation of fatigue failure during the period 1852-1869 in Berlin, where he established an experiment station. He observed that the strength of steel railway axles subjected to cyclic loads was appreciably lower than their static strength. Wohler studies involving bending, torsion and axial loading included fatigue tests on full-scale railway axle and on a variety of structural components used in small machines. His work also led to the characterization of fatigue behaviour in terms of stress amplitude-life (S-N) curves and to the concept of fatigue "endurance limit". Another well-known fatigue researcher of this era (1864) was W. Fairbairn's, who performed tests on riveted wrought iron girders for the British Board of Trade; in some cases, as many as $3,1 \cdot 10^6$ cycles were applied. Based on his experiments, Fairbairn inferred that the wrought iron girders subjected to cyclic stress with a maximum of only 1/3 of the ultimate strength would fail. The notion that the elastic limit of metals in reversed loading can be different from that observed in monotonic deformation was popularized by Bauschinger (1886). In 1886, Bauschinger spread the notion that the elastic limit of metals in reversed loading can be different from that observed in monotonic deformation. Bauschinger's work essentially identified the occurrence of cyclic softening and cyclic strain hardening. Ewing, Rosenhain and Humfrey showed that slip bands intersecting the polished surface caused slip step in the form of elevation and depression. In 1910, O.H. Basquin proposed empirical laws to characterize the S-N curves of metal. He showed that a log-log plot of the stress versus the number of fatigue cycles resulted in a linear relationship over a large range of stress.

Furthermore, the notion that plastic strains are responsible for cyclic damage was established by Coffin and Manson: they proposed an empirical relationship between the number of load reversal to fatigue failure and the plastic strain amplitude. The stress analysis by Inglis (1913) and the energy concepts by Griffith (1912) provided the mathematical tools for quantitative treatments of fracture in brittle solids. However, these ideas could not be directly employed to characterize the fatigue failure of metallic materials. Progress in this field came with the pioneering studies made by Irwin (1957) who showed that the amplitude of the stress singularity ahead of a crack could be expressed in terms of the scalar quantity known as the stress intensity factor, K , with the advent of this so-called linear elastic fracture mechanics

approach. Some attempts were made to characterize the growth of fatigue cracks also in terms of the stress intensity factor. The effects of various mechanical, microstructural and environmental factors on cyclic deformation as well as on crack initiation and growth in a vast spectrum of engineering materials have been the topics of considerable researches in the past decades. Thompson, Wadsworth and Louat (1956) demonstrated that slip bands along which deformation during continued cycling even after some material was removed near the surface; they termed these surface marking “persistent slip bands”.

3.1 Overview

J. A. Bannantine, J. J. Comer and J. L. Handrock [1] define metal fatigue as a process which causes premature failure or damage (Figure 2) of a component subjected to repeated loading. It is a complicated molecular process that is difficult to describe and model. Despite these complexities, fatigue analysis methods have been developed. The primary fatigue analysis methods are the stress-life approach, the strain-life approach and the fracture mechanics approach. These methods have their own region of application with some degree of overlap between them. Historically, two over-riding considerations have promoted the development of fatigue analysis method. The first has been the need to provide designers and engineers methods that are practically, easily implemented and cost effective. The second consideration has been the need to reconcile these analytical approaches with physical observations. One of the most important physical observations is that the fatigue process can generally be broken into two distinct phases: initiation life and propagation life. The initiation life encompasses the development and early growth of a small crack. The propagation life is the portion of the total life spent growing a crack to failure. However, it is often very difficult, if not impossible, to define the transition from initiation to propagation. Often an engineering size crack for smaller components is assumed to be on the order of 0.25 mm. Synthetically, stress life approach is used mainly for long life application where stress and strain are elastic; strain life method is usually considered as an initiation approach (elastoplastic behaviour) and fracture mechanics is used to predict propagation life from an initial crack or defect.

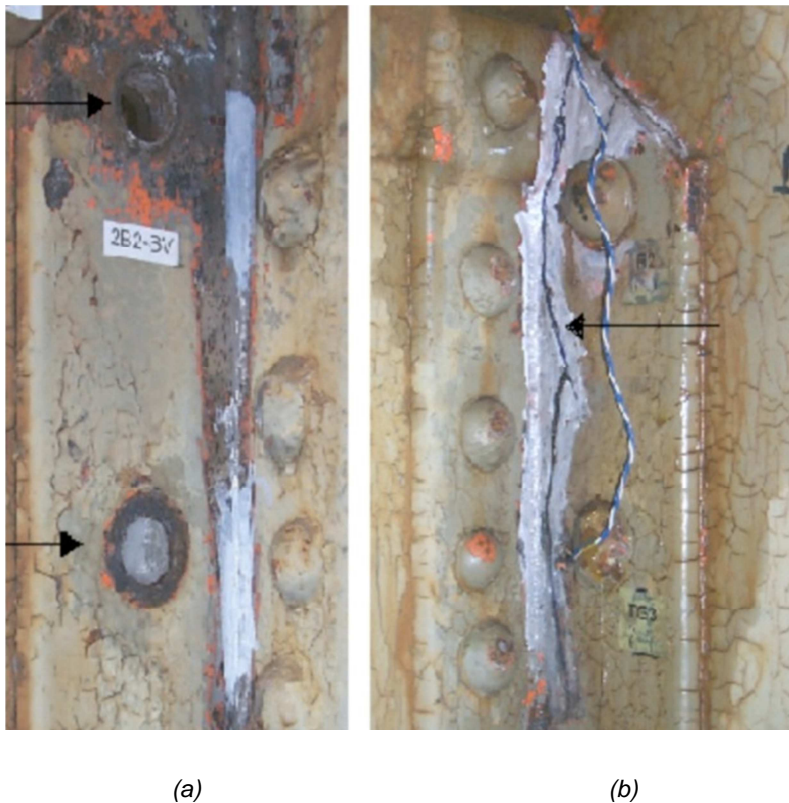


Figure 2. Example of fatigue damage in stringer-to-floor-beam connections: (a) at the junction between the rivet head and shank; (b) at the external leg of the connection angle [2].

3.2 Micromechanical process

Wood, in 1958, recognized the mechanism of the origin of fatigue in metals and alloys for first. Repeated cyclic straining of the material leads to different amounts of net slip on different glide planes, the consequent roughening of material rise from the irreversibility of shear displacement along the slip bands. This roughening is manifested as microscopic hills and valley at sites where slip bands emerge at the free surface. So The valleys generated function as micro-notches and the effect of stress concentration at the root of the valleys promotes additional slip and fatigue crack nucleation. The first documentation of slip-induced surface roughening during fatigue was made by Forsyth in 1953, the valleys and the hills are commonly referred to as “intrusions” and “extrusions”, respectively (Figure 3).

Nevertheless, Wood's hypothesis on the creation of surface roughness due to the *to-and-fro* motion of slip bands does not explain why the intrusions deepen progressively. Mott, in 1958, proposed a qualitative model in which screw dislocation moving along different paths by cross slip. The screw dislocation completes a circuit during a fatigue cycle; the volume encompassed by a circuit is then translated parallel to the dislocation by a distance equal to its Burgers vector. This displacement manifests itself in the form of an extrusion at the specimen surface. In 1979 Lin and Lin observed that the formation of obstacles to dislocation motion, such as creation of jogs as a consequence of edge-screw intersections and the intersection of two screw dislocations with a third dislocation at a node in a free surface, have all been suggested as possible gating mechanisms which would provide net irreversible slip during fatigue. The first quantitative statistical model for random slip leading to the formation of hills and valleys on fatigued surfaces was published by May in 1960 who adapted a variation of Mott's cross slip mechanism.

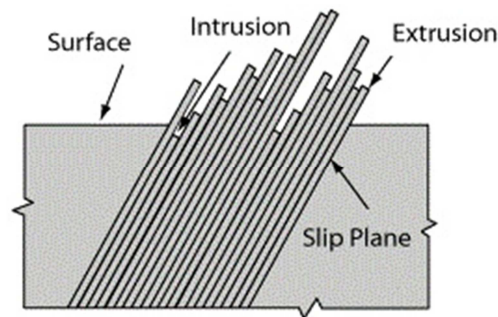
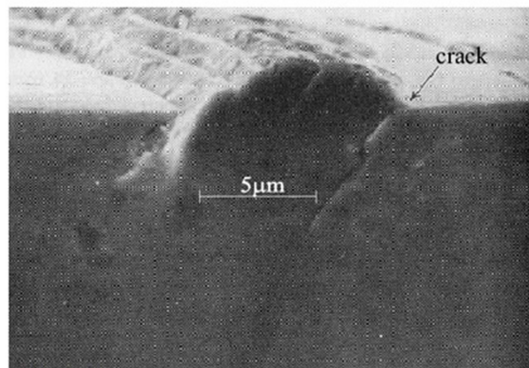


Figure 3. Intrusions and extrusions [3].

In engineering, components made of commercial materials, the principal sites of heterogeneous fatigue crack nucleation include voids, slag or gas entrapments, inclusion, dents, scratches, forging laps and folds, macroscopic stress concentration, as well as regions of microstructural and chemical non-uniformity. While surface grains are the most likely locations for crack initiation in metals and alloys of high purity, the formation of fatigue cracks is feasible at both near surface and interior locations in commercial alloys. The fatigue lifetime and the maximum fatigue strength of commercial alloys decreased by the presence of inclusion and pores (generally classified as defects). The mechanism of fatigue crack initiation at defects depends upon a number of mechanical, microstructural and environmental factors. These factors involve the relative strength values of the matrix and the defects, the slip characteristic of the matrix, the strength of the matrix-inclusion interface and the relative susceptibility to corrosion in the fatigue environment. If the cyclically loaded engineering component is exposed to a chemically aggressive medium during service, preferential attack of the environment at select locations on the material surface may provide nucleating sites for fatigue cracks. These sites are generally corrosion pits which form at surface locations where the slip steps or intrusion are created at the surface, the grain boundaries intersect the surface, the protective oxide layer on the surface is partially broken exposing the underlying fresh metal to preferential chemical attack, inclusion debonds from the surrounding matrix at near-surface locations and one of the constituent phase in a multiple alloy is preferentially corroded. Corrosion pits are typically smaller than a millimetre in depth and serve as micro-notches which locally elevate the stress level. Moreover, the pH level can be more acid causing possible acceleration in rate of fatigue crack growth. Experimental results have established that the formation of corrosion pits on the initially smooth surface of the fatigue specimen results in a significant reduction in the fatigue strength.

The analysis of fatigue cracking is generally based on the premise that fully compressive cyclic loads imposed periodically do not significantly modify the inception and crack growth. However, specific test, established that far-field compressive stresses can have a marked effect on both the initiation and propagation of fatigue cracks. Neglecting the influence of compression cycles in fatigue can lead to a non-conservative estimate of the useful fatigue life. The application of uniaxial cyclic compressive loads to notched plates of metallic materials causes the nucleation and growth of fatigue cracks along the plane of the notch, in a direction normal to the far-field compressive stress. The cracks propagate at a progressively slower rate until complete crack arrest takes place at a fatigue crack length. Hubbard (1969) found that fatigue cracks grew from the tip of

the notch over distances of several millimetres. The mechanism by which a fatigue crack initiates and advances in a direction normal to the imposed compression axis is dictated by the development of a cyclic plastic zone ahead of the notch tip upon unloading from the far-field compressive stress. For more details about initiation and propagation refer to [3].

3.3 Fatigue design

The preceding chapter concerned the crack initiation and propagation. The Stress-life and Strain-life methodologies are able to define the fatigue life of a component as a total number of cycles or time to induce fatigue damage and to initiate a dominant fatigue flaw which is propagated to final failure [3]. The philosophy underlying the cyclic stress/strain based approach is distinctly different from that of defect-tolerant methods to be considered previously where the fatigue life is taken to be only that during which a pre-existing fatigue flaw of some initial size is propagated to a critical size. Wohler, in the 1960s, introduced these methodologies introducing the concept of an “endurance limit” which characterizes the applied stress amplitude below which a defect-free material is expected to have an infinite fatigue life. This empirical method has found widespread use in fatigue analysis, mostly in applications where low-amplitude cyclic stresses induce primarily elastic deformation in a component which is designed for long life (*high cycle fatigue - HCF*) applications. When considerable plastic deformation occurs during cyclic loading (high stress amplitude or stress concentration) the fatigue life is markedly shortened. Here, fatigue design is called *low cycle fatigue – LCF*, and the important role of plastic strains had been highlighted by Coffin and Manson in 1954.

3.3.1 S-N curves and mean stress

Wohler characterized the fatigue life in terms of nominal stress amplitudes using experimental data obtained from rotating bend test on smooth (un-notched) specimens. From such an experiment, the stress amplitude σ_a for fully reversed loading is plotted against the number of fatigue cycles to failure N_f . The line illustrates (Figure 4) the stress-life plot observed for mild steels and other materials which harden by strain-ageing. Under constant amplitude loading conditions, these

THEORETICAL BACKGROUND

alloys exhibit a plateau in the stress-life plot typically beyond about 10^6 fatigue cycles. Below this plateau level, the specimen may be cycled indefinitely without causing failure. The value of σ_e is from 35% up to 50% of the tensile strength σ_{TS} for most steel alloys. The intercept of stress life curves with the ordinate is σ_{TS} at $\frac{1}{4}$ of the first fatigue cycle.

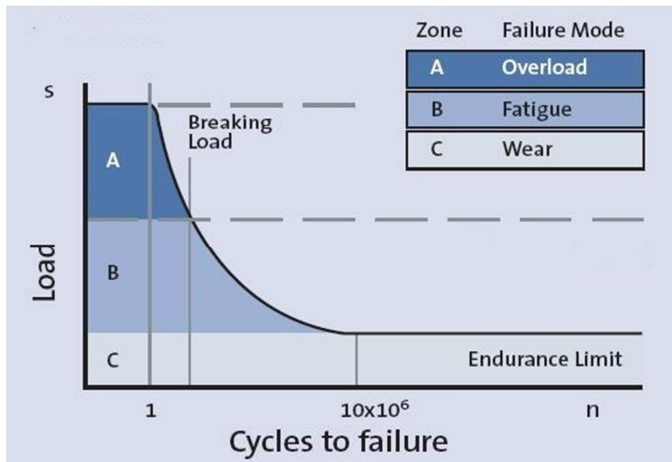


Figure 4. S-N Curve.

Many high strength steels do not generally exhibit a fatigue limit, σ_a continue to decrease and the endurance limit is defined as the stress amplitude which the specimen can support for at least 10^7 fatigue cycles. A linear relationship is observed if S-N curve is redrawn on a log-log scale. According to Basquin (1910) the resulting expression relating the stress amplitude (Equation (1)), in a fully reversed, constant amplitude fatigue test to the number of load reversal to failure, $2N_f$ is:

$$\sigma_a = \frac{\Delta\sigma}{2} = \sigma'_f (2N_f)^b \quad (1)$$

where:

σ'_f = fatigue strength coefficient (\cong fracture strength σ_f)

b = fatigue strength exponent which, for most metals, is -0.05: -0.12.

The S-N curve strictly pertains to the total fatigue life of a nominally smooth-surfaced, defect free material. Here, total life implies the number of cycles to initiate fatigue cracks in the smooth specimen plus the number of cycles to propagate the dominant fatigue crack to final failure. The fraction of the fatigue life which is expended in nucleating a dominant fatigue crack of engineering size (fraction of a mm) may vary from 0%, for specimens containing severe stress concentrations, rough surface or other surface defects, to as high as 80% in very carefully prepared, nominally defect free, smooth specimen of high purity materials.

The aforementioned empirical descriptions of fatigue life pertain fatigue loads where the mean stress $\sigma_m = 0$. Moreover, fully reversed stress cycles with a zero mean stress are not always representative because the mean level play an important role in influencing the fatigue behaviour. In case of sinusoidal waveform (Figure 5) with a nonzero mean stress, the stress amplitude and the mean stress are defined as (Equations (2) ÷ (5)):

$$\Delta\sigma = \sigma_{max} - \sigma_{min} \quad (2)$$

$$\sigma_a = \frac{\sigma_{max} - \sigma_{min}}{2} \quad (3)$$

$$\sigma_m = \frac{\sigma_{max} + \sigma_{min}}{2} \quad (4)$$

$$R = \frac{\sigma_{min}}{\sigma_{max}} \quad (5)$$

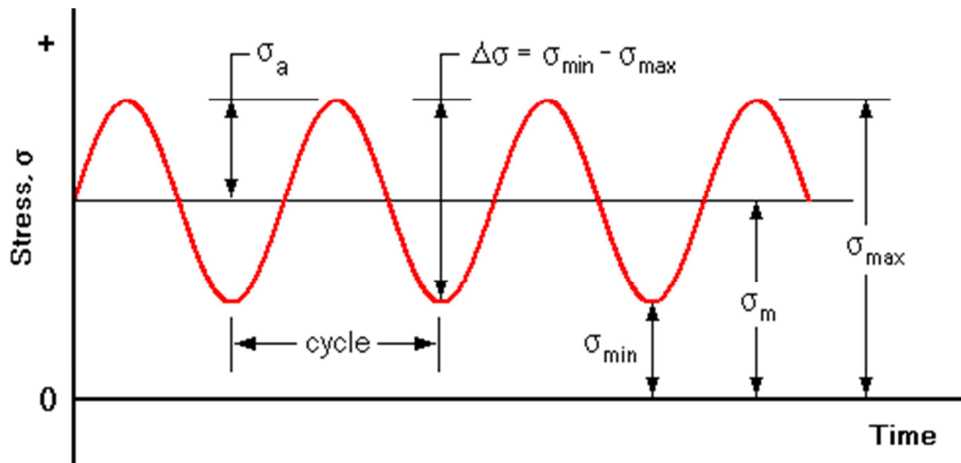


Figure 5. Sinusoidal waveform.

The load ratio R is equal to -1 for fully reversed loading, $R=0$ for zero-tension fatigue and $R=1$ for a static load. When the stress amplitude from a uniaxial fatigue test is plotted as a function of the number of cycles to failure, the curve is generally a strong function of the applied mean stress: a decreasing fatigue life with increasing mean stress value. Different combination of the stress amplitude and mean stress providing a constant fatigue life are modelled by Garber (1874), Goodman (1899) and Soderberg (1939) (Figure 6) (Equations (6) ÷ (8)).

$$\sigma_{a-Soderberg} = \sigma_a \left(1 - \frac{\sigma_m}{\sigma_y} \right) \quad (6)$$

$$\sigma_{a-Goodman} = \sigma_a \left(1 - \frac{\sigma_m}{\sigma_{TS}} \right) \quad (7)$$

$$\sigma_{a-Gerber} = \sigma_a \left(1 - \left(\frac{\sigma_m}{\sigma_{TS}} \right)^2 \right) \quad (8)$$

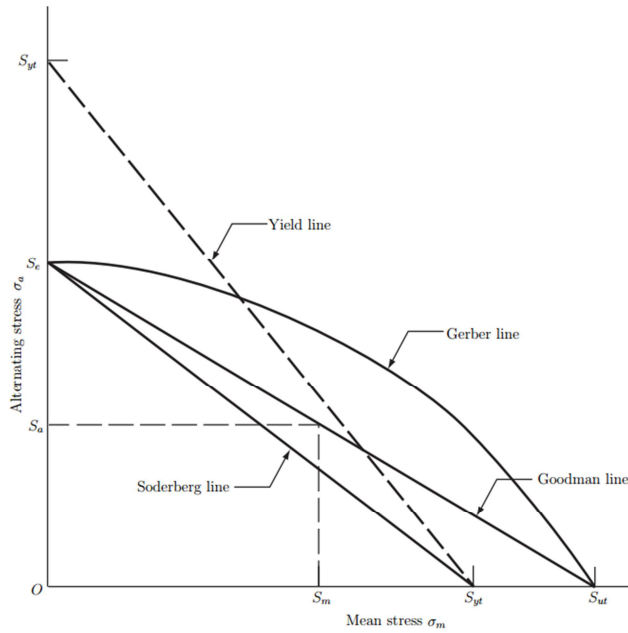


Figure 6. Life plots.

The constant life diagram for different mean stress levels is schematically represented in the Haigh diagram, Figure 7 affords a convenient graphical representation of the effects of mean stress on S-N curve.

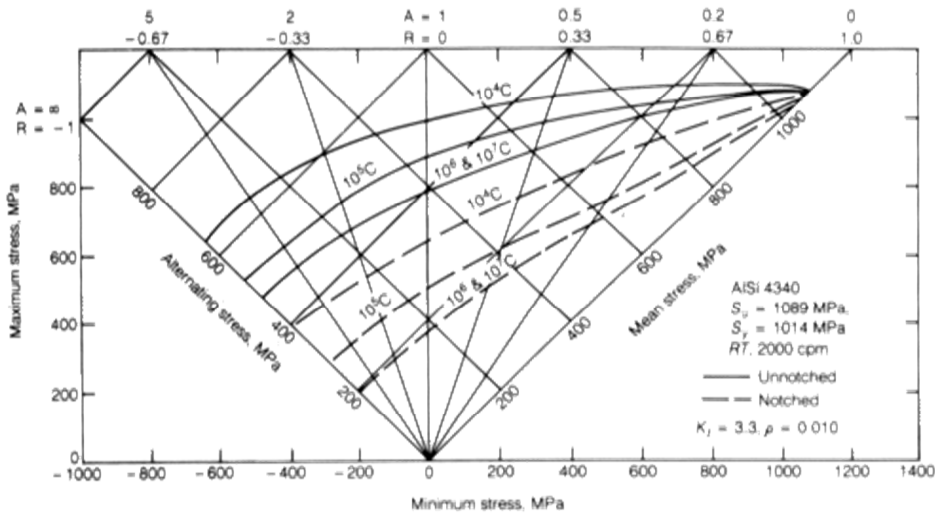


Figure 7. Haigh diagram.

Morrow, in 1968, has presented a modification of the Basquin relation [3] which accounts for mean stress effects in the following form (Equations (9) and (10)):

$$\sigma_a = (\sigma_f' - \sigma_m)(2N_f)^b \quad (9)$$

$$N_f = \left(1 - \frac{\sigma_m}{\sigma_r'}\right)^{1/b} \cdot N_{f|\sigma_m=0} \quad (10)$$

where N_f is the number of cycles to fatigue failure for any nonzero mean stress and $N_{f|\sigma_m=0}$ is the number of cycles to failure for zero mean stress.

3.3.2 *Damage, surface roughness and statistical reflection*

Engineering components are inevitably subjected to varying cyclic stress amplitudes, mean stresses and loading frequency. A simple criterion for predicting the extent of fatigue damage induced by a particular block of constant amplitude cyclic stresses is provided by Palmgren-Miner cumulative damage rule. In this loading sequences consisting of various blocks of different stress amplitudes the number of stress cycles imposed on a component gives the fraction of damage, the order in which the stress blocks of different amplitudes are imposed does not affect the fatigue life and the fatigue occurs when the linear sum of the damage from each load level reaches a critical value. If n_i is the number of cycles corresponding to the i -th block of constant stress amplitude σ_{ai} in a sequence of m blocks, and if N_{fi} is the number of cycles to failure at σ_{ai} , then the Palmgren-Miner damage rule (Equation (11)) states that failure would occur when:

$$\sum_{i=1}^m \frac{n_i}{N_{fi}} = 1 \quad (11)$$

The damage accumulation and the failure under variable amplitude loading condition are dictated by several concurrent mechanisms and that linear damage rule may lead to erroneous predictions of variable amplitude fatigue behaviour in many situations [3]. It is well established that tensile overloads applied to notched and cracked metallic materials reduce the rate of fatigue crack growth and the application of compressive overloads generally has the opposite trend. Even for smooth specimens, the linear damage rule provides incorrect results because of its omission of load sequence effects. Damage may occur even if a certain $\Delta\sigma$ is below the endurance limit (damage induced by previous loading) otherwise the application of load may enhance the fatigue limit even if lower than the fatigue limit itself (coaxing phenomenon).

A common site for the nucleation of a fatigue crack is the free surface of a component, the manner in which surface is prepared during the manufacturing of the component has a device role in dictating the initiation life for fatigue cracks. The valleys on the rough surface serve as stress concentration, which, in turn, induce different levels of resistance to fatigue crack nucleation. In addition to the roughness of the surface, the residual stresses that are induced by the surface treatments have an important effect on fatigue life. Moreover, residual stresses affect the fatigue behaviour of materials in the same way as the static mechanical stresses superimposed on a cyclic stress amplitude. Evidently, the residual stresses are favourable, if compressive, and detrimental, if tensile. The beneficial effect of residual stresses introduced by surface treatments becomes less significant at larger applied stresses because a large amplitude of the pulsating stress easily relaxes the residual stress. A widely used technique for improving the fatigue life of many engineering structural parts is shot-peening. The maximum compressive residual stress generated by the localized plastic deformation of the surface layer can reach about $\frac{1}{2}$ the yield strength of the material. As the shot-peen surface layer has a compressive mean stress, it acts to enhance significantly the total fatigue life by reducing the damaging effect of the tensile portion of fully reversed cyclic loads.

There are a number of sources of uncertainty in the analysis of fatigue results arose from uncertainties and errors in the estimation of material proprieties which include:

- microstructural variability or errors in the measurement of properties in the same batch of materials;
- uncertainties in the modelling of applied stresses for a given service condition and environmental (variability in stress amplitude during a known service cycle and lack of knowledge about the exact distribution of stress cycles);
- uncertainties in estimation of variation in loading intensity (traffic load);

- uncertainties in modelling.

A basic concept commonly adopted (Equations (12) ÷ (14)) for the statistical characterization of fatigue data include the coefficient of variation C_{var} , the mean $m_{x,rv}$ and the standard deviation $\sigma_{x,rv}$:

$$C_{var} = \frac{\sigma_{x,rv}}{m_{x,rv}} \quad (12)$$

$$m_{x,rv} = \frac{1}{N_s} \sum_{i=1}^{N_s} x_{rvi} \quad (13)$$

$$\sigma_{x,rv}^2 = \frac{1}{N_s} \sum_{i=1}^{N_s} (x_{rvi} - m_{x,rv})^2 \quad (14)$$

where N_s denotes the samples number of a random variable x_{rv} . A distribution in the value of the random variable is usually characterized in terms of log-normal distribution, Weibull distribution or normal distribution (Equation (15)):

$$f_n(x_{rv}) = \frac{1}{\sqrt{2\pi}(\sigma_{x,rv})} \exp \left[-\frac{1}{2} \left(\frac{x_{rv} - m_{x,rv}}{\sigma_{x,n}} \right)^2 \right] \quad (15)$$

Usually, the fatigue strength or the endurance limit values listed form experiments represent the arithmetic mean derived from multiple experiments. Since there is variability in solid property experiments conducted on the same material may not give the same arithmetic mean of the critical strength parameter. To address this issue, Weibull in 1939 proposed the concept of probability of failure P at given failure strength, σ_f normalized by an average value of a critical stress $\sigma_{cr,ave} = \sigma_e$ (Equation (16))

$$P = 1 - \exp \left[- \left(\frac{\sigma_f}{\sigma_{f,0}} \right)^{m_w} \right] \quad (16)$$

Weibull diagram is obtained taking the logarithm.

3.3.3 Stress concentration

Engineering structures may contain stress concentration which are the principal sites for the inception of fatigue flaws. The stress and the deformation fields in the immediate vicinity of stress concentration have a strong bearing on how the fatigue cracks nucleate and propagate [3]. The theoretical elastic stress concentration factor K_t relates the local stress ahead of the notch tip to far-field loading and it is defined as the ratio of the maximum local stress σ_{max} to the nominal stress S . Under fatigue loading condition, the elastic stress concentration factor is replaced by the fatigue notch factor K_f (un-notched bar endurance limit/notched bar endurance limit). Fatigue experiments suggest that notches produce a less concentrating effect than predicted by theoretical elastic analysis. Notch sensitive index (Equation (17))

$$q = \frac{K_f - 1}{K_t - 1} \quad (17)$$

measures the degree of agreement between theoretical predictions and actual effects. The parameter varies from zero (no notch effect) to unity (full effect predicted by elasticity theory) K_t , (Equation (18)) studied by Peterson (1959) is a function only of the component geometry and loading mode.

$$K_f \cong 1 + \frac{K_t - 1}{1 + \frac{A_n}{\rho}} \quad (18)$$

where A_n is a constant whose value depends on the strength and ductility of the material (0.25 mm → 0.025 mm) and ρ is the notch-root radius. This method is unsuitable for situations where considerable plastic deformation occurs ahead of the stress concentration. Considering a notched member that is subjected to cyclic loading with a nonzero mean stress in such a way that only elastic conditions prevail at all times throughout the member. If S , S_m and S_a are the instantaneous value, the mean value, and the amplitude, respectively, of the nominal far-field cyclic stress imposed on the notch member, the local stress amplitude and mean stress (Equations (19) and (20)) at the tip of the notch can be computed from the fatigue notch factor K_f such that

$$\sigma_a = K_f S_a \quad (19)$$

$$\sigma_m = K_f S_m \quad (20)$$

In order to assess the effect of the mean stress on fatigue life, the modified Goodman equation may be employed.

An interesting phenomenon associated with tensile fatigue cracks growing ahead of stress concentration involves the non-propagating flaws. Frost and Dugdale (1957) observed that fatigue cracks emanating from notches can arrest completely after growing some distance. Experimental measurements based on total life have shown that the non-propagation or arrest of fatigue flaws occurs only ahead of sharp notches, above a certain critical value of K_t .

Considering a fatigue specimen, which is subject to multiaxial cyclic loads, the proportional loading is considered to occur if, during changes and fluctuations in the imposed loads, the different components of the stress tensor vary in constant proportion to one another. At given reference point in the material, proportional loading exists if principal stresses at point $\sigma_1, \sigma_2,$ and σ_3 vary in the following manner (Equation (21)):

$$\frac{\sigma_2}{\sigma_1} = \lambda_1; \frac{\sigma_3}{\sigma_1} = \lambda_2 \quad (21)$$

where λ_1 and λ_2 are scalar constants which may vary from point to point, but are constant for a given material point in the solid. If fully reversed cyclic loading is present, where all cyclic loads are perfectly in phase with one another, σ_x , σ_y and σ_z denote the three normal components of stress applied to a fatigue specimen and let τ_{xy} , τ_{yz} and τ_{zx} denote the three shear stress components. The effective stress, which characterizes the deformation of the material is then assumed to be that given by the von Mises criterion (Equation (22)) based on the octahedral shear stress:

$$\sigma_e = \frac{1}{\sqrt{2}} \sqrt{(\sigma_x - \sigma_y)^2 + (\sigma_y - \sigma_z)^2 + (\sigma_z - \sigma_x)^2 + 6(\tau_{xy}^2 + \tau_{yz}^2 + \tau_{zx}^2)} \quad (22)$$

One of the major drawbacks of such effective stress approaches is that the differing effects of axial tension and compression mean stress in multiaxial fatigue test may not be accurately captured. In addition, the orientation of fatigue cracks with respect to the loading axes is not quantitatively determined from such criteria. A wide variety of experimental observations reveals that the normal stress also plays a critical role in influencing fatigue life in multiaxial loading.

For pure torsion loading, a variety of independent experimental studies (Sines 1959) shown that a superimposed mean static torsion has no effect on the fatigue limit of metals, although a superimposed static tension or bending stress has a marked effect on the fatigue life in normal cyclic loading. Essentially, throughout the fatigue life, failure occurs on planes of maximum shear. This damage process is classified as *regime A*: the cracks were confined to the planes of maximum shear through the fatigue life. The fraction of life expended in initiating a dominant shear cracks is less than 10%; the remaining 90% of life is spent in propagating this shear crack. Form 10^6 cycles (for example), the local mode of failure (*regime B*) occurs on planes oriented normal to the local principal tensile stress, with the microscopic tensile cracks oriented at 45° to the shear cracks. If the material is subjected to axial tension fatigue, a different failure pattern emerges throughout the life. In both low-cycle and high-cycle fatigue failure regimes, the macroscopic crack plane is approximately normal to the tensile loading axis. The *regime A* begin before 10^5 cycles (for example), the local mode of microscopic cracking is along planes of maximum shear stress. This microscopic mode of initial crack advance in tension fatigue is commonly referred to as *Stage I* where single slip failure along planes of local maximum shear induces a serrated or faceted fracture morphology. Within regime A, the fraction of life expended in nucleating a dominant fatigue crack

gradually rises from approximately 40% at 10^5 cycles. Over 10^6 cycles, regime B, a tensile mode of failure emerges under imposed tension fatigue, with the fraction of total life expended in nucleating a dominant fatigue flow (1 mm in size) gradually rising to as high as 90% at 10^7 cycles. Such a mode of failure is commonly referred to a *Stage II*. The extent to which regimes A and B individually dominate the total fatigue life, and the fraction of total life expended in creating a dominant flaw within each of these regimes is a strong function of the composition and microstructure of the material, and of the test environment. Locally tensile failure patterns can also be induced in some alloys subjected to cyclic torsion, especially in the high-cycle fatigue regime.

3.3.4 Strain based design

In many practical applications, engineering components generally undergo a certain degree of structural constraint and localized plastic flow, particularly at locations of stress concentrations. In this situation it is more appropriate to consider the strain-life approach to fatigue. Coffin and Manson (1954) proposed a characterization of fatigue based on the plastic strain amplitude, the logarithm of the plastic strain amplitude was plotted against the logarithm of the number of load reversal to failure a linear relationship resulted is (Equation (23)):

$$\frac{\Delta\varepsilon_p}{2} = \varepsilon'_f (2N_f)^c \quad (23)$$

where:

ε'_f = fatigue ductility coefficient (\cong true fracture ductility ε'_f in static tension)

c = fatigue ductility exponent (-0.5: -0.7).

The total strain amplitude (Equation (24)) is the sum of elastic strain amplitude $\frac{\Delta\varepsilon_e}{2}$ and the plastic strain amplitude $\frac{\Delta\varepsilon_p}{2}$:

$$\frac{\Delta\varepsilon}{2} = \frac{\Delta\varepsilon_e}{2} + \frac{\Delta\varepsilon_p}{2} \quad (24)$$

The equation can be rewritten as (Equation (25)):

$$\frac{\Delta\varepsilon_p}{2} = \frac{\sigma'_f}{E} (2N_f)^b + \varepsilon'_f (2N_f)^c \quad (25)$$

and form the basis for strain-life approach to fatigue design and has found widespread application in structural practice. In order to examine the implications of the variations of the elastic, plastic and total strain amplitudes, it is useful to consider a transition life that is defined as the number of reversal to failure at which the elastic and plastic strain amplitudes are equal. At short fatigue lives plastic strain amplitude is more dominant than the elastic strain amplitude and the fatigue life of the material is controlled by ductility. At long fatigue life lives the elastic strain amplitude is more significant than the plastic strain amplitude and the fatigue life is dictated by the rupture strength. Optimizing the overall fatigue properties thus inevitably requires a judicious balance between strength and ductility (Mitchell 1968). Mean stress effects also been incorporated into strain life relationship (Equation (26)):

$$\frac{\Delta\varepsilon_p}{2} = \frac{\sigma'_f - \sigma_m}{E} (2N_f)^b + \varepsilon'_f (2N_f)^c \quad (26)$$

Cycle-dependent relaxation of the mean stress under strain-controlled fatigue loading is a counterpart of the cyclic creep mechanism, for example considering a ductile solid which is subjected to a fixed amplitude of cyclic strains (mean strain is tensile). If the material exhibits cyclic softening behaviour, the flow stress at the imposed strain level is expected to be lower than the previous cycle. With a tensile mean strain level, the tendency for similar behaviour in compression is not significant, and consequently, the shape of the hysteresis loop will be roughly the same. The rate of decrease in mean stress progressively diminishes as the mean stress level approaches zero.

The local strain approach relates deformation occurring in the immediate vicinity of a stress concentration to the remote stresses and strain. The local stress and strain histories at the tip of the notch must be known: either simple analytical expressions or detailed finite element simulations of the notch tip deformation are developed to relate the local stresses and loading to far field loading; alternatively, the notch tip deformation is experimentally monitored with the aid of strain gages. In the second

part, fatigue life that can be expected for the local stress and strain histories must be determined: the damage accumulation from the local stress and strain histories must also be estimated so that the safe fatigue properties measured on smooth laboratory test specimen.

4 HISTORICAL BRIDGES

4.1 Steel

The production of steel in the end of the 19th and the beginning of the 20th century was performed by pouring the melt steel from the oven in to a chill mould. The cooling process in the mould started from the borders, pure steel formed and unwanted alloys and impurities increase towards the centre of the melt. Concentrations of unwanted particles on the top of the chill mould are then removed before rolling. Due to this manufacturing process, impurities and blisters increases in the middle of the steel. Nowadays, steel produced under these circumstances is considered appropriate as structural steel. The high concentrations of unwanted compounds in the middle of the steel that drastically lower the quality of the rolled products formed from these steels and the blister formations makes these steels not good. A plate manufactured with the technique described above has steel with very good qualities at the surface while the centre of the plate will have more brittle properties. Based on different investigation and studies, the European Guidelines provide the following reference values (Table 1 and Table 2):

Reference values		
Ultimate tensile strength f_u	370÷460	MPa
Yield stress f_y	240	MPa
Young's modulus E	200	GPa
Shear modulus G	81	GPa
Density ρ	78,5	kN/m ³
Resistance factor γ_R	1,10	-
Ultimate elongation $\lambda_{10}\lambda_5$	20÷25	%

Table 1

Stress limits		
Traction, compression, bending (net section) f_y	220	MPa
Shear (gross section) τ_R	125	MPa
Bearing pressure for rivets	440	MPa

Table 2

This information is the basis for static and cyclic considerations about old riveted structures ([4]). The technique of riveting bridges is obsolete and knowledge concerning riveted structure's ability to withstand fatigue has not been investigated to the same extent as for modern structures assembled by welding.

4.2 Fatigue design code

The fatigue design code proposed in Europe is EN 1993-1-9 [5]. A constant amplitude cyclic loading is not particularly common in structures. The constant amplitude fatigue limit starts at $N = 5 \cdot 10^6$ cycles. By contrast, if the loading varies, the design curve will have an inclination $m = 5$ and the cut-off limit appears at $N = 10^8$ cycles. In the evaluation process to determine appropriate detail categories, the value of the stress range $\Delta\sigma_c$ corresponding to a value of $N = 2$ million cycles were evaluated with a 75% confidence level of 95% survival probability in $\log N$. The fatigue resistance is obtained from the following equations, for constant amplitude nominal stress (Equation (27)):

$$\Delta\sigma_R^m * N = \Delta\sigma_c^m * 2 * 10^6 \tag{27}$$

where $m=3$ and $N \leq 5 \cdot 10^6$. See Figure 8.

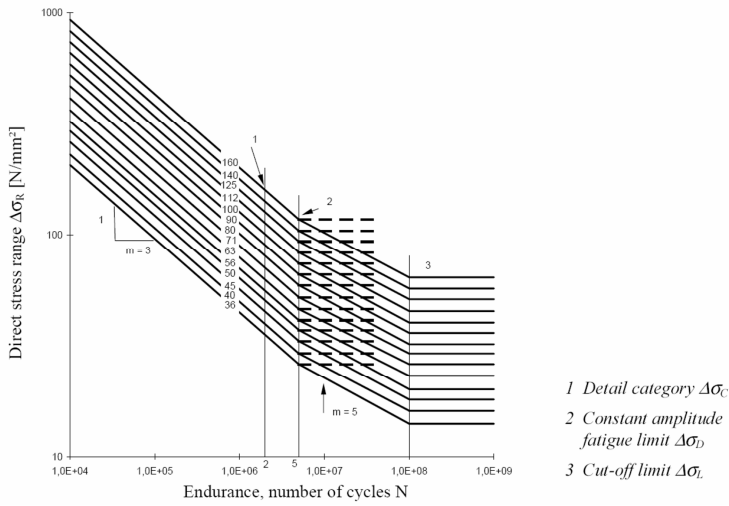


Figure 8. EN 1993 -1-9: fatigue strength curves

The fatigue strength curves for shear stress ranges are arranged in a similar way:

$$\Delta\tau_R^m * N = \Delta\tau_C^m * 2 * 10^6 \quad (28)$$

where $m=5$ and $N \leq 5 * 10^8$. See Figure 9 for more details.

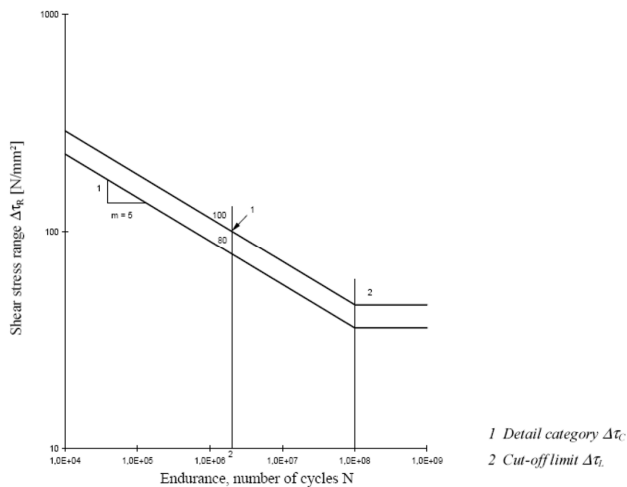


Figure 9. EN 1993 -1-9: fatigue shear strength curves

4.3 Riveted structures

In order to be able to make accurate assessments of existing bridges, it is of great importance to know the stress concentration inside the material. Elastic deformation of steel is related to the cohesive powers between atoms in the “smallest” part in the steel (Ferrite and Austenite). When the atomic structure is exposed to a force, its “body” alters form, from a cubic shape to a more stretched rectangular box. When the force is removed the atomic structure takes its original shape. Plastic deformations do not occur in a similar way. In metals, there are dislocations in the atomic structure. Dislocation moves in atomic slip planes, the movements are a result of shear stress acting on grains. Fatigue failures occur when microscopic crack in the material weaken the structure. The crack will continue to propagate until the remaining material can no longer stand the load and so it fails. In order to assess the fatigue in structures, the only concern is the variable stress near the holes, in the rivet shank and in the plates. Wöhler discovered that fatigue tests are characterised by a big scatter of the results. Further test evaluations have been carried out, components are retrieved from bridges that have been in service for 100 years or more. Often, the number of cycles that the components have been exposed during their service, are not known. A brief summary of fatigue test has been reported in the follow (refer to [4]). Fatigue tests are plotted in log scale diagrams with the number of cycles on the horizontal axis and the stress range on the vertical axis (Figure 10). All tests are compared to detail category $C = 71$, in the legend of the diagrams each research has been assigned to a different symbol. The endurance of plate and truss girders has been evaluated as the 5% fractile with a 75% significance level as suggested in EN 1993-1-9 ([5]).

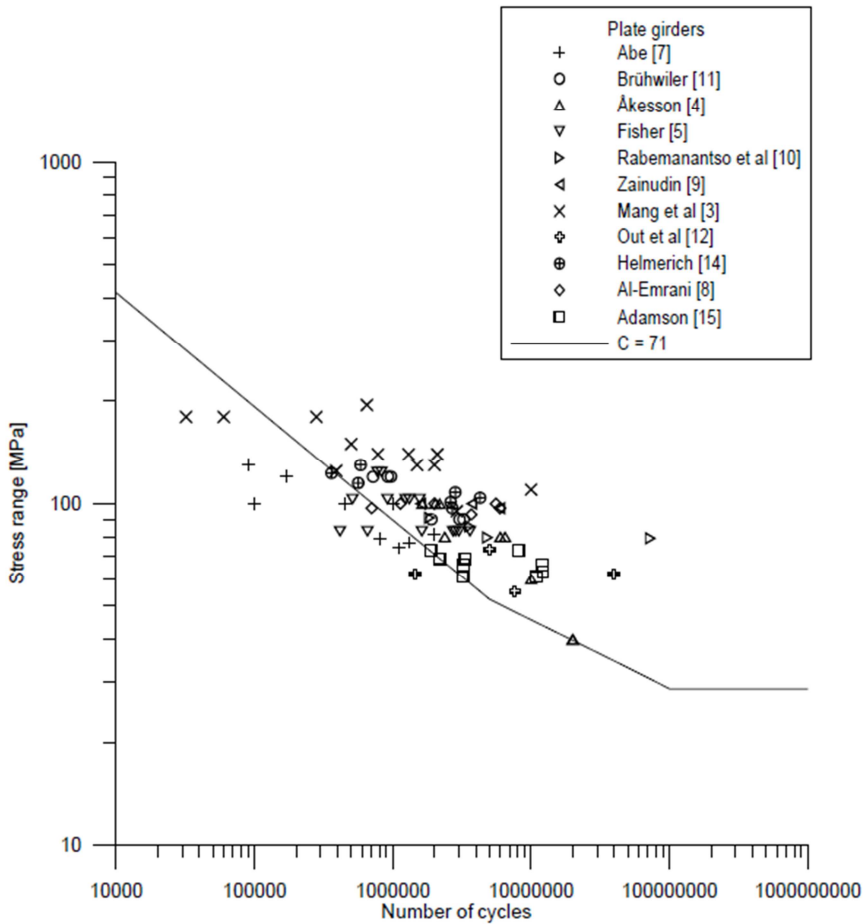


Figure 10. Category C=71.

The endurance of many of the tests in Figure 10 is lower than predicted by detail category C = 71. Tests with heavy corrosion were removed in order to separate its influence. From investigations conducted by Forsberg [6] the effect of corrosion and notches lowered the fatigue endurance by several detail categories. From this results one can see that an acceptable fit is achieved with the 5% fractile and C = 71 for $N \leq 5 \cdot 10^6$ cycles. The evaluation has been carried out to obtain an indication of the feasibility of using the detail category C =71 to predict the fatigue endurance of riveted plate girders in railway bridges. The detail category of a distribution should according to EC EN 1993-1-9 [87] be the 5% fractile with a 75% significance level.

4.4 Remaining life

For determination of the remaining life of structures due to fatigue, the most applied method is Miners rule. Miners rule is a linear approach able to determine the accumulated damage caused by variable stress cycles. The damage at a certain stress range is proportional to the number cycles (Equation (29)):

$$\sum_{i=1}^n \frac{n_i}{N_i} = \frac{n_1}{N_1} + \dots + \frac{n_2}{N_2} = 1 \quad (29)$$

where:

- N_i is the fatigue endurance at a constant stress range $\Delta\sigma$ indicates the space for the available cycles to occur;
- n_i is the number of cycles at a certain stress range have affected a detail.

Miners rule is not exact, however for the majority of stress spectra it will provide a safe estimation. For example, when the stress range contains large amounts of cycles under the cut off limit (stress level where no fatigue accumulation occurs), Miners rule will overestimate the fatigue life. The equivalent constant amplitude stress spectrum is obtained by (Equation (30)):

$$\sigma_e = \Delta\sigma_{max} \sqrt[m]{\sum_{i=1}^n \frac{n_i}{n} \left(\frac{\Delta\sigma_i}{\Delta\sigma_{max}}\right)^m} \quad (30)$$

for $n \leq 5 \cdot 10^6$, $m=3$ and n = total number of cycles.

5 RIVETS OVERVIEW

A rivet is a monolithic steel element composed by two heads and one short bar (Figure 11). The cylindrical portion of the rivet is called shank or body and the lower portion of shank is known as tail. Riveted joints are widely used in order to make permanent fastening between the plates. Permanent fastenings cannot be disassembled without destroying the connecting components. The function of rivets in a joint is to make a connection that has strength and tightness. The strength is necessary to prevent the failure of the joint [7]. The tightness is necessary in order to involve the friction between the plates. In a rivet joint, the holes in the plates are punched and reamed or drilled. Punching is the cheapest method and is used for relatively thin plates and in structural work (Figure 12). Since punching injures the material around the hole, therefore drilling is used in most marine and aeronautic engineering. In structural riveting, the diameter of the rivet hole is usually 1.5 mm larger than the nominal diameter of the rivet.

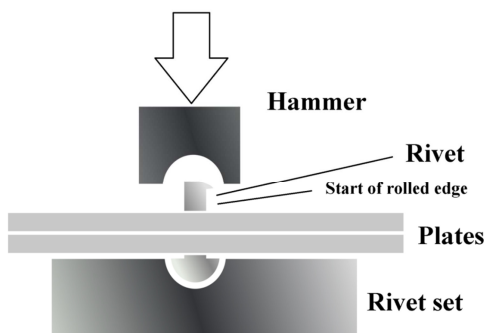


Figure 11. Rivet schematic realization.



Figure 12 Rivet installation.

The plates are drilled together and then separated to remove any burrs or chips so as to have an accurate joint. A red-hot rivet (Figure 13) is introduced into the plates and the second head is then formed. The riveting is done by hand or by a riveting machine. In hand riveting, the original rivet head is backed up by heavy bar, then the die is placed against the end to be headed and a hammer applies the blows.

This causes the expansion of the shank thus filling the hole and the tail is converted into a point. As the rivet cools, it tends to contract. The lateral contraction will be slight, but there will be a longitudinal tension introduced in the rivet that holds the plates firmly together. In machine riveting, the die is a part of the hammer that is operated by air, hydraulic or steam pressure. For more details see [8].

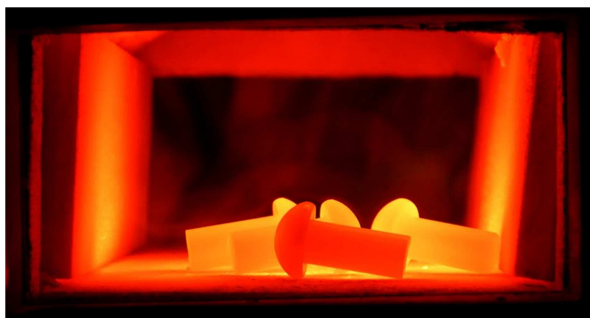


Figure 13 Hot rivet.

During the manufacturing process some imperfections may occur due to the low mechanization level. Usually, the manufactured head is regular but the driven head exhibits characteristic imperfections such as head irregularity (Figure 14, Figure 15 and Figure 16) and head misalignment (Figure 17). Some imperfections might relate the shank including trapezoidal shape and excessive length (Figure 18 and Figure 19). An ulterior joint imperfection may involve the plates alignment, the curvature (Figure 20 and Figure 21) or the hole shape (Figure 22). All these unwanted flaws produce a weakness in the riveted joint and a more fragile behaviour.

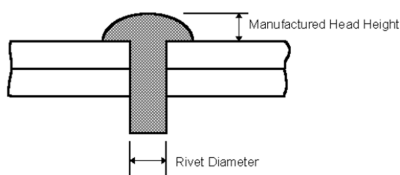


Figure 14. Manufactured Rivet.

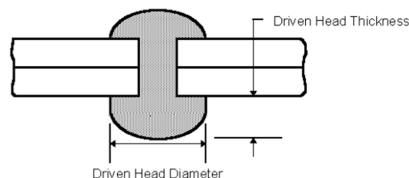


Figure 15. Driven Rivet.

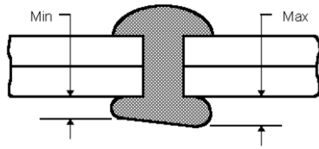


Figure 16. Driven Head imperfections.

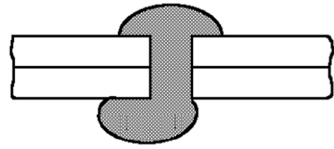


Figure 17. Driven Head misalignment.

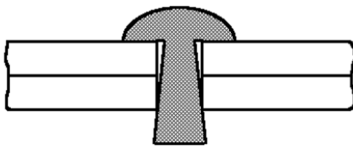


Figure 18. Shank imperfection.

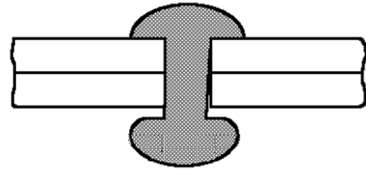


Figure 19. Shank deformation.

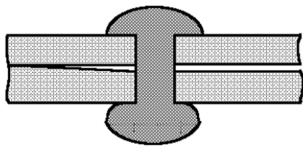


Figure 20. Plate gap.

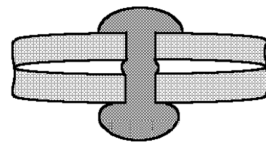


Figure 21. Plate curvature.

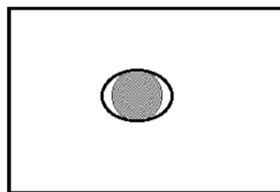


Figure 22. Hole imperfection.

For more details about rivet see [8].

5.1 Historical considerations

Riveting is one of the oldest methods of joining materials. Moreover, rivets were the principal fasteners adopted in the early 20th century for most structures such as bridges and buildings (Figure 24). It had long been known that hot-driven rivets generally produced clamping forces. The axial force was not controlled and it varied substantially by the reason of the manufacturing technique. However, it could not be evaluated for design. Rivets are made from bar stock by either hot- or cold-forming the manufactured head. Usually, the head is of the high button-type. Their use has declined steadily since the introduction of the high-strength bolts. Nowadays they are infrequently used in other fields or shop connections, whereas high-strength bolts or welds are used almost exclusively in new works. In Italy, many rivets are now replaced by bolts because they provide an equal or superior connection and their cost of installing is cheaper. The stress versus strain relationships for typical, un-driven A502 rivets with 12,82 mm diameter are shown in the Figure 23 below:

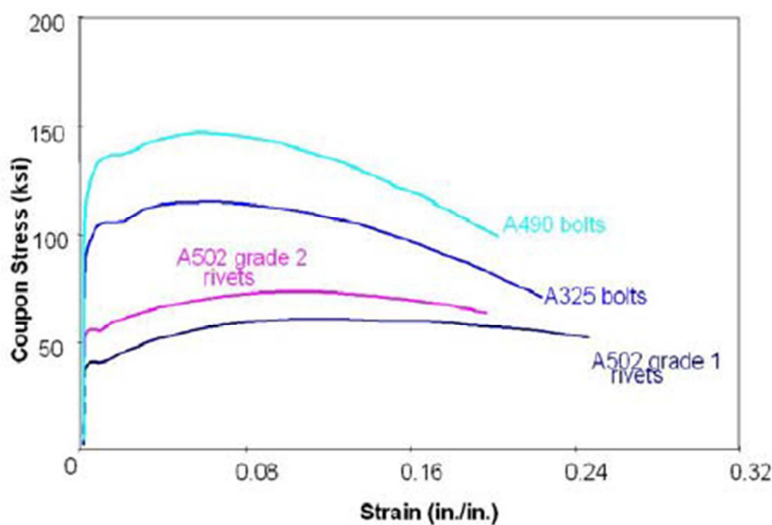


Figure 23. Stress – Strain diagram.

The graph (Figure 23) points out that bolts have a high yield and strength value compared to rivets. However, the ductility is the same. The increasing importance of evaluation and retrofitting of existing structures will require a well-informed designer

having expertise about riveted connections. Structural rivet steels are of three types [9]:

- ASTM A502 grade 1, carbon rivet steel (comparable to ASTM A141);
- ASTM A502 grade 2, high-strength structural steel rivets;
- ASTM A502 grade 3, similar to grade 2 but with enhanced atmospheric corrosion resistance.

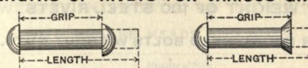
The mechanical Brinell hardness requirements for A502 rivet steel are: (Table3)

Grade	1		2		3	
	Min	Max	Min	Max	Min	Max
Brinell, 10 mm ball	103	126	137	163	137	197

Table3

BETHLEHEM STEEL COMPANY. 267

LENGTHS OF RIVETS FOR VARIOUS GRIPS.



Grip of Rivet, Inches.	DIAMETER OF RIVET.					DIAMETER OF RIVET.					Grip of Rivet, Inches.
	1/4"	3/8"	1/2"	3/4"	1"	1/2"	3/8"	1/2"	3/4"	1"	
1/8	1 1/4	1 3/8	1 7/8	2	2 1/8	1 1/4	1 1/4	1 1/4	1 3/8	1 3/8	1/8
3/16	1 5/8	1 7/8	2	2 1/8	2 1/4	1 1/4	1 3/8	1 3/8	1 3/8	1 3/8	3/16
1/4	1 3/4	2	2 1/8	2 1/4	2 3/8	1 3/8	1 3/8	1 3/8	1 3/8	1 3/8	1/4
5/16	1 7/8	2 1/8	2 1/4	2 3/8	2 3/4	1 3/8	1 3/8	1 3/8	1 3/8	1 3/8	5/16
3/8	2	2 1/4	2 3/8	2 3/4	2 3/4	1 3/8	1 3/8	1 3/8	1 3/8	1 3/8	3/8
1/2	2 1/8	2 3/8	2 3/4	2 3/4	2 3/4	1 3/8	1 3/8	1 3/8	1 3/8	1 3/8	1/2
5/8	2 3/8	2 3/4	2 3/4	2 3/4	2 3/4	1 3/8	1 3/8	1 3/8	1 3/8	1 3/8	5/8
3/4	2 3/4	2 3/4	2 3/4	2 3/4	2 3/4	1 3/8	1 3/8	1 3/8	1 3/8	1 3/8	3/4
7/8	2 3/4	2 3/4	2 3/4	2 3/4	2 3/4	1 3/8	1 3/8	1 3/8	1 3/8	1 3/8	7/8
1	2 3/4	2 3/4	2 3/4	2 3/4	2 3/4	1 3/8	1 3/8	1 3/8	1 3/8	1 3/8	1
1 1/8	2 3/4	2 3/4	2 3/4	2 3/4	2 3/4	1 3/8	1 3/8	1 3/8	1 3/8	1 3/8	1 1/8
1 1/4	2 3/4	2 3/4	2 3/4	2 3/4	2 3/4	1 3/8	1 3/8	1 3/8	1 3/8	1 3/8	1 1/4
1 1/2	2 3/4	2 3/4	2 3/4	2 3/4	2 3/4	1 3/8	1 3/8	1 3/8	1 3/8	1 3/8	1 1/2
1 3/4	2 3/4	2 3/4	2 3/4	2 3/4	2 3/4	1 3/8	1 3/8	1 3/8	1 3/8	1 3/8	1 3/4
1 5/8	2 3/4	2 3/4	2 3/4	2 3/4	2 3/4	1 3/8	1 3/8	1 3/8	1 3/8	1 3/8	1 5/8
1 7/8	2 3/4	2 3/4	2 3/4	2 3/4	2 3/4	1 3/8	1 3/8	1 3/8	1 3/8	1 3/8	1 7/8
2	2 3/4	2 3/4	2 3/4	2 3/4	2 3/4	1 3/8	1 3/8	1 3/8	1 3/8	1 3/8	2
2 1/8	2 3/4	2 3/4	2 3/4	2 3/4	2 3/4	1 3/8	1 3/8	1 3/8	1 3/8	1 3/8	2 1/8
2 1/4	2 3/4	2 3/4	2 3/4	2 3/4	2 3/4	1 3/8	1 3/8	1 3/8	1 3/8	1 3/8	2 1/4
2 1/2	2 3/4	2 3/4	2 3/4	2 3/4	2 3/4	1 3/8	1 3/8	1 3/8	1 3/8	1 3/8	2 1/2
2 3/8	2 3/4	2 3/4	2 3/4	2 3/4	2 3/4	1 3/8	1 3/8	1 3/8	1 3/8	1 3/8	2 3/8
2 1/2	2 3/4	2 3/4	2 3/4	2 3/4	2 3/4	1 3/8	1 3/8	1 3/8	1 3/8	1 3/8	2 1/2
2 3/4	2 3/4	2 3/4	2 3/4	2 3/4	2 3/4	1 3/8	1 3/8	1 3/8	1 3/8	1 3/8	2 3/4
2 5/8	2 3/4	2 3/4	2 3/4	2 3/4	2 3/4	1 3/8	1 3/8	1 3/8	1 3/8	1 3/8	2 5/8
2 3/2	2 3/4	2 3/4	2 3/4	2 3/4	2 3/4	1 3/8	1 3/8	1 3/8	1 3/8	1 3/8	2 3/2
2 7/8	2 3/4	2 3/4	2 3/4	2 3/4	2 3/4	1 3/8	1 3/8	1 3/8	1 3/8	1 3/8	2 7/8
3	2 3/4	2 3/4	2 3/4	2 3/4	2 3/4	1 3/8	1 3/8	1 3/8	1 3/8	1 3/8	3
3 1/8	2 3/4	2 3/4	2 3/4	2 3/4	2 3/4	1 3/8	1 3/8	1 3/8	1 3/8	1 3/8	3 1/8
3 1/4	2 3/4	2 3/4	2 3/4	2 3/4	2 3/4	1 3/8	1 3/8	1 3/8	1 3/8	1 3/8	3 1/4
3 1/2	2 3/4	2 3/4	2 3/4	2 3/4	2 3/4	1 3/8	1 3/8	1 3/8	1 3/8	1 3/8	3 1/2
3 3/8	2 3/4	2 3/4	2 3/4	2 3/4	2 3/4	1 3/8	1 3/8	1 3/8	1 3/8	1 3/8	3 3/8
3 1/2	2 3/4	2 3/4	2 3/4	2 3/4	2 3/4	1 3/8	1 3/8	1 3/8	1 3/8	1 3/8	3 1/2
3 3/4	2 3/4	2 3/4	2 3/4	2 3/4	2 3/4	1 3/8	1 3/8	1 3/8	1 3/8	1 3/8	3 3/4
3 5/8	2 3/4	2 3/4	2 3/4	2 3/4	2 3/4	1 3/8	1 3/8	1 3/8	1 3/8	1 3/8	3 5/8
3 3/2	2 3/4	2 3/4	2 3/4	2 3/4	2 3/4	1 3/8	1 3/8	1 3/8	1 3/8	1 3/8	3 3/2
3 7/8	2 3/4	2 3/4	2 3/4	2 3/4	2 3/4	1 3/8	1 3/8	1 3/8	1 3/8	1 3/8	3 7/8
4	2 3/4	2 3/4	2 3/4	2 3/4	2 3/4	1 3/8	1 3/8	1 3/8	1 3/8	1 3/8	4
4 1/8	2 3/4	2 3/4	2 3/4	2 3/4	2 3/4	1 3/8	1 3/8	1 3/8	1 3/8	1 3/8	4 1/8
4 1/4	2 3/4	2 3/4	2 3/4	2 3/4	2 3/4	1 3/8	1 3/8	1 3/8	1 3/8	1 3/8	4 1/4
4 1/2	2 3/4	2 3/4	2 3/4	2 3/4	2 3/4	1 3/8	1 3/8	1 3/8	1 3/8	1 3/8	4 1/2
4 3/8	2 3/4	2 3/4	2 3/4	2 3/4	2 3/4	1 3/8	1 3/8	1 3/8	1 3/8	1 3/8	4 3/8
4 1/2	2 3/4	2 3/4	2 3/4	2 3/4	2 3/4	1 3/8	1 3/8	1 3/8	1 3/8	1 3/8	4 1/2
4 5/8	2 3/4	2 3/4	2 3/4	2 3/4	2 3/4	1 3/8	1 3/8	1 3/8	1 3/8	1 3/8	4 5/8
4 3/2	2 3/4	2 3/4	2 3/4	2 3/4	2 3/4	1 3/8	1 3/8	1 3/8	1 3/8	1 3/8	4 3/2
4 7/8	2 3/4	2 3/4	2 3/4	2 3/4	2 3/4	1 3/8	1 3/8	1 3/8	1 3/8	1 3/8	4 7/8
5	2 3/4	2 3/4	2 3/4	2 3/4	2 3/4	1 3/8	1 3/8	1 3/8	1 3/8	1 3/8	5

For field rivets add 1/4 inch to tabular lengths.

Figure 24. Historical rivets.

5.2 Realization process and static behavior

One of the most important aspect in the rivet connection is the installation procedure. The riveting process consists of inserting the rivet in matching holes of the connection and subsequently forming a head on the protruding end of the shank. Rapid forming forms the head with a pneumatic hammer or by continuous practice and the holes are generally 2/10 mm bigger than the nominal diameter of un-driven rivet. Hot rivet, the most common type, is heated to approximately 1000 °C before being installed. In addition to forming the head, the diameter of the rivet is increased, resulting in a decreased hole clearance. As the rivet cools, it shrinks and squeezes the connected plies together. A residual internal tension (clamping force) results in the rivet. The magnitude of the residual clamping force depends on the critical installation conditions (driving and finishing temperature), joint stiffness and the driving pressure. Literature shows that hot-driven rivets can develop clamping forces that approach the yield load of a rivet. However, a considerable variation is observed. If the grip length increases the residual clamping force tends to increase because the thermal contraction is highest. The residual clamping force contributes to the slip resistance of the joint although the clamping force in the rivet is difficult to control, is not great and cannot be relied upon. During the cooling process, the rivets shrink diametrically and longitudinally. The amount of hole clearance that results also depends on how well the rivet filled the hole prior to shrinkage. The holes are almost completely filled for relatively short grip rivets. As the grip length increase, clearances between rivet and plate material tend to increase due to the differences in working the material during driving. Installation of hot-driven rivets involves many variables, such as the driving time, initial temperature, finishing temperature and driving technique. After the installation, rivets, become the most important elements in the joint. Taking in consideration Figure 23, the tensile strength for un-driven rivets vary from 414 MPa (grade 1) to 551 MPa (grade 2 and 3). The tensile capacity of a rivet is (Equation (31)):

$$T_u = \sigma_u \cdot A_{eff} \quad (31)$$

where σ_u it the tensile strength and A_{eff} is cross sectional area. In Europe, referring to [10], the recommended values are (Table 4):

Shear	190	MPa
Traction	75	MPa

Table 4

The tensile strength of a driven rivet depends on the mechanical properties of the rivet material before driving and the driving temperature. Some tests indicated that varying the driving temperature between 980 and 1260 °C had little effect on the tensile strength. It was also concluded that the soaking time had a negligible effect on the ultimate strength. Driving generally increases the rivet tensile strength by about 20%. If the drive is carry out by a pneumatic hammer the increase is about 10%. A considerable reduction in elongation was observed to accompany the increase in strength. Most tension tests of driven rivets showed a tendency to decrease in strength as the grip length was increased. This is due to a greater “upsetting” effect (the driving energy per unit volume for a short rivet is more favourable) and strength value are based on the full hole area, implying that the driven rivet completely fills the hole. This is not true for longer grip rivets (the gap increases with increasing grip length) nevertheless the differences in strength of short and longer rivets is neglected [11]. The design resistance of rivets is given in [12] as (Equation (32)):

$$F_{Rd} = \frac{0,6 * f_{ur} \cdot A_0}{\gamma_{M2}} \quad (32)$$

where f_{ur} is the ultimate strength of the rivet material. A_0 is the area of the hole and γ_{M2} is a partial factor (recommended value 1,25). The residual clamping force in driven rivets has no influence on their strength and the yielding of the rivet minimizes the effect of the clamping force and does not affect the ultimate strength.

5.3 Clamping force

When the hot rivet has been inserted into the hole of the plates and the second head has been formed, the rivet shortened in length due to cooling. Nevertheless, most of the shrinkage of the free rivet is restrict by the consequently compressed plates [13]. The tensile force in rivet and the compressive force in the plates are

self-equilibrated. The clamping force is normally assumed to be evenly distributed through the plate with an angle α of 30-45° (Figure 25). Following the theory of Fernlund [14] the lateral stress distribution at the mid-plane by assuming the plates acted as an elastic soil which deforms under the pressure from the clamping force. The clamping force generates a gradually decreased tri-axial stress state in the connected plates. Moreover, the plates are subjected to radial and circumferential stresses. The rivet compresses the plate and the material wants to expand radially. This expansion is restricted by hoop rings, which are compressed near the rivet hole and expanded in the outer part of the region (Figure 26).

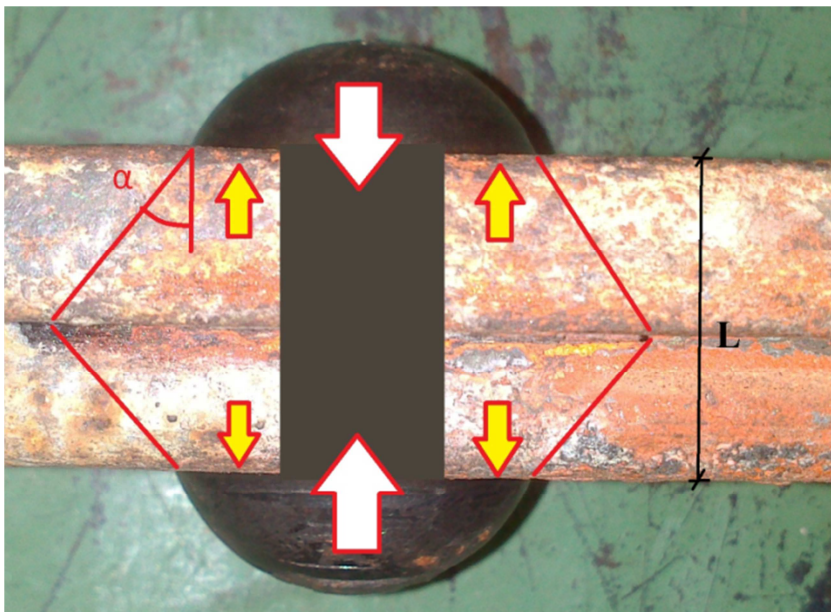


Figure 25. Schematic clamping forces.

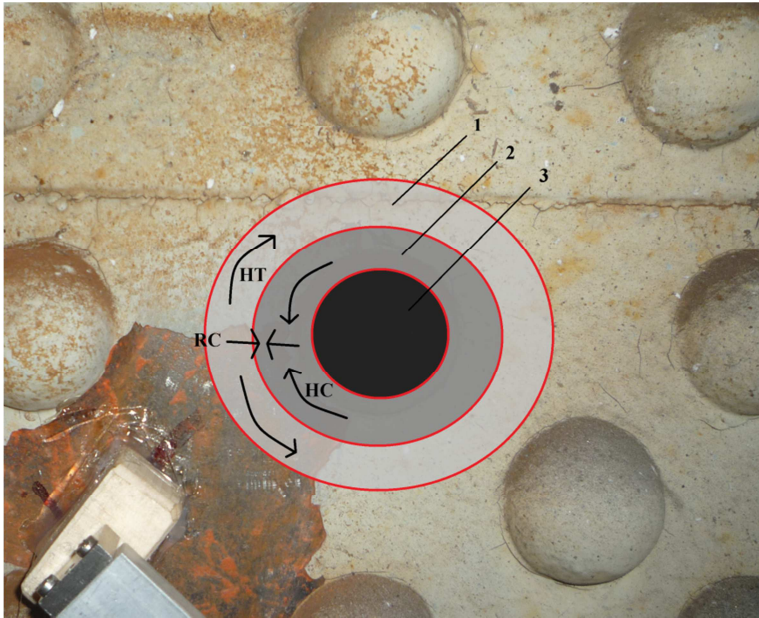


Figure 26. Different clamping areas. Zone 1: Hoop tension (HT), Zone 2: Hoop compression (HC), Zone 3: Rivet hole; RC = radial compression.

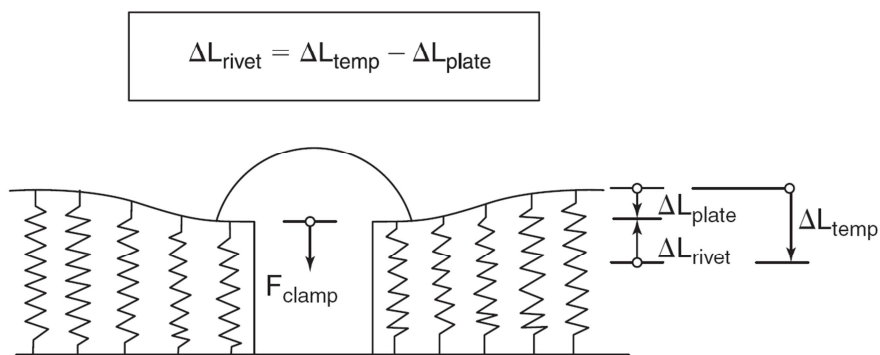
The results of Wilson and Thomas work [15] shows that the initial tension in the rivet is approximately 70% ($\pm 15\%$) of the yield stress independently of the riveting method. Typically, the clamping force is increased as the grip length is increased. Taking in consideration that the longer the rivet shank, the more it wants to contract when cooling nevertheless this contraction is restricted by the increased thickness plates. As the thickness of the plate increases, the ratio between the axial stiffness of the plates and the axial stiffness of the rivets increases too (Figure 27). When the grip length increases the compressed contact area between the plates also increases as well. In conclusion, when increasing total plate thickness, the reducing effect on the axial stiffness is counterbalanced by an increased area. The rivet does not have this compensating effect when increasing in length. It has been observed that when the grip length is increased there is a gap between the plate hole edge and the rivet shank, which increases as the shank length increases (Poisson effect). The magnitude of clamping force is (Equation (33)):

$$F_{cl} = 0,7 * \sigma_y * A_{riv} \quad (33)$$

where σ_y is the yield value and A_{riv} is the rivet shank area. The corresponding elongation is (Equation (34)):

$$\Delta L_{riv} = \frac{F_{cl} * L}{E * A_{riv}} \quad (34)$$

where L is the grip length.



ΔL_{rivet} = Residual elongation (due to restricted contraction) of the rivet

ΔL_{temp} = Total thermal contraction (unrestricted condition)

ΔL_{plate} = The compression of the connected plates

Figure 27. Springs deformation.

Referring to Figure 26 the tensile force in the rivet should be balanced by the compressive force in the plates (Equation (35)):

$$F_{riv} = \Delta L_{riv} \frac{(E * A_{riv})}{L_{riv}} \Rightarrow F_{riv} = F_{pl} \quad (35)$$

$$F_{pl} = \Delta L_{pl} \frac{(E * A_{pl})}{L_{pl}}$$

The Equation (35) becomes (Equation (36)):

$$\Delta L_{riv} * A_{riv} = \Delta L_{pl} * A_{pl} \quad (36)$$

and then (Equation (37))

$$\Delta L_{pl} = \Delta L_{riv} * \frac{A_{riv}}{A_{pl}} \quad (37)$$

5.4 Combined effect

Many tests have been performed to evaluate the shear capacity of a rivet and the shear strength is expressed in terms of its tensile strength. An average shear strength to tensile strength ratio varies from 0.67 to 0.83 (average value 0.75) has been reported. The grade of the rivet material had unimportant effect on these values. In the typical load versus deformation curves for double-shear tests rivets is mentioned in [11]. Test results of two different grip lengths indicate the same shear strength. In the initial load stages the longer rivet shows a larger deformation, largely due to bending effects. Some data indicate a small decrease in strength for rivets in single shear as compared with the double shear loading condition. In most single shear test joints, the rivet is not subjected to a pure shear load condition (Figure 28). This is caused by out-of-plane forces and secondary stresses on the rivet due to the inherent eccentricity of the applied load. When a single shear specimen is restrained so that no secondary stresses and out-of-plane deformations are introduced, the difference in the single and double shear strength is insignificant.

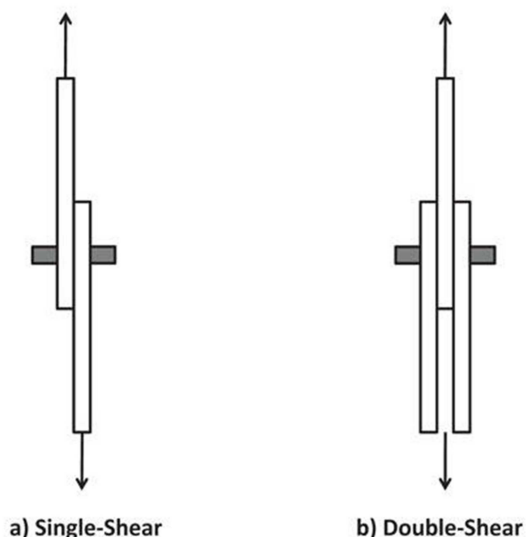


Figure 28. Shear type.

Since driving a rivet increases its tensile strength, the shear strength increases as well. Shear strengths is taken between 310 and 414 MPa for grade 1 rivets and between 448 and 552 MPa for grade 2 or grade 3 rivets (Equation (38)):

$$310MPa < \tau_{u,static} < 552MPa \quad (38)$$

As mentioned above the shear strength is (Equation (39)):

$$\tau_u = 0,75 * \sigma_u \quad (39)$$

and is directly proportional to the available shear area and the number of critical shear planes. As the loading condition changed from pure tension to pure shear (Figure 29), a significant decrease in deformation capacity was observed. The rivet diameter, driving procedure, manufacturing process and grades of rivets did not have a significant influence on the results. Only the long grip rivets tended to show a decrease in strength. This was expected and was compatible with rivets subjected to shear alone. The character of the fracture and the deformation capacity changed

substantially as the loading condition changed from shear to combined shear tension.

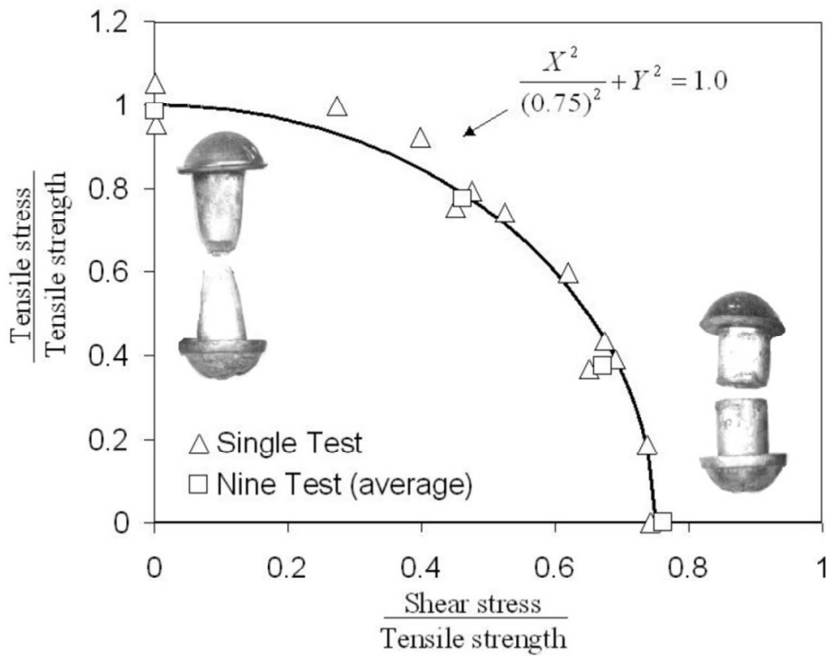


Figure 29. Different shear to tension load ratios.

An elliptical interaction curve [16] defined the strength of rivets subjected to a combined tension and shear loading (Equation (40)):

$$\frac{x^2}{0,75^2} + y^2 = 1 \quad (40)$$

where (Equation (41)):

$$x = \tau / \sigma_u \quad (41)$$

that is the ratio of the shear stress on the shear plane to the tensile strength of the rivet (Equation (42))

$$y = \sigma / \sigma_u \quad (42)$$

or rather the ratio of the tensile stress to the tensile strength. Figure 29 shows the test results and the elliptical interaction curve.

NOTE: the fatigue shear strength of rivets is (Equation (43)):

$$\tau_{u,fatigue} = 100MPa \quad (43)$$

Following the indication of [17] rivets were produced of very tough, ductile steels, because a plastic behaviour was necessary after implementing in the structure [4]. Following the indication of United Kingdom Railtrack Line Code [18] for old metal bridges, the mechanic characteristics are (Table 5):

Type	Yield strength (MPa)	Ultimate strength (MPa)
Rivet past 1905	300	385

Table 5

5.5 Connections

Riveted joints are conveniently classified according to the type of forces to which the fasteners are subjected. These classes are (1) shear, (2) tension, and (3) combined tension and shear. The simplest type of structural connection subjecting fasteners to axial shear is the flat plate-type splice and its name is "butt splice". In the lap plate splice (Figure 30) the fasteners act in single shear. The eccentricity of the loads causes bending and thus this type of connection is only used for minor connections.

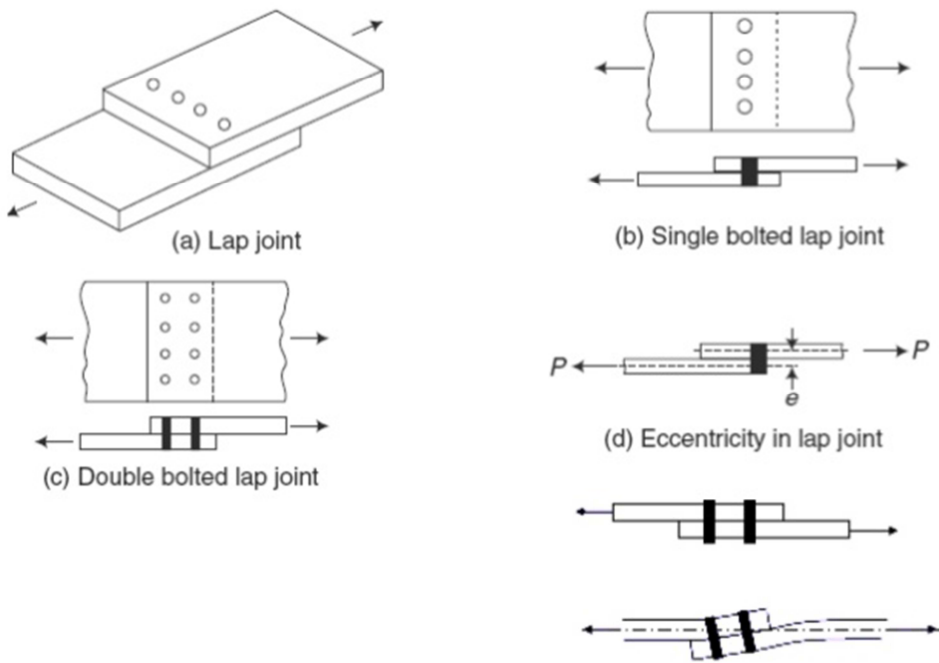


Figure 30. Connection types.

In the joint, the clamping force provided by shrinkage of the rivets, is present (Figure 31). If the joint is subjected to an in-plane load four characteristic loading stages exist (Figure 32).

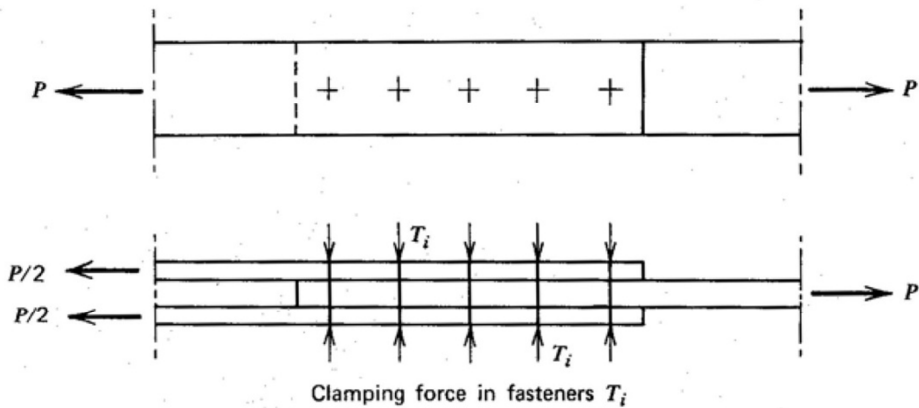


Figure 31. In plane load.

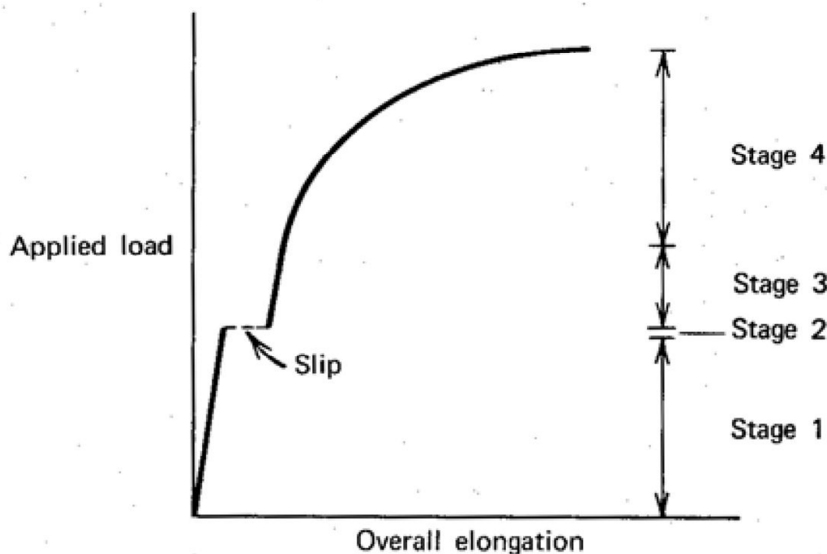


Figure 32. Load – elongation.

- Stage 1: static friction prevents slip;
- Stage 2: load has exceeded the frictional resistance and the joint slips into bearing;
- Stage 3: the fasteners and plates deform elastically (linear load versus deformation relationship);
- Stage 4: yielding of plates, fasteners, or both occurs and results in plate fracture or complete shearing of the fasteners.

The initial clamping force present in the rivets has usually been completely dissipated by the time joint failure occurs; the rather small fastener elongations that produced the preload have been released by shear deformation and plate yielding. Overlapping effects may make the distinctions between the various stages less clear-cut than depicted. In splices subjected to shearing loads the forces transfer is possible by friction or by shear and bearing. In a slip-resistant joint, since slip does not occur, the load on the connection is completely transferred by the frictional resistance on the contact surfaces. Moreover, the rivets are not actually stressed in shear, and bearing is not a consideration. Depending on the available slip resistance, joint slip may occur before the working load of the connection is reached. Slip brings the connected parts to bear against the sides of the fasteners, and the applied load is then transmitted partially by frictional resistance and partially by shear on the fasteners, depending on joint geometry. Rivets are not very suitable

for use in slip-resistant joints, since the magnitude of the axial bolt clamping force, which affects directly the frictional resistance of the connection, cannot be controlled. Additionally, a clamping force may be developed, it is not reliable. In conclusion, riveted joints are usually considered as bearing-type joints.

5.5.1 Slip coefficient

One of the significant factors influencing the slip resistance of a connection is the slip coefficient k_s . Moreover, the value of the rivet clamping force is of prime importance when determining the value of slip coefficient k_s [19] [20] [21] [22]. In many cases structural members are connected together with a natural faying surface (clean mill scale). An analysis of the available data in clean mill scale condition for A7, A36, A440, Fe37 and Fe52 structural steels shows an average slip coefficient k_s of 0.33, with a standard deviation of 0.07 [23]. If the mill scale is removed a decrease in friction resistance of 25 to 30% (compared with normal hand brushing mill scale surfaces) is observed [24]. The surface irregularities, which are essential for providing the frictional resistance, are reduced and then a decrease in k_s is shown.

When the frictional resistance of a joint is exceeded, the movement is stopped when the hole clearance is taken up and the rivets are in bearing. The load is now mainly transferred by means of shear and bearing (Figure 33). The shear strength of the rivets and the local bearing stresses in the plate around the fasteners are the critical parameters, not the rivet clamping. The ultimate shear strength of rivets is not dependent upon the amount of preload in the fasteners.

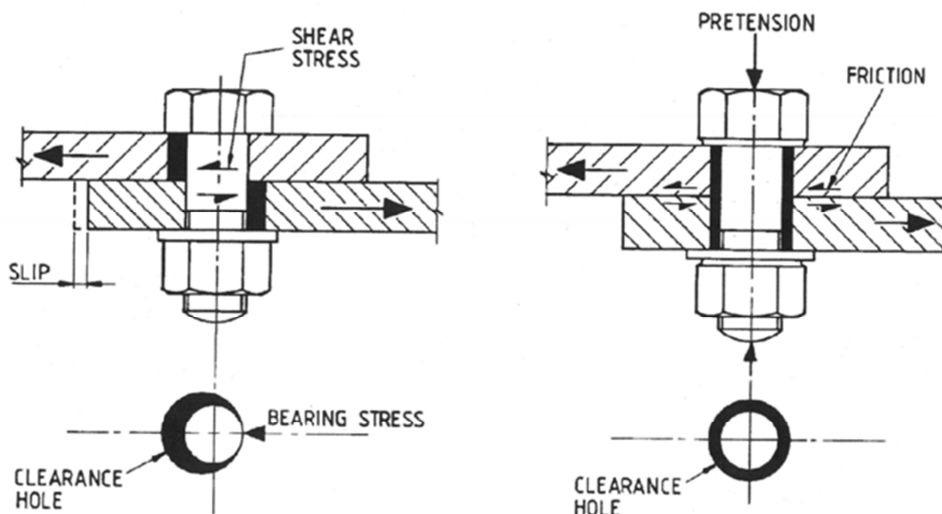


Figure 33. Pretension effect.

In most joints, a combination of friction or shear and bearing effects is likely to occur under normal service loads. Elastic models and experimental investigations show that the load is initially transferred by friction forces at the ends of the joints [25]. The deformation of a rivet during the load stage depends on the differences in plate elongations (main plate and lap plates, Figure 34) between any two adjacent transverse rows of fasteners. The differential elongations are greater at the ends of the joint (e.g., the main plate may have yielded while the lap plates are still elastic), the end rivets are carrying greater loads than the interior rivets. As the load increases, the zone of friction extends toward the centre of the joint. The slip zone proceeds inward from the ends toward the centre of the joint. When the applied load exceeds the frictional resistance over the entire faying surface of the connection, large relative displacements occur. When major slip occurs, only the end rivets may come into bearing against the main one and splice plates. As the applied load increases, the end rivets and holes deform further until the succeeding rivets come into bearing. In many situations, the joint will not slip at all under live loads because the joint is often in bearing by the time the rivets are clamped. This might be due to small misalignments inherent to the fabrication process. Generally, slips under live loads are so small that they rarely have a serious effect on the structure.

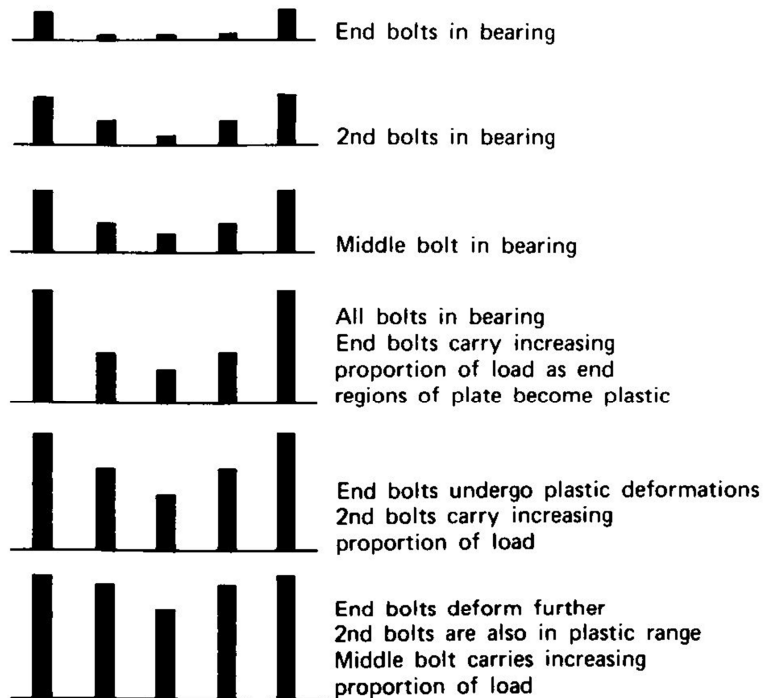


Figure 34. Forces distribution.

Following the indications of [7], ultimate load partition in riveted joint is shown. The theoretical load solution is based on the assumptions [26] :

- the fasteners transmit all the applied load by shear and bearing once major slip has occurred;
- frictional forces may be neglected in the region between major slip and ultimate load.

The solution satisfies the equilibrium condition and assure that continuity will be maintained throughout the joint length for all load levels. Referring to Figure 35 the equilibrium conditions in the main plate can be written as (Equation (44)):

$$P_{i,i+1} = P_g - \sum_{i=1}^i R_i \quad (44)$$

where P is the load per gage strip, " i " denote the i -th rivet, P_G is total load on strip and $\sum R_i$ is the sum of the loads on all bolts. Similarly, for the lap plates is (Equation (45)):

$$Q_{i,i+1} = \sum_{i=1}^i R_i \quad (45)$$

where Q is the load per gage. The general equation of equilibrium is (Equation (46)):

$$P_G - \sum_{i=1}^n R_i = 0 \quad (46)$$

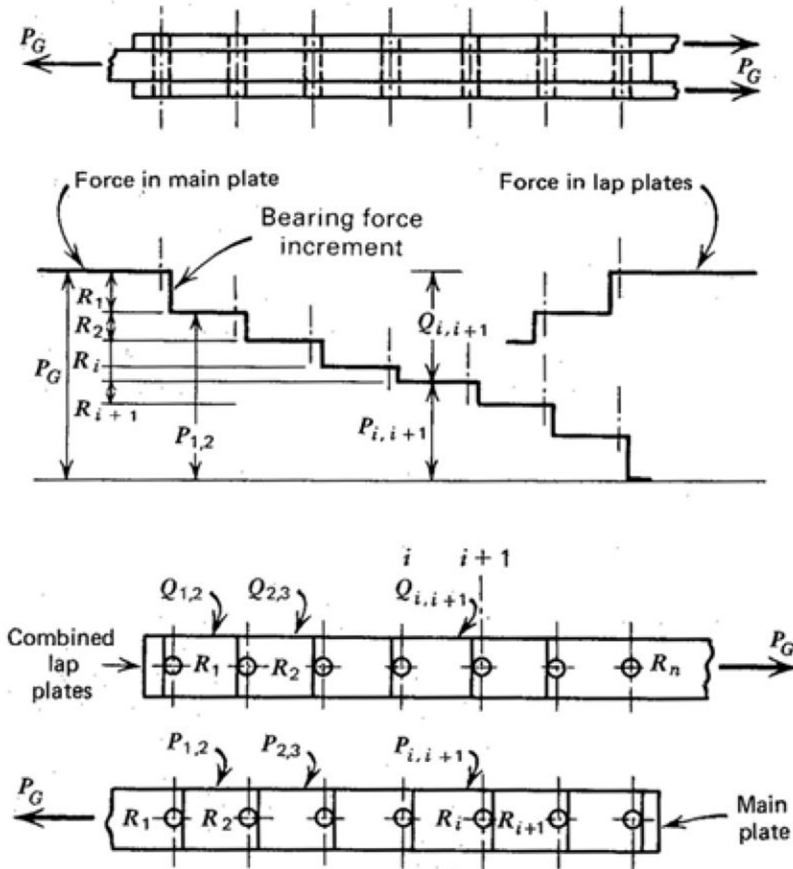


Figure 35. Forces.

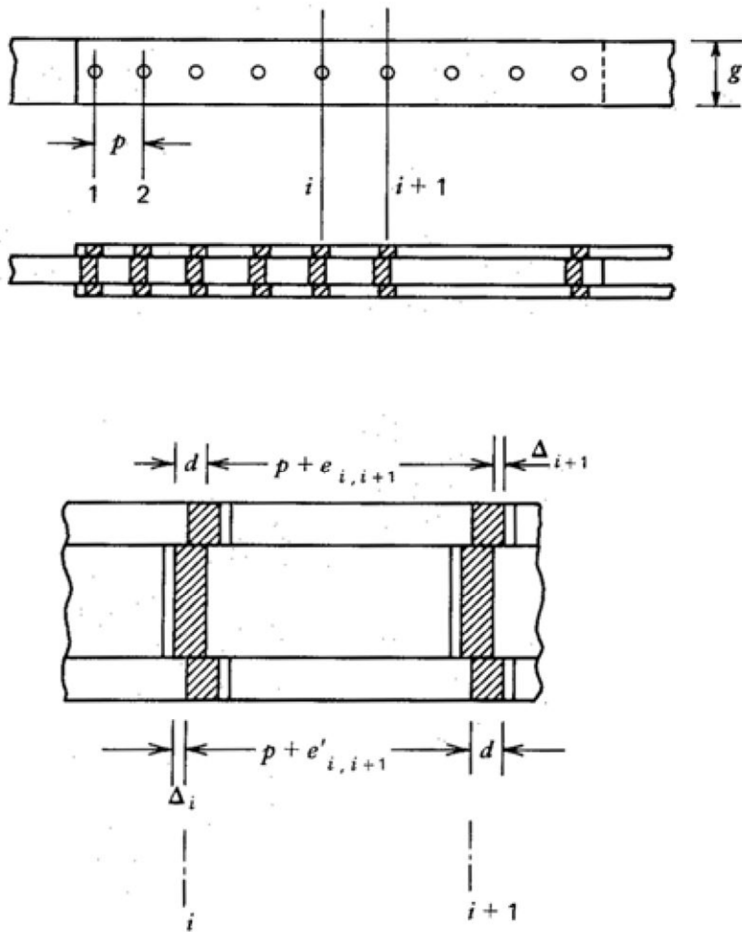


Figure 36. Plates slip.

In order to ensure the compatibility and, as a result of the applied load, the main plate will have elongated so that the distance between the main plate holes is $p + e_{i,i+1}$ (Figure 36). The lap plates will also have elongated, and the distance between the lap plate holes is $p + e_{i,i+1}$. Bolts will have undergone deformations, which include the effects of shear, bending, and bearing of the fastener and the localized effect of bearing on the plates. The compatibility equation became (Equation (47)):

$$\Delta_i + e_{i,i+1} = \Delta_{i+1} + e_{i,i+1} \quad (47)$$

with Δ_i = deformations of the fastener.

If the rivet deformations as functions of the fastener loads and the plate elongations are expressed as functions of load in the segments of the joint between rivets, Equation (47) became (Equation (48)):

$$f(R_i) + \Psi(Q_{i,i+1}) = F(R_{i+1}) + \Phi(P_{i,i+1}) \quad (48)$$

in which:

$f(R_i)$ represents the i-th bolt deformations;

$F(R_{i+1})$ is the (i+1)-th bolt deformations;

$\Phi(P_{i,i+1})$ is the main plate elongation;

$\Psi(Q_{i,i+1})$ is the lap plate elongation.

These may be solved to give the loads acting on the rivets when the relationships between the load and elongation for the various components are known.

5.5.2 Failure mechanisms

Two different types of riveted joints are realizable: lap joint and butt joint (Figure 37 and Figure 38). Lap joints have a plate that overlaps the other, moreover, butt joints have the main plate kept in alignment butting each other with cover plates placed on one side or both side of the main plate. Friction radically influences the joints behaviour and the consequent failure mechanism. For example, if the friction is active, the force migrations does not involve the shear resistance of rivets.

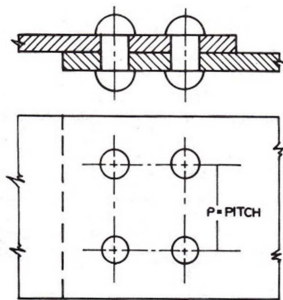


Figure 37. Double riveted lap joint.

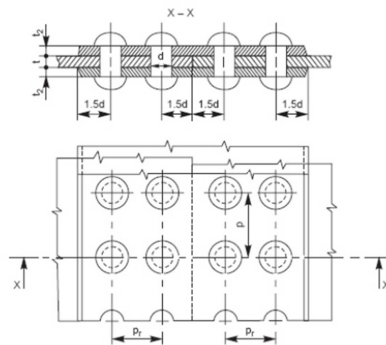


Figure 38. Double strap butt joint.

A joint may fail due to tearing of the plate at an edge (Figure 39). This can be avoided by keeping the margin, $m = 1.5 d$, where d is the diameter of the rivet hole.

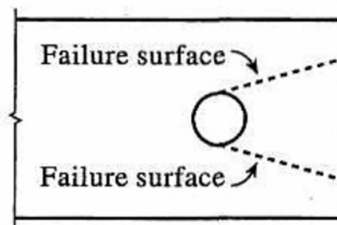


Figure 39. Plate tearing.

Due to the tensile stresses in the main plates, the main plate or cover plates may tear off across a row of rivets as shown in Figure 40. The tearing resistance is (Equation (49)):

$$P_t = \sigma_t * (p - d) * t \quad (49)$$

where P_t is the tearing resistance, σ_t is the permissible tensile stress, p is the pitch of rivets, d is the diameter of hole and t the plate thickness.

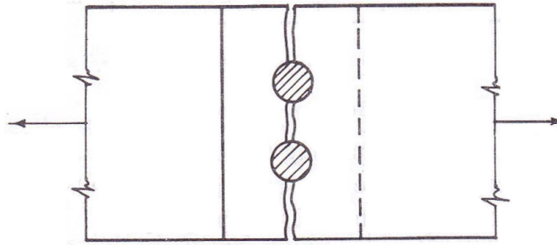


Figure 40. Tearing across the rivets.

The plates which are connected (Figure 41) by the rivets exert tensile stress on the rivets and, if the rivets are unable to resist the stress, they are sheared off.

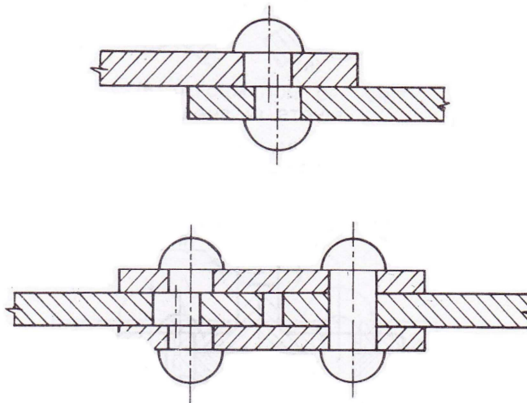


Figure 41. Shearing off a rivet, lap and butt joint.

The resistance offered by a rivet to be sheared off is (Equation (50)):

$$P_s = \tau_t * A_{res} \tag{ 50 }$$

where P_s is the shearing resistance and A_{res} is the resistant rivet shank. The rivets may not actually shear off under the tensile stress but the rivet hole becomes oval shaped and hence the joint becomes loosened (Figure 42). The area that resists this action is the projected area of the hole or rivet on diametrical plane.

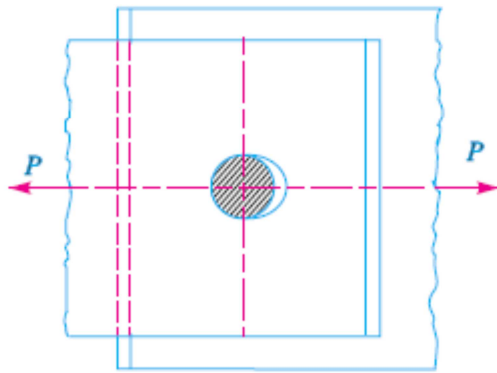


Figure 42. Crushing.

It is appropriate to understand the joint friction behaviour to estimate correctly the remaining fatigue life.

5.5.3 Behaviour under repeated loading

The behaviour of a riveted connection under repeated loading is directly influenced by the type of load transfer in the connection. Assuming that the external load is completely transmitted by friction on the faying surfaces, this implies a high concentration of shear stresses at the interface between main plate and lap plate. These results from the large differences in strain between the plates. The interface would be required to transmit a highly concentrated shear force at the discontinuity if it were not relieved by micro-slip at that point. The cracks initiated in the gross section, in front of the first bolt hole, on the faying surfaces of the connected plates (Figure 43).

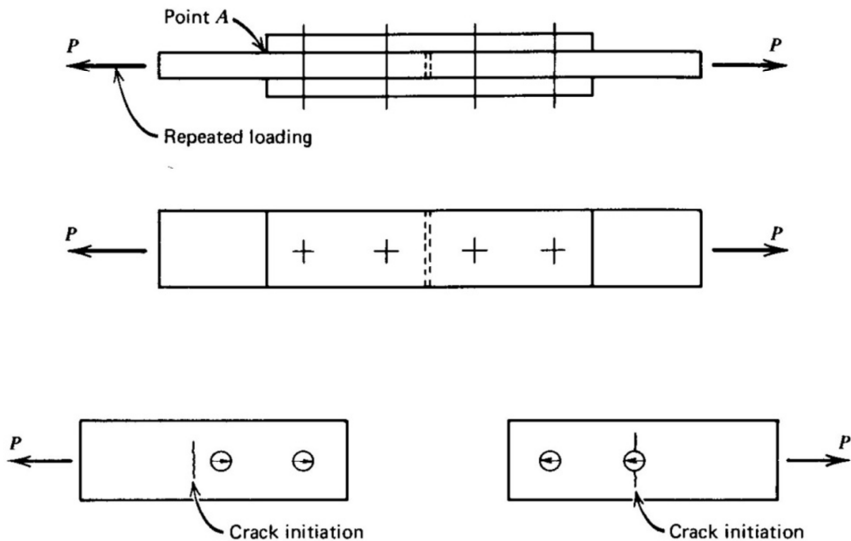


Figure 43. Crack initiation.

Fretting phenomena occurs at the interface between metallic surfaces that are in contact and that slip minute amounts relative to each other under the action of an oscillating force [27]. Stress concentrations are also introduced and the faying surfaces is damaged. In many cases, this phenomena, leads to crack initiation and a further reduction in fatigue strength. Tests have indicated that high contact pressures only exist in a small area around the rivet hole [14] [28]. The normal stress due to the clamping force decreases rapidly from a maximum condition at the edge of the hole. The region where the normal stress acts depends on geometrical factors such as the plate thickness and rivet diameter. The circular pressure area falls typically within twice the diameter of the bolt: the crack initiates at a section between the end of the lap plate and the bolt hole where the combination of micro slip and normal pressure is more critical (Figure 43, bottom left). In the bottom right figure (Figure 43) the crack initiates at the edge of the hole and grows in the region of the net section. This rupture occurs when most of the load exceeds the slip resistance transmitting shear and bearing. Often, final failure occurs partly through the net section and partly through the gross section.

6 SAN STINO'S RAILWAY BRIDGE

The bridge analysed in this work is a truss disused railway bridge located near San Stino di Livenza, in the Northeast of Italy (Figure 44). The bridge is 34,4 m long, and it belongs to the Italian State Railways and it has been operational for about a century. The bridge was built in 1922 along the Venezia – Trieste railway line to connect two banks of Canal Fosson. The structure was assembled using rivets and its simple supported reticular bridge had 5300 mm width and 3500 mm high. Ten identical fields compose the lattice structure that included longitudinal elements (named “longherine” or rail bearers), transversal beam (“traversi” or cross girders) and vertical bracing (Figure 45, Figure 46, Figure 52 and Figure 53). In the lack of original design every bridge dimension and structural consideration have been evaluated experimentally. In the follow some documents and photos, taken during the preliminary survey, have been shown.



Figure 44. San Stino di Livenza, Venice, Italy.



Figure 45 Frontal view.



Figure 46 Lateral view.

The thermal expansions and contractions were permitted by a steel roller on Portogruaro (Venice) side. A steel roller on Portogruaro side permitted thermal expansion and contractions. (Figure 47 and Figure 48). The rail bearer is a composite plate section 3360 mm long, 500 mm high, about 10 mm thick and 250 mm wide. During the service time, the rails and the associate loads were supported directly by the rail bearers (Figure 49 and Figure 50). Moreover, the cross girder is 280 mm wide, about 800 mm high and supports rigidly the rail bearers. Typical rivets used in this structure have a shank diameter equal to 25 mm. More information about the rail bearers and rivets can be found in the follow paragraph. A couple of concrete abutment sustained the structure nevertheless a relevant state of corrosion was observed in the last decades.

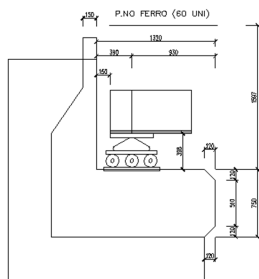


Figure 47. Bridge support (Portogruaro side).

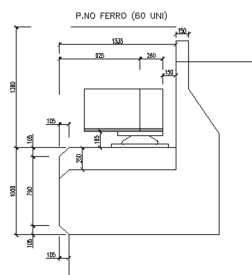
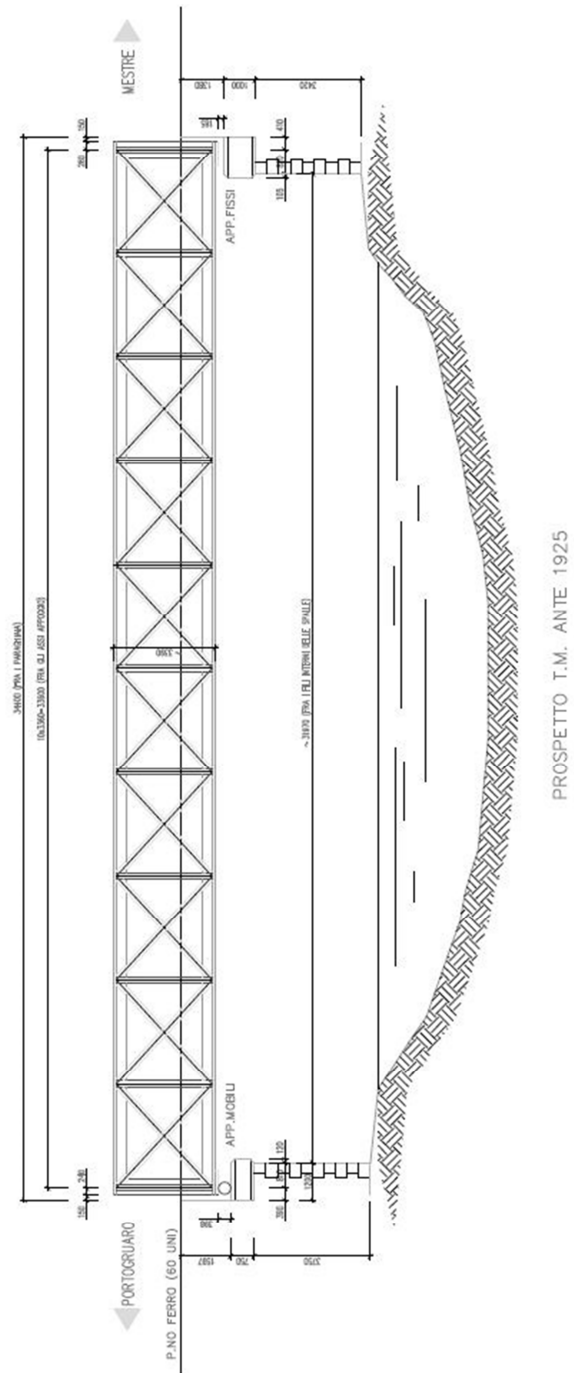


Figure 48. Bridge support (Mestre side).

San Stino's bridge were designed and built before standardisation and widespread use of design codes. Therefore, the only features associated with these structures do not facilitate the assess of their remaining fatigue life and in many cases the conclusions are structure-specific. In July 2011, the bridge was replaced due to the high number of cycles that it is been subjected and for the damages reported during WWII. Some elements were taken (Figure 51) in order to test their static and fatigue behaviour at Padova Laboratory (DICEA, Department of Civil and Environmental Engineering).



PROSPETTO T.M. ANTE 1925

Figure 49 Bridge Lateral View.

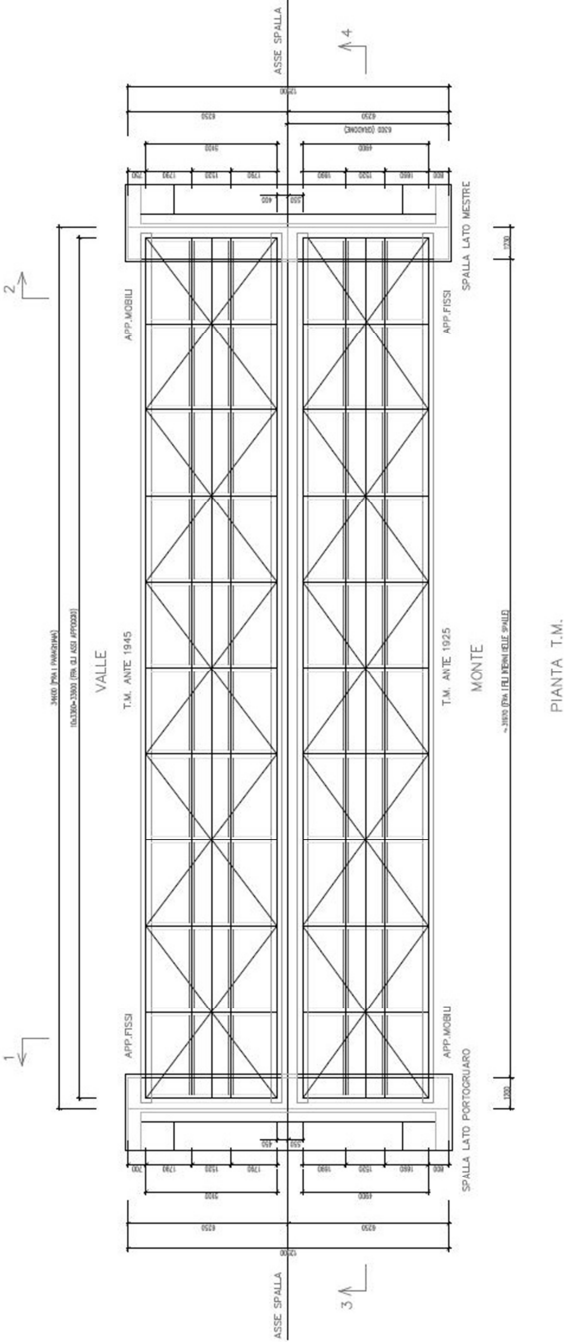


Figure 50. Bridge Plan.

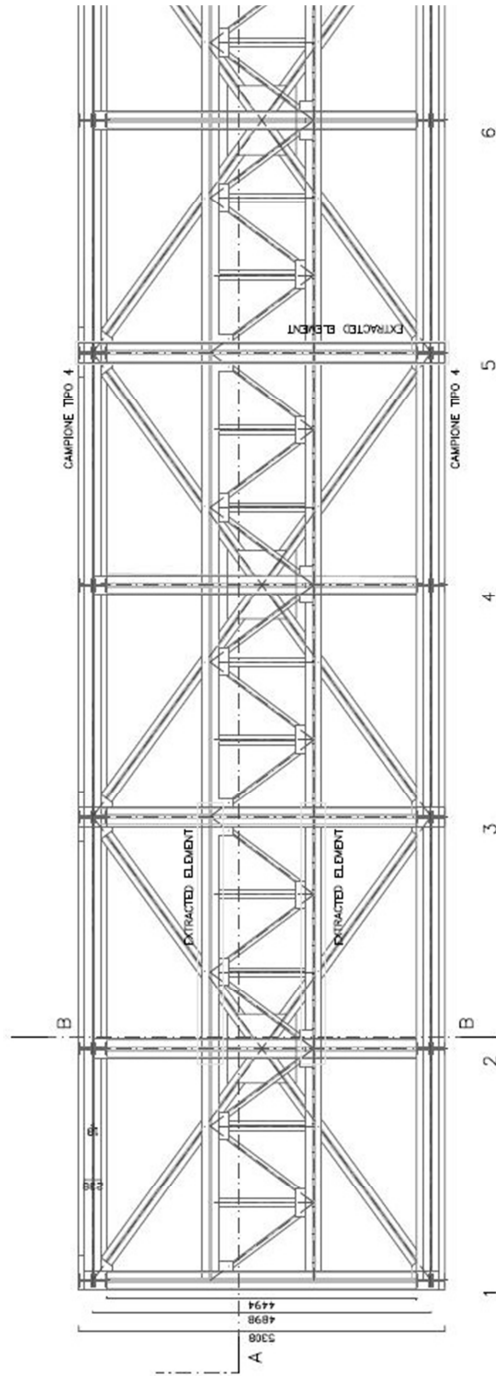


Figure 51. Extracted elements.

6.1 Reticular structure

The reticular structure is only apparently simple. The reticular longitudinal elements were composed by overlapping plates, in order to follow the bridge bending moment. The plates compose a 460 mm high and 400 mm width T section. Figure 52 and Figure 53 show the difference between the mid span bridge zone (6 plates overlapped) and the lateral zone (only 1 plate elements).



*Figure 52*Lateral plates zone.



*Figure 53*Mid-span plates zone.

The diagonal elements were composed by a coupled 80 x 80 mm angular profile and converging on reticular nodes (Figure 54). The rail bearers and the cross girders compose the principal bridge element as shown in Figure 55. In order to evaluate the bridge safety, before bridge disassembly, two rail bearers and two cross girders have been extracted. The cuts were executed using a gas blowpipe with consequent damage of steel in a region of about 5÷10 cm (Figure 56).

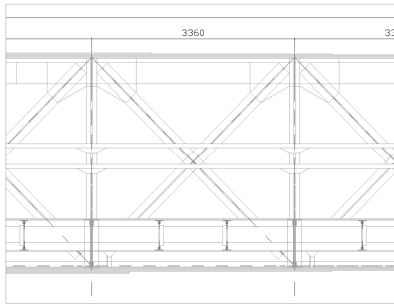


Figure 54. Lateral view: diagonals detail.

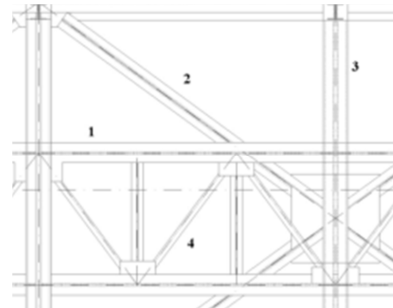


Figure 55. Plan view.
1) rail bearers, 2) principal diagonal, 3) cross girders 4) secondary diagonal.

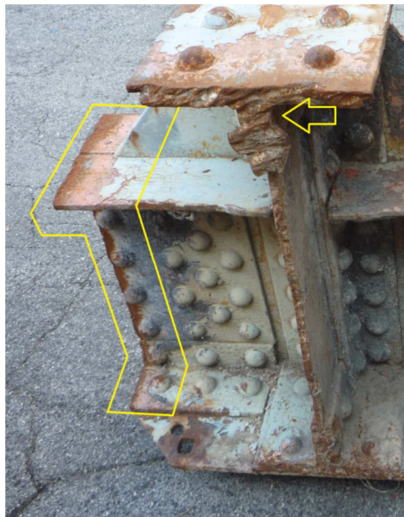


Figure 56. Blowpipe cut.

As shown in Figure 57, the extract elements have some damage like WWII machine gun hole or corrosion degradation. A multilayer protective coat was present all over the bridge, in first analysis it is lead oxide (Minium, Pb_3O_4) (Figure 59). Minium is an orange colour pigment widely used in alkyd paints that serve as primary paints on steel for corrosion. This oxide promotes the passivation on the steel surface.



Figure 57. Rail bearer: corrosion and damage.

Figure 58 show the cross girders during the movement, and highlighted the rail bearers intersection after the cut. In the first approximation the rail bearers are considered fixed at the cross girder (before the demolition) nevertheless a rotational spring is more appropriate.



Figure 58. Cross girders and longitudinal intersections.

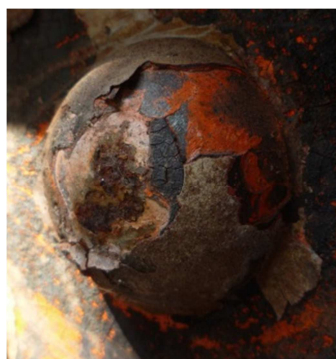


Figure 59. Protective coating, Pb_3O_4 .

The rail bearer, as mentioned above, is 3360 mm long, about 500 mm high, the flanges are about 250 mm wide and 15 mm thick. The extracted elements, in order to avoid sample perturbations, include portions of cross girders and part of contiguous rail bearers. A triangular plate connects the rail bearer to the cross girders. The girder webs instability and the transversal bending are influenced by the portions of secondary diagonal elements. The mass of each element is about 0.5 tons. The images below show the extracted elements (Figure 60, Figure 61 and Figure 62).

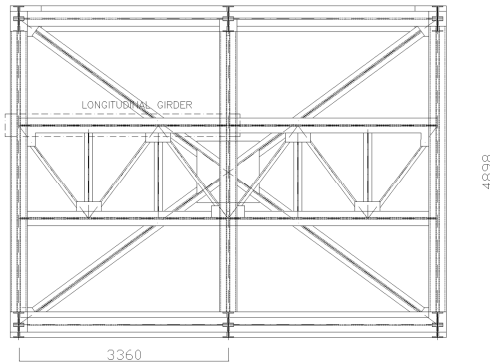


Figure 60. Longitudinal and cross girders (plan).

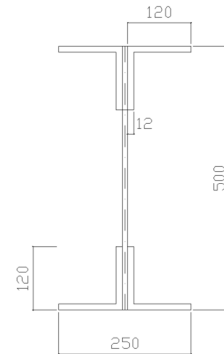


Figure 61. Rail bearer (section).



Figure 62. Rail bearer (plan).

The cross girders are more rigid, higher and heavier than the rail bearers. The element is about 4900 mm length, about 800 mm high and the flanges are 280 mm wide. The mass of each elements is about 1.3 tons (Figure 63 and Figure 64).

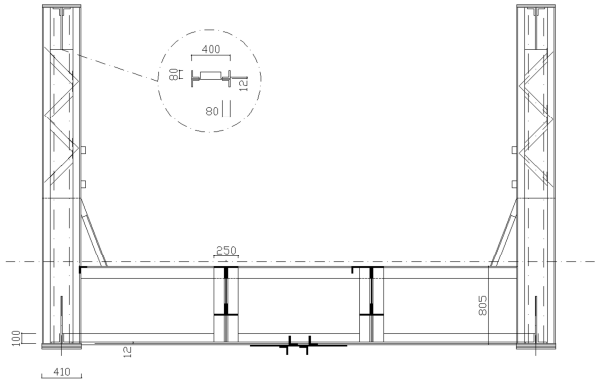


Figure 63. Cross girder: frontal view.

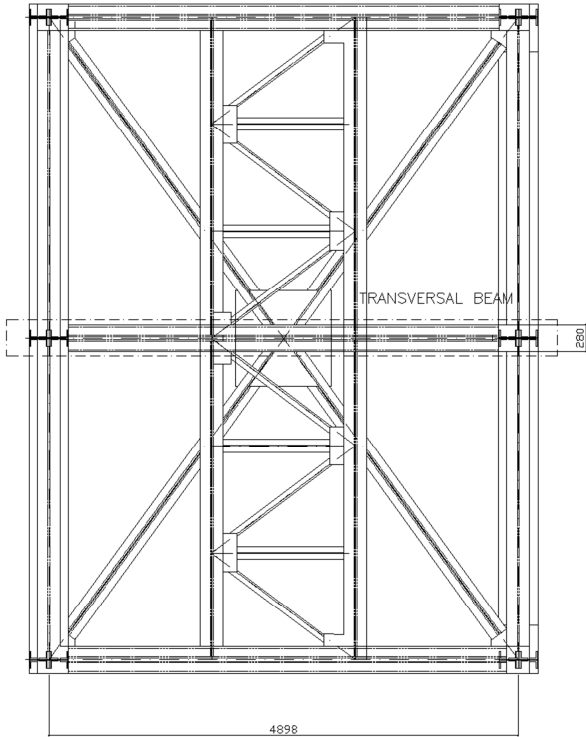


Figure 64. Cross girders: plan.

An approximated Fem analysis model is carried out in order to estimate the global and local structural behaviour (Figure 65 and Figure 66). Using Straus 7 Software

([29]) and introducing beam elements the static and dynamic analysis has been evaluated. Nine type of beam and more than 300 elements are present. In first approximations, referring to longitudinal and cross girders, each beam element is connected to each other by a node without end release attribute (Figure 67). Moreover, the nodal offsets are introduced like as the beam inertia and historical steel material. The bridge supports are modelled appropriately using simple supports and hinges. Every element has been modelled with the follow parameters:

Young modulus	$E=190'000\text{MPa}$
Density	$\rho=7850\text{kg/m}^3$

For modulus of elasticity see §6.2. Referring to the work of [30] and [31] the Fem model [29] has been calibrated in order to catch the real behaviour of the structure. In this work, carried out in June 2011, the response of the bridge was recorded using a piezoelectric acceleration transducer (range: 0-100 Hz, accuracy $6 \cdot 10^{-6} \text{ m/s}^2$). The dynamic ambient response was captured by three reference accelerometers at fixed position at bridge centreline. In addition, a set of roving sensors, were placed in different acquisition points along the structure and simultaneously moved into different setup schemes in order to cover the whole surface of the bridge. The number of gaining points used is needed to characterize appropriately the shape of the most relevant modes of vibration.

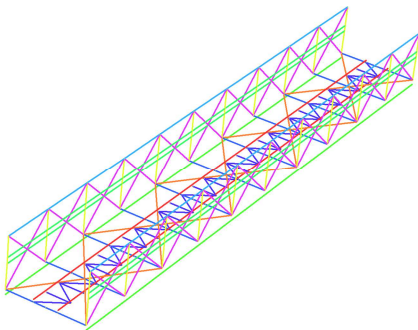


Figure 65. Schematic Fem model.

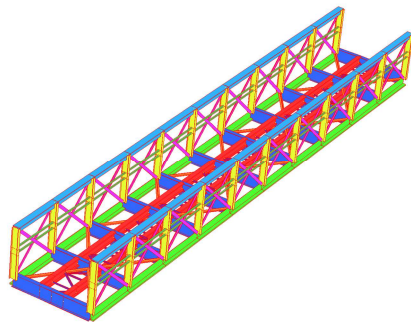


Figure 66. 3D Fem model.

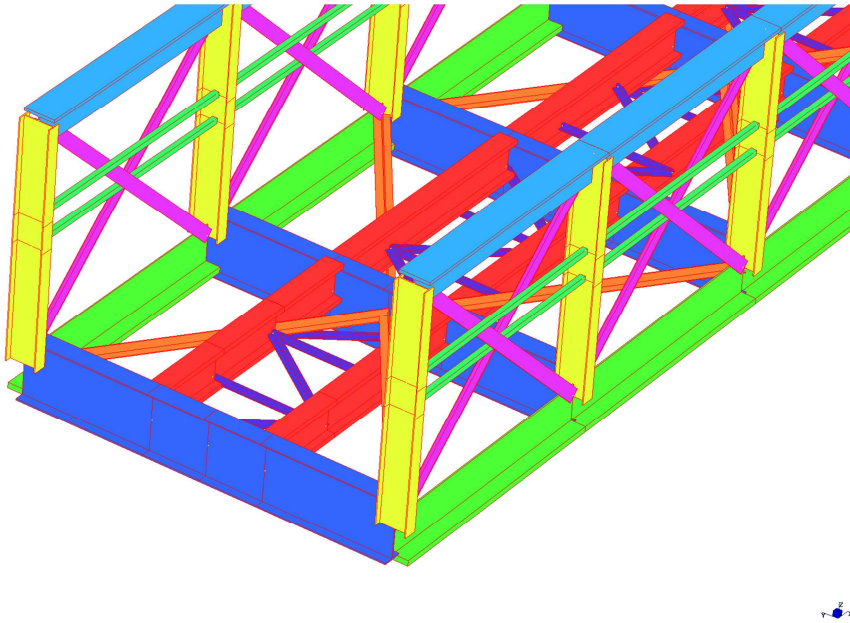


Figure 67. Cross girders and rail bearers model.

The relative frequencies acquired is shown in the table below (Table 6):

Mode	FDD f[Hz]	Direction
1	3,98	Horizontal
2	6,64	Vertical

Table 6

In the follow the Fem solution is presented. The natural frequency solver is used to calculate the free vibration frequencies and corresponding vibration modes. The natural frequency analysis problem, is formulated (Equation (51)) as the following eigenvalue problem:

$$[K]\{x\} = \omega^2[M]\{x\} \quad (51)$$

where “K” is the global stiffness matrix, “M” the global mass matrix, “x” the vibration mode vector and “w” is the natural frequency. The principal frequency is (Table 7):

Mode	Fem f[Hz]	Direction	Mass (%)
1	4,33	Horizontal	58
2	5,45	Vertical	78

Table 7

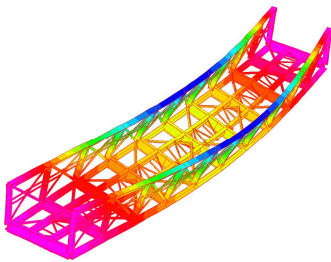


Figure 68. Mode 1: 4,33Hz.

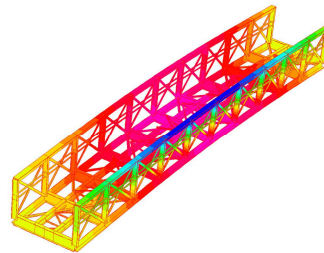


Figure 69. Mode 2: 5,45 Hz.

There is a positive correlation between the Fem simulation (Figure 68 and Figure 69) and the acceleration registered by the transducers. The preliminary results are summarized in the following Table 8:

Mode	FDD f[Hz]	Fem f[Hz]	Reliability
1	3,98	4,33	92%
2	6,64	5,45	82%

Table 8

Note that the Fem model is only superficially calibrated: node non-structural-mass and gusset plate are neglect moreover no rigid links were introduced. For more information about the entire bridge model referring to [30]. This thesis focus on the rail bearers and their fatigue behaviour.

6.2 Steel characterization

In order to acquire sufficient information about bridge characteristics, some steel samples were extracted (Figure 70) and some tests were carried out. The samples dimensions are about 800 x 300 x 18 mm and have been taken from the reticular elements. Mechanical, chemical, fragility and hardness tests have been carried out. A high level of perturbation is present on the sample edge due to the high temperature cut procedure. In order to avoid any inconvenience, 50 mm of material has been sacrificed. Note that x and y directions are fundamental in mechanical tests and are strictly related to the original plate orientation. For this sample, the y direction is aligned to the longitudinal bridge axe.

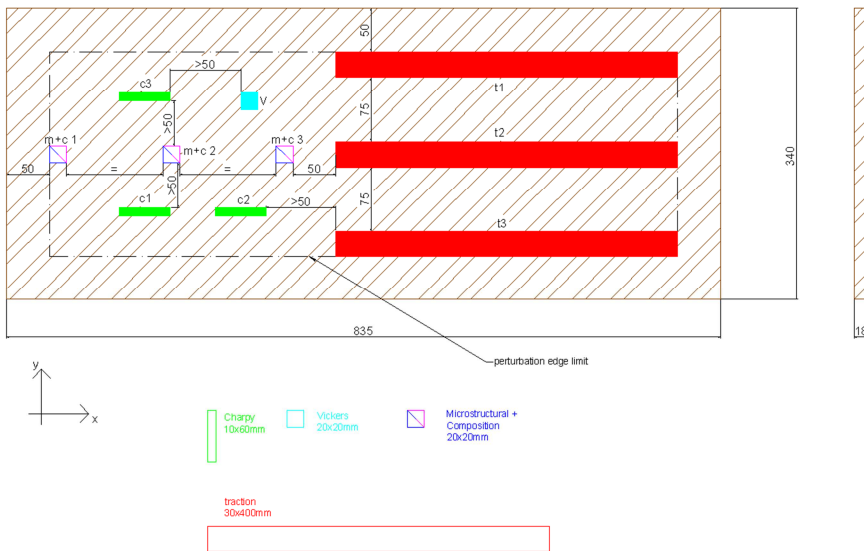


Figure 70. Sample plate.

A brief overview on the type and number of tests are summarized in the following Table 9:

Type	Test	Sample dimensions (mm)	Number of repetitions
Mechanical	Tensile test	30x400	4
	Fragility	60x10	3
	Hardness	20x20	1
	Fatigue	200x16x15,7	3
Chemical	Microstructural analysis	20x20	3
	Composition	20x20	3

Table 9. Test

6.3 Traction test

The traction test is one of the most important examination. Elastic modulus, tensile strength, yield strength, elastic and plastic deformation are deductible analysing the data set. The test is performed according to the standardizations [32], the detail are represented in Figure 71.



Figure 71. Tensile test specimen.

Padova laboratory is equipped with Galdabini ("Sun 60" model) tensile machine (Figure 72 and Figure 73). The test process involves placing the test specimen in the testing machine and slowly extending and recording the applied force (Figure 74). The elongation measurement is calculated as follow (Equation (52)):

$$\varepsilon = \frac{\Delta L}{L_0} \quad (52)$$

where ΔL is the change in gauge length and L_0 is the initial gauge length. The stress is calculated by (Equation (53)):

$$\sigma = F_n/A \tag{ 53 }$$



Figure 72. Galdabini machine.



Figure 73. Tensile test.

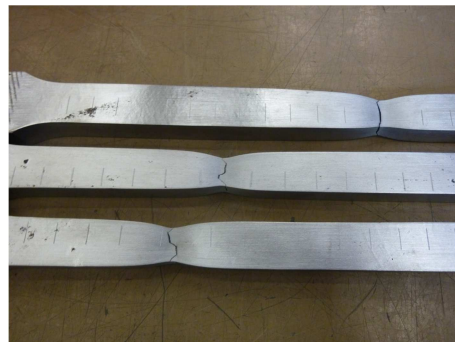


Figure 74. Some specimens after test.

In Figure 75, the San Stino's steel stress-strain diagram is represented. Common low carbon steel generally exhibits a linear stress–strain relationship up to a yield point. After the yield point, the curve slightly decreases because of dislocations escaping from Cottrell Atmospheres. If deformation continues, the stress increases on account of strain hardening until it reaches the ultimate tensile stress. The cross-sectional area decreases uniformly because of Poisson contractions (Figure 74). San Stino steel has a good elastic stage followed by a typical plastic deformation. The yield point and the ultimate load are the same for all the specimen nevertheless a different ultimate elongation is observed. The results are summarized in Table 10. It is important to observe that the statistical consideration is poor due to the low number of specimen.

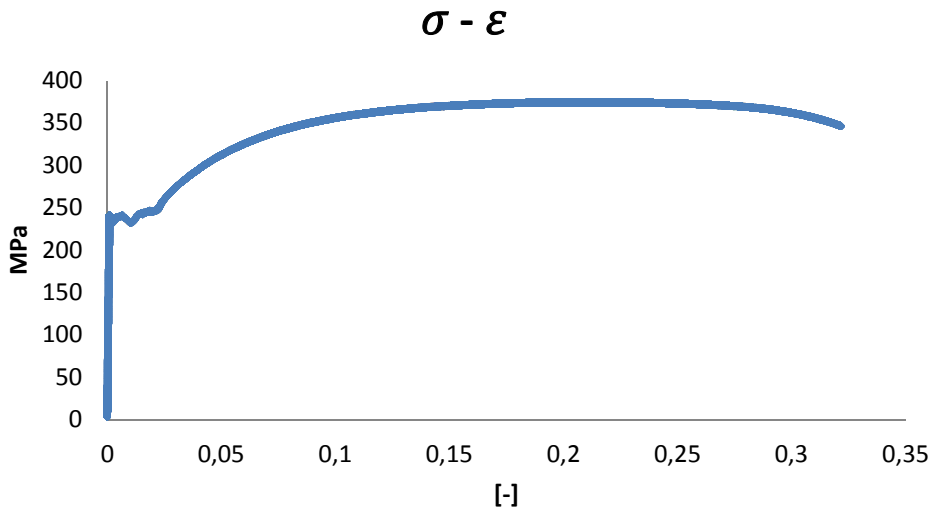


Figure 75. Constitutive law.

Sample	Yield (MPa)	Ultimate (MPa)
T1	233	401
T2	245	398
T3	246	400
T4	236	374
Average	240	393

Table 10. Results overview.

Referring to the average values, the Elastic Young Modulus is:

$$E=190.000 \text{ MPa}$$

These values are in line with the considerations of chapter §4.1, San Stino's steel is comparable to Mild Steel (similar to Fe37/A36).

6.4 Impact test

The Charpy impact test determines the amount of energy absorbed by a material during fracture. This absorbed energy acts as a tool to study brittle behaviour. Figure 76 shows the specimen size and the characteristic V notch. All the aspects of the test and equipment used are described in detail in [33] (Figure 77).

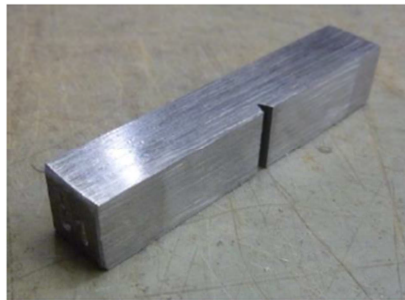
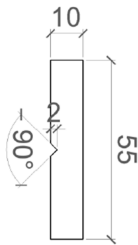


Figure 76. V-notches sample.



Figure 77. Charpy apparatus.

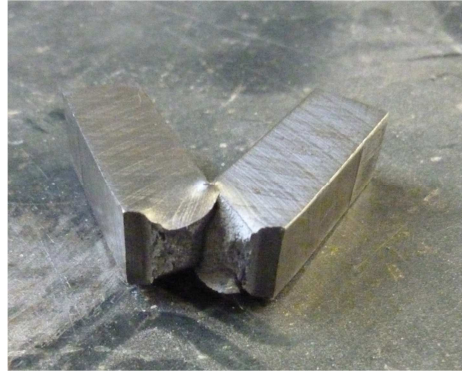


Figure 78. Post-test sample.

The results are summarized in Table 11. San San Stino's steel (Figure 78) can be classified as KV300 = 53J: this value is higher than the minimum requested (27J) by the current regulations.

Sample	Energy (Joule)
C1	68
C2	52
C3	38
Average	53

Table 11. Charpy test results

6.5 Vickers test

Hardness is a characteristic of a material and is defined as the resistance to indentation, and it is determined by measuring the permanent depth of the indentation (Figure 79).

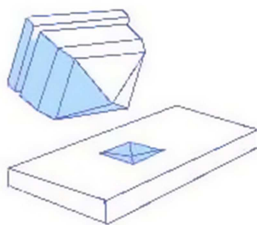


Figure 79. Vickers test.

Indentation hardness value is obtained by measuring the depth or the area of the indentation using standardized test methods. The Vickers hardness test method is based on an optical measurement system [34]. The micro-hardness test procedure specifies a range of light loads using a diamond indenter to make an indentation that is measured and converted to a hardness value. A square base pyramid shaped diamond is used to test in the Vickers scale. Referring to [34] and adopting 136° pyramidal angle the hardness is (Equation (54)):

$$HV = \frac{\sin 136^\circ / 2 * F * 2 * 0,102}{d^2} = 0,189 * \frac{F}{d^2} = 114MPa \quad (54)$$

where (Equation (55))

$$d = \frac{\left| \begin{matrix} 22,86 & 23,56 \\ \hat{x}_2 & - \hat{x}_1 \end{matrix} \right| + \left| \begin{matrix} 17,45 & 18,15 \\ \hat{y}_2 & - \hat{y}_1 \end{matrix} \right|}{2} = 0,7 \quad (55)$$

and F is the force applied equal to 294,18 N. San Stino's steel is consequently classified as 114 HV 30/5. Referring to [35] the ultimate strength is about 385 MPa according to experimental tensile test (§6.3).

6.6 Optical microscope analysis

An optical microscope is used to investigate the material. The specimen is purposely prepared: two zone were created using different abrasive superficies in order to evaluate the grain organization (Figure 80). In Figure 81 is shown the opaque portion with 200x magnification: the picture evidences a good grain distribution. The black part is perlite, the white one is ferrite and they are predominant.

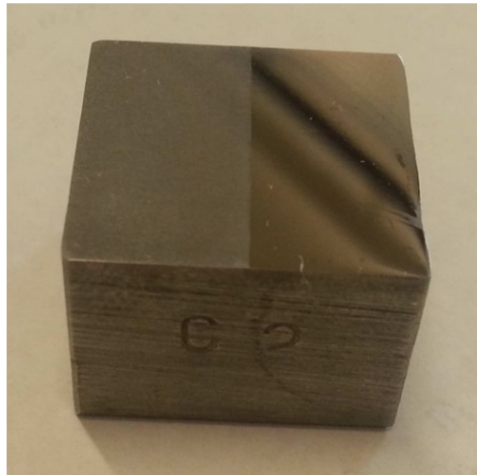


Figure 80. Specimen.

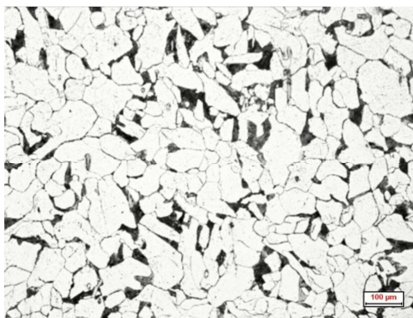


Figure 81. 200x magnification.

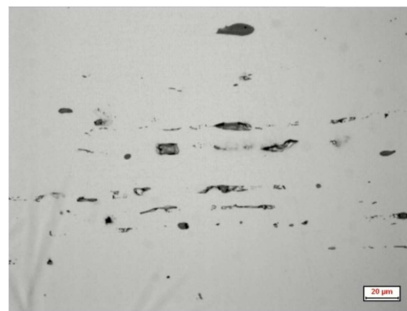


Figure 82. 500x magnification.

The shiny portion has been magnified 500 times (Figure 82) in order to estimate the amount of inclusions, porosity and slip bands. In conclusion, it can be argued that the steel has a good texture and a low imperfection index.

6.7 Quantometer analysis

The metal analyser is used mainly for determine all of the elements in the metal analysis such as carbon, phosphorous, sulphur and nitrogen. The emission spectrometry analysis allows verifying the chemical composition of the metallic alloy. The technique of the emission spectrometry analysis uses a high energy discharge created between an electrode and a sample of the material to be tested. The discharge produces an emission of radiation from the surface of the sample excited with wavelengths characteristic of the elementary composition. The radiation spectrum is separated into distinct elementary lines and the intensity of each line is measured. At the end, these intensities are converted accurately into concentration values for each element present (Figure 83).

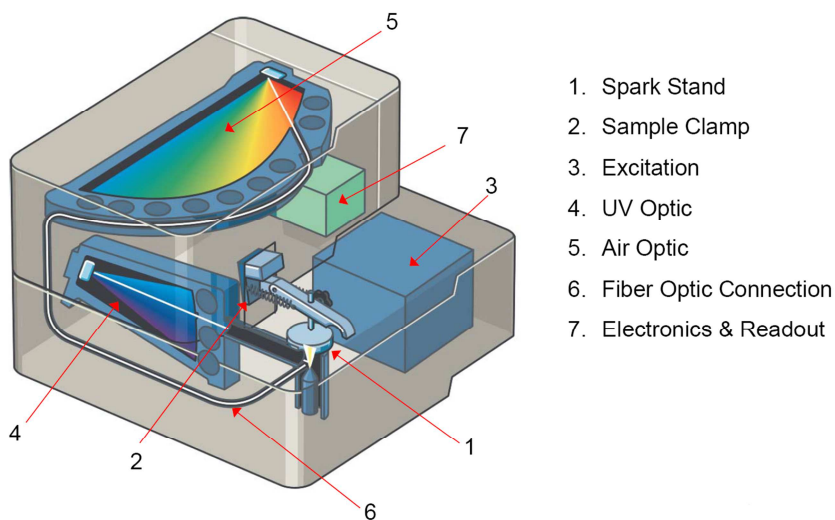


Figure 83. Quantometer.

The analysis showed a steel produced in the 1920s due to the high level of Arsenic and for the inadequate disulphate. Hypothetically, Martin-Siemens furnace

produced the steel. The results of 3 specimen inspection are summarized in Table 12:

	C	Si	Mn	P	S	Cr	N	Cu	Ni	Al
S1	0,115	0,036	0,562	0,028	0,062	0,168	0,011	0,101	0,041	0,010
S2	0,105	0,035	0,565	0,030	0,071	0,168	0,011	0,102	0,041	0,008
S3	0,110	0,036	0,553	0,027	0,057	0,166	0,012	0,100	0,040	0,009
Average	0,110	0,036	0,560	0,028	0,063	0,167	0,011	0,101	0,041	0,009

Table 12. San Stino's Steel composition

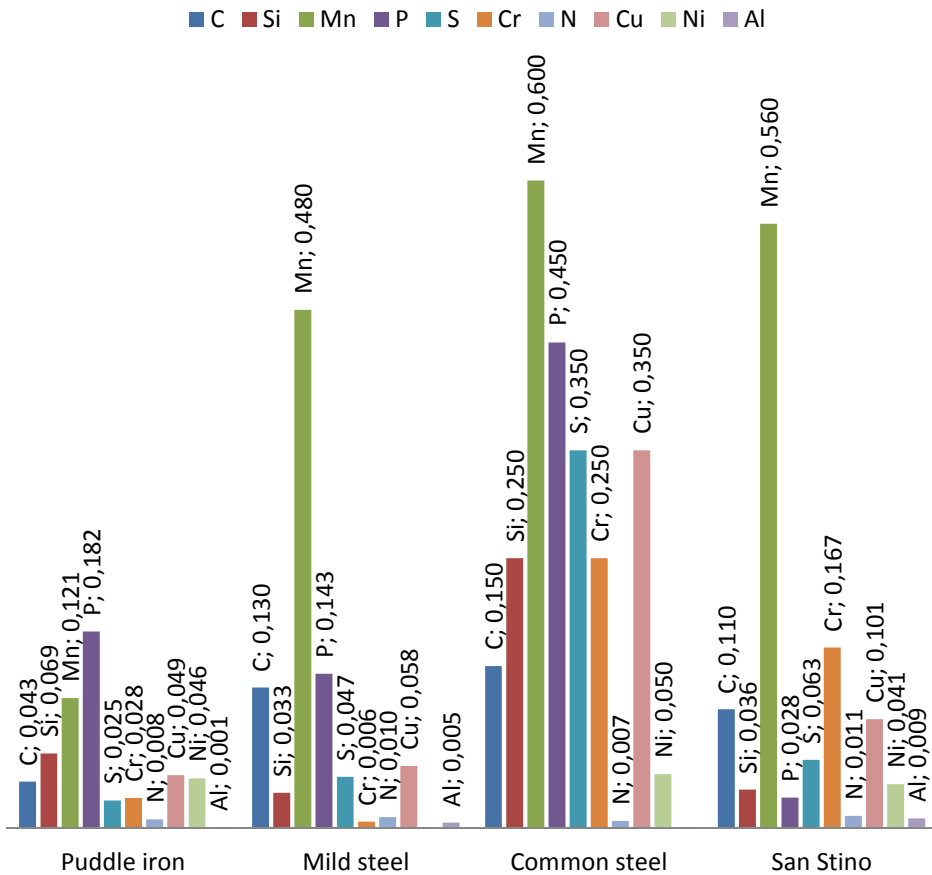


Figure 84. Steel composition.

In conclusion, San Stino's steel (Figure 84) is quite similar to mild steel and more information about steel characteristics are available in §6.2.

6.8 Material fatigue test

The objective of a fatigue test is to determine the fatigue life of a test-piece subjected to a prescribed sequence of stress amplitude. By simplifying the test conditions, it would be possible to vary one or more of the factors, that influence the fatigue life and to state their effects. Even if these conditions are fulfilled, there will always remain a number of unknown and uncontrollable factors that produce a large scatter in fatigue life even of test-piece which are considered identical. Constant-amplitude test is the simplest sequence of amplitude obtained by applying reversals of stress of constant-amplitude to the test-piece until failure occurs. Different specimens of the test series will be subjected to different stress amplitude but for each individual item, the amplitude will never be varied. A short-life test has been performed. The stress levels are above the yield stress and some of the specimens may fail statically at the application of the load. Three specimens have been obtained by a dismantled plate from San Stino's bridge. The bar characteristics and a picture are reported below (Table 13):

H	16	mm	
B	15,7	mm	
L	200	mm	
J	5359	mm ⁴	

Table 13

where H is the height, B is the width, L is the length and J is the moment of inertia. The specimens respect the De Saint Venant beam restrictions. A simple three points bending test has been carried out repeating the imposed load with the intention of investigate the fatigue behaviour. The machine utilized for carrying out the tests (Figure 85) has the following characteristics (Table 14):

Max load	20	kN
Frequency	2÷10	Hz
Force transducer (up to)	20	kN

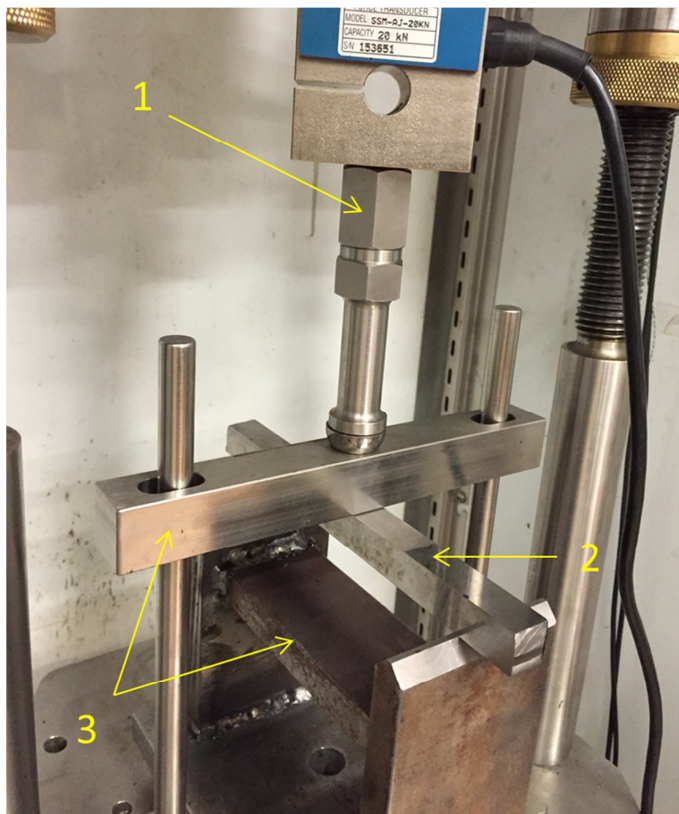
Table 14*Figure 85. Test set up: 1. Actuator and force transducer 2. Specimen 3. Supports.*



Figure 86. Acquisition system.

In Figure 85 is shown the machine, the specimen, and the support steel frame. Figure 86 shows the 3 channel acquisition: two inductive transducers have been positioned in order to obtain the vertical displacement. Preliminarily a non-linear fem simulation has been carried out with the intention to model, with high precision, the steel stress. 100'000 bricks elements (see [29]) have been utilized and the San Stino's steel has been introduced in the model (Figure 87). This Fem solution allows to gauge the tension and the plastic zones.

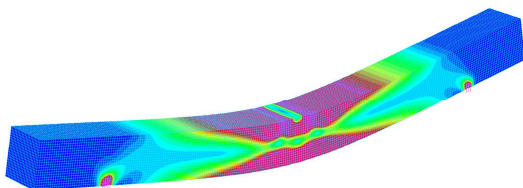


Figure 87. Non-linear model.

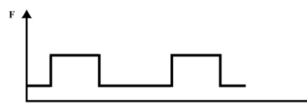


Figure 88. Quadratic wave.

For each specimen a different force level has been introduced. The cycles have been introduced with quadratic wave (Figure 88) and with $R=0$ (§3.3.1). After a different number of cycles, the specimens show fatigue cracks. The principal stresses are located near the support and at the centre line. See Table 15 for more details.

Specimen	Force (kN)	Maximum stress (MPa)	Cycles
1	9,5	350	8,28E4
2	7,9	240	3,96E5
3	10,4	380	8,66E4

Table 15

In the images below (Figure 89 and Figure 90) the fatigue cracks on the specimens are shown.

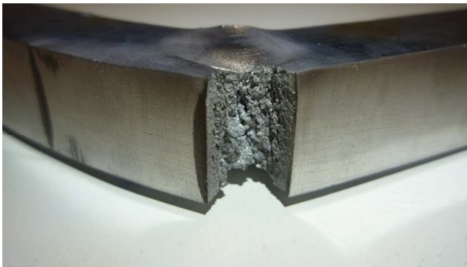


Figure 89. Sample 1 crack.



Figure 90. Sample 2 crack.

The results are presented in Figure 91. The Wohler diagram is fundamental to investigate the fatigue behaviour (see §3.3.1). The lower and the upper fatigue class, respectively 36 and 160 MPa, are marked with straight lines. Moreover, the horizontal lines evidence the yield and the ultimate stress range. The three samples show a good fatigue behaviour approaching the following class (Table 16):

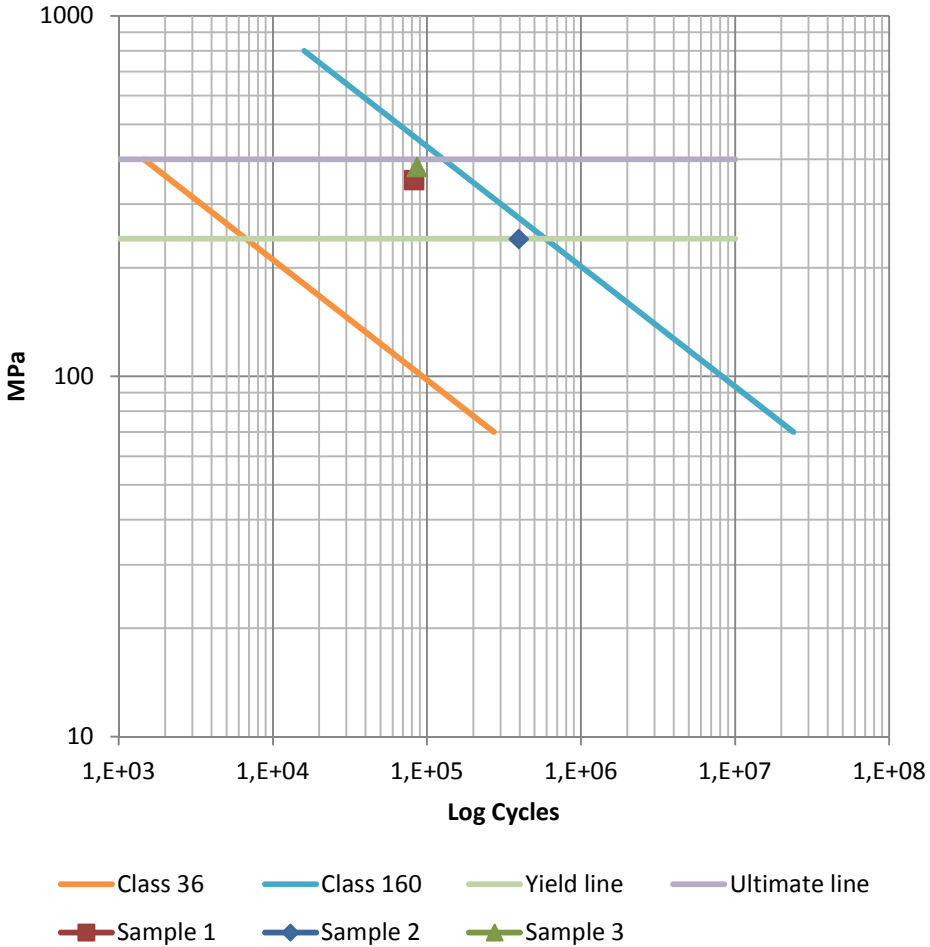


Figure 91. S-N curves.

Sample	Class identified
1	120
2	140
3	130

Table 16

The read values are compatible with the actual regulations [5]: the reference classes are between 125 and 160. These first evaluations suggest a good fatigue behaviour for San Stino's steel. For the pure material, the web and the flanges

subjected to bending moment seem indicate a Fatigue Class 130. It is noteworthy that the samples have been taken from a cross girder web without any information about the previous fatigue condition. Other tests are planning with the intention of classify San Stino's steel.

6.9 Final considerations

The bridge is 34,4 m long, belongs to the Italian State Railways and it has been operational for about a century. San Stino's bridge was assembled using rivets and its simple supported reticular bridge had 5300 mm width and 3500 mm high. In the lack of original design, every bridge dimension and structural consideration have been evaluated experimentally. San Stino's bridge was designed and constructed before the standardisation and the widespread use of design codes. In July 2011, some elements were taken in order to test their static and fatigue behaviour. The reticular longitudinal elements were composed by overlapping a different number of plates in order to follow the bridge bending moment. A multilayer protective coat was present all over the bridge, in first analysis it is lead oxide. The extracted elements have some damages like as WWII machine gun holes or corrosion degradation. In first approximation the rail bearer static scheme is considered fixed to the cross girder. A preliminary Fem analysis model is carried out in order to estimate the global and local structural behaviour. In a previous identification, carried out in July 2011, the dynamic response of the bridge was recorded using piezoelectric acceleration transducers. A good correlation between the Fem simulation and the acceleration registered by the sensors has been observed. In order to acquire sufficient information about the characteristics of the bridge, some steel samples were extracted and some tests were carried out. The traction test shows that San Stino's steel is comparable to Mild Steel (Yield point: 240 MPa, $E=190000$ MPa). Some other physical and chemical tests confirm the consideration regarding the modern steel manufacture. A simple three points bending test has been carried out with the intention of investigating the fatigue behaviour. Different specimens have been subjected to different stress amplitude but for each individual item, the amplitude will never be varied. A short-life test has been performed; moreover, the steel stress has been modelled with a non-linear fem simulation. Preliminaries evaluations suggest a good fatigue behaviour for San Stino's steel. The pure material, subjected to bending moment, seem indicate a Fatigue Class 130. Other tests are planned with the intention of classifying San Stino's steel.

SAN STINO'S RAILWAY BRIDGE

Despite the age of the bridge, the steel quality and the manufacture process guarantee a sufficient safety factor.

7 TORSIONAL CLAMPING TESTS (TCT)

7.1 Original clamping force

The clamping force constitute essential aspects of the construction process which can affect the strength and the lifetime of old riveted structures. Referring to §5.3 and using the consideration from §5.4 the Equation (33) becomes:

$$F_{cl,t=0} = 0,7 * \sigma_y * A_{riv} = 0,7 * 300 * 419 = 103kN \quad (56)$$

which correspond clamping stress (Equation (57)):

$$\sigma_{cl,t=0} = \frac{F_{cl,t=0}}{A_{\phi 25}} = 210MPa \quad (57)$$

for standard San Stino's rivet ($\phi 25$) at year of construction. The equation (58) gives:

$$\Delta L_{riv,t=0} = \frac{F_{cl} * L}{E * A_{riv}} = \frac{103 * 30}{2E5 * 419} = 0,037mm \quad (58)$$

where L= 30 mm in the rail bearer web. These values refer to the age of bridge construction nevertheless the clamping force decreases due to thermal load, vibrations, electric flows and others effects.

7.2 Current clamping force

The evaluation of clamping force is usually carried out by destructive tests or simply referring to the initial steel yield stress. As stated above, the clamping force is a fundamental parameter to investigate the fatigue behaviour of riveted structures. Rivets are very difficult to monitor for the following reasons:

- they are inside the web plates and removing them may cause excessive perturbations,
- the rounded head impedes every traction catch attempt, nevertheless an adequate anchor may compromise the result,
- the standard traction test would be too cumbersome for the bridge geometries,
- many other static tests may wreck the rivet function.

The analysis of the bridge condition provides an essential information regarding the performance of the bridge. In particular, for metal bridges, reporting cracks and repairs provides valuable information (see prEN 1090-2; 2005) for bolted and riveted connections. The number of rivets inspected overall in a structure shall be at least of 5%, with a minimum of 5. Heads of driven rivets shall be visually inspected and shall satisfy the following acceptance criteria (in some cases provisions for detection of nonconformities will not be available):

- the rivet heads shall be well formed and shall not show cracks or pits;
- the rivet heads shall be centred. The head eccentricity relative to the shank axis shall not exceed $0.15 d_0$ where d_0 is the hole diameter;
- a small well-formed and centred lip may be accepted if only a small number of rivets in the group is concerned;
- the rivets shall be in satisfactory contact with the assembled parts both at the outer surface of the plies and in the hole. No movement or vibration shall be detected when the rivet head is lightly tapped with a hammer;
- outer faces of plies free of indentation by the riveting machine may be specified.

Inspection of satisfactory contact shall be done by lightly ringing the rivet head with a hammer of 0.5 kg mass. The inspection is carried out in a sequential fashion according to the sequential method for bolt tightening inspection. The visual inspection of the rail bearers and cross girders is also very important. In this thesis an innovative clamping test is proposed (§7.1). Revealing the clamping force, a more precise fatigue evaluation is possible.

7.2.1 TCT - Experimentation

With the purpose of estimating the actual clamping force with an improved precision, a specific and innovative test has been conceived. The idea is to evaluate the clamping force by means of torsion test (TCT). The applied torsional moment is proportional to the force generated by the frictional ring area of the rivet head subjected to clamping force (Figure 92, Equation (59)). The rivet is subjected to a rigid rotation.

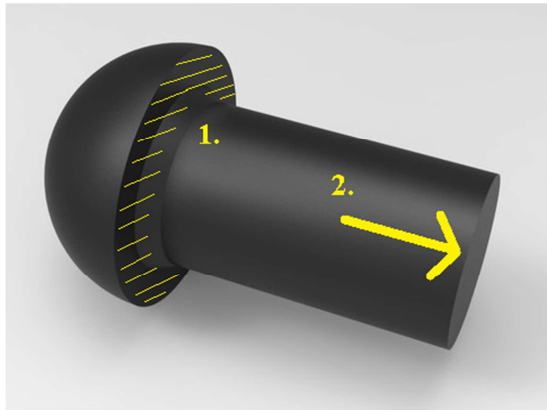


Figure 92. Rivet 1. Frictional area 2. Clamping force.

$$M_{ext} = \underbrace{C * K_s}_{M_{int}} \quad (59)$$

where M_{ext} is the torsion effect applied externally using an instrumented wrench, C is the internal clamping force, K_s the friction coefficient and M_{int} is the resisting moment (see Figure 93, Figure 94).



Figure 93. External moment.

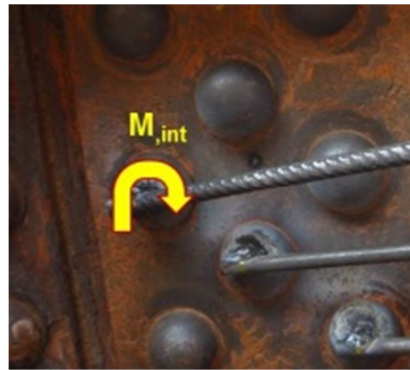


Figure 94. Resisting moment.

A non-destructive test is recommended with the intention of extending this investigation campaign to other in-service bridges. An external rail bearer node has been tested in order to preserve the beam static behaviour. First of all, the rivets heads have been cleaned to remove any protective paint. Afterwards a nut has been welded, both internally and externally, above the rivet head using an arc welding machine. Few weld points guarantee an adequate connection without compromising the rivet stress condition (Figure 97). The welding involves only the external rivet head portion preserving the internal stress distribution (Figure 96). On the same rivet, but on the other side, a similar procedure has been adopted so as to weld a steel rod (Figure 95).

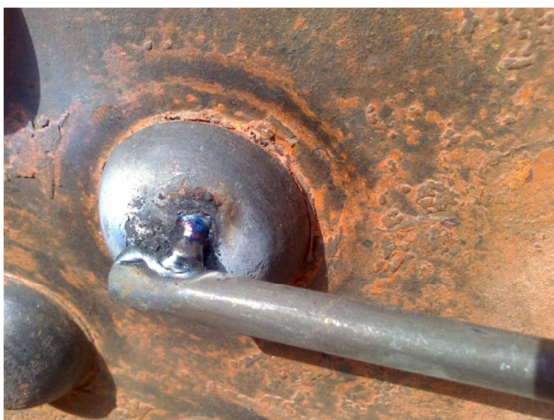


Figure 95. Welded rod.



Figure 96. Monolithic nut connection.



Figure 97. Nut welding.

The same procedure has been repeated on other two rivets (distributed diagonally) with the purpose of collecting more data and investigate the clamping force distribution in the joint. For "a" and "A" series the rod is about 290 mm length, for "m" and "M" series the rod is about 231 mm and for "b" and "B" series the rod is about 210 mm.

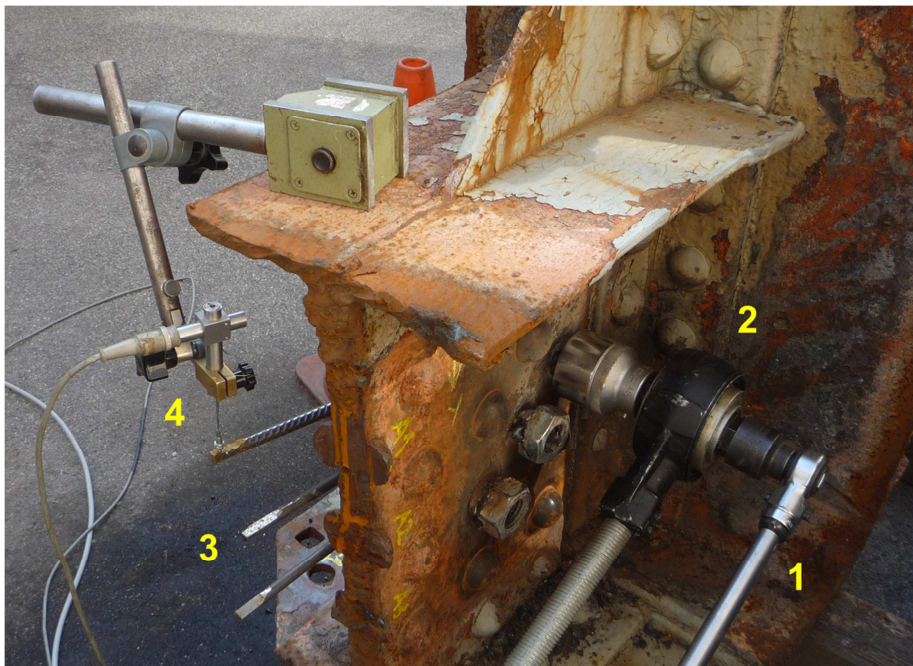


Figure 98. Test set up: 1) instrumented wrench
2) force multiplier 3) rod 4) displacement transducer.

TORSIONAL CLAMPING TESTS (TCT)

As shown in Figure 98, the setup has a wrench that introduces the torsional force, a multiplier to increase the wrench force, a rod in order to enhance the transducer gauge and the inductive transducer which is necessary to acquire the displacement. The multiplier (Figure 99) increases the force applied 5 times and it is necessary due to the high rivet clamping level.



Figure 99. Wrench.



Figure 100. Rods.

The rod is indispensable owing to the very small rivet head rotation (Figure 100). Every rod has been calibrated to gauge an angle approximately equal to the sine. The acquisition has been made by MGC plus HBM controller, software HBM Catman professional 5.0 at 10 Hz frequency (Figure 101). The force has been measured using up to 2000 N load cell, furthermore the displacement transducer is inductive type with a precision of 1/100 mm and +/- 10 mm shift.



Figure 101. HBM controller.

The force applied by the wrench introduces a rigid rivet rotation hindered by the rivet friction. The clamping force is proportional to the force required to overcome

the static friction. This is the aim of the test: to estimate the clamping force by means of torsional stress. Preliminary evaluations have highlighted that the only rivet area interested by the friction is the rivet head ring. The shank is free to move due to the increased hole diameter and for the cooling diameter reduction (see §7.2.2.1). In this preliminary test, 3 rivets have been measured repeating the gauges several times. First data series (wrench length: 0,5 m) is marked as lowercase and a relative small rod displacement is measured. Second data series (wrench length 1 m) is marked as uppercase and a bigger displacement is measured. The upper rivet is called "a" or "A", the medium is "m" or "M" and the bottom one is "b" or "B". For each series and for each rivet more data have been collected. The "small displacement" series is more accurate and most suitable than the "big displacement" series that has been performed to evaluate the post - slip behaviour.

7.2.2 TCT: Small displacement

7.2.2.1 "a" series

The first series of data refer to top rivet (Figure 102), the test results are shown below.

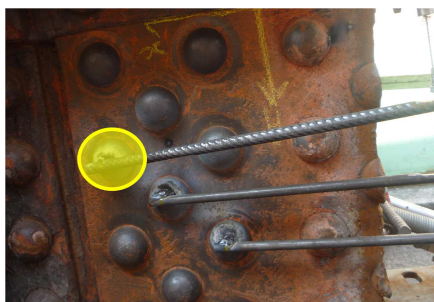


Figure 102. Top rivet.

Figure 103 shows the Force – Rod displacement correlation. Approximately the same behaviour for each repetition is observed, nevertheless the force variability is notable. The force varies from 1 to 2 kN, the displacement is not greater than

TORSIONAL CLAMPING TESTS (TCT)

12 mm. Figure 104 shows the force - time trend: each test lasted about 40 seconds. Figure 105 shows Rod displacement Vs. Time and highlight the unconventional displacement for the 3rd repetition. Test 2a failed and results are not reported.

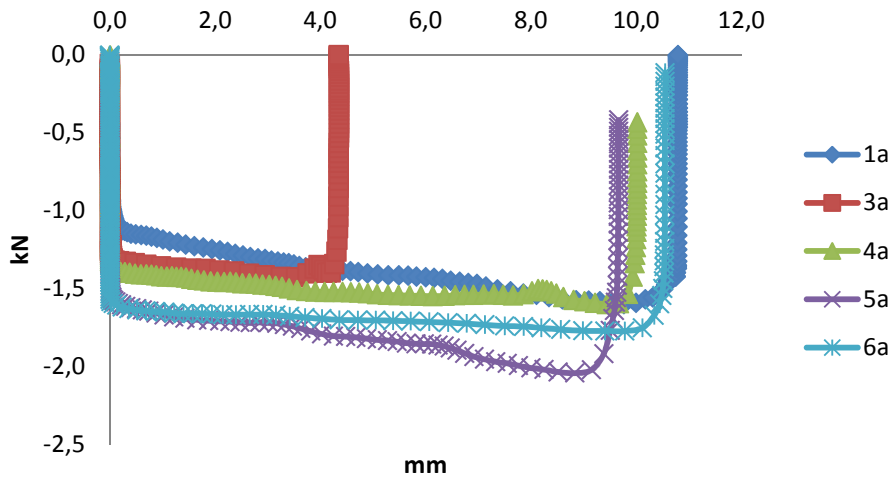


Figure 103. Force – Rod displacement.

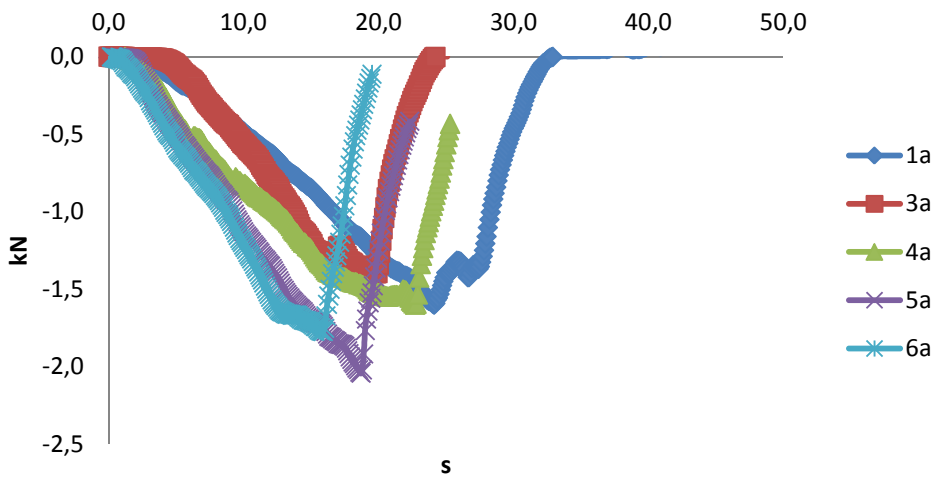


Figure 104. Force – Time.

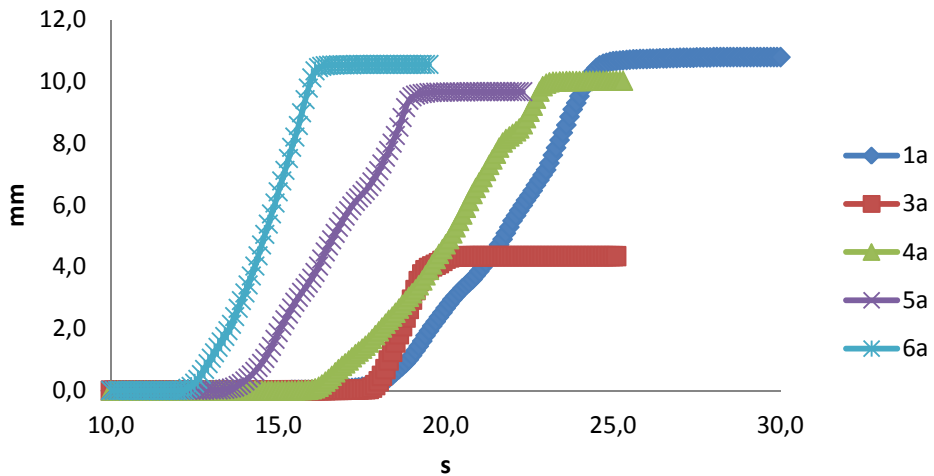


Figure 105. Rod displacement – Time.

Predictably, rivets behaviour is unstable and has a large variability. Starting from these measures the goal is to estimate the activation slip force. The first method intercepts the line slope whereas the second one assumes the activation force directly from a pre-established head rotation. In the images below (Figure 106, Figure 107, Figure 108, Figure 109 and Figure 110) the tangent method is presented: the line intercept describes the activation slip force.

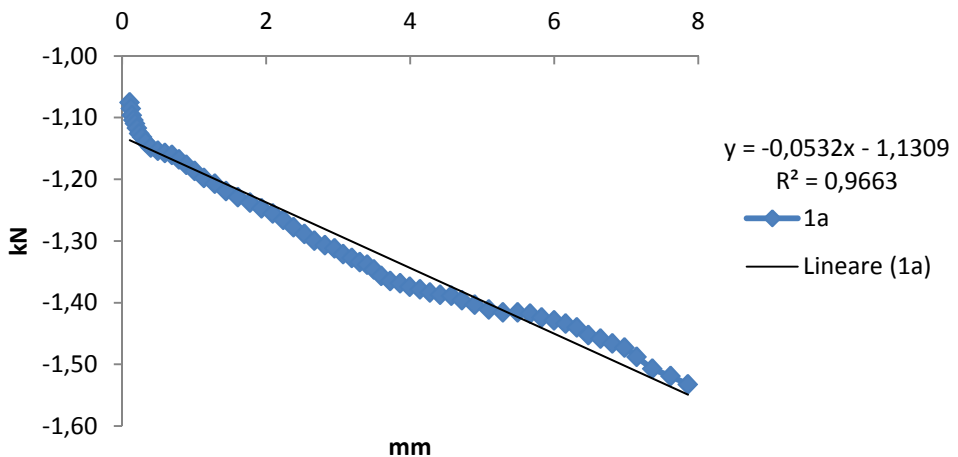


Figure 106. Tangent method (1a).

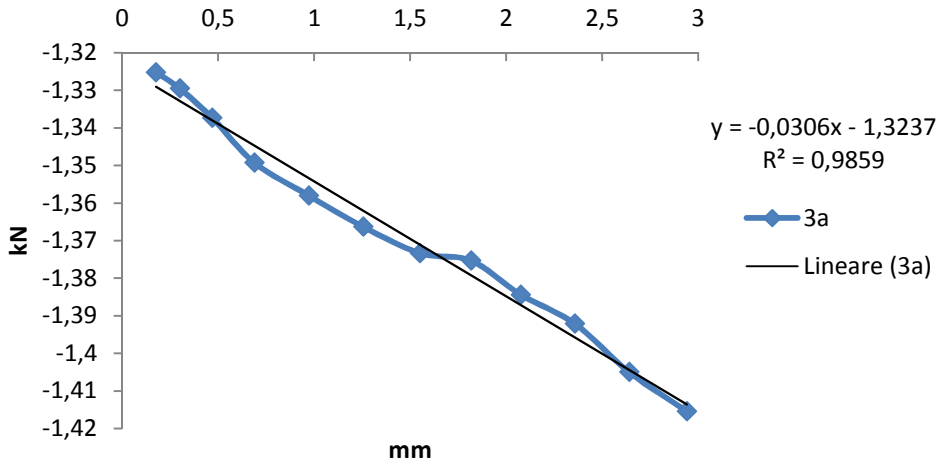


Figure 107. Tangent method (3a).

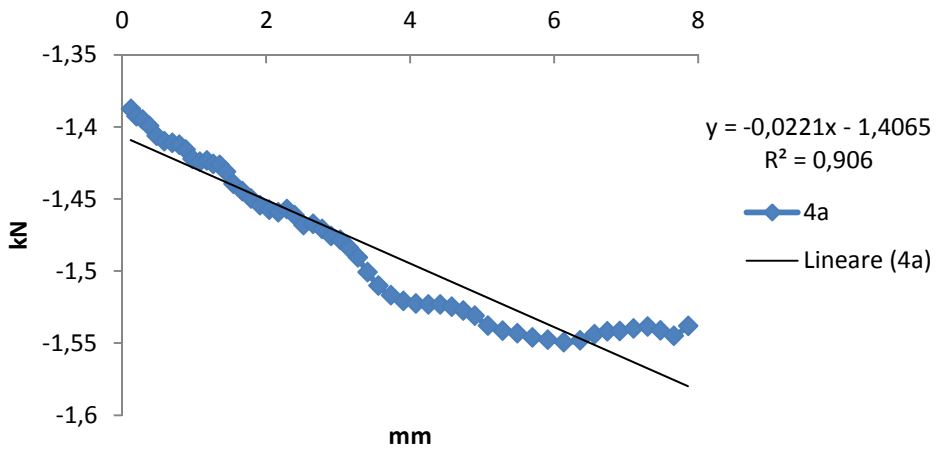


Figure 108. Tangent method (4a).

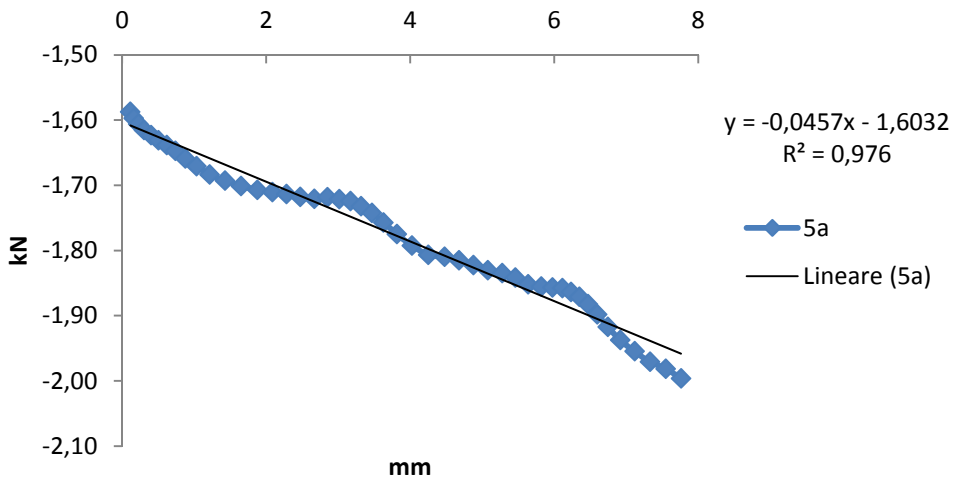


Figure 109. Tangent method (5a).

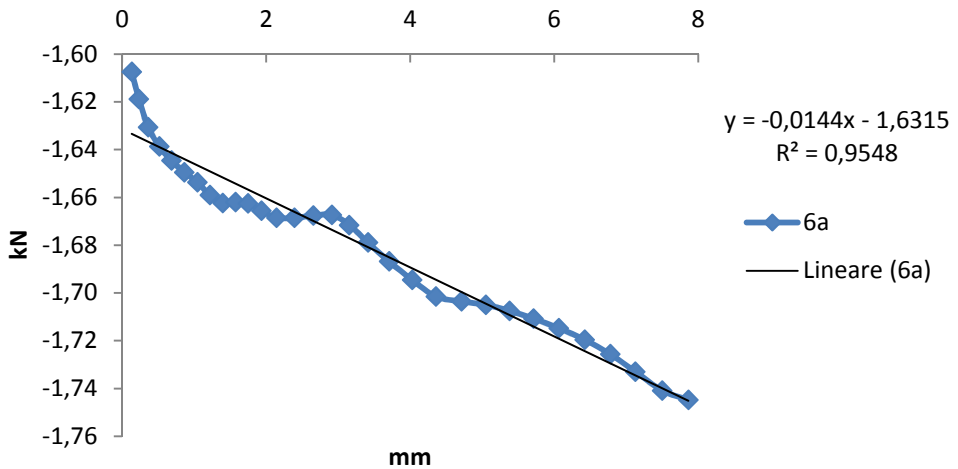


Figure 110. Tangent method (6a).

This method is not reliable when the slope changes repeatedly, for example see "6a" case (Figure 110). An additional method is to establish a rotation threshold: in this thesis, 1/100 degree is arbitrarily taken. This method has the advantage of being more stable and assume a more accurate initial slip force. Results are summarized in Table 17.

	Tangent method				
	1a	3a	4a	5a	6a
Activation Force (kN)	1,1309	1,3237	1,4065	1,6032	1,6315
	Rotation method				
Activation Force (kN)	1,0241	1,3216	1,3779	1,5702	1,596458

Table 17

Table 17 is synthesized in Figure 111.

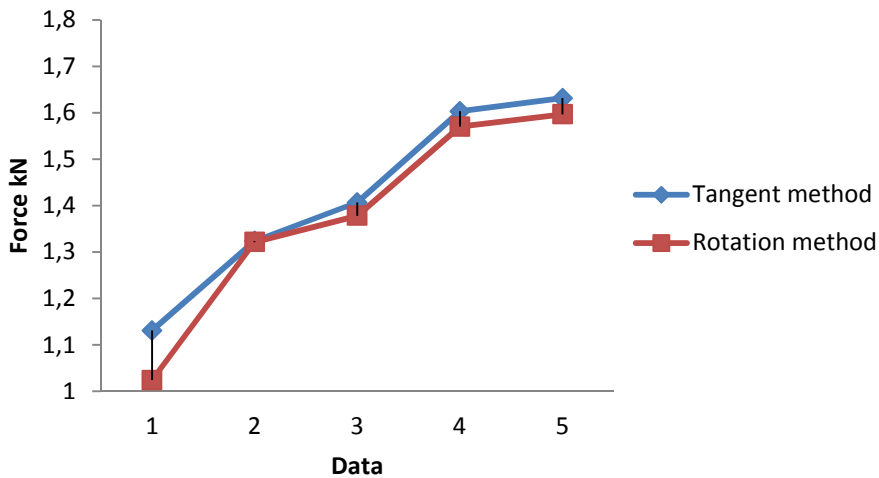


Figure 111. Methods comparison.

Each repetition increases the torsional force that cause the start of the slip. This phenomenon is not related to the non-uniform torsion due to the circular shank shape. A detailed Fem simulation, using brick elements and introducing torsional moment, has been carried out in order to check the stress and strain distribution along the rivet shank. No significant shank deformations, that could indicate friction inside the plate hole (Figure 112), have been observed.

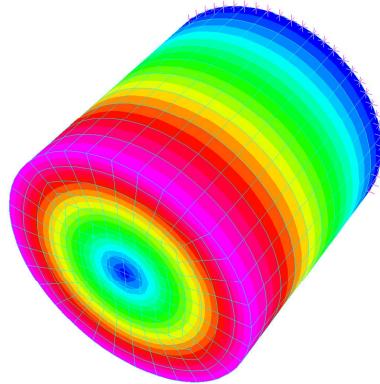


Figure 112. Shank deformation (Fem).

This phenomenon is explained as follow: the force application creates torsional stress on the rivet shank that may produce differential rotations in the rivet heads. The rotational effect might emphasize the rivet imperfections (Figure 113), in particular the non-parallelism of the rivet heads. The configuration change may produce an increment of friction activation moment due to the forcing of head position (Figure 114).

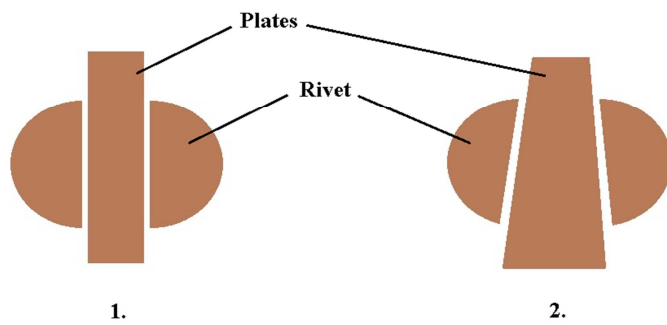


Figure 113. Schematic union: 1. Ideal connection 2. Real connection.

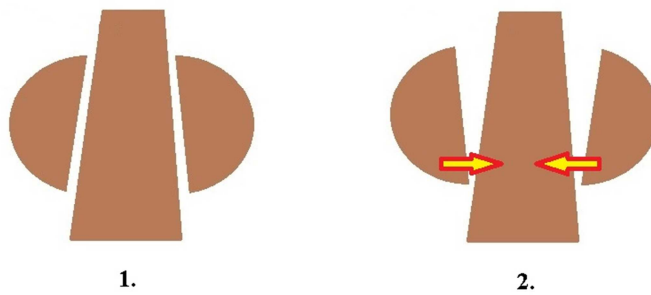


Figure 114. Schematic union: 1. Original position 2. Post-torsion position.

The ratio between the first acquisition (1a) and the subsequent one (ia) is given by the “Increment factor” (Eq. (60)):

$$I_f = \frac{F^{1a}}{F^{ia}} \tag{60}$$

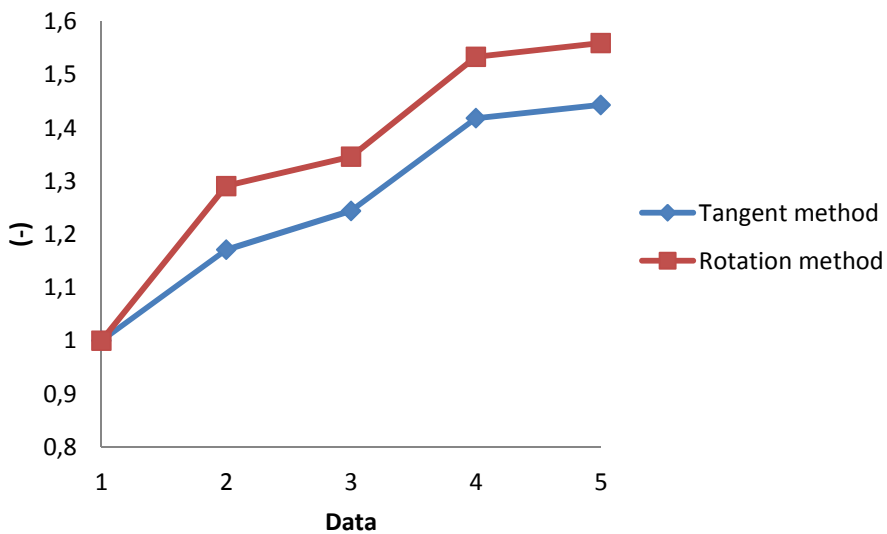


Figure 115. Increment factor.

This comparison shows an increase of about 0,57 kN (precisely $I_{f,max}=1,56$; average value 1,38 kN) of the force needed to start the friction effect (Figure 115). A similar but more interesting representation is given in Figure 116 where Force is correlated to the rivet head Rotation. Here the head rotation is less than $2,5^\circ$.

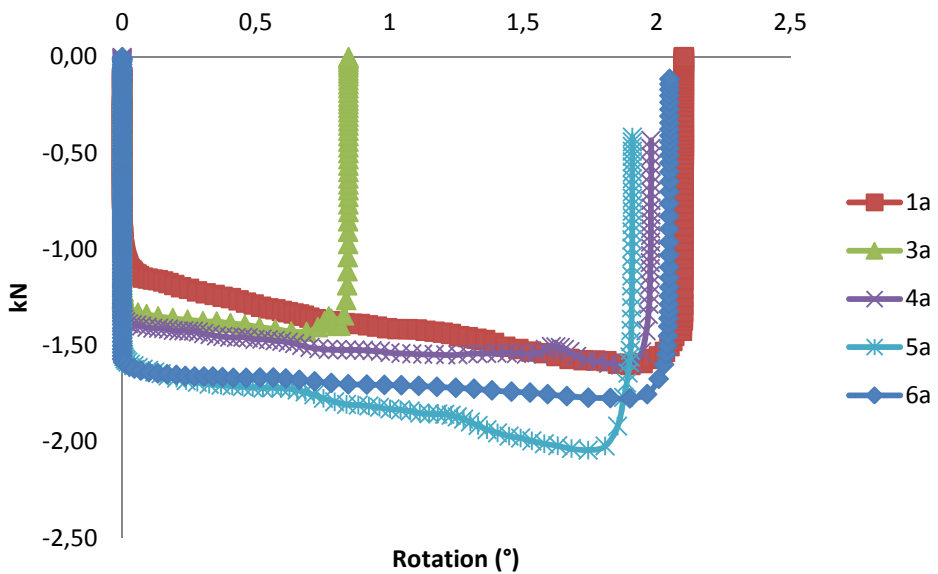


Figure 116. Force – Wand rotation (“a” Rivet).

Figure 117 shows the relationship between rotation and moment whereas torque trend is represented in Figure 118.

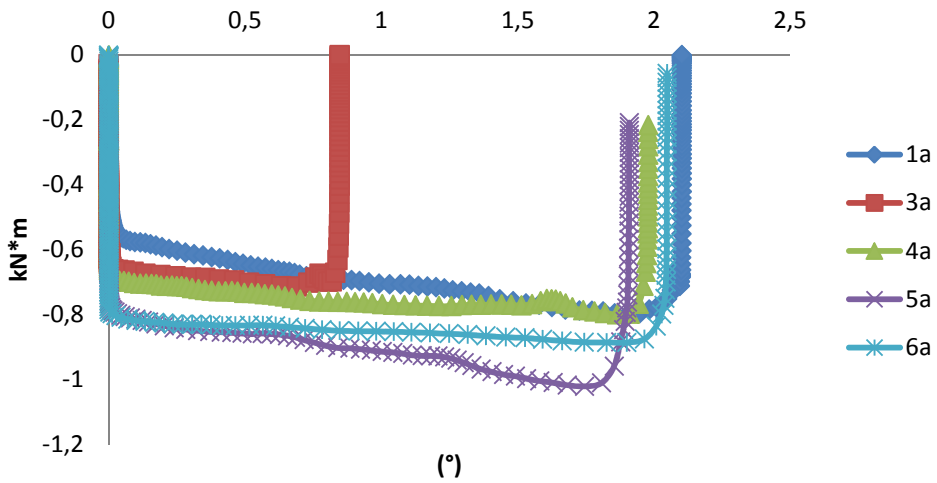


Figure 117. Moment – Wand rotation ("a" Rivet).

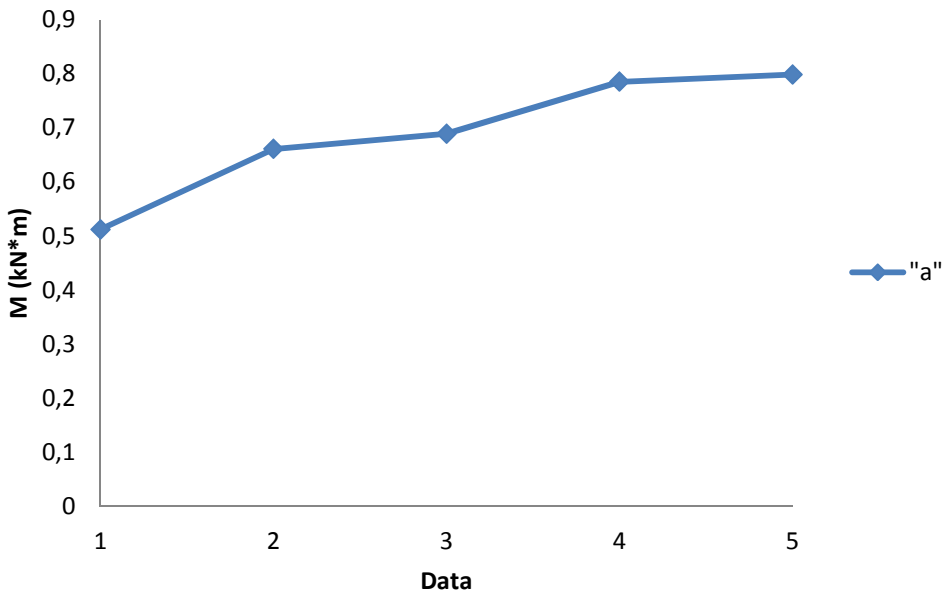


Figure 118. Activation torque.

In the image below (Figure 119) the hysteresis is shown.

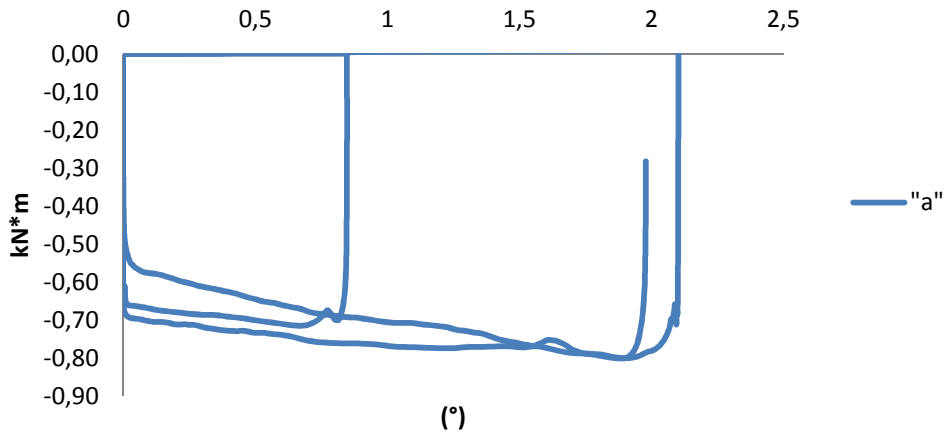


Figure 119. Hysteresis.

For this first data series the activation moment is about 0,7 kN*m and each repetition increases the force needed to start slip.

7.2.2.2 "m" series

For the medium rivet (Figure 120) the same data were collected. Results are summarized from Figure 121 to Figure 127 and in Table 18.

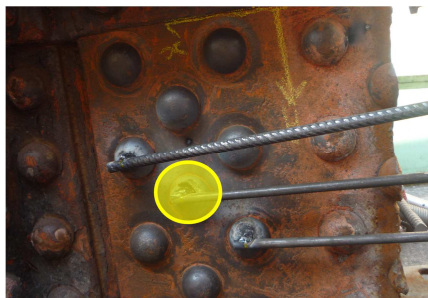


Figure 120. Medium rivet.

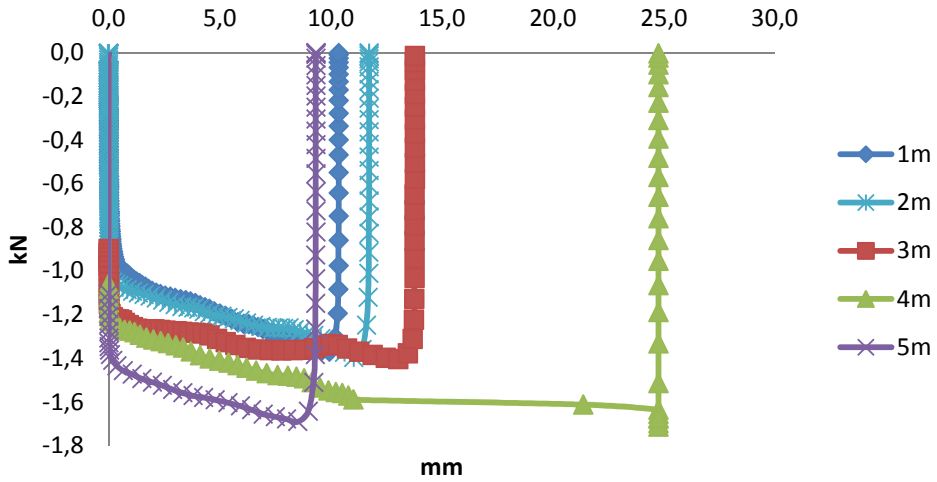


Figure 121. Force – Wand displacement (“m” Rivet).

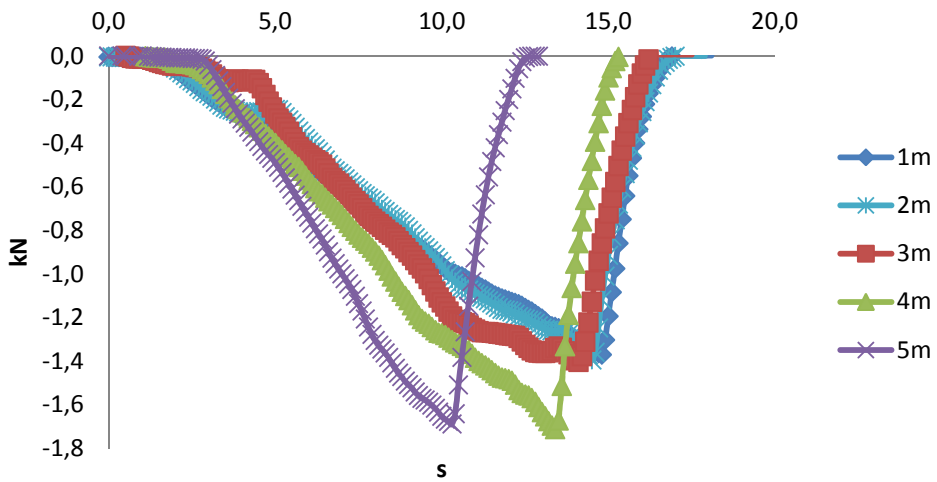


Figure 122. Force – Time (“m” Rivet).

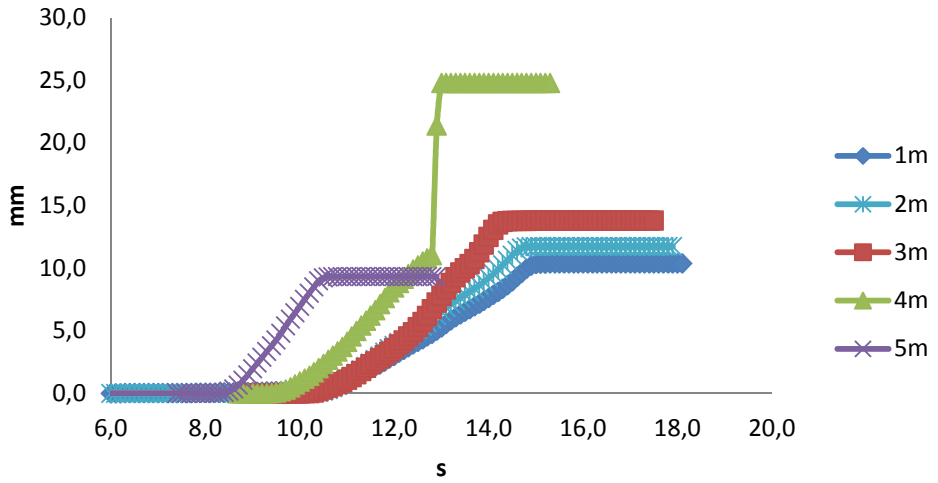


Figure 123. Wand displacement – Time (“m” Rivet).

For 4m data series, an irregular rivet slip has been recorded.

	Rotation method				
	1m	2m	3m	4m	5m
Activation Force (kN)	0,7163	1,0370	1,1963	1,2187	1,383391

Table 18.

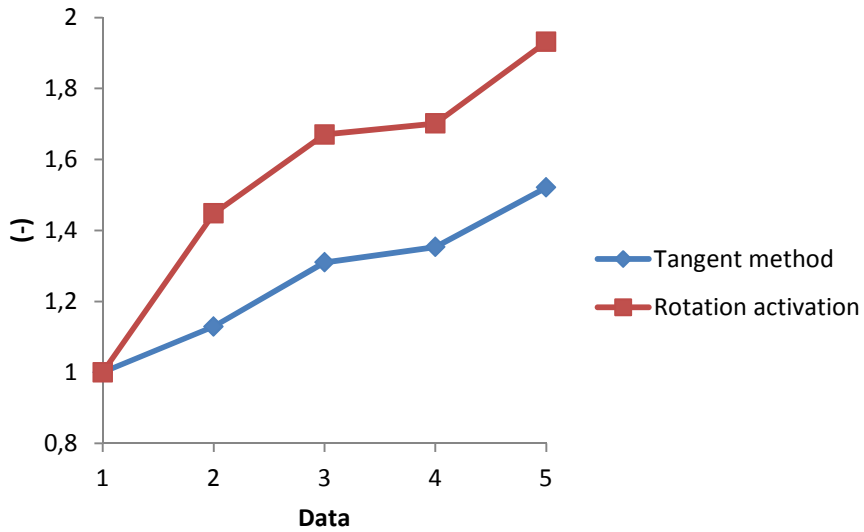


Figure 124. Increment factor.

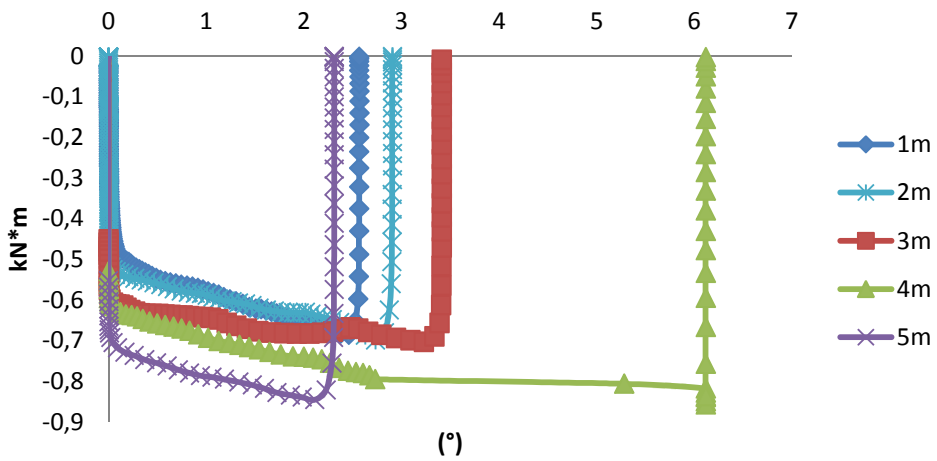


Figure 125. Moment – Wand rotation (“m” Rivet).

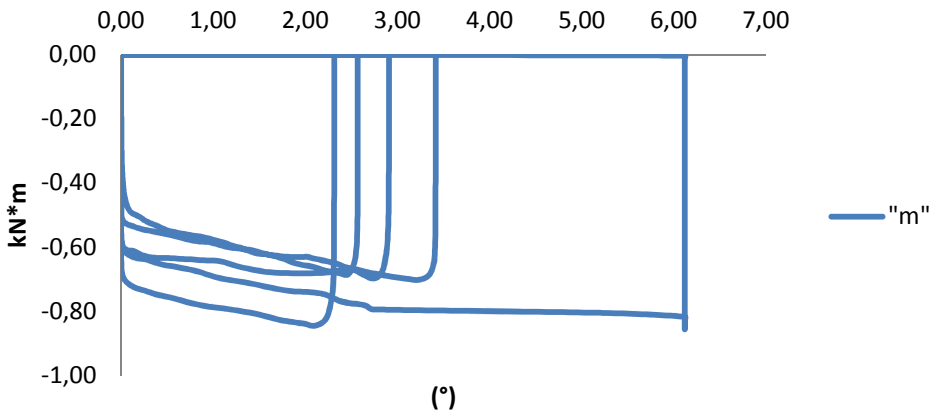


Figure 126. Hysteresis.

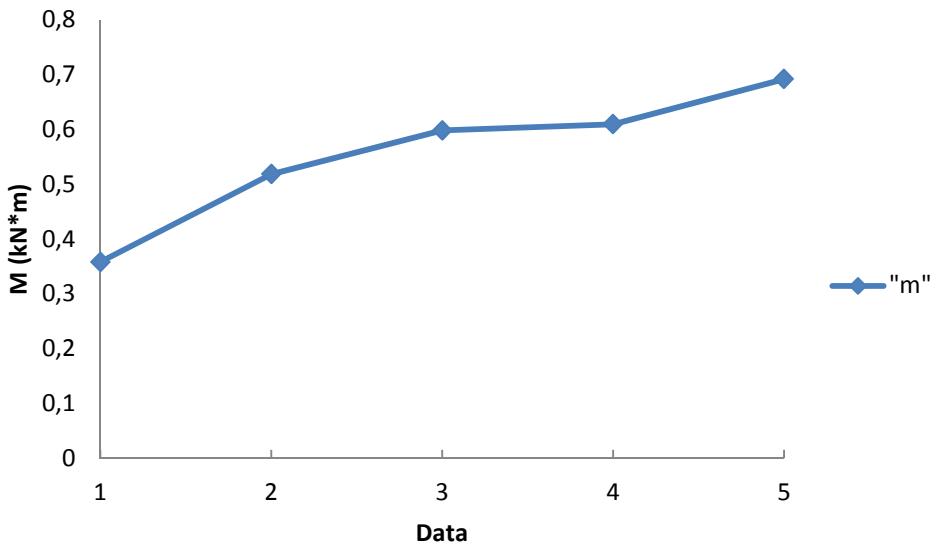


Figure 127. Activation torque.

The incremental factor, for "m" series, is $I_{f,max}=1,93$ with average value 1,11 kN and increment of 0,67 kN. For the second data series, the activation moment is about 0,6 kN*m and each repetition increases the force needed to start slip.

7.2.2.3 "b" series

For the bottom rivet (Figure 128) results are summarized from Figure 129 to Figure 135 and Table 19.

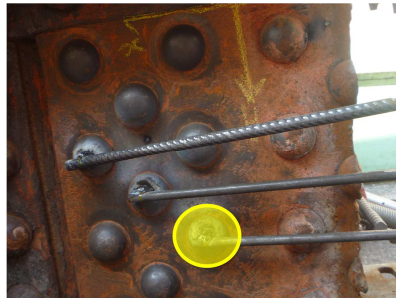


Figure 128. Bottom rivet.

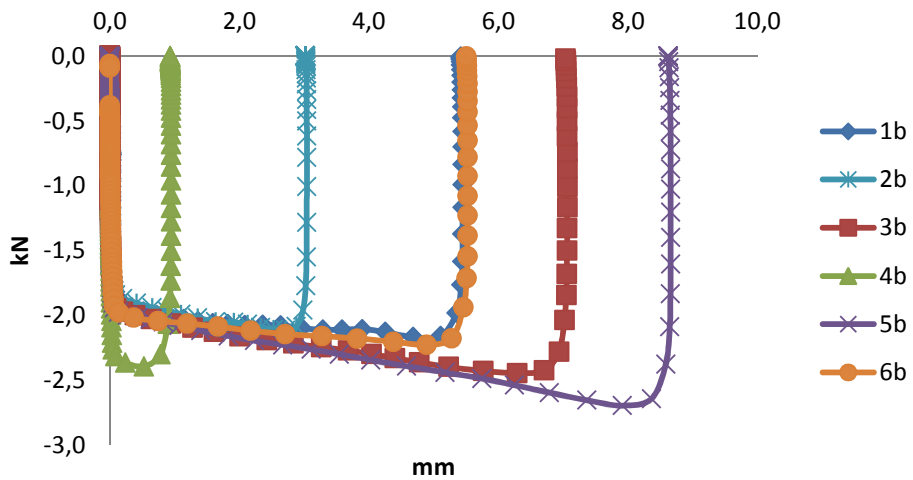


Figure 129. Force – Wand displacement ("b" Rivet).

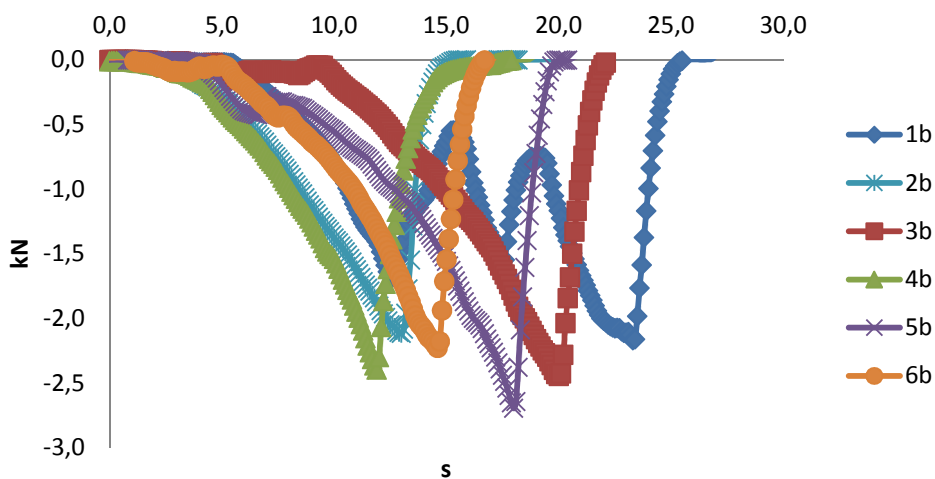


Figure 130. Force – Time ("b" rivet).

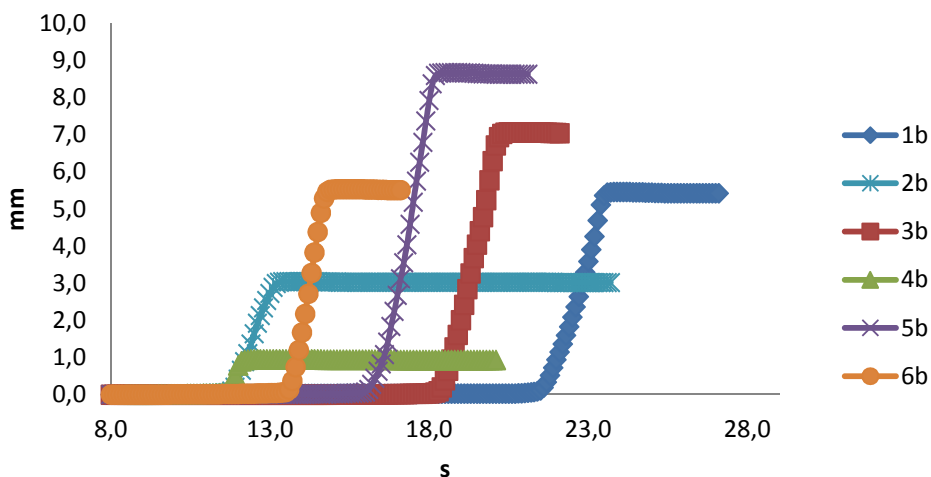


Figure 131. Wand displacement – Time ("b" Rivet").

	Rotation method (kN)					
	1b	2b	3b	4b	5b	6b
Act. Force	1,6694	1,7899	1,8702	2,2117	1,8311	1,7014

Table 19.

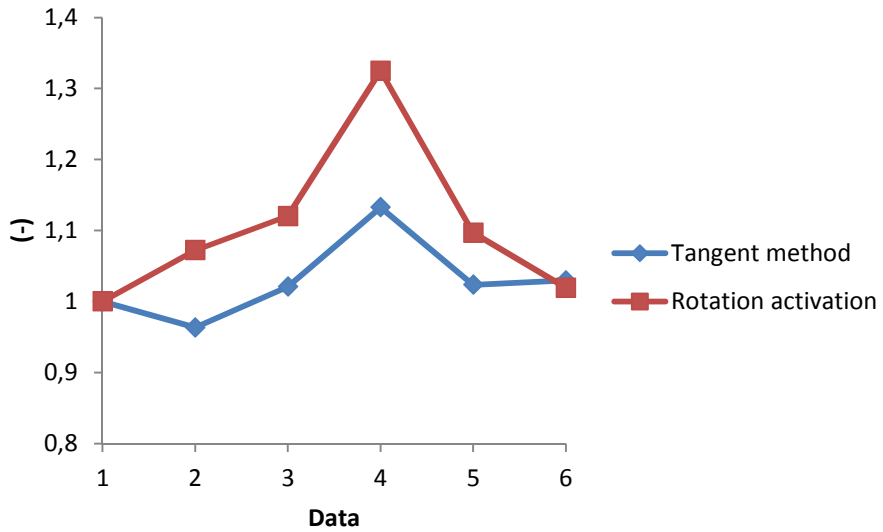


Figure 132. Increment factor.

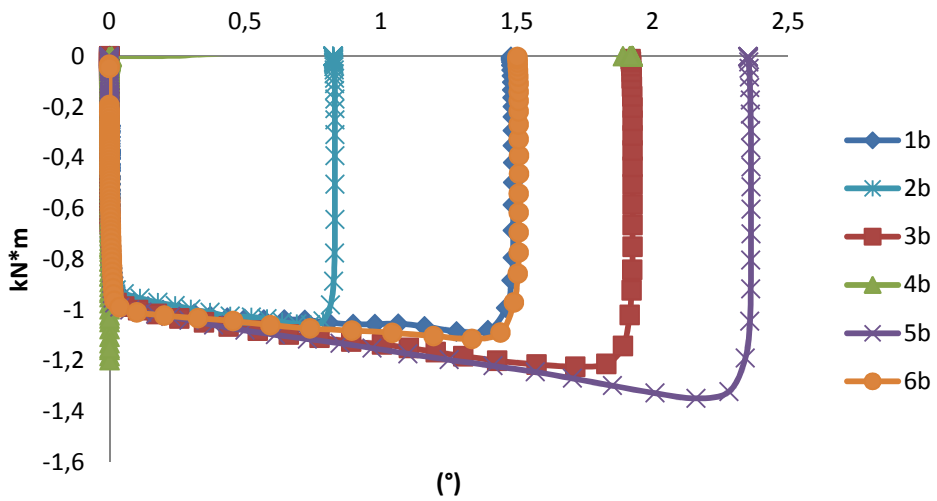


Figure 133. Moment – Wand rotation (“b” Rivet).

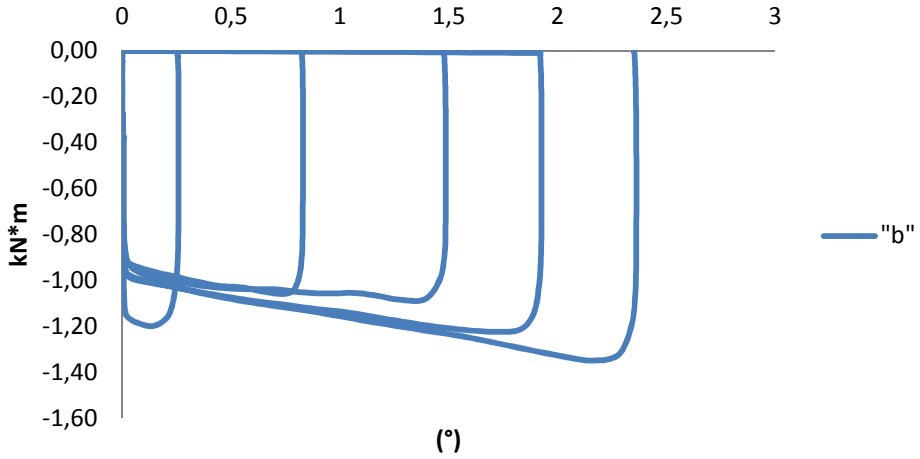


Figure 134. Hysteresis.

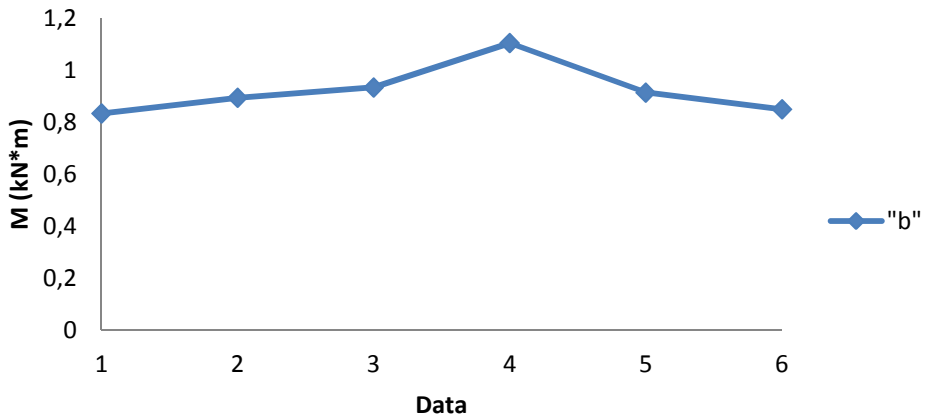


Figure 135. Activation torque.

The incremental factor, for "b" series, is $I_{f,max}=1,32$ with average value 1,85 kN and increment of 0,54 kN. For the last data series, the activation moment is about 0,9 kN*m: only the 4th repetition gives an outlier value.

TORSIONAL CLAMPING TESTS (TCT)

7.2.3 TCT: Big displacement

For the same rivets a further data set has been collect going beyond the (relatively) small rivet head rotation cited in §7.2.2. These data will help to understand the rivet behaviour and the clamping effect.

7.2.3.1 "A" series

For the upper rivet (Figure 136), results are summarized from Figure 137 to Figure 143 and in Table 20.



Figure 136. Top rivet.

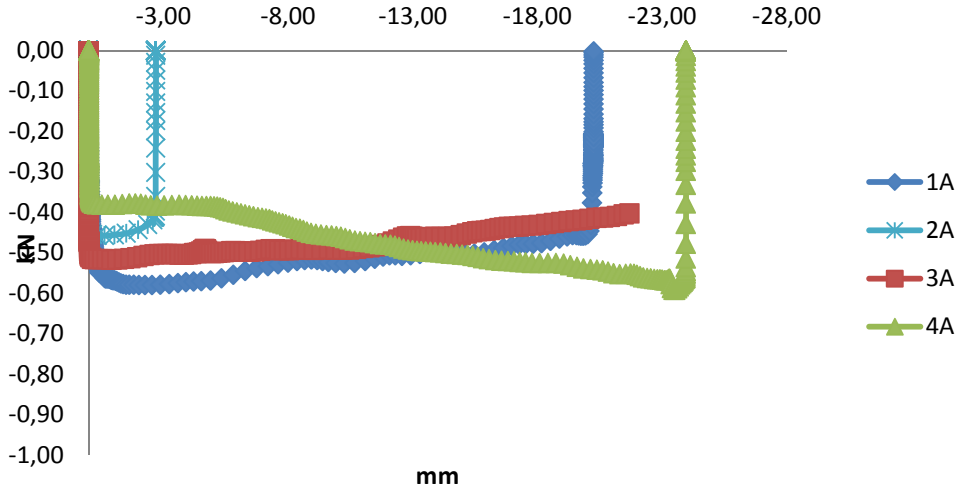


Figure 137. Force – Wand displacement (“A” Rivet).

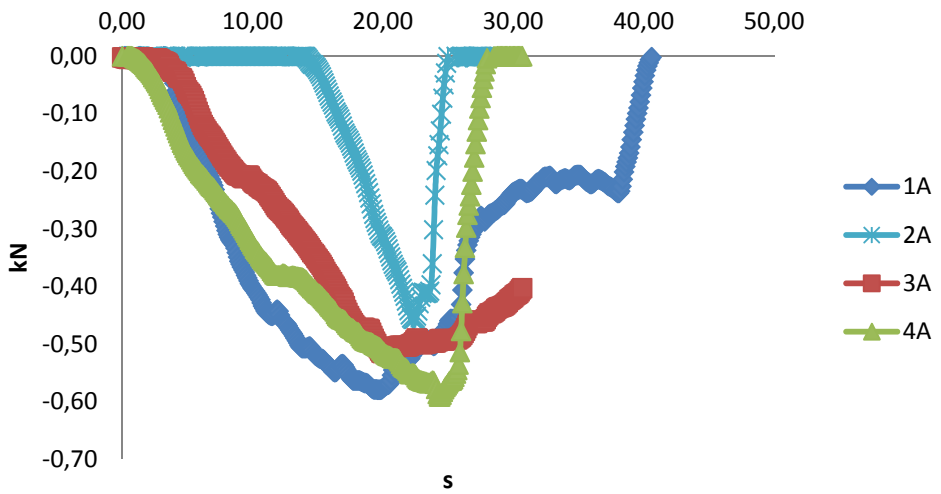


Figure 138. Force – Time (“A” Rivet).

TORSIONAL CLAMPING TESTS (TCT)

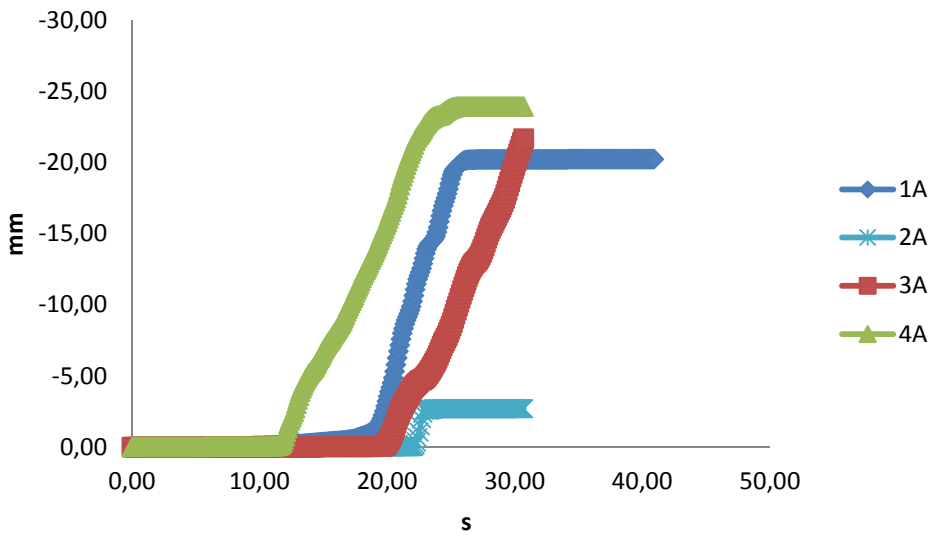


Figure 139. Wand displacement – Time (“A” Rivet).

	Rotation method			
	1A	2A	3A	4A
Act. Force (kN)	0,2946	0,4422	0,5040	0,3108

Table 20

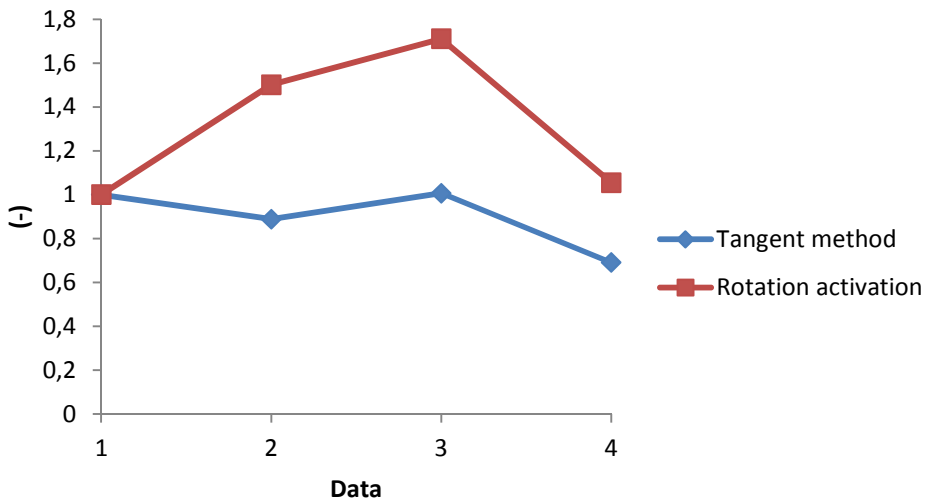


Figure 140. Increment factor.

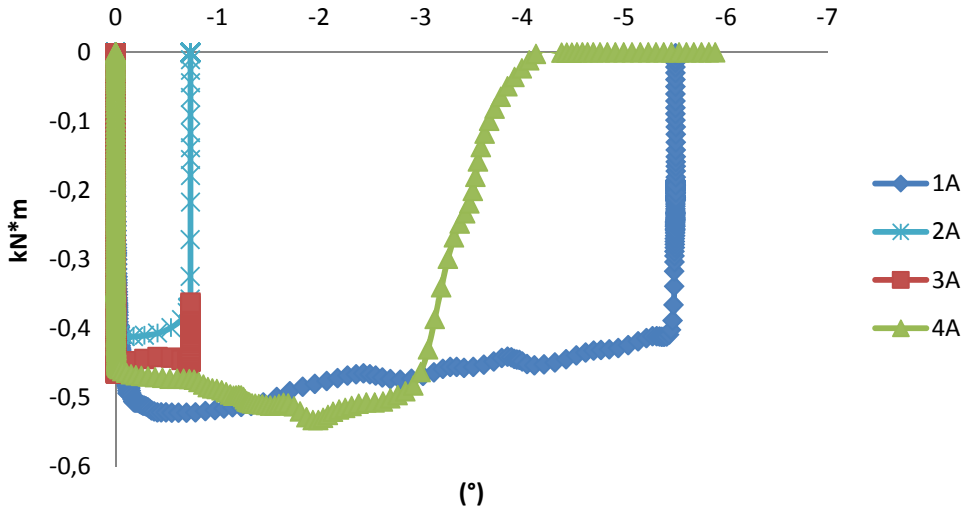


Figure 141. Moment – Wand rotation ("A" Rivet).

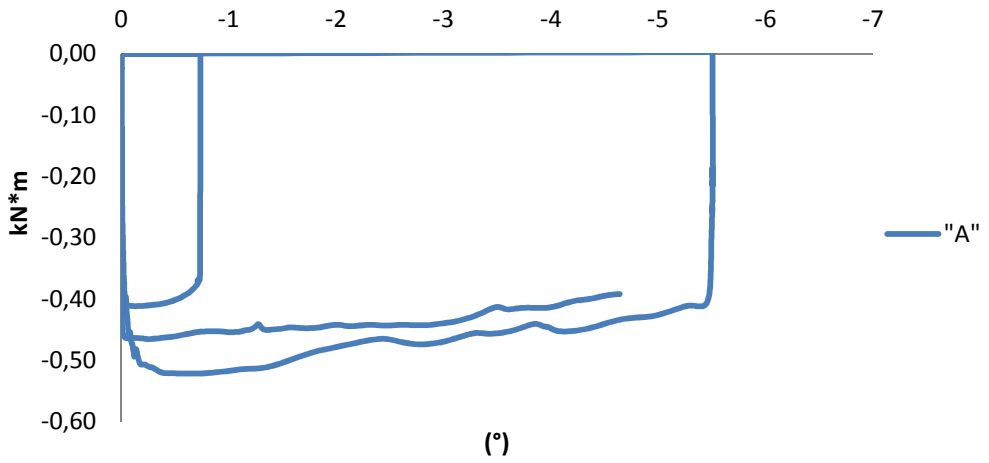


Figure 142. Hysteresis.

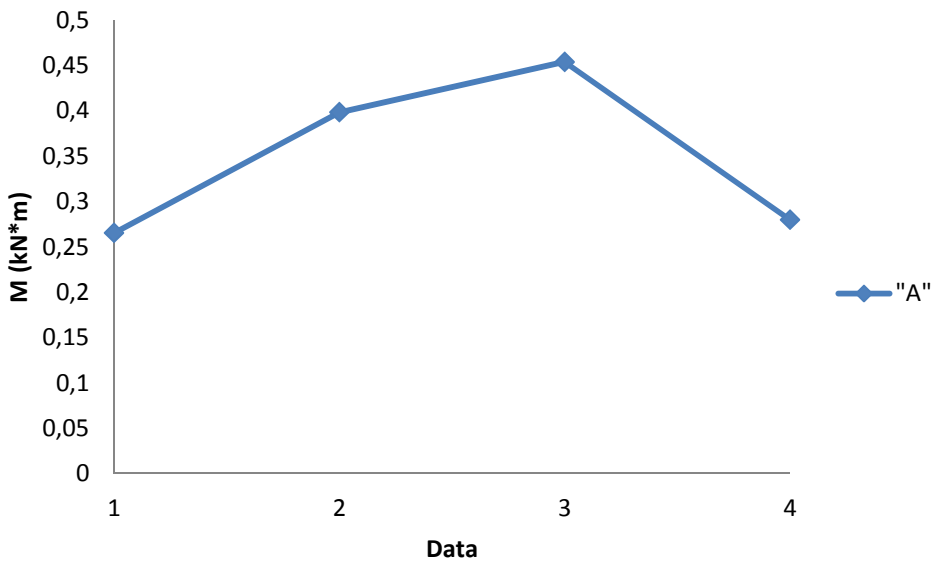


Figure 143. Activation torque.

The incremental factor, for "A" series, is $I_{f,max}=1,71$ with average value 0,39 kN and increment of 0,21 kN.

7.2.3.2 "M" series

For the medium rivet (Figure 144), results are summarized from Figure 145 to Figure 151 and in Table 21.

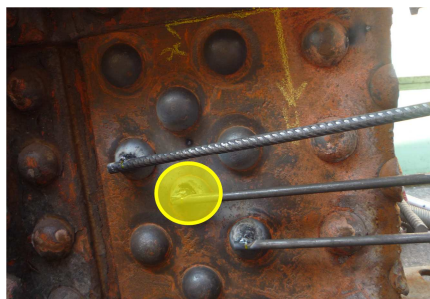


Figure 144. Medium rivet.

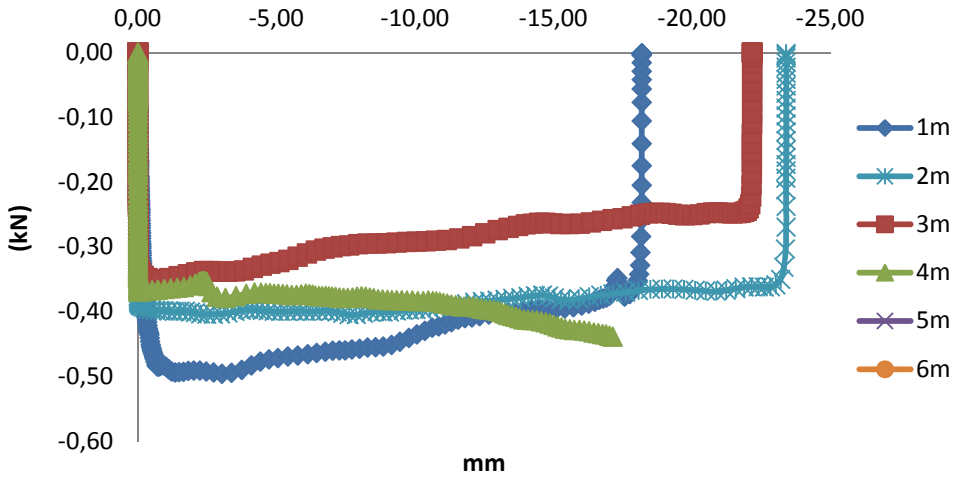


Figure 145. Force – Wand displacement (“M” Rivet).

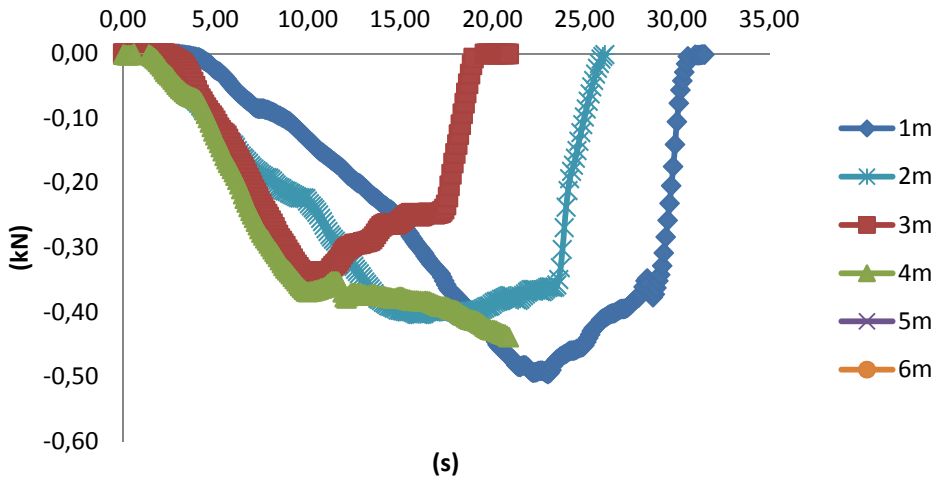


Figure 146. Force – Time (“M” Rivet).

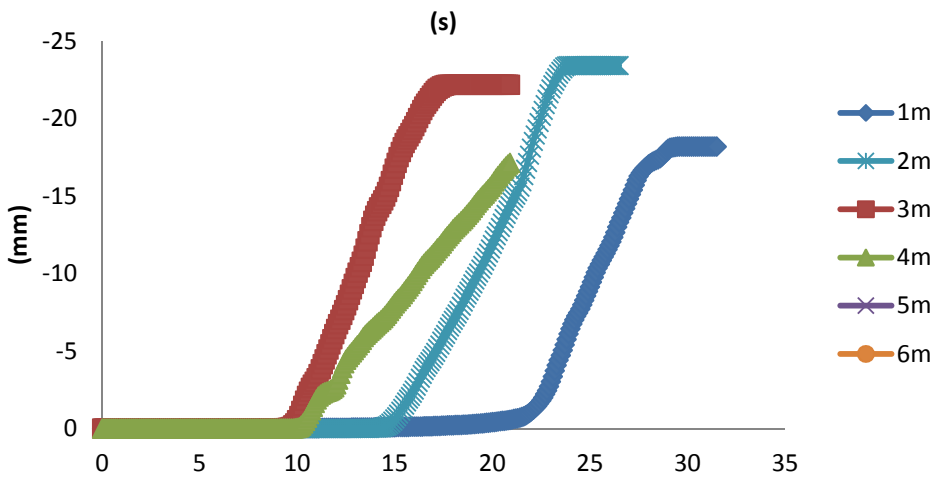


Figure 147. Wand displacement – Time (“M” Rivet).

	Rotation method			
	1M	2M	3M	4M
Act. Force (kN)	0,1536	0,3864	0,3306	0,3690

Table 21

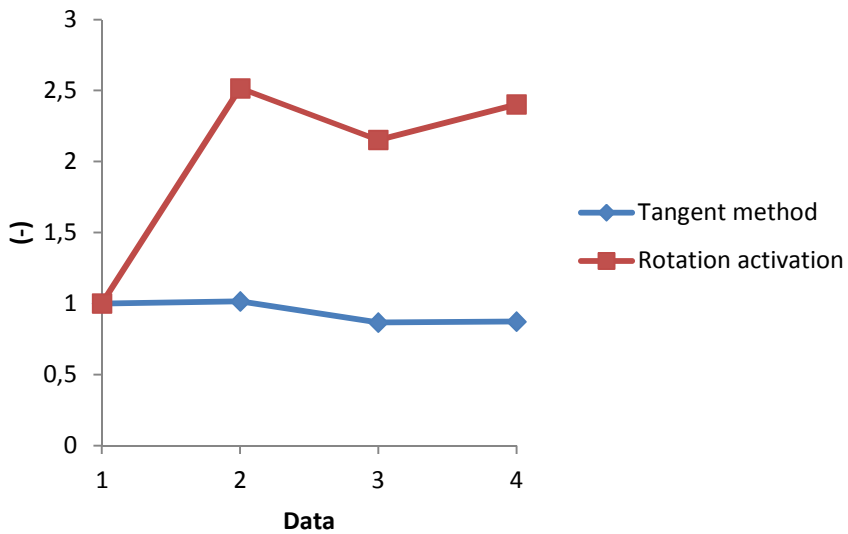


Figure 148. Increment factor.

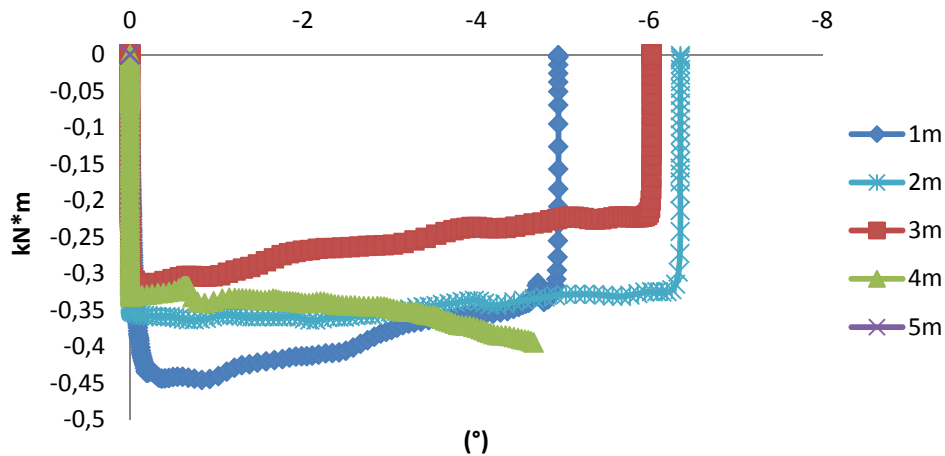


Figure 149. Moment – Wand rotation ("M" Rivet).

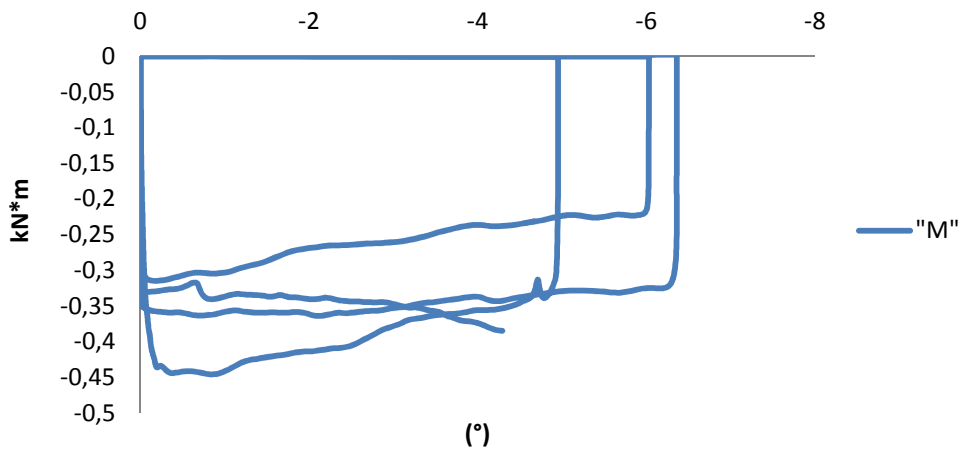


Figure 150. Hysteresis.

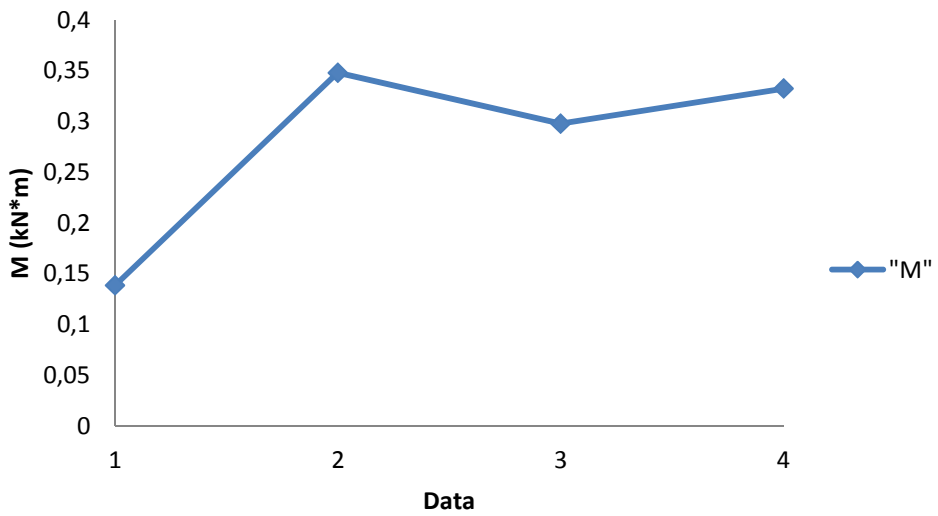


Figure 151. Activation torque.

The incremental factor, for "M" series, is $I_{f,max}=2,51$ with average value 0,31 kN and increment of 0,23 kN.

7.2.3.3 "B" series

For the bottom rivet (Figure 152), results are summarized from Figure 153 to Figure 159 and in Table 22.

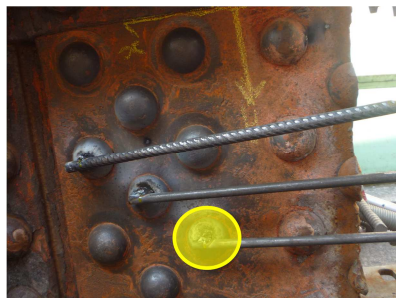


Figure 152. Bottom rivet.

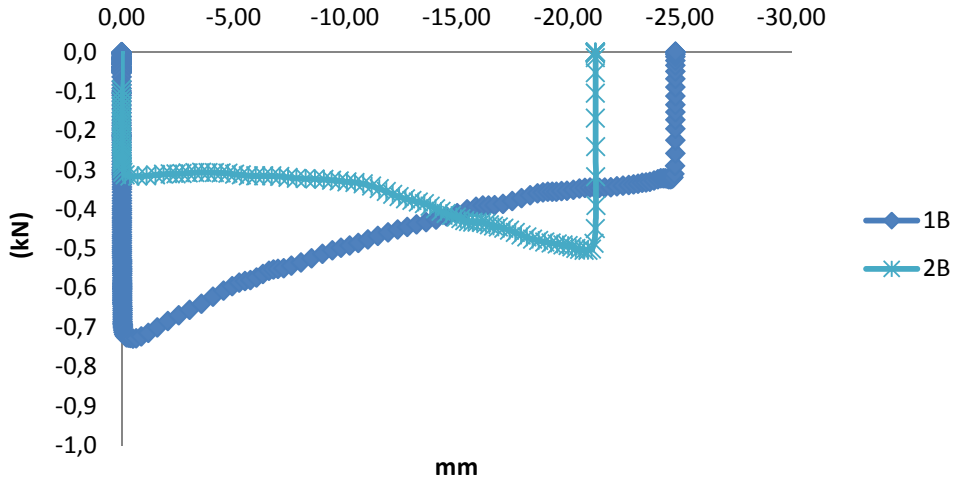


Figure 153. Force – Wand displacement ("B" Rivet).

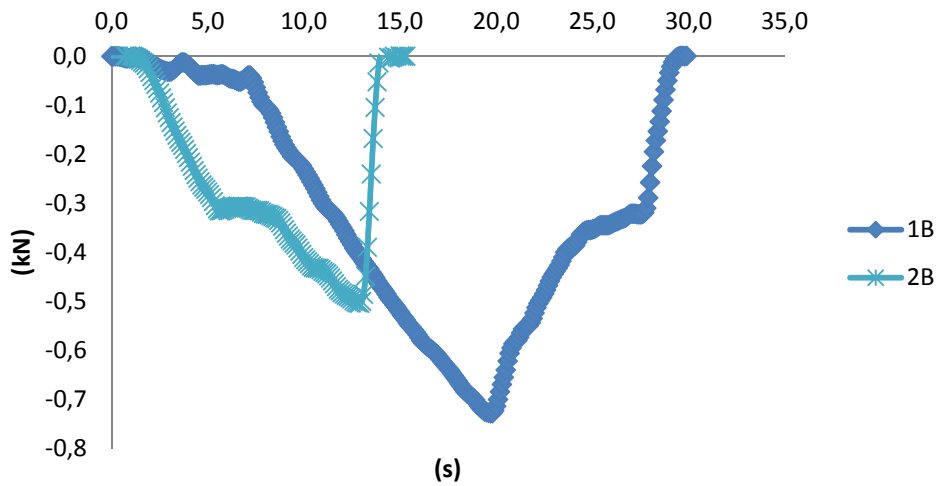


Figure 154. Force – Time ("B" Rivet).

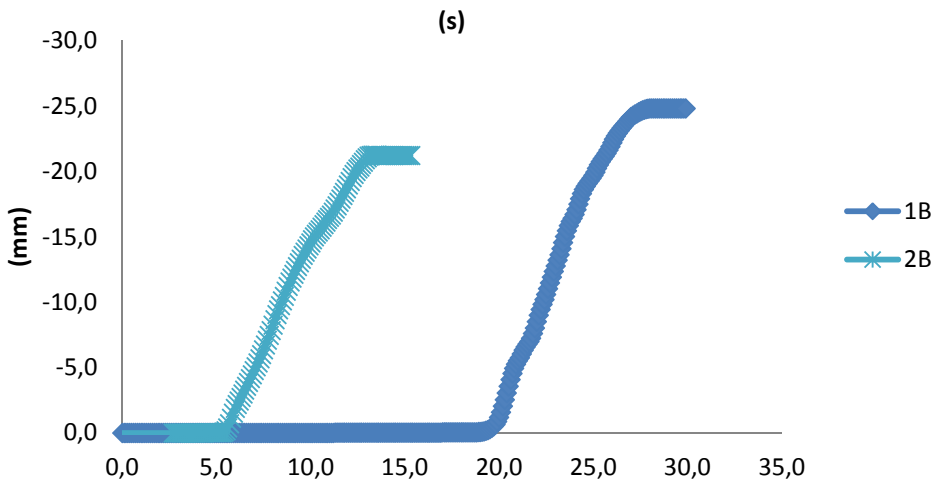


Figure 155. Wand displacement – Time (“B” Rivet).

	Rotation method	
	1B	1B
Act. Force (kN)	0,6738	0,3054

Table 22

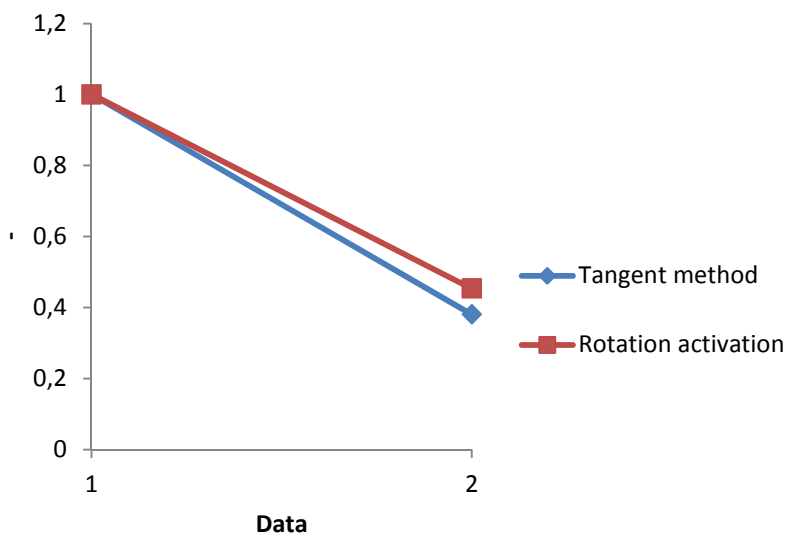


Figure 156. Increment factor.

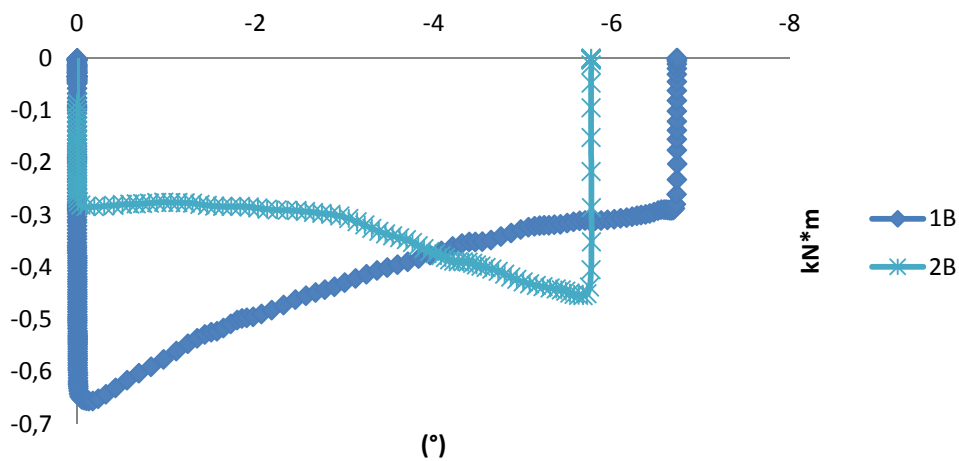


Figure 157. Moment – Wand rotation ("B Rivet).

After the campaign test, rivets, show the effects of the imposed rotation. The rivets have been marked in order to control the rotation (Figure 160 and Figure 161). The protective coat has been damaged in the contact zones due to the slip (Figure 162).



Figure 160. Post-test rivet.



Figure 161. Head rotation.



Figure 162. Protective coat slip.

7.2.4 TCT: Clamping force measured

The rivet shank is twisted by a moment M_t (see §7.2.5). The left-end is assumed fixed; the right-end will rotate with a small angle. The torsion theory assumes (see Figure 163, Equations from (61) to (63)):

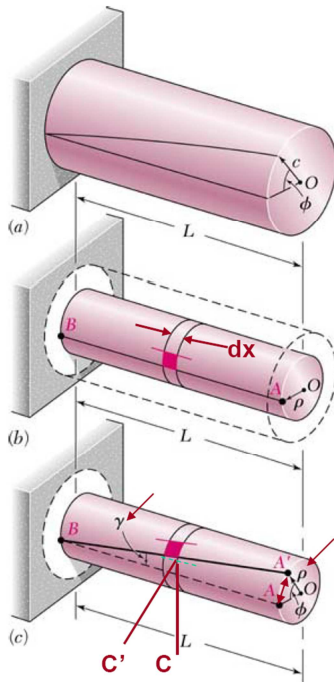


Figure 163. Torsion.

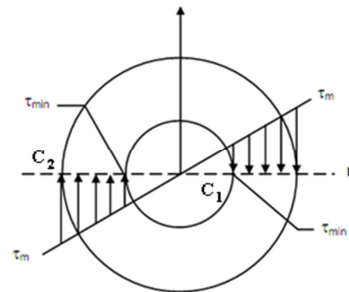


Figure 164. Stress distribution.

$$\gamma = \frac{\overline{CC'}}{dx} \tag{61}$$

$$\overline{CC'} = \rho d\phi \quad (62)$$

$$\gamma = \frac{\rho\phi}{L} \quad (63)$$

The maximum shear strain on the surface of the cylinder occurs when $\rho = c$ (Equation (64)):

$$\gamma_{max} = \frac{c\phi}{L} \quad (64)$$

For hollow circular sections (Figure 164, Equations (65) and (66)):

$$\gamma_{max} = \frac{c_2\phi}{L} \quad (65)$$

$$\gamma_{min} = \frac{c_1\phi}{L} \quad (66)$$

where C_1 is the internal radius and C_2 the external radius. The rivet head transmits the torsion to the shank however, the friction acts on the head ring spreading the torsional tension in order to ensure the equilibrium (Figure 164, Equation (67)).

$$\tau_{max} = G * \lambda_{max} \quad (67)$$

The equation of moment equilibrium gives (68):

$$M_t = \frac{\tau_{max}}{c} \int_A \rho^2 dA \rightarrow \tau_{max} = \frac{T * r}{I_p} \quad (68)$$

where I_p is the polar moment of inertia.

For “a1” the average force applied value is 1,38 kN that generates a $M_t = 689026 \text{ N}\cdot\text{mm}$ (for wrench length 0,5 m). This external torsional moment is equilibrated by the friction forces generated by the heads (Figure 165 and Figure 166).



Figure 165. M_t external

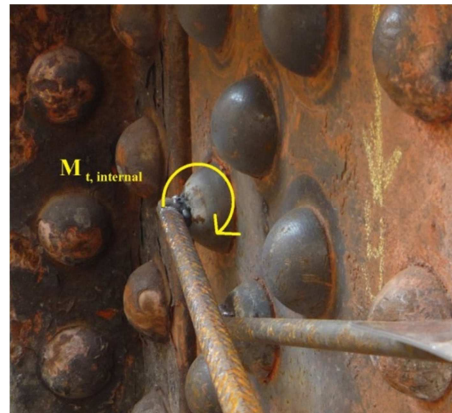


Figure 166. M_t internal

The τ distribution suggest a distance between the internal forces equal to 32,5 mm. The resistance friction moment split into the two rivet heads. The clamping force is given by the equation below (Equation (69)):

$$C_{a1} = \frac{M_{t1}}{b} / k_s * 2 = \frac{344513 \text{ N}\cdot\text{mm}}{32,5 \text{ mm}} / 0,33 * 2 = 64,24 \text{ KN} \quad (69)$$

where M_t is torsional moment on each head, k_s is the friction coefficient (see §7.2.5) and the coefficient “2” is needed to consider both the couple of forces.

7.2.4.1 Fem simulation

A non-linear fem simulation [29] has been carried out with the intention of validating the analytical estimates. Figure 167 shows the rivet head ring (green colour) and the plate (orange colour). Plate Quad 8 has been used in order to recreate the rivet head and the plates. The material characteristics has been chosen according to §6.2. The interface has been modelled using "Point contact" elements with the following characteristics (Table 23):

Type	Stiffness in compression	Stiffness in tension	Friction
Normal	1E6 N/mm	0 N/mm	0,33

Table 23

Rigid link elements have been used to transfer the torsional moment to each node of rivet head (Figure 168). The torsional moment has been introduced with the intention of finding the clamping value that leads to equilibrium.

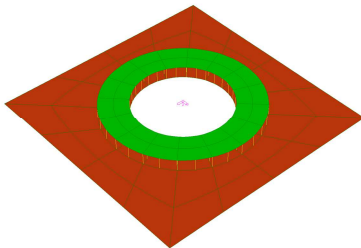


Figure 167. Rivet heads and plate.

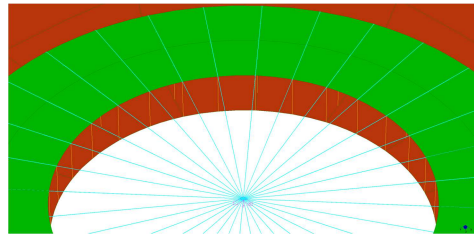


Figure 168. Points contact and rigid links.

At first, the clamping force has been introduced. Subsequently the torsion moment has been applied intending to find the unbalanced force (Figure 169). The iterations give the clamping value for each data series (Figure 170), the results are summarized in the following tables (Table 24 and Table 25).

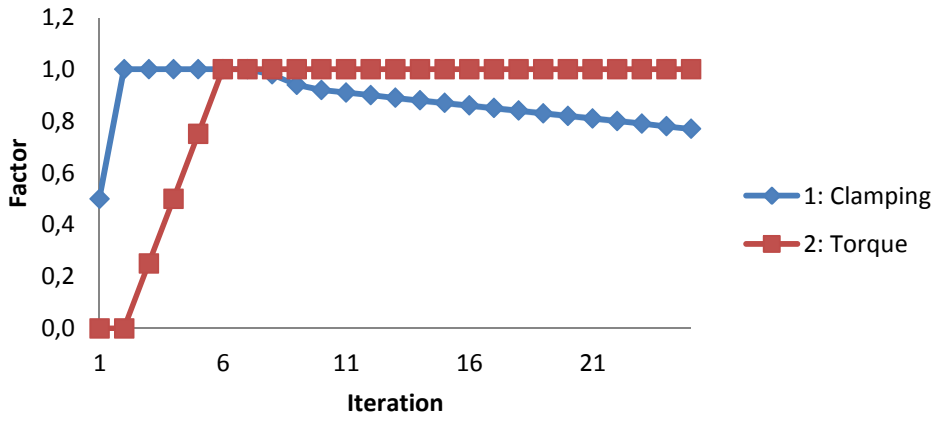


Figure 169. Fem non-linear analysis.

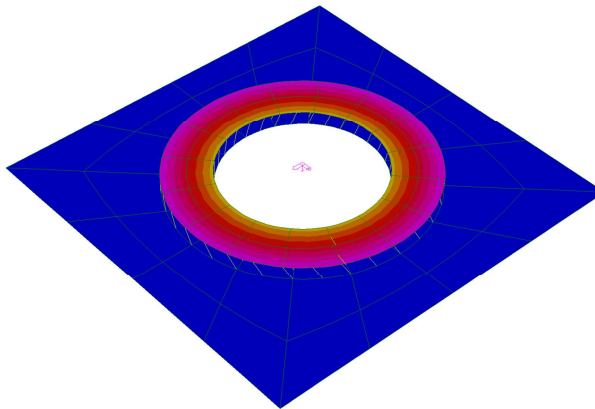


Figure 170. Non-linear Fem solutions.

Clamping (kN) - Little displacement									
Rivet	Repetition						Average	Fem NL	Correlation (%)
	1	2	3	4	5	6			
Upper	47,74	61,62	64,24	73,20	74,43	-	64,24	56,00	87
Medium	33,39	48,35	55,77	56,82	64,49	-	51,76	44,00	85
Bottom	77,83	83,44	87,19	103,11	85,37	79,32	86,04	74,70	87
Average							67,35	58,23	86

Table 24

Clamping (kN) - Big displacement					
	Repetition				Average
Rivet	1	2	3	4	
Upper	24,72	37,11	42,29	26,08	32,55
Medium	12,89	32,43	27,74	30,97	26,01
Bottom	56,54	25,63	-	-	40,41
				Average	32,99

Table 25

Figure 171, Figure 172 and Figure 173 show the clamping force trend.

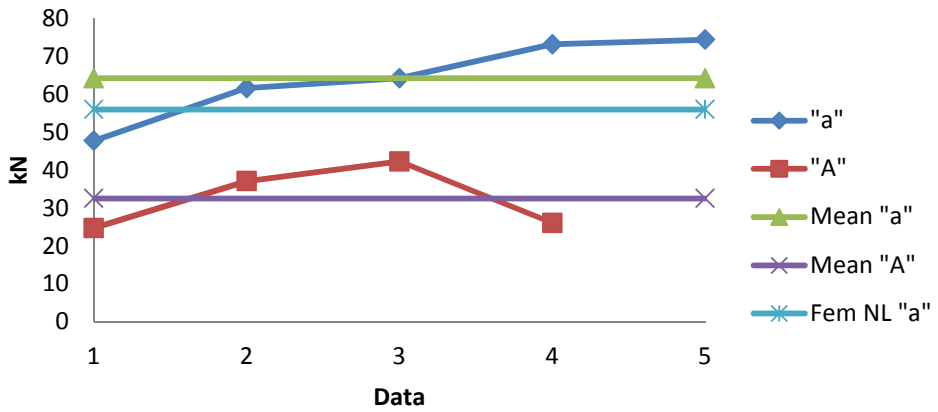


Figure 171. Clamping: upper rivet.

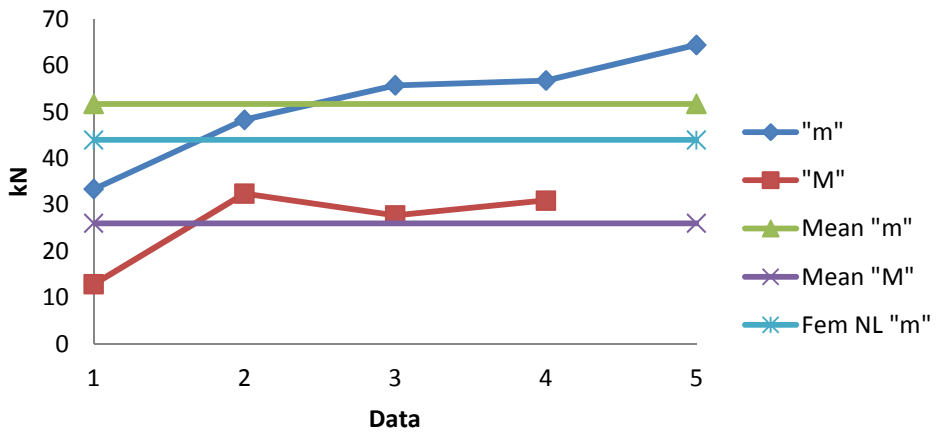


Figure 172. Clamping: medium rivet.

TORSIONAL CLAMPING TESTS (TCT)

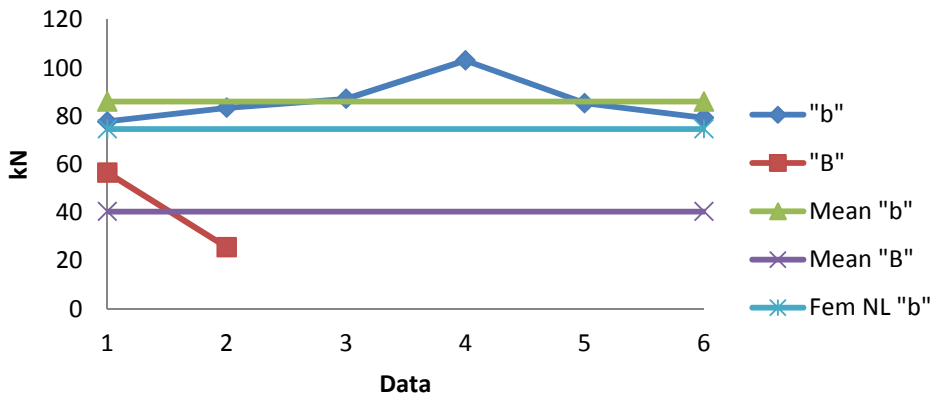


Figure 173. Clamping: bottom rivet.

7.2.5 Notes on frictional coefficient

As mentioned in §5.5, one of the significant factors influencing the slip resistance of a connection, is the slip coefficient k_s . Much research has been done in the United States, Europe, Japan, and elsewhere to determine the magnitude of coefficient for different steels, different surface treatments and surface conditions. An analysis of 327 tests [7] show that the clean mill scale condition for Fe37 and Fe52 is (Table 26, Figure 174):

k_s	0.33
σ (standard deviation)	0.06

Table 26. Friction coefficient

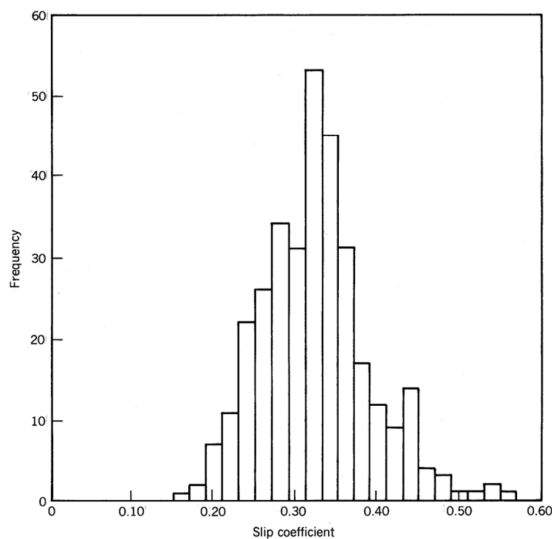


Figure 174. Distribution of slip condition: clean mill scale surfaces.

This value has been adopted in this thesis. A simple test has been carried out and coefficient 0,33 has been confirmed.

7.3 Final considerations

The clamping force are essential aspects of the construction process that can affect the strength and the lifetime of old riveted structures. Referring to the age of bridge construction, the clamping force is about 100 kN. Nevertheless, the clamping force decreases due to thermal load, vibrations, electric flows and other effects. The evaluation of clamping force is usually carried out by destructive tests or simply referring to the initial steel yield stress. With the purpose of estimating the actual clamping force with an improved precision, a specific and innovative test has been conceived. A non-destructive test is recommended with the intention of extending this investigation campaign to other in-service bridges. The idea is to evaluate the clamping force by means of torsion test (TCT) on rivets. The applied torsional moment is proportional to the force generated by the frictional ring area of the rivet head subjected to clamping force. Preliminary evaluations highlights that the only rivet area interested by the friction is the rivet head ring. Each repetition increases the torsional force that causes the slip start. This phenomenon is not related to the non-uniform torsion due to the circular shank shape. The force application creates

torsional stress on the rivet shank that may produce differential rotations in the rivet heads. The rotational effect might emphasize the rivet imperfections, in particular the non-parallelism of the rivet heads. The configuration change may produce an increment of friction activation moment due to the forcing of head position. The clamping force has been calculated analytically and by software. A non-linear fem simulation has been carried out with the intention of validating the analytical estimates. Approximately, the same behaviour for each repetition is observed for "a", "m" and "b" series. Moreover, the fem simulation gives a good validation of analytical results. The rivet manufacturing process has compromised the rivet regularity thus a variability in clamping force is observed. Experimental results show an average value of about 60 kN i.e. about 2/3 of original clamping force. In the lack of a more extended test campaign and analysing "small displacement" results, it is conceivable that a considerable amount of clamping force is lost. Beyond the "small rotation" field, rivets show a more stable clamping value: the rivet deformation smooth the contact plates. In conclusion, San Stino's elements have currently a significant amount of clamping force.

8 SAN STINO'S RAIL BEARER TESTS

In the following chapters a complete overview of rail bearers is introduced. The two identical beams (named "A" and "B") has been extracted and accurately examined in order to plan the subsequent tests. These collected information will be used for Fem calibration and for fatigue evaluations (see § 8.5).

8.1 Rail bearer "A" characteristics

The girder is 3360 mm long, it is divided into three parts respectively 1120 mm and 1110 mm length. The web is 500 mm high, 300 minus of cross girder web (Figure 175). Each beam has two side named "A" and "B". Side "A" shows the anti-winding supports whereas side "B" looks clear.

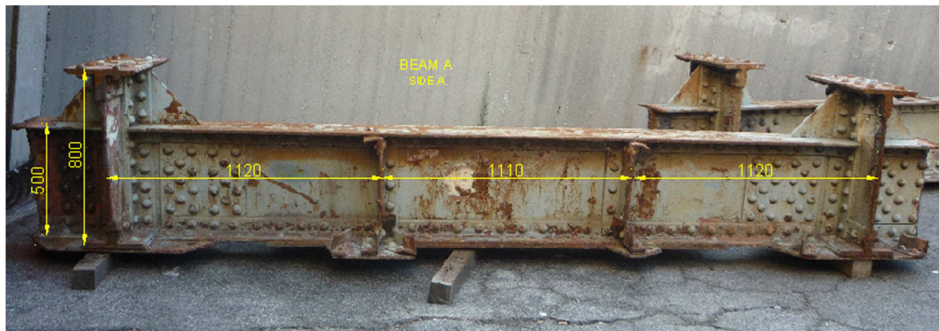


Figure 175. Rail bearer "A".

The beam is a plate composite section. Figure 176 shown the intersection between rail bearer and cross girder. The element, as well as the entire structure, is bring together by rivets. The main elements composing the beam are the web, the "L" shape flanges and riveted cover plates. Near the node a triangular gusset plate connects the rail bearer to the transversal. The image below (Figure 177) show the beam section intersected with the girder. Oxyacetylene flame cut is evident. In the former tests, the beam is collocated upside down in relation to its improved stability.



Figure 176. Node detail.



Figure 177. Section.

A series of non-destructive test has been performed with the intent of revealing the original structure. Grind molar has been used to remove the superficial material and to show up the rivet shape (Figure 178). The entire bridge was covered by protective paint skin aged and partially removed (Figure 179). Altogheteher, the structure was slightly corroded and, except the WWII damages, well preserved.



Figure 178. Surface treatment.



Figure 179. Corrosion.

During the Second World War, the bridge, has been damaged by artillery and some treatment has been carried out to avoid further damage (Figure 180). A shielding material fills the irregular holes protecting the bridge from corrosion and avoiding stress concentrations.



Figure 180. WWII damages + shielding material.

8.1.1 Rivets

In the following chapter, a precise estimation of rivets dimensions and positions is carried out. Three external rivets (named “A1”, “A2” and “A3”) and relative holes have been inspected due to their exposed position (Figure 181).

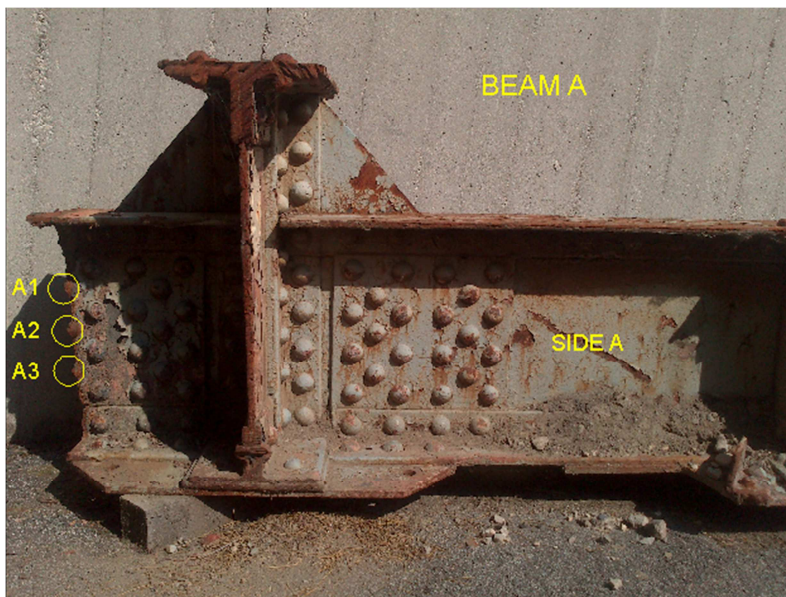


Figure 181. Exposed rivets.

A schematic rivet is represented in Figure 182 with the purpose of define the principal dimensions. For instance, "A1" rivet has 66 mm shank length: easy to measure compared to other still working rivets (Figure 183). These three rivets have revealed a good geometry regularity and a high level of quality manufacturing. The surface inside the holes is clean and without corrosion (Figure 184). Other rivets dimensions have been gained (Figure 185) and some details are summarized in Table 27.

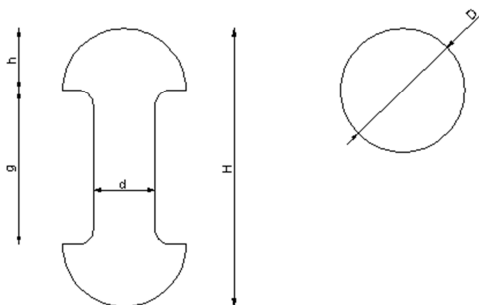


Figure 182. Rivet dimension.



Figure 183. Rivet section (Girder "B").



Figure 184. Rivets hole (Girder "B").



Figure 185. Height measurement.

	Rivet		
	A1	A4	A5
h (mm)	16,63	-	-
D (mm)	40,12	-	-
d (mm)	24,48	-	-
H (mm)	-	60,72	60,38
g (mm)	-	25,3	25,32

Table 27. Dimensions.

Table 28 and Table 29 show diameter (Figure 186) and shank rivets gauges. For each side different gauges of vertical and horizontal diameter are taken in order to evaluate the regularity of rivets head. Moreover, a schematic localization is carried out referring to rows and columns (Figure 187).



Figure 186. Diameter and shank gauge.

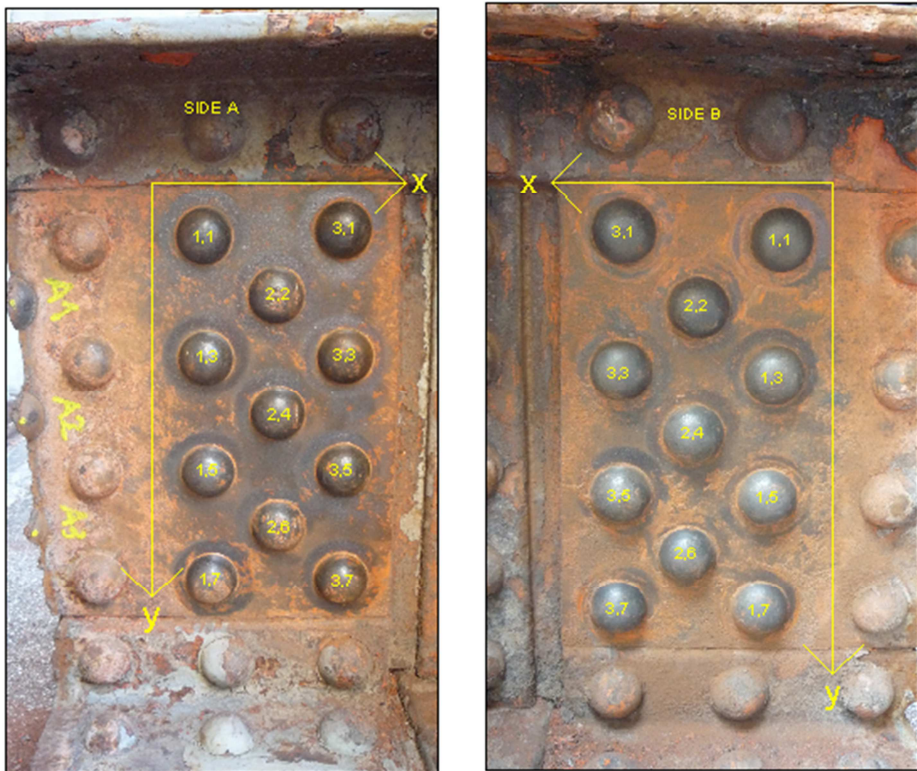


Figure 187. Rivets position.

Rivet coordinate	Diameter		
	$\phi_{vertical}$ [mm]	$\phi_{horizontal}$ [mm]	ϕ_{mean} [mm]
1,1	41,52	41,17	41,35
3,1	41,71	41,38	41,55
2,2	41,31	41,46	41,39
1,3	41,40	41,46	41,43
3,3	41,43	41,6	41,52
2,4	41,44	41,85	41,65
1,5	41,53	41,85	41,69
3,5	41,57	42,17	41,87
2,6	41,51	42,21	41,86
1,7	42,48	42,24	42,36
3,7	41,36	42,23	41,80
		Average	41,68

Table 28. Rivets diameter (Side A).

Rivet coordinate	$\phi_{vertical}$ [mm]	$\phi_{horizontal}$ [mm]	ϕ_{mean} [mm]
1,1	40,46	42,04	41,25
3,1	41,63	41,94	41,79
2,2	41,70	42,05	41,88
1,3	42,36	42,24	42,30
3,3	42,42	42,80	42,61
2,4	43,01	42,02	42,52
1,5	42,83	42,09	42,46
3,5	43,70	44,37	44,04
2,6	41,38	41,86	41,62
1,7	45,18	42,45	43,82
3,7	42,05	43,17	42,61
		Average	42,44

Table 29. Rivets diameter (Side B).

Rivets have good head regularity, independently of any horizontal or vertical direction, and the average head diameter is 42 mm. An important aspect of riveted joint is the manufacturing process as mentioned in §5.2. Figure 188 show the rivet section highlighting a good head and shank regularity moreover the plates have a sufficient contact between them. The diameter variation is between 2 and 6%

(correlated to the average diameter) proving the good manufacturing level (see Figure 189 to Figure 194).

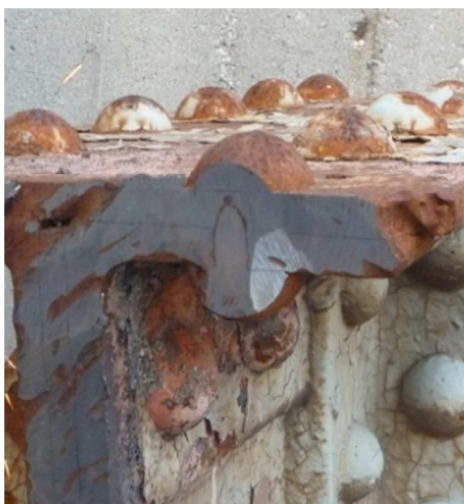


Figure 188. Rivet section.

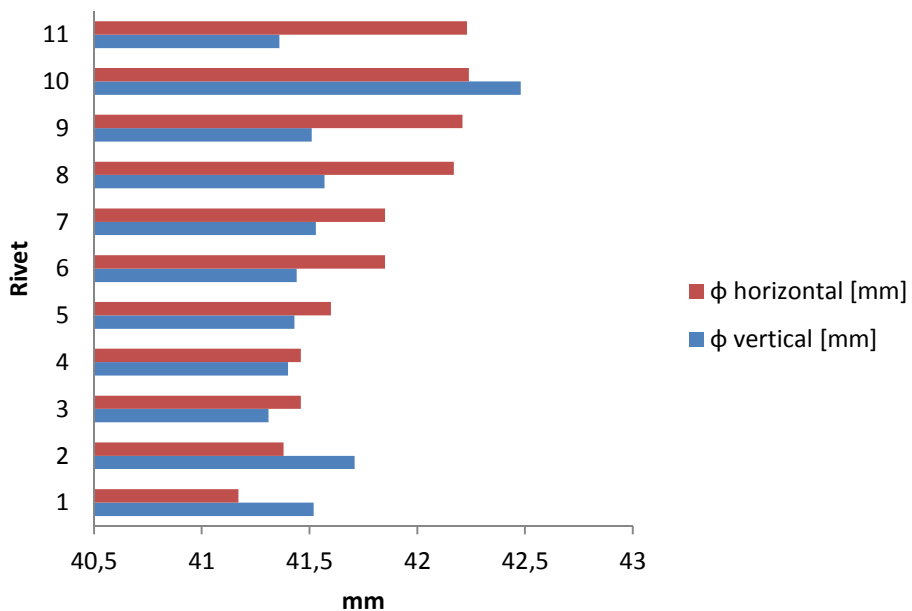


Figure 189. Rivets head diameter -side A-.

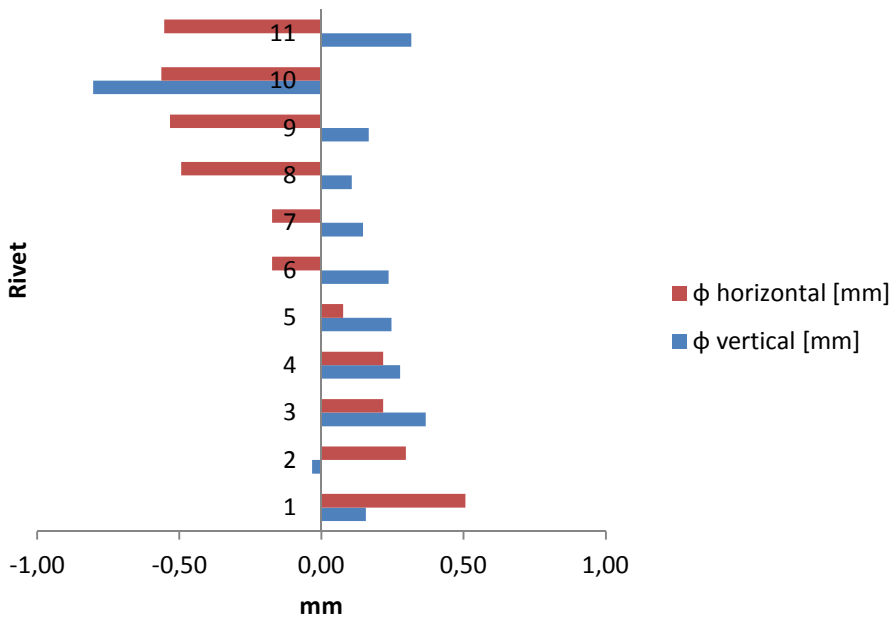


Figure 190. Variations -side A-.

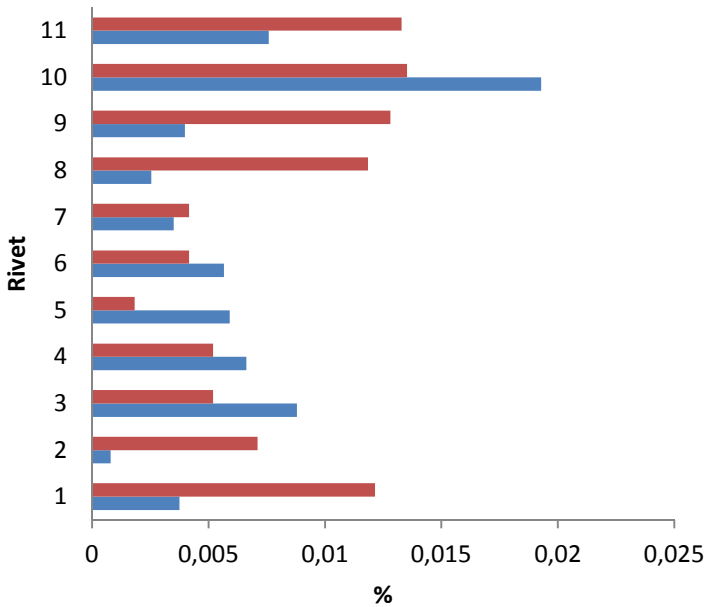


Figure 191. Variations % -side A-.

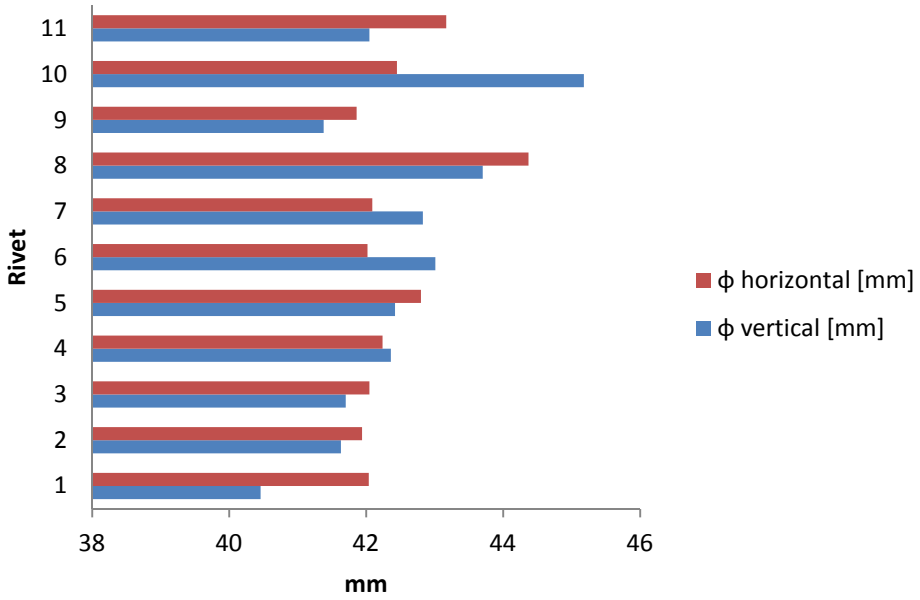


Figure 192. Rivets head diameter -side B-.

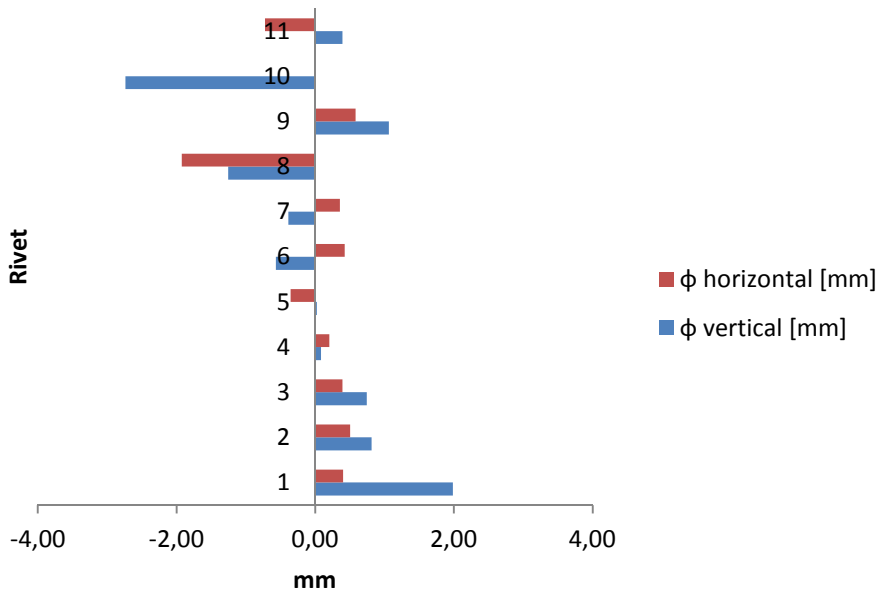


Figure 193. Variations -side B-.

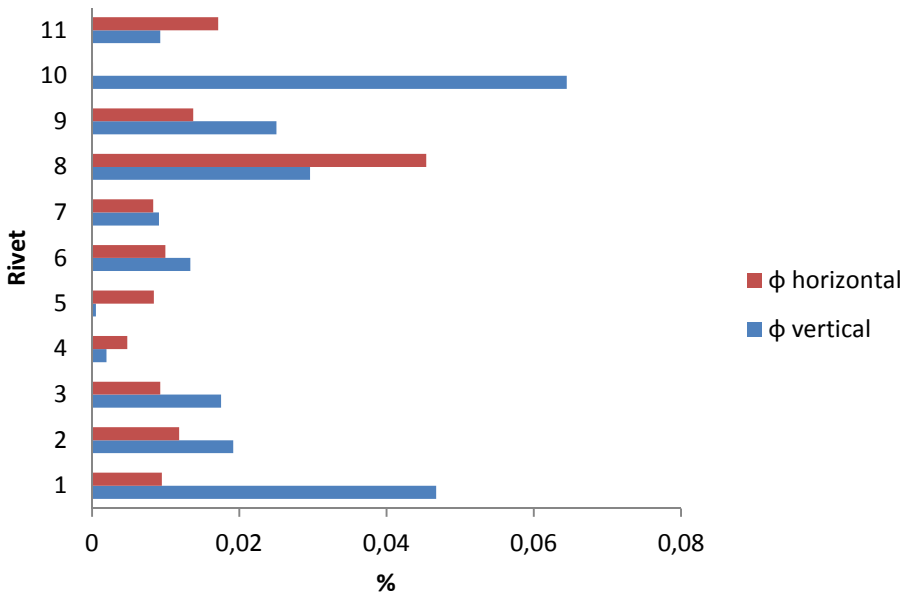


Figure 194. Variations % -side B-.

8.1.2 Holes and rivets standard dimensions

Some holes have been inspected and the average diameter is about 26 mm (Figure 195). The edge of the holes is well defined and without damages. Referring to Figure 182, the standard San Stino's rivet has the dimension summarized in Table 30.



Figure 195. Typical hole.

D	40	mm
h	20	mm
d	25	mm
H	60	mm
g	25	mm
Hole	26	mm

Table 30. Standard rivet

8.1.3 Plates dimensions and rivets distribution

The riveted joint and the relative dimension are summarized in Figure 196. The element respect the traditional historical size, the inter-axial spacing is 5ϕ or more and the edge distance is between 0.6 and 0.9ϕ .

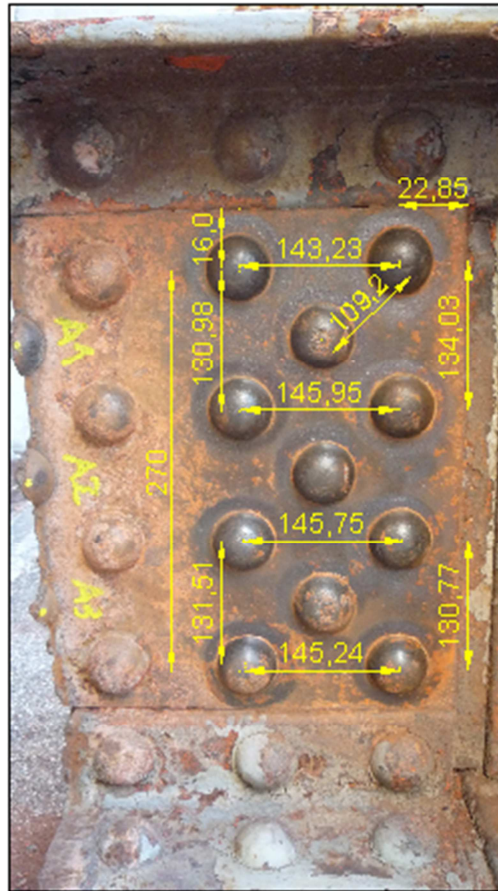


Figure 196. Riveted joint.

8.2 Loads, remaining life and fatigue verifications

In this paragraph, a brief overview on the in-service beam condition is reported. In first analysis, and referring to the mid-span bridge elements, the rail bearers are fixed between the two cross girders. The static schemes in-service condition and during the test campaign are substantially different due to the cross girders constraints. It is essential to investigate both the static schemes with the intention of estimating the remaining fatigue life. For about a century the San Stino's rail bearers were fixed between crossbeam moreover the fatigue test will operate in simple supported static scheme. Rail traffic assessment of an existing railway bridge requires special emphasis on the modelling of the railway load.

Nevertheless, a detailed load history is not available due to the age of bridge. The only information regarding the loads acted on San Stino's bridge refers to the line informations. In the follow a simplified load scheme is represented. The train moving effect is sophisticated due to the continuous changing in static scheme. In the sequence below (Table 31), the load pass over the beam, is shown.

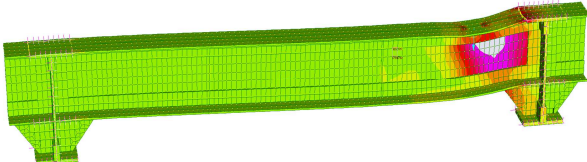
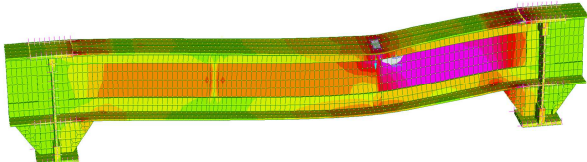
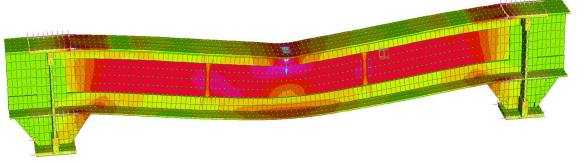
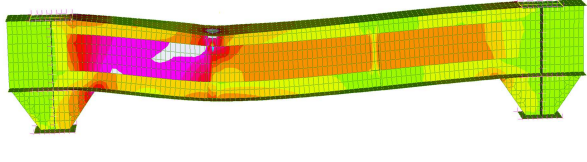
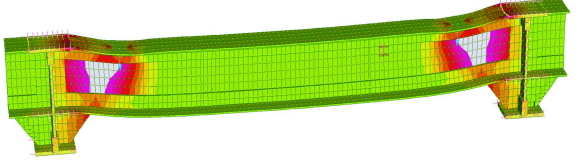
Sequence	Moving load
1	
2	
3	
4	
5	

Table 31. Wheel effect.

Considering the various train typologies and assuming the static scheme shown in Figure 197, a typical fatigue verification is carried out for rail bearers. This force distribution leads to the highest stress level in the beam and will take as reference load scheme. It is specified that the wheels inter-axle spacing varies from 2400 to 2600 mm.

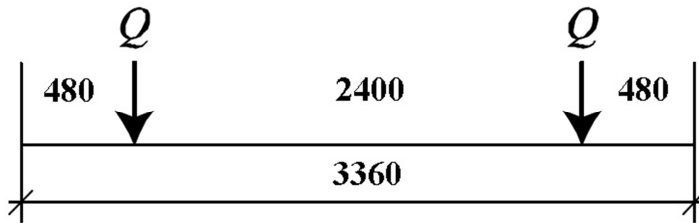


Figure 197. Fatigue static scheme (rail bearer).

In Table 32 the adopted wagons are reported. It has been subdivided regarding the service ages due to the different weights. The table refers directly to the wheel force instead of axial load with the intention of calculate directly the rail bearer stress. A brief loads counting is shown in the last column.

Age	Wagon type	Name	Wheel load(kN)	Supported cycles (estimate)
1920-1960	Motor unit	Mu	75	2,15E+06
	Car (full)	Cf	105	2,50E+06
	Car (empty)	Ce	33	2,00E+05
	Coach	C	48	4,35E+06
1960-2010	Motor unit	Mu	105	5,28E+06
	Car (full)	Cf	105	4,89E+06
	Car (empty)	Ce	33	4,25E+05
	Coach	C	48	9,23E+06

Table 32

Referring to §4.2 and §4.3, a linear elastic Fem model has been created [29]. The steel characteristics and the beam inertia are representative for San Stino's elements. The Fem simulation refers to nominal stress according to [5]. More of 2300 plates have been modelled and the graphical output for 100 kN wheel load is shown in Figure 198.

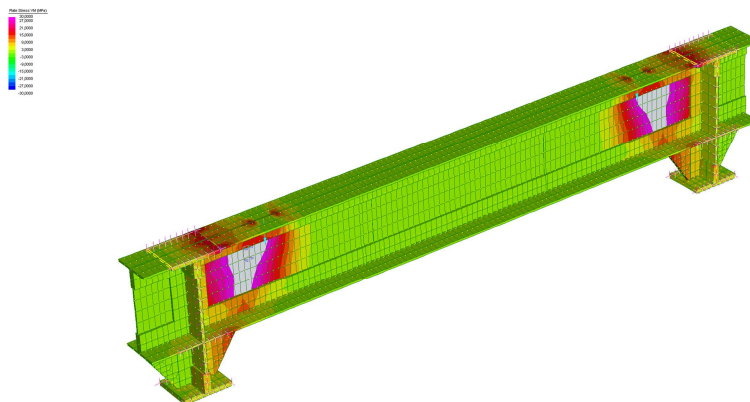


Figure 198. Nominal stress ($F = 2 \times 100 \text{ kN}$).

The constraints simulate the cross girder effects: in first approximation the rail bearer is fixed to the cross girder. The maximum stress range is focused in the web, under the forces application area, and is about 37 MPa (Von Mises criteria). 20 MPa has been observed in the flanges. For the specific train load cases, the results are summarized below (Table 33):

Wagon types	Wheel load(kN)	Supported cycles	Stress (MPa)
Motor unit	75	2,15E+06	28
Car (full)	105	2,50E+06	39
Car (empty)	33	2,00E+05	12
Coach	48	4,35E+06	18
Motor unit	105	5,28E+06	39
Car (full)	105	4,89E+06	39
Car (empty)	33	4,25E+05	12
Coach	48	9,23E+06	18

Table 33

The fatigue class is FAT 71 (Table 34, see [4]):

71	
----	--

Table 34

Referring to §4.4, Equation (27) gives (Equation (70)):

$$\sum_{i=1}^n \frac{n_i}{N_i} \cong 0,60 \tag{70}$$

where the resistant cycles are correlated to Class 71. The preliminary analysis show that the fatigue life of rail bearer is ending rapidly due to the greater traffic and greater loads. In the lack of precise information regard traffic loads, the Equation (70) gives the minimum threshold value of the damages accumulated. Moreover, a fatigue verification is carried out with the intention of evaluating the rail bearer condition. Referring to §4.2, the fatigue verification for Motor Unit (after 1960) gives (Equation (71)) :

$$\frac{\Delta\sigma_{Mu}}{\Delta\sigma_D} = \frac{39MPa}{52MPa} = 0,75 < 1 \tag{71}$$

For the others wagon types, the results are summarized in Table 35.

Age	Wagon type	Verification (%)	
1920-1960	Motor unit	54	<1
	Car (full)	75	<1
	Car (empty)	23	<1
	Coach	35	<1
1960-2010	Motor unit	75	<1
	Car (full)	75	<1
	Car (empty)	23	<1
	Coach	35	<1

Table 35

It is notable that, preliminarily, the fatigue verification is satisfied. The greater contribution is given by the motor unit instead coaches and empty cars do not affect the remaining fatigue life [36]. In order to investigating with more precision, laboratory tests and Fem simulations have been carried out. Nevertheless, the

stress distribution is completely different respect the laboratory condition and it is not replicable due to the cross girder cut. For more details, see §8.3.

8.3 Experimental campaign: fatigue identification test

A fatigue identification test has been carried out with the intention of predicting the fracture behaviour. The three points bend test (Figure 199) is a classical experiment used to measure the deformation of a beam. The beam, of length L , rests on two roller supports and it is subject to a concentrated load P in the middle. In this test special supports have been used to elevate the beam. The supports are steel box type. They contrast the vertical force permitting the lateral expansion due to the flexural deformation. The hydraulic actuator introduces the force up to 3000 kN. Moreover, the max actuator displacement is 200 mm. Many steel and lead plates have been positioned between the specimen and the actuator in order to fill the rivet head gap (Figure 200). Applying force uniformly is essential to avoid stress concentrations and for perform test correctly.

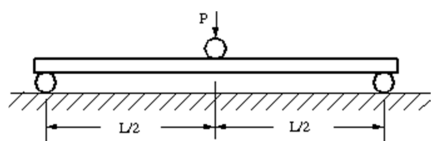


Figure 199. Static scheme.



Figure 200. Plates for rivets gap.

The rail bearers of San Stino's Bridge have been taken and statically tested in order to identify the structural behaviour. Some imperfections are present in the supports and the only way to gain reliable measurements is to exclude supports by the acquisition. This is possible thanks to an additional aluminium beam (Figure 201) necessary to fix the displacement transducers.



Figure 201. Aluminium bar.

The steel frame used during the tests (Figure 204 and Figure 205) contrasts rigidly the beam deformation. An 8 channels acquisition (Figure 202 and Table 36) has been used intending to gain the entire beam structural behaviour. The displacement transducer is a unit that converts the movement of a probe tip into an electrical signal. Conversion is carried out with the aid of strain gauges inside the unit, located in a full bridge circuit on the measuring probe tip. The frequency acquisition is 10 Hz. The displacement transducers have a precision of 1/100 and 1/1000 millimetre (Figure 203). The most accurate displacement transducer (DD1) have been placed on the splice plates. Moreover, the less accurate one, measures the flange vertical displacement.



Figure 202. 8 channels acquisition.

Ch0	Force transducer
Ch1	DD1 for plate deformation (horizontal)
Ch2	Inductive trans. for vertical displacement (lower flange)
Ch3	Inductive trans. for vertical displacement (upper flange)
Ch4	Inductive trans. for vertical displacement (lower flange)
Ch5	Inductive trans. for vertical displacement (upper flange)
Ch6	Inductive trans. for vertical displacement (lower flange)
Ch7	DD1 for plate deformation (diagonal)

Table 36. Acquisition configuration

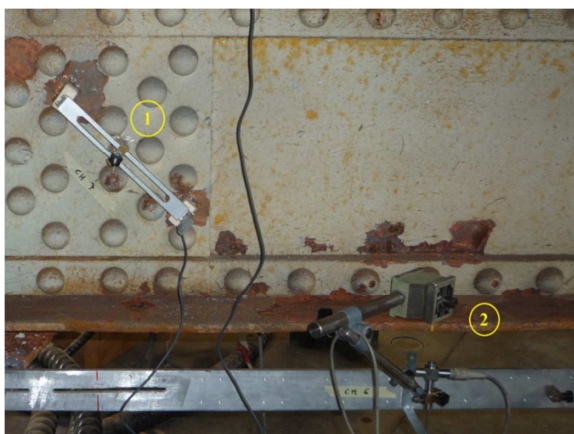


Figure 203. 1) DD1 transducer, 2) inductive transducer.



Figure 204. Side B.



Figure 205. Side A.

The test has been carried out performing five different load steps to check the structural integrity during the experiment (Table 37).

Step 1	100 kN
Step 2	200 kN
Step 3	300 kN
Step 4	400 kN
Step 5	500 kN

Table 37

The static scheme is very simple (Figure 206) nevertheless the beam deformation is very complex: many geometric imperfections are present and the element is composed by several different plates bound together by rivets. In the follow paragraph (See § 8.5) the experimental results are compared to the elastic (Table 38) and elasto-plastic behaviour.

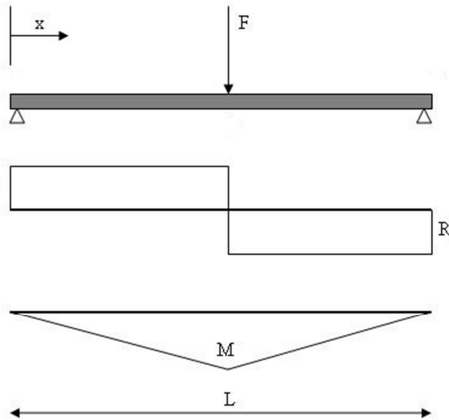


Figure 206. Static scheme.

Reaction		Moment	Maximum deflection
R1	R2	M	$\delta(x)$
$\frac{F * b}{L}$	$\frac{F * a}{L}$	$\frac{F * a * b}{L}$	$\frac{F * a * b}{E * J * L} \sqrt{\frac{a * (L + b)^3}{243}}$

Table 38

8.3.1 Symmetric test

In this paragraph the results for mid span force are summarized. The first graph (Figure 207) shows the transducers located in the lower flange. The transducer located in the centreline of the beam is the transducer number 4. Moreover, the other two transducers are collocated at the 1/4 of the beam length.

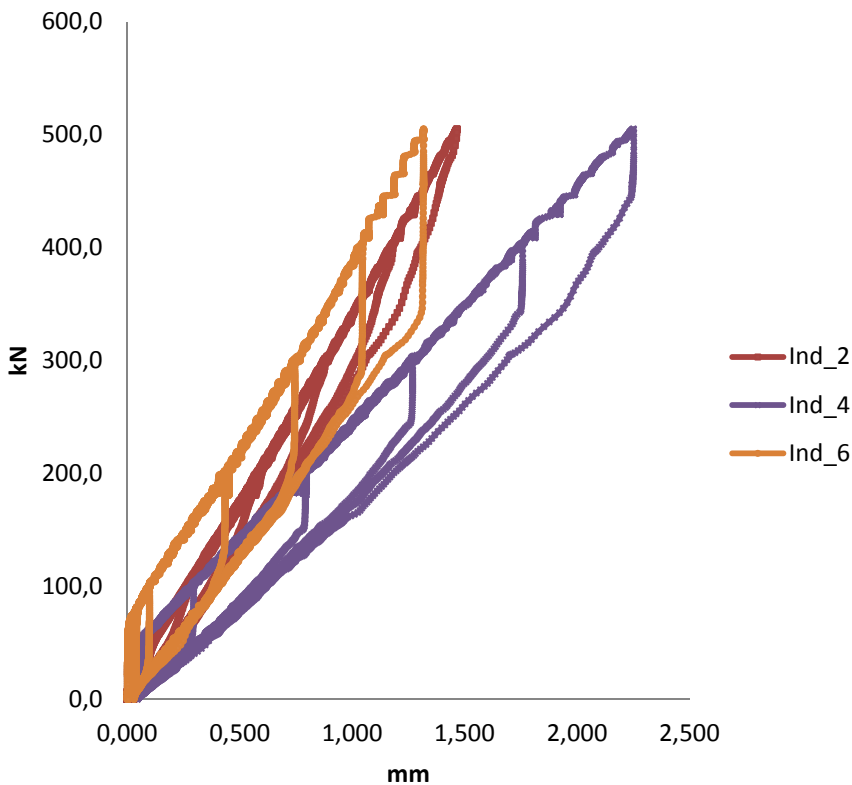


Figure 207. $F - \delta$ (500kN Midspan).

For all the channels, the force increases without any displacement due to friction and settling effects. After the preliminary phase, Channel 2 and Channel 6 show a similar behaviour with a difference in vertical displacement of 0,15 mm. The rise line is straight and this indicates an elastic behaviour. For more detail about the train load (in relation to this test execution) see §8.2. Each load increment traces the previous curve proving the elastic state. There are some similarities between Channel 4, Channel 2 and 6 even if a different displacement magnitude is recorded. At 500 kN the maximum displacement for Channel 4 is 2,24 mm, for Channel 2 is 1,314 mm and for Channel 6 is 1,455 mm. An equivalent graph (Figure 208) has been created for the Channel 3 and 5. The sensors are positioned at 1/3 of beam length. These transducers collect the upper flange displacements. Channel 3 and Channel 5 show a similar behaviour with a maximum displacement (at 500 kN) of 2 mm. Each load increment traces the previous curve indicating the elastic state. DD1 sensor collects the data from the plate deformation (Figure 209). Very small

deformations (10^{-4}) are recorded due to the low stress field. For more details about plates and rivets interaction see §7. Channel 1 (horizontal plate deformation) shows a linear behaviour nevertheless Channel 7 (diagonal plate deformation) shows a nonlinear behaviour. The max deformation reached by the DD1_7 is 1,5 ‰. Positive sensor values indicate an elongation by contrast negative values indicate a shortening.

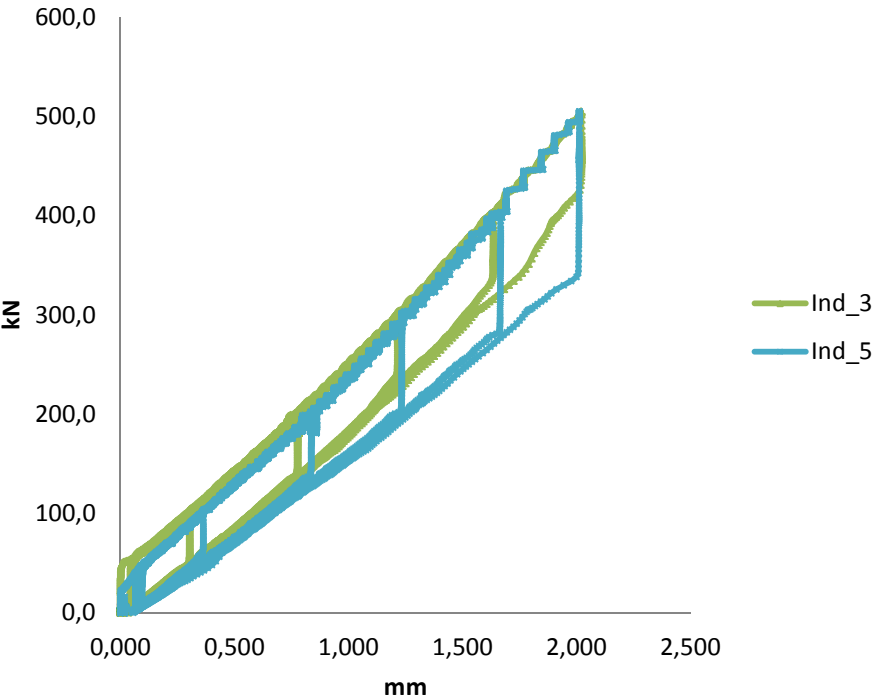


Figure 208. $F - \delta$ (500 kN Midspan).

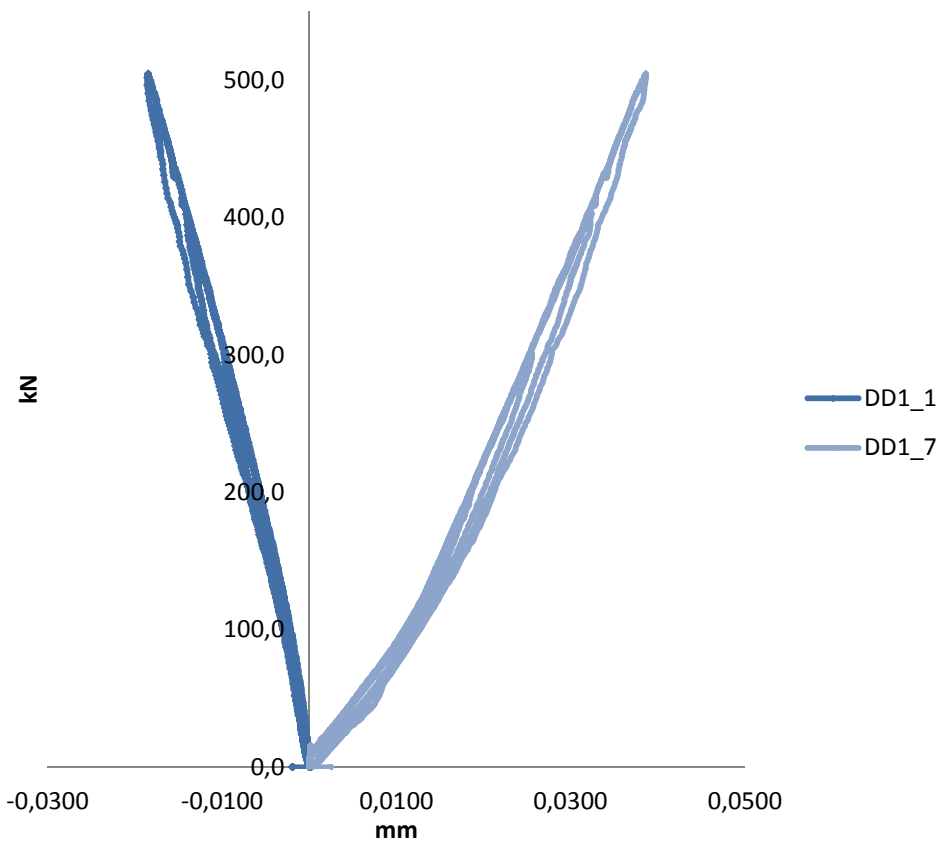


Figure 209. Force – deformation (500 kN Mid-span).

8.3.2 Asymmetric test and additional acquisition

Analogically to the symmetric test and maintaining the same acquisition configuration, a second test has been carried out. In this case, the force is applied at 1/3 of length (Figure 210) with the intention of investigating the beam behaviour under asymmetric load (Figure 212). The force is concentrated at the gusset plate (Figure 211). The test was conducted on the element tested in §8.3.1 considering the elastic field.

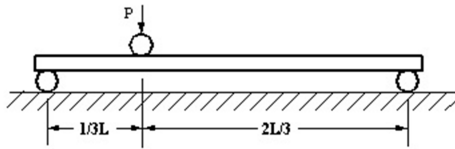


Figure 210. Static scheme.



Figure 211. Force position.



Figure 212. Eccentric load configuration.

The test has been carried out performing four different load steps in order to check the structural integrity during the experiment (Table 39).

Step 1	100 kN
Step 2	200 kN
Step 3	300 kN
Step 4	350 kN

Table 39

The beam deformation is very complex: many geometric imperfections are present and the element is composed by several different plates bring together by rivets. The experimental results are compared to the elastic and elasto - plastic behaviour. In the follow the results for 1/3 span force are summarized. The first graph (Figure 213) shows the transducers located in the lower flange.

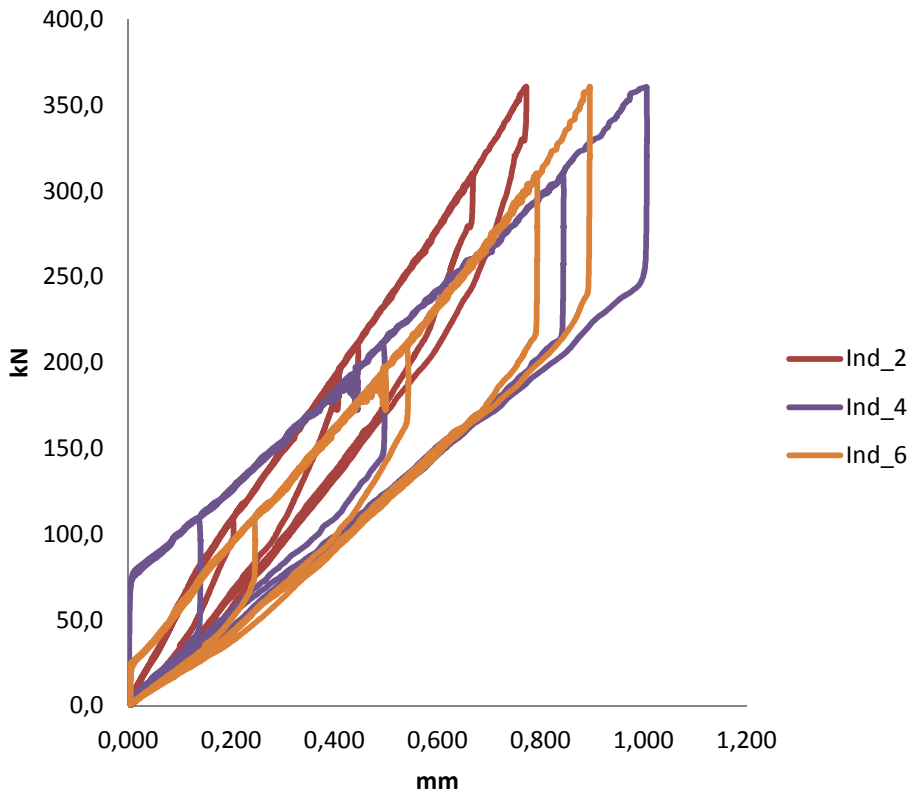


Figure 213. 350 kN at 1/3 length.

For all the channels, the force increase without any displacement due to friction and settling effects. After the preliminary phase, Channel 2 and Channel 6 show a different slope with a difference in vertical displacement of 0,12 mm. The rise line is straight and this indicate an elastic behaviour. Each load increment traces the previous curve proving the elastic state. There are some similarities between Channel 4, Channel 2 and 6 even if a different displacement magnitude and different slope are recorded. At 350 kN the maximum displacement for Channel 4 is 1 mm, for Channel 2 is 0,77 mm and for Channel 6 is 0,89 mm. An equivalent graph (Figure 214) has been created for the Channel 3 and 5. These transducers collect the upper flange displacements. Channel 3 and Channel 5 show a different slope with a maximum displacement (at 350 kN) of 1,96 mm. Each load increment traces the previous curve indicating the elastic state. DD1 sensor collects data from the plate deformation (Figure 215). Channel 1 (horizontal plate deformation) and Channel 7 (diagonal plate deformation) show a nonlinear behaviour. The max deformation reached by the DD1_7 is 0,001 mm. Positive sensor values indicate an elongation and by contrast, negative values indicate a shortening.

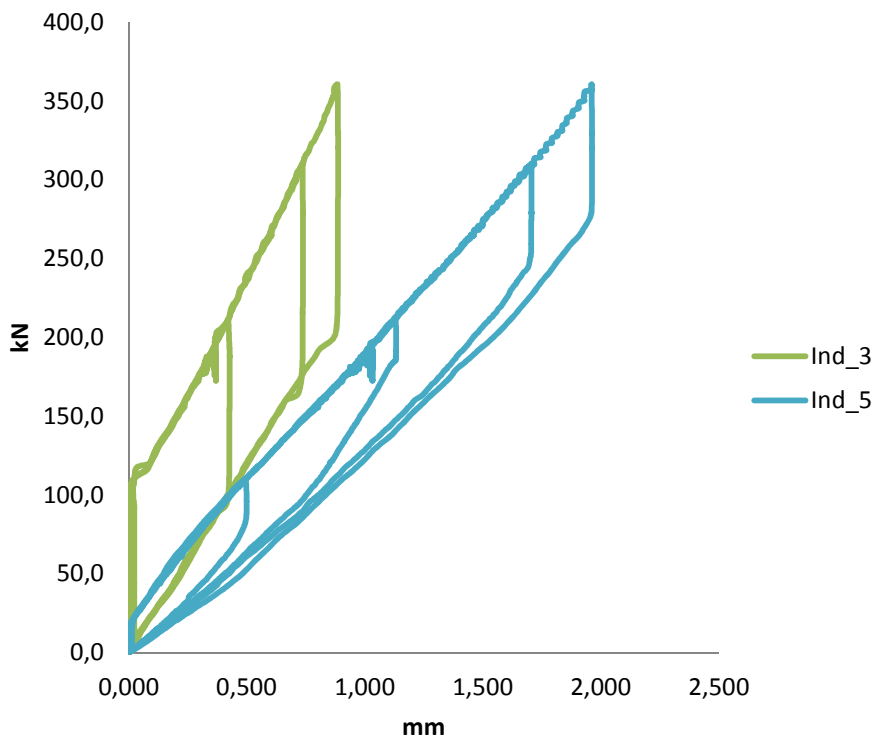


Figure 214. 350 kN at 1/3 length.

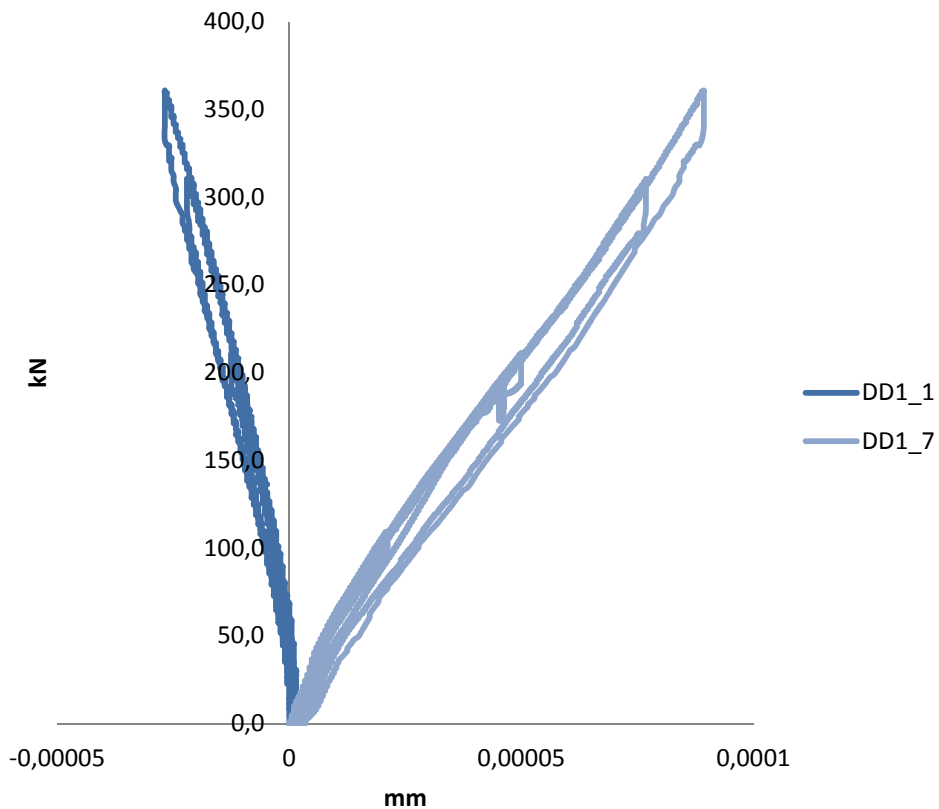


Figure 215. Force – deformation, 350 kN at 1/3 length.

In asymmetric configuration an additional test has been performed. The DD1 sensors have been placed on the plates and on the rivets in order to gain the deformation and the relative displacements between web and cover plates (Figure 216) and between rivets (Figure 217). This kind of test is essential in order to understand the static (and then the fatigue) behaviour. The joint may activate the friction between the plates changing the forces distribution. An 8 channels acquisition has been adopted and DD1 sensors have been positioned horizontally, vertically, diagonally, between plates and between rivets.



Figure 216. Plate sensor (Side B).



Figure 217. plate sensor (side A).

The force transducer uses Channel 0, Channel 4 is dedicated to the Inductive transducer located at the beam mid-span while the other Channels are used for DD1 sensors (see Table 40).

Sensor	Slope	Element
DD1_1	Diagonally	Rivets
DD1_2	Horizontally	Plate
DD1_3	Vertically	Rivets
Ind_4	-	-
DD1_5	Diagonally	Plate - Web
DD1_6	Diagonally	Plate - Web
DD1_7	Diagonally	Rivets

Table 40

The aim is to measure plates and rivets displacements precisely. During the asymmetric test the force and the mid-span displacement has been recorded. The sensor gauges the displacement of the joint close to the applied force. Channel number 1, 5 and 6 are located on Side B then Sensor number 2, 3 and 7 are on side A. The first graph (Figure 218) shows the displacement of DD1_1 and DD1_7. Channel 1 records maximum displacement of 0,003 mm, moreover Channel 7 records 0,02 mm. Channel 1 shows a non - linear behaviour. On the contrary, Channel 7 is linear. Each load increment traces the previous curve hypothesizing the elastic state.

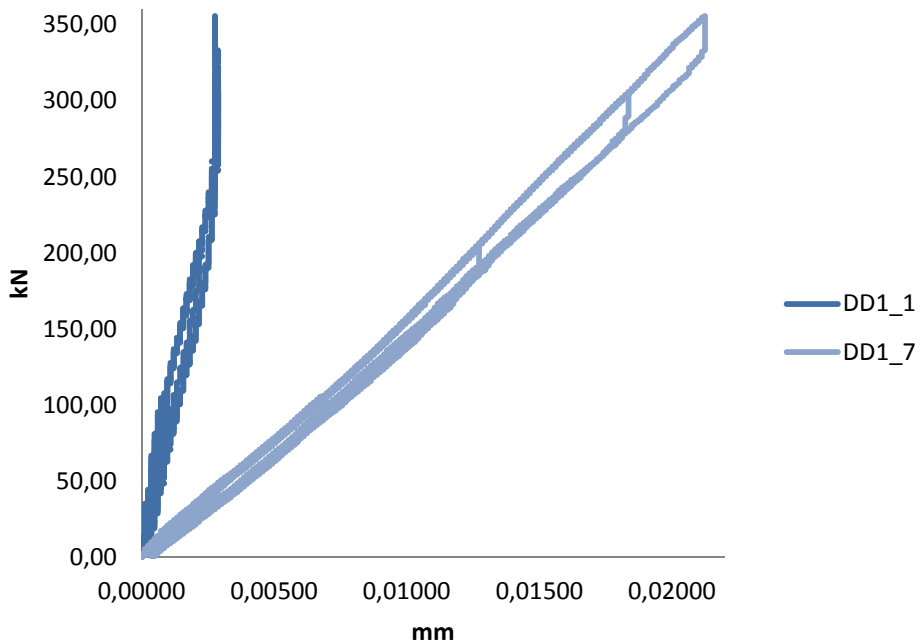


Figure 218. 350 kN at 1/3 length (High accuracy).

DD1_2 records about 0,005 mm then DD1_3 is approximately zero (Figure 219). Figure 220 shows the displacement of Channel 5 and 6. The rise line is straight and this indicate an elastic behaviour. Each load increment traces the previous curve proving the elastic state. These transducers collect data from the slip between web and plates. The slip recorded is about 0,02 mm for Channel 5 and 0,01 mm for Channel 6.

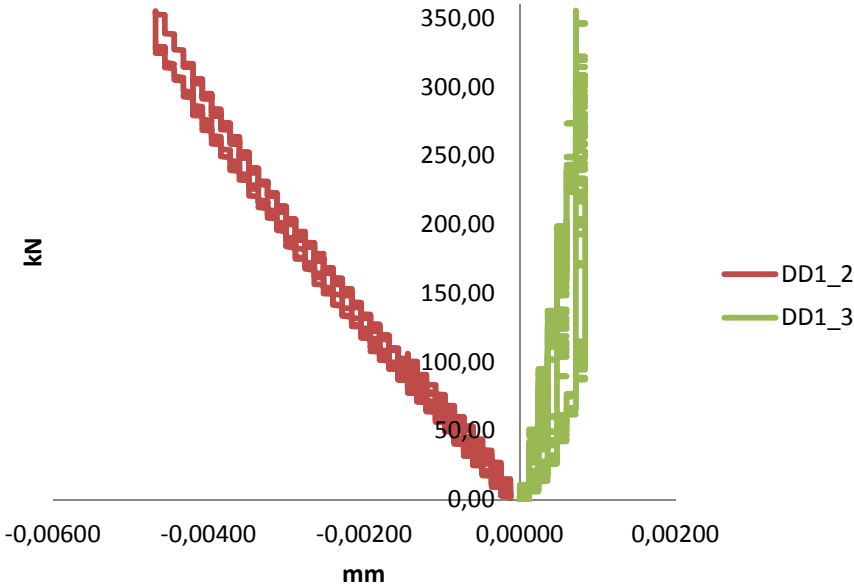


Figure 219. 350 kN at 1/3 length (Ha).

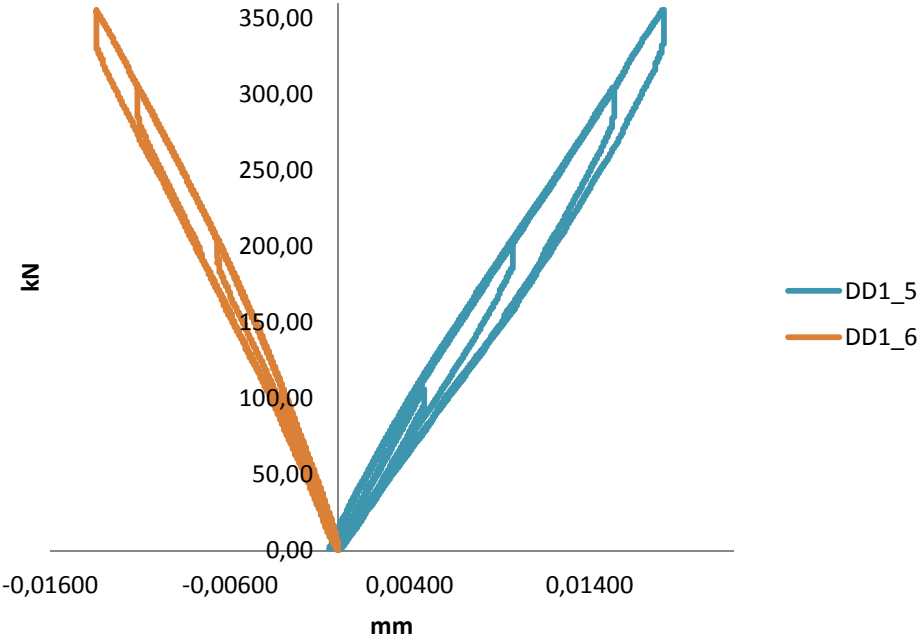


Figure 220. 350 kN at 1/3 length (Ha).

A schematic joint behaviour is synthesized in Figure 221 and Figure 222. Neglecting the small displacements of Sensors 1 and 2, other Channels provide an insight of different motion behaviour of each component. The cover plates attach together the two parts of beam web. The main web element rotates compared to the joint plate. The rail bearer is composed by many plates bring together by the rivets. In particular, the web is disconnected long the beam axis due to the cross girder insertion. The joint structural continuity is reactivated by the riveted joint. The missing column of rivets highlights the structural interruption. Sensor number 2 is located precisely on this invisible plate edge (Figure 221). The interpretation of these results and other consideration about global and local beam behaviour are mentioned in the next paragraph (§8.5).

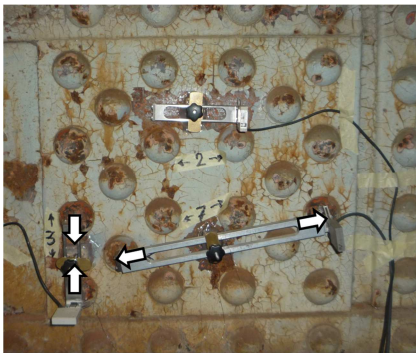


Figure 221. Side A.

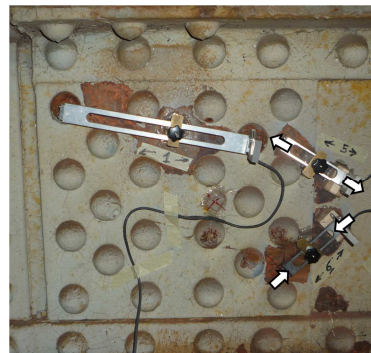


Figure 222. Side B.

The ultimate limit state (ULS) and the fatigue limit state (FLS) differ for various aspects. In the ULS the forces are high and the friction has been passed moreover, in the FLS, the friction may be active. These two scenarios may lead to a completely different strength evaluation. Analysing the previous results is clear that the friction is still active and the rivets shank does not transfer shear force to the plates. For this force levels the rivets shank strength and the consequently Fem modelling can be neglected.

8.4 Elastic Fem simulation

The collected information regarding rail bearers allows to modelling the beam accurately. Moreover, the static beam behaviour is very complex due to the friction involvement. A calibrated elastic simulation is needed with the intention of deducing

the fatigue weakening. First solution (Figure 223) models 3-point bending test with simple supports. The entire rail bearer has been modelled using "Quad 8" Plates Elements and using San Stino's steel. The Fem recreates the tests situation disregarding the friction and the local plasticization. Each hole and each thickness variation have been modelled furthermore load area has been modelled using rigid link elements. The sensors positions have been reproduced on the Fem model (reference points) and the displacements have been recorded.

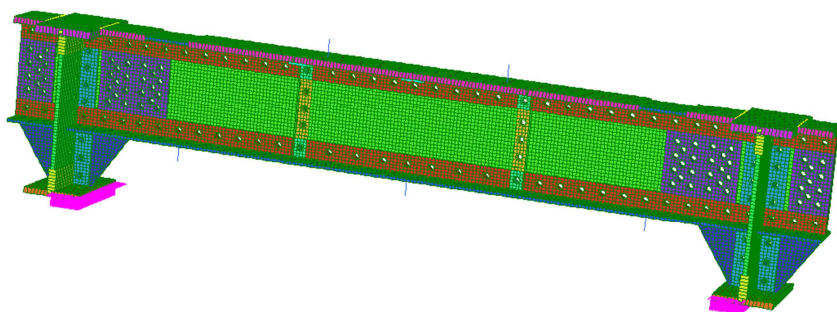


Figure 223. Elastic model.

Respecting the test campaign both symmetric and asymmetric scheme have been applied with the same forces increase. In the images below (Figure 224 and Figure 225) Von Mises stress is shown: for symmetric static scheme the force applied is 500 kN moreover 350 kN, for the asymmetric scheme, is applied.

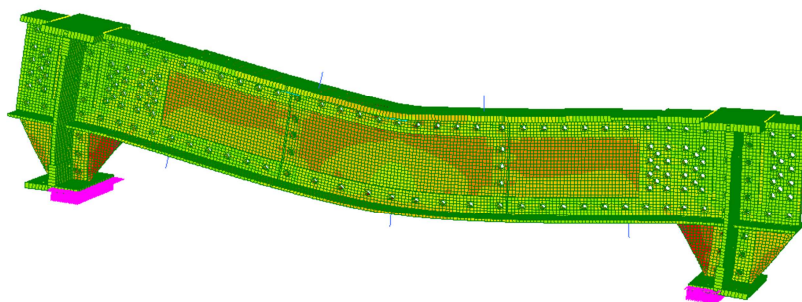


Figure 224. Symmetric static scheme.

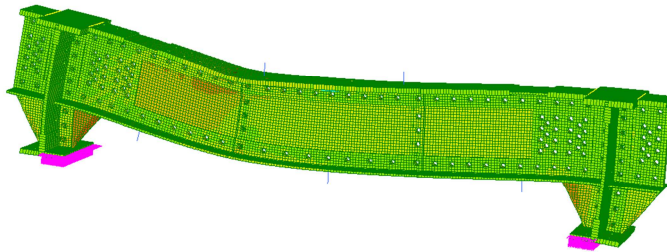


Figure 225. Asymmetric static scheme.

For the *symmetric static scheme*, the elastic results of Fem simulation are shown below (Figure 226 to Figure 231). In order to validate the model, the displacements are compared with the experimental results. The displacements over the beam are graphed: the displacements are shown on x axis moreover on y axis the force applied is shown. Figure 226 shows, for example, the correlation between the Fem simulation and the experimental data. The straight lines are divergent due to the different structural beam behaviour. The same effect, more or less marked, is present (from Figure 227 to Figure 230) in the others reference points.

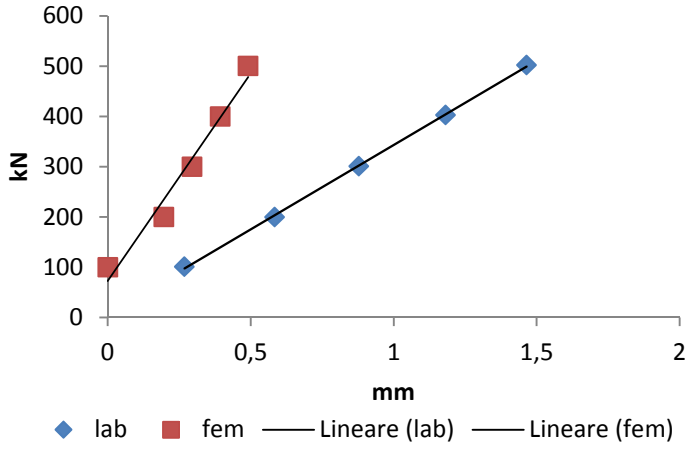


Figure 226. Channel 2.

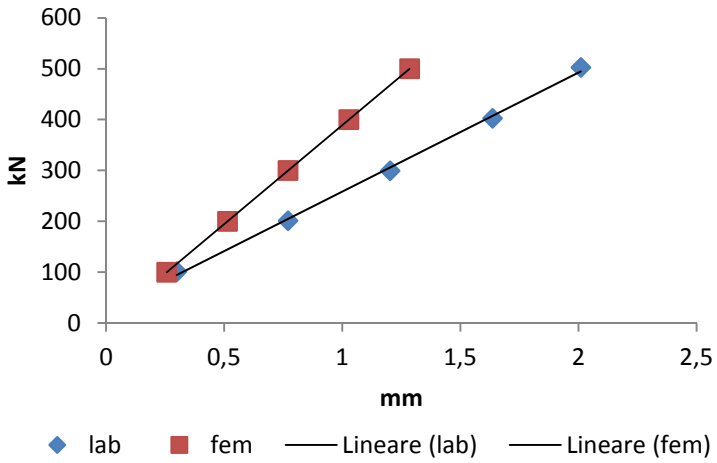


Figure 227. Channel 3.

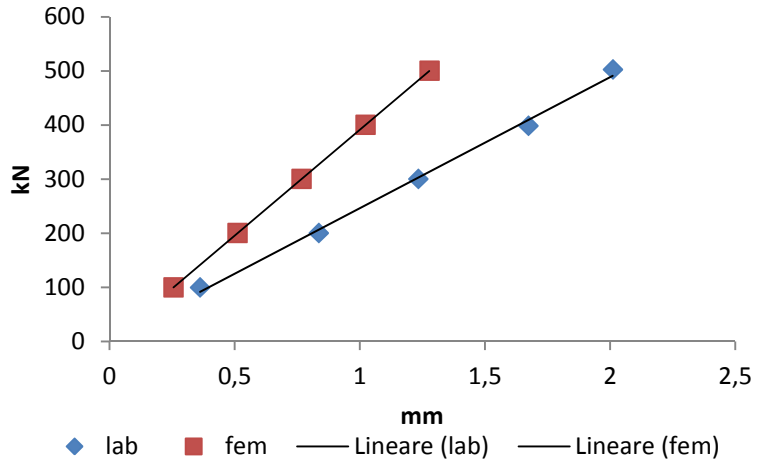


Figure 228. Channel 5.

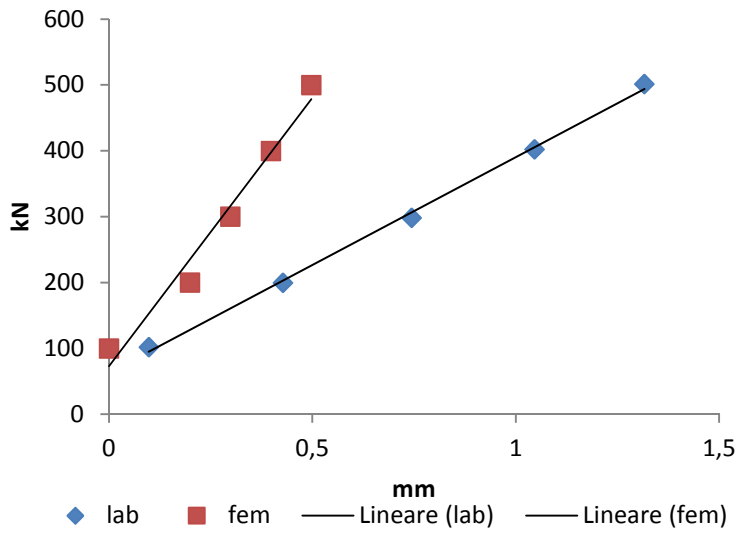


Figure 229. Channel 6.

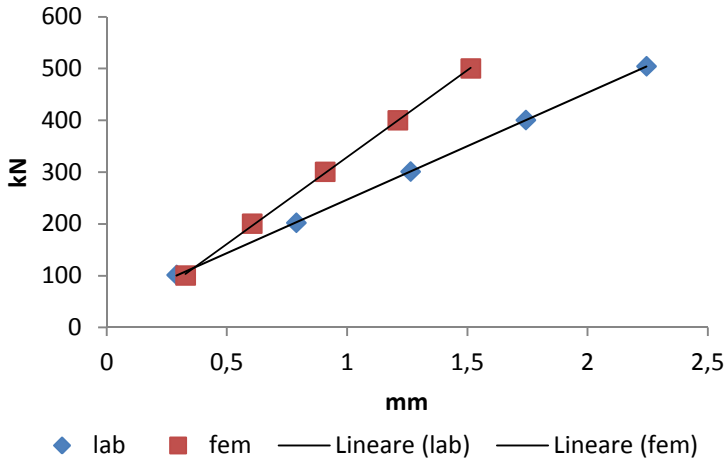


Figure 230. Channel 4.

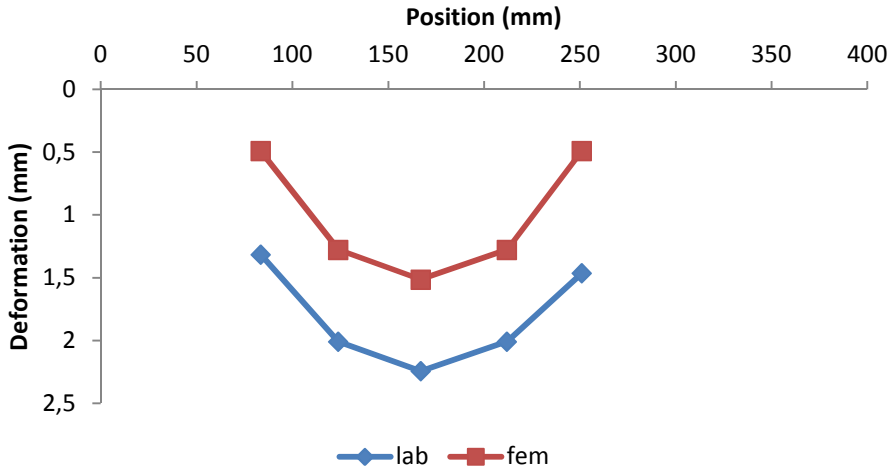


Figure 231. Elastic deformation.

It is notable that only for 100 kN the precision is acceptable whereas for higher loads the accuracy decrease rapidly. The difference between the solutions varies until 1 mm. Figure 231 shows the beam elastic deformation: the difference between the laboratory test and the numerical solution is about 1 mm. The Fem model output of symmetric static scheme is shown in Figure 232. The maximum plate stress (Von

Mises) on the flange is about 220 MPa located near the force application area. The maximum plate stress (Von Mises) on the web is about 110 MPa located near the force application area. Near the support the gusset plate stress is about 150 MPa. In this model the entire beam behaviour is elastic moreover only near the area of force application and in the support gusset plate the stress is relative high.

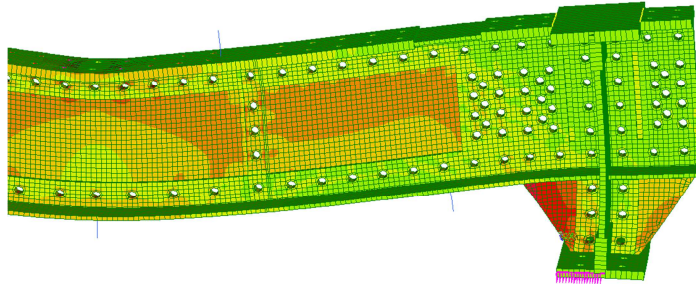


Figure 232. Symmetric load.

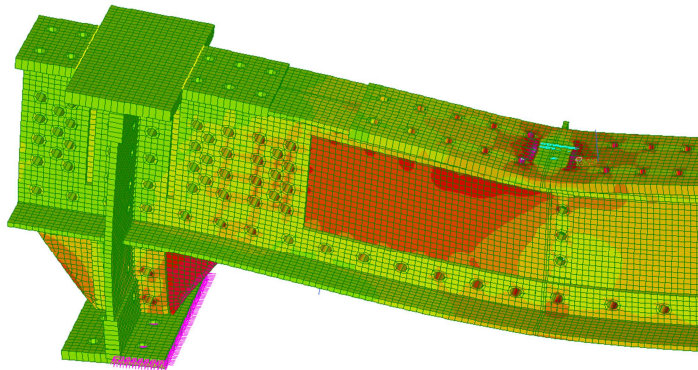


Figure 233. Asymmetric load.

The Fem model output of *asymmetric static scheme* is shown in Figure 233. The maximum plate stress (Von Mises) on the flange is about 100 MPa located near the force application area. The maximum plate stress (Von Mises) on the web is about 80 MPa located near the force application area. Near the support the gusset plate

stress is about 100 MPa. In this model the entire beam behaviour is elastic moreover only near the area of force application and in the support gusset plate the stress is relative high. It is important to note that the stress is proportionally higher in relationship with the symmetric static scheme. The elastic results of Fem simulation are shown below (Figure 234 to Figure 239). In order to validate the model, the displacements are compared with the experimental results. The displacements over the beam are graphed: the displacements are shown on x axis moreover on y axis the force applied is shown. Figure 234 shows, for example, the correlation between the Fem simulation and the experimental data. The straight lines are divergent due to the different structural beam behaviour. The same effect, more or less marked, is present (from Figure 234 to Figure 239) on the Channel 5 and Channel 6. In Channel 3 and Channel 4 the lines cross indicating a good fit only for few values. The simple linear elastic model prevents a deep understanding behaviour of the rail bearers. In the next paragraph (§8.5) a nonlinear solution is presented.

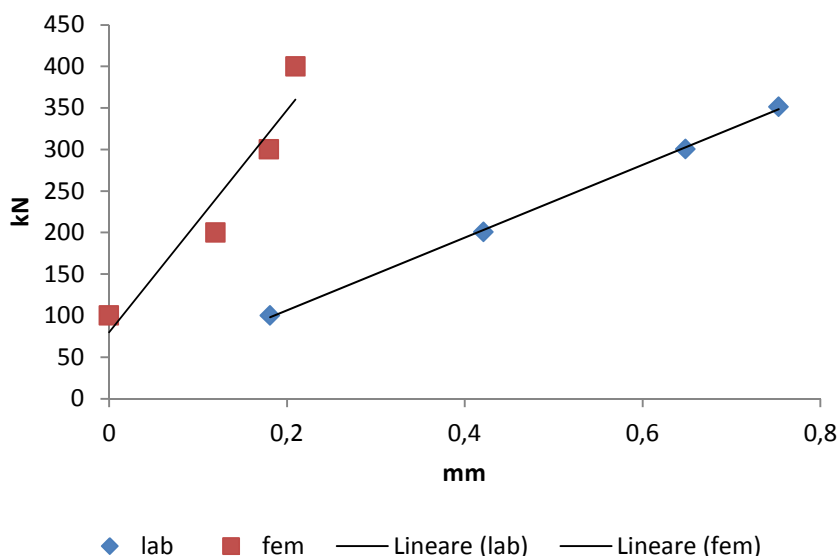


Figure 234. Channel 2.

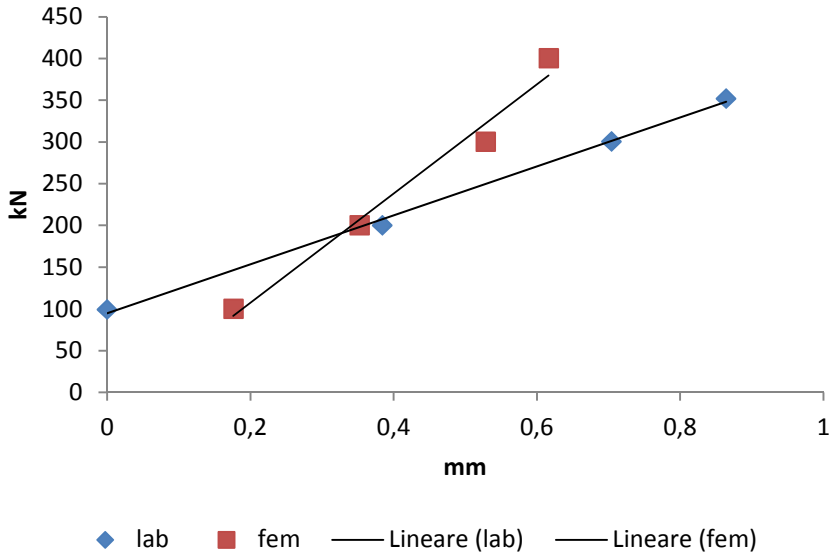


Figure 235. Channel 3.

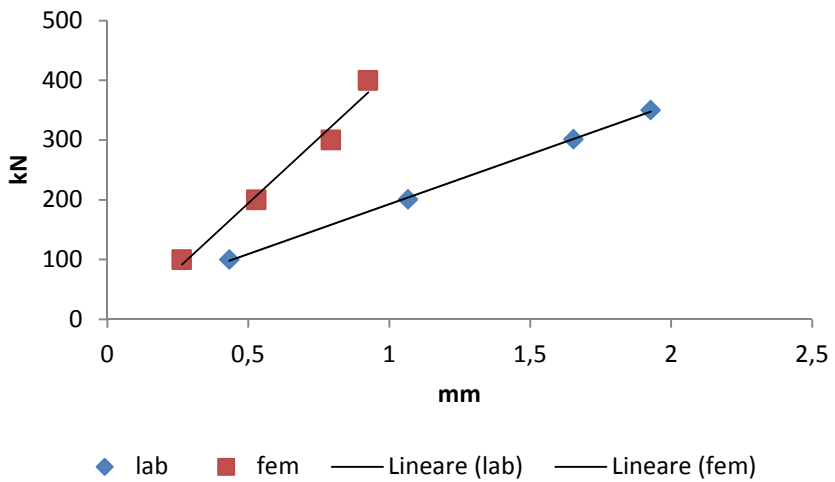


Figure 236. Channel 5.

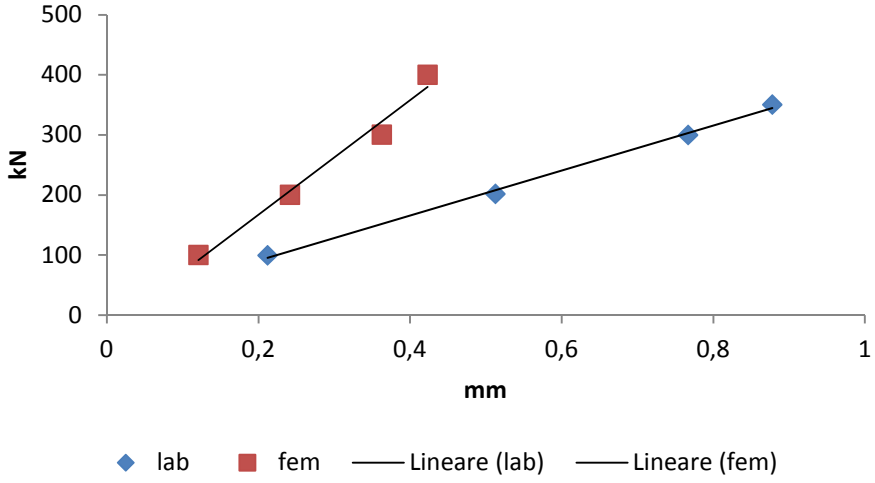


Figure 237. Channel 6.

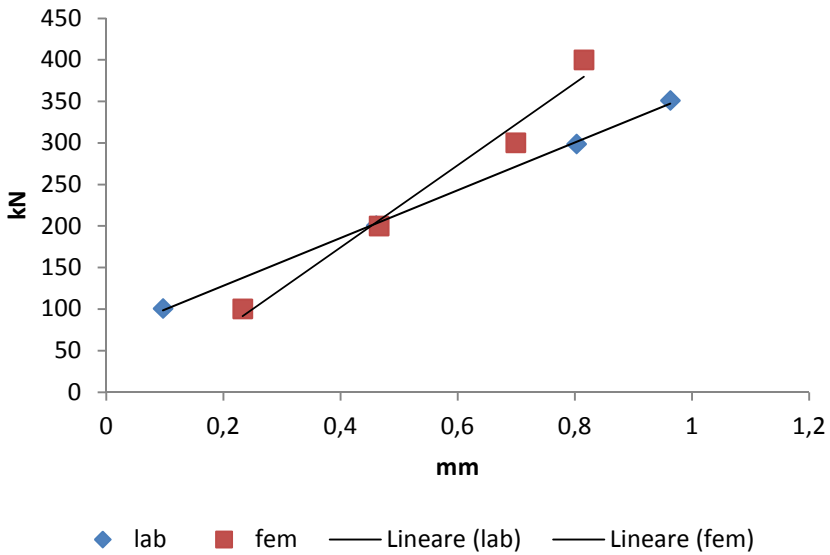


Figure 238. Channel 4.

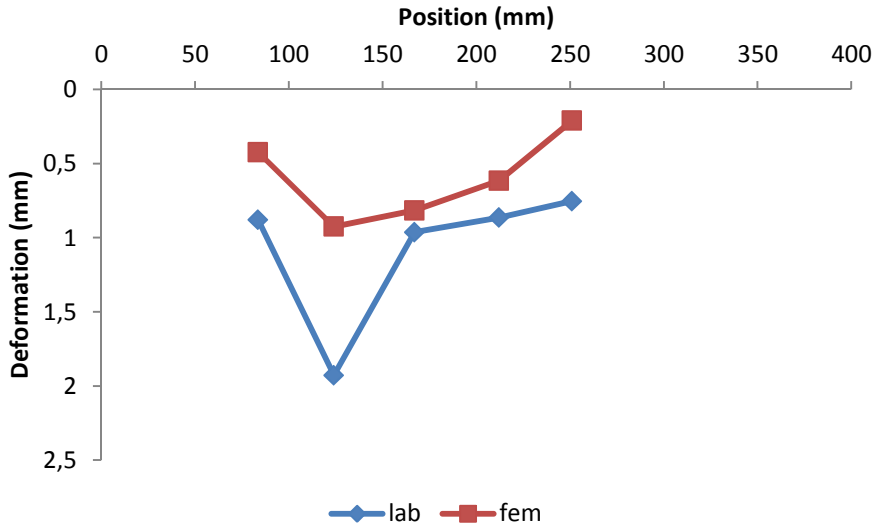


Figure 239. Elastic deformation.

8.5 Non-linear Fem simulation

Nonlinear solution allows to take into consideration different aspects. The nonlinear material constitutive law has been considered, the joint friction and the rivet clamping have been added. A sophisticated Fem model with more than 31000 Quad 8 plates and more than 24000 points contact has been needed. In order to reduce the Solver task and for optimizing the friction interactions, the problem has been resolved introducing the displacement and checking the equilibrium. The element has been modelled as a composition of various plates (Figure 240). The connections have been represented by rivets and cover plates (Figure 241). The friction has been modelled (Figure 242) by Point Contact elements. For more information about the friction see §5.5.1. The San Stino's steel refers to §6.2, the rivets characteristics refers to §7.2.4 with the following characteristics (Table 41):

Rivets clamping	58kN
Friction coefficient	0,3

Table 41

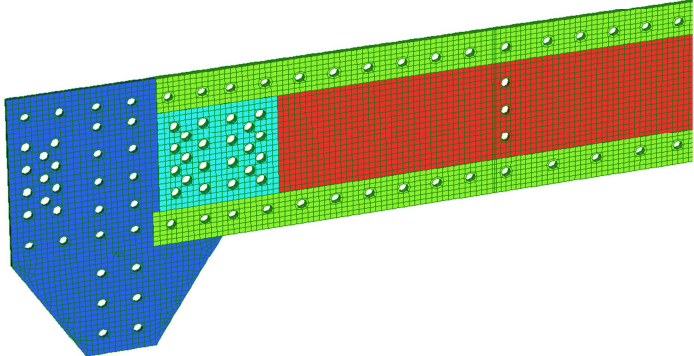


Figure 240. Plate composition.

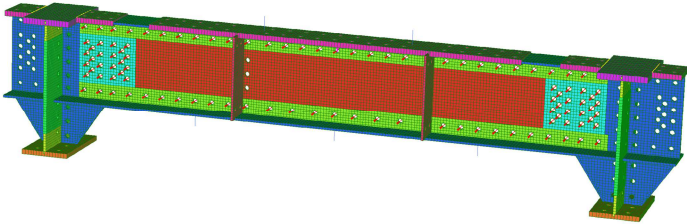


Figure 241. Non-linear model.

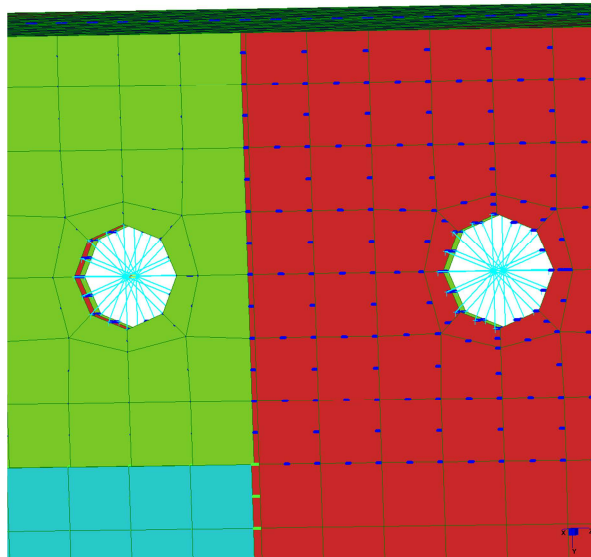


Figure 242. Point contact.

An important aspect of the non-linear model are the supports. Simply schematized as a simply supported beam the element, instead, is affected by the supports. The two steel supports allow micro slip due to the beam deflection. The supports rigidity has been introduced in the model with the intention of calibrating the entire system. Respecting the test campaign both symmetric and asymmetric scheme have been applied with the same forces increase. The correct (respect to the laboratory test) solution has been searched introducing the relative displacement and checking the system equilibrium. The non-linear results of Fem simulation are shown in the images below (Figure 243), Von Mises stress is shown for symmetric static scheme (force applied is 500 kN).

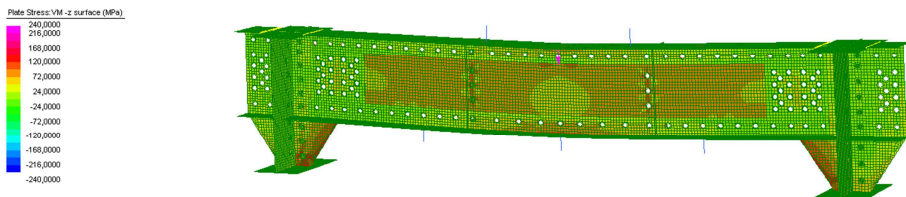


Figure 243. Symmetric static scheme (500kN).

In order to validate the model, the displacements are compared with the experimental results. The displacements over the beam are graphed: the displacements are shown on x axis moreover on y axis the force applied is shown. The straight lines are parallel due to the goodness of simulation. The same effect is present (from Figure 244 to Figure 248) in the others reference points. Figure 249 shows, for example, the convergence process in non-linear solver. Figure 250 shows the global Fem simulation highlighting the good level of precision.

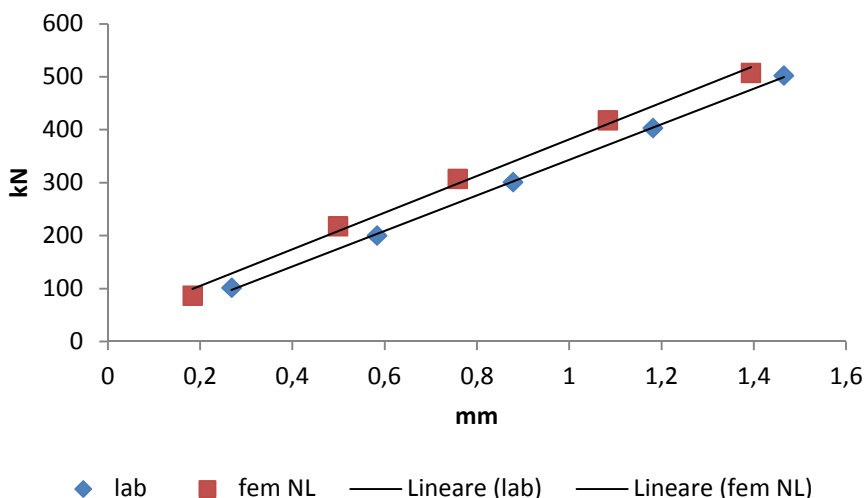


Figure 244. Channel 2.

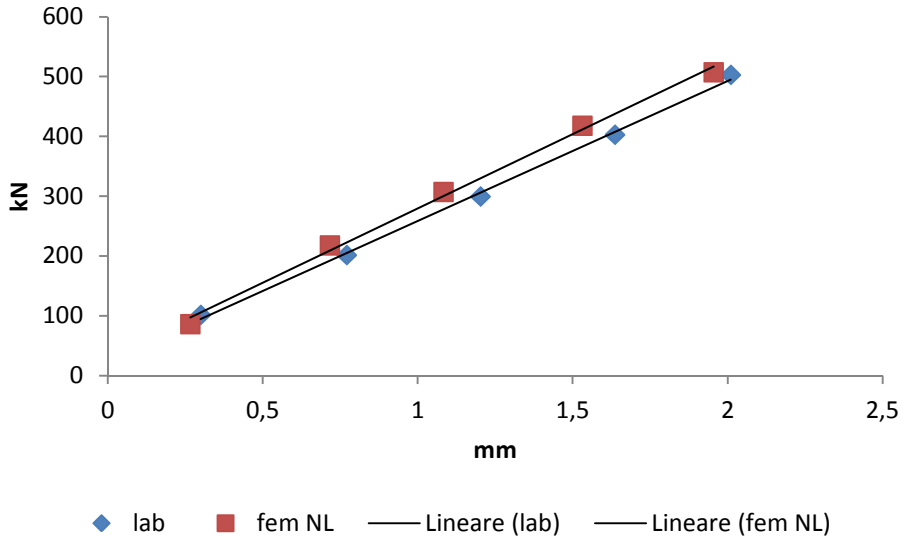


Figure 245. channel 3.

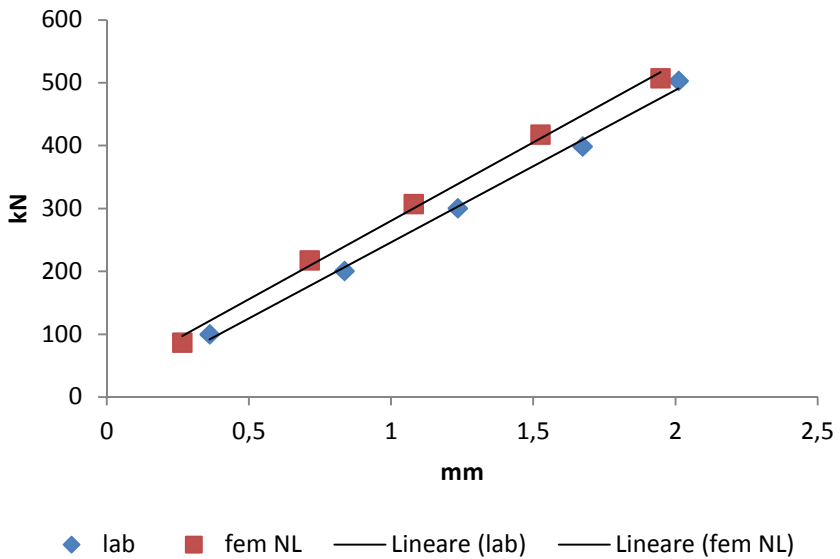


Figure 246. Channel 5.

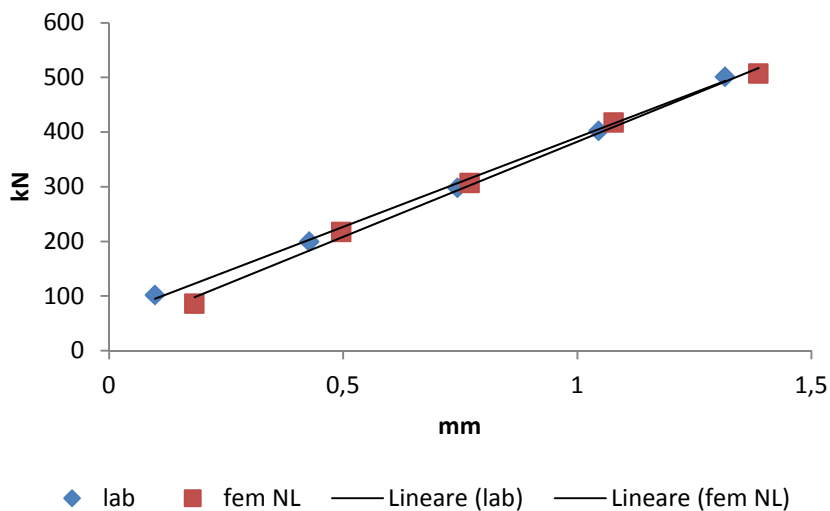


Figure 247. Channel 6.

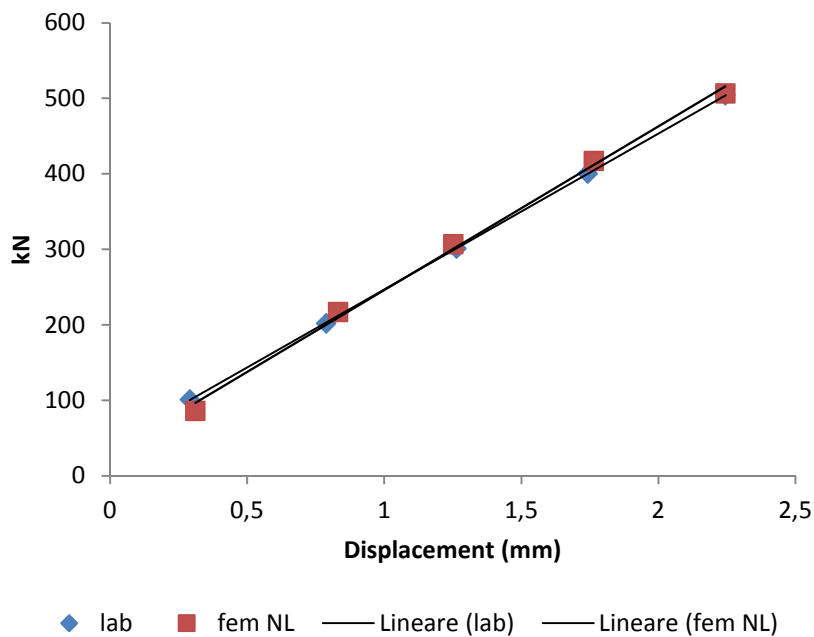


Figure 248. Channel 4.

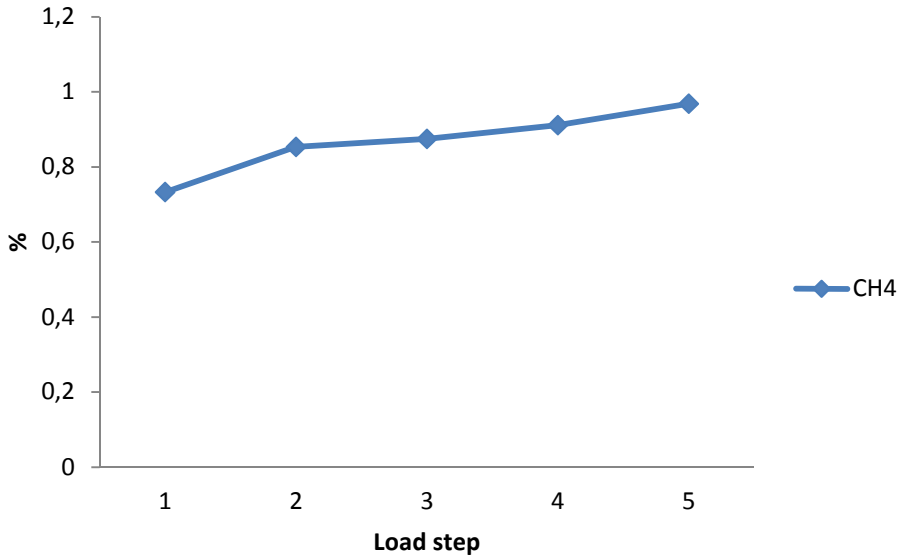


Figure 249. Iterations.

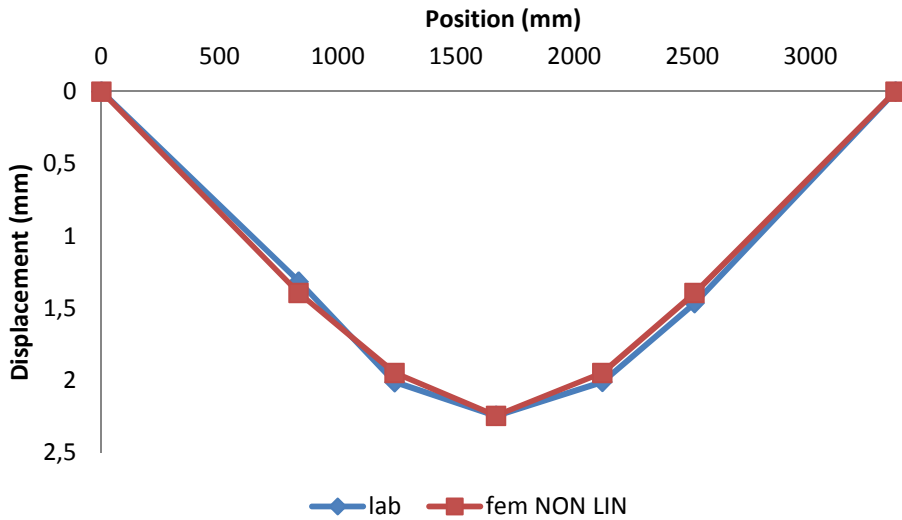


Figure 250. Beam displacement (500 kN).

It is notable that, in non-linear model, the precision is acceptable for each load step. The difference between the solutions varies until 1/10 mm. Figure 250 shows the beam non-linear deformation: the differences between the laboratory test and the numerical solution is about 1/10 mm. The Fem model output for symmetric static scheme is shown in Figure 243. The maximum plate stress (Von Mises) on the flange is about 140 MPa located near the force application area. The maximum plate stress (Von Mises) on the web is about 110 MPa located near the force application area. Near the support the gusset plate stress is about 140 MPa. In this model the entire beam behaviour is non-linear moreover only near the area of force application and in the support gusset plate local plasticization are present. In the adjacent zones, the stress range, is about 80 MPa. The Fem model output of *asymmetric static scheme* is shown in Figure 251. The maximum plate stress (Von Mises) on the flange is about 130 MPa located near the force application area. The maximum plate stress (Von Mises) on the web is about 50 MPa located near the force application area. Near the support the gusset plate stress is about 70 MPa. In this model the entire beam behaviour is non-linear moreover only near the area of force application and in the support gusset plate the stress is relative high. It is important to note that the stress is proportionally higher in relationship with the symmetric static scheme. The elastic results of Fem simulation are shown below (Figure 252 to Figure 256). In order to validate the model, the displacements are compared with the experimental results. The displacements over the beam are graphed: the displacements are shown on x axis moreover on y axis the force applied is shown. The straight lines are parallel due to the goodness of simulation. Figure 258 shows the correlation between the Fem simulation and the experimental data. The non-linear elastic model represents properly the element static behaviour. An important note regards the misalignment of force and beam web. Figure 257 shows that Channel 5 record an excessive displacement related to the other sensors. This occurs due to the irregularity of the rivets in the up flange that has led to an eccentricity (about 25 mm). The force acts on the flange, bending the plate and moving the sensor. The model, taking into account this irregularity, follows the experimental deformation with a good approximation.

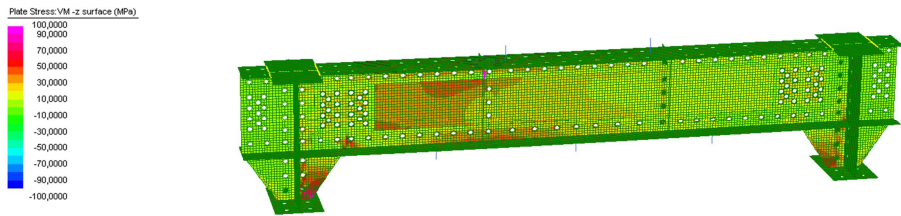


Figure 251. Asymmetric static scheme (300kN).

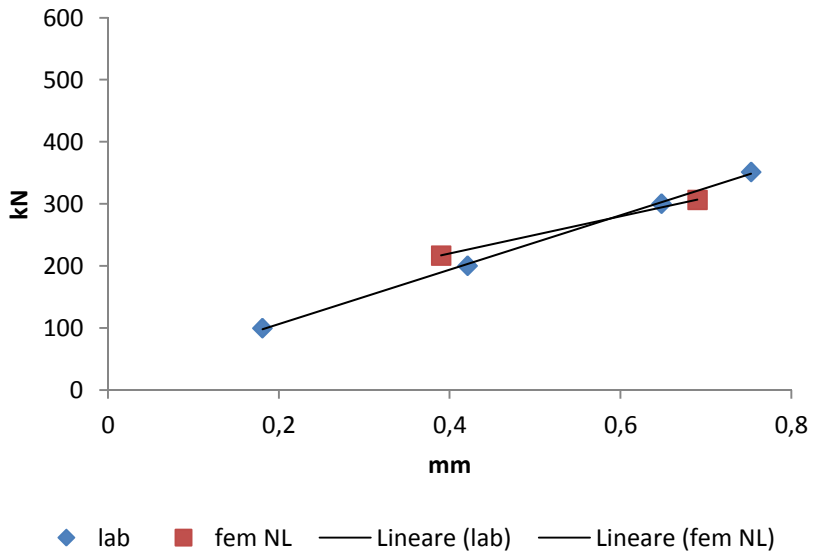


Figure 252. Channel 2.

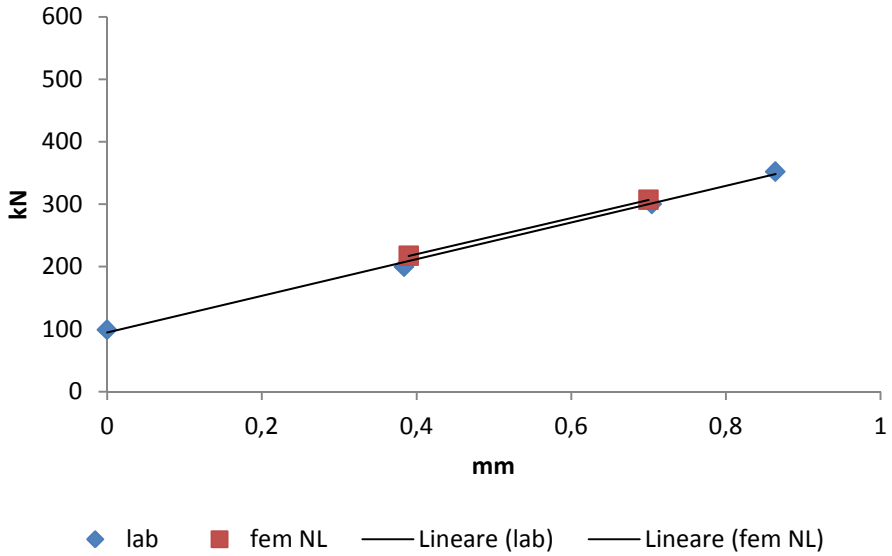


Figure 253. Channel 3.

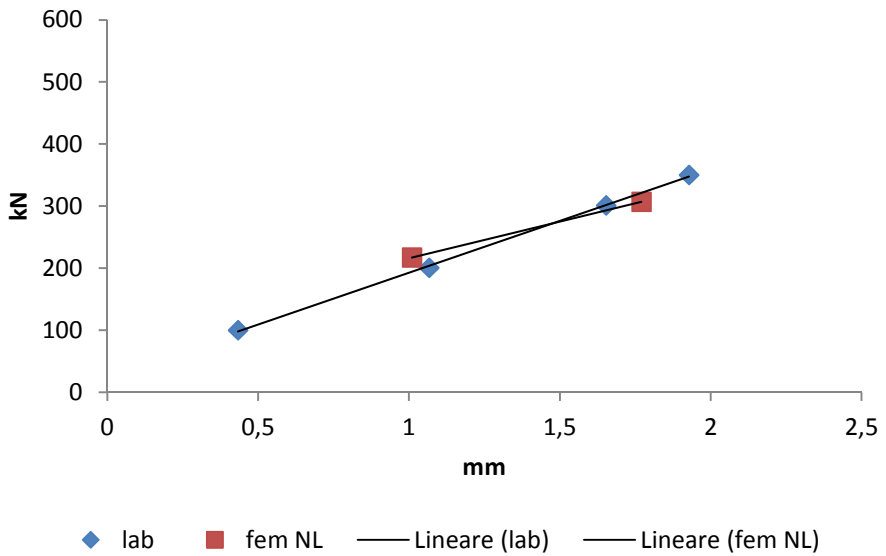


Figure 254. Channel 5.

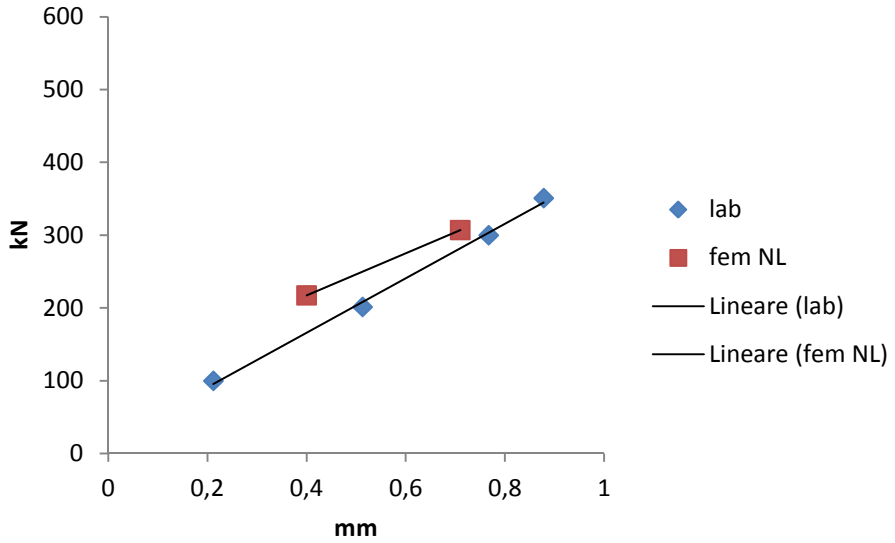


Figure 255. Channel 6.

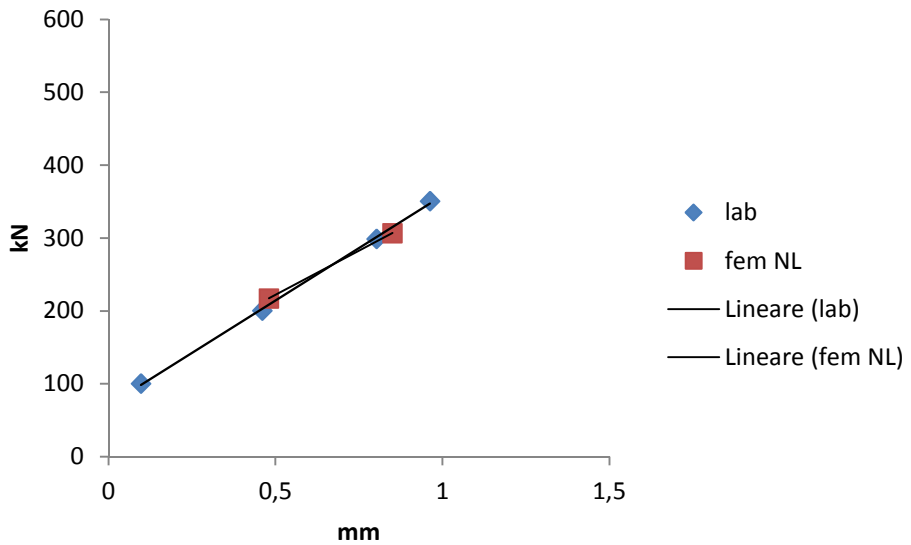


Figure 256. Channel 4.

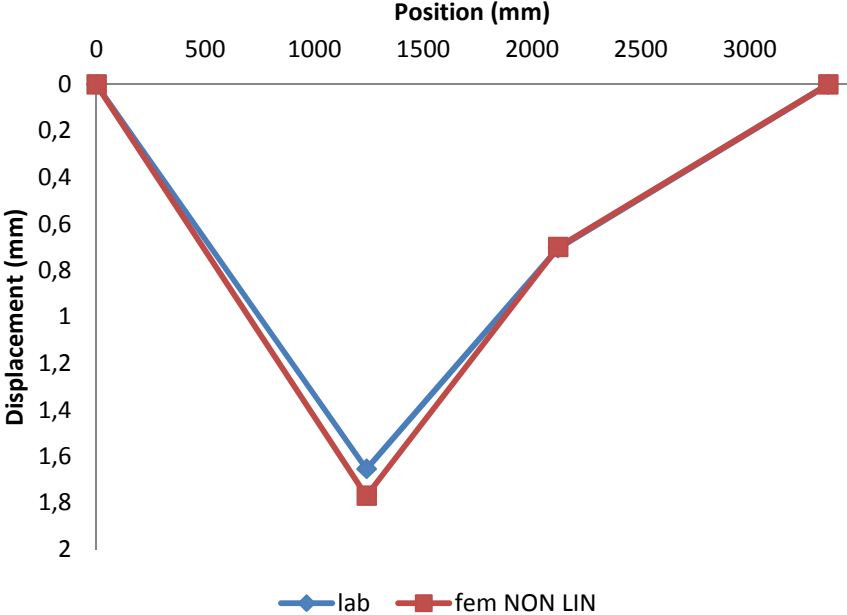


Figure 257. Up flange.

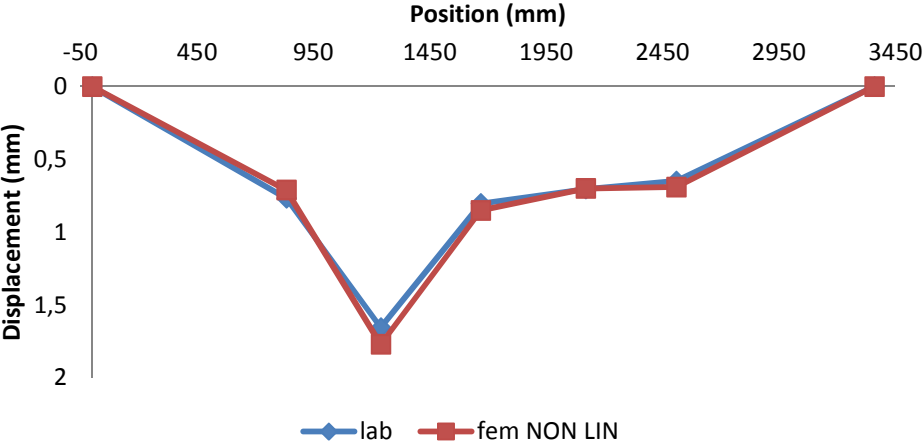


Figure 258. Beam displacement (300 kN).

Referring to §8.3.2, the fem model shows a good fit for the plates displacements. The collected data from the laboratory test confirm the correctness of clamping force and friction modelled in the Fem.

8.6 Final considerations

A complete overview of rail bearers has been introduced. The element, as well as the entire structure, is brought together by rivets. The main elements composing the beam are the web, the flanges and riveted cover plates. Near the node, a triangular gusset plate connects the rail bearer to the transversal. A series of non-destructive tests has been performed with the intention of revealing the original structure. The beam is a plate composite section. Grind molar has been used to remove the superficial material and to show up the rivet shape. The entire bridge was covered by protective paint skin aged and partially removed. Altogether, the structure was slightly corroded and, except for the WWII damages, well preserved. A precise estimation of rivets dimensions and positions is carried out. The rivet section highlights a good head and shank regularity; moreover, the plates have a sufficient contact between themselves. Rivets have good head regularity, independently of any horizontal or vertical direction, and the average head diameter is 42 mm. The diameter variation is between 2 and 6% proving the good manufacturing level. Some holes have been inspected and their average diameter is about 26 mm. The shank diameter is 25 mm and a 1 mm gap is present. The riveted joint and the relative dimension respect the traditional size: the inter-axial spacing is 5ϕ or more and the edge distance is between 0.6 and 0.9ϕ . A brief overview on the in-service beam condition has been reported. The static schemes in-service condition and during the test campaign are substantially different. For about a century the San Stino's rail bearers have worked fixed between crossbeams; moreover, the consecutive fatigue test will operate in simple supported static scheme. A detailed load history is not available due to the bridge age. The train moving effect is sophisticated due to the continuous changing in static scheme. Considering the various train typologies, a typical fatigue verification is carried out for rail bearers. The constraints simulate the cross girder effects (fixed at both ends). The maximum stress range is focused in the web, under the forces application area, and it is about 37 MPa (Von Mises criteria). Moreover, 20 MPa has been observed in the flanges. The preliminary analysis shows that the fatigue life of the rail bearer is ending rapidly due to the greater traffic and greater loads. In first analysis the fatigue

verification is satisfied. Nevertheless, the stress distribution is completely different compared to the laboratory condition and it is not replicable due to the cross girder cut. A fatigue identification test has been carried out with the intention of predicting the fracture behaviour. A multi channels acquisition has been used intending to gain the entire beam structural behaviour. The static scheme is very simple although the beam deformation is very complex: many geometric imperfections are present and the element is composed by several different plates bound together by rivets. The test has been carried out performing different load steps in order to check the structural integrity during the experiment. In force – displacement graph the rise line is straight and this indicates an elastic behaviour. Each load increment traces the previous curve proving the elastic state. Analogically to the symmetric test and maintaining the same acquisition configuration, an asymmetric test has been carried out. An elastic behaviour is observed. In asymmetric configuration, an additional test has been performed: accurate sensors have been placed on the plates and on the rivets. The deformation and the relative displacements between web and cover plates and between rivets have been gained. An elastic behaviour is observed. The friction is still active and the rivets shank does not transfer shear force to the plates. The collected information regarding rail bearers allow modelling the beam accurately. The elastic Fem recreates the tests situation disregarding the friction and the local plasticization. The simple linear elastic model prevents a deep understanding behaviour of the rail bearers. A nonlinear solution allows to take into consideration different aspects: the nonlinear material constitutive law has been considered, the joint friction and the rivet clamping have been added. The element has been modelled as a composition of various plates. The supports rigidity has been introduced in the model with the intention of calibrating the entire system. The model follows the experimental deformation with a good approximation. Moreover, there is a good correlation between the fem model and the plates – to - plates displacements. Starting from this considerations, in § 9, a fatigue test has been carried out.

9 LABORATORY EQUIPMENT AND FATIGUE TEST

9.1 Introduction

The real scale fatigue tests are essential to understand the real structural behaviour. The Department of Civil and Environmental Engineering of Padova (ICEA) started to test elements under repeated loads. A specific metallic frame has been designed with the intention to test until 1,8 m high elements under 1500 kN force. The standard fatigue design is not accepted in the metallic frame due to detail complexity. In this chapter, a brief overview of advanced design methods of welded structures and the frame design are mentioned.

9.1.1 *Welded components: nominal stress*

Fatigue failures in welded structures lead to loss of life consequently various standards and fatigue design codes have introduced this topic. In some cases, the foundation of such codes rely on old concepts that do not easily translate to the output from modern computer software and are also limited to rather simplified structures. A better understanding of the influence of fatigue strength and the limits of the different fatigue design methods due to the weld quality will improve the development of new fatigue loaded products. The modern development of fatigue life predictions of welded structures started in this century when the nominal stress approach was introduced. The nominal stress of welded component was calculated analytically or with reference books. The fatigue strength was taken from tabulated S-N curves for a variety of welded joints and the fatigue structural life was estimated by linear damage rule. For complex welded components the nominal stress can be difficult to define even if the stress distribution is very well described with FEM. Therefore, new improved methods to predict fatigue have been developed. Nowadays there are Nominal Stress, Structural Stress, Effective Notch Stress and Linear Elastic Fracture Mechanics methods to predict fatigue on welded components. Nominal stress is the stress calculated in the sectional area under elastic behaviour and some simplifications [37]. The local stress raising effects of

the welded joint are neglect but the stress raising effects of the macro-geometric shape of the component in the vicinity of the joint, such as e.g. large cut outs, are including. A macro-geometric discontinuity is a global discontinuity usually not taken into account in the collection of standard structural details, such as a large opening, a curved part in a beam, a bend in a flange not supported by diaphragms or stiffeners, discontinuities in pressure containing shells, eccentricity in a lap joint.

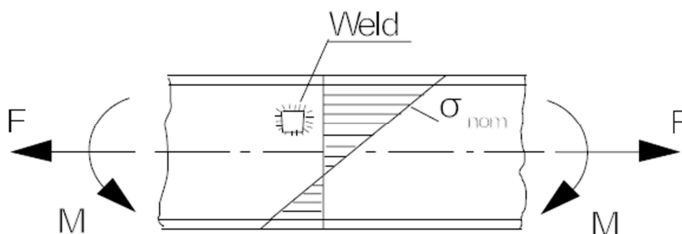


Figure 259. Nominal stress: excluding micro-detail.

Over the section, the nominal stress may vary. For example, at a beamlike component, using de Saint Venant theory, the modified nominal stress and the variation over the section can be calculated. However, the effect of a welded on attachment is ignored (Figure 259). The effects of stress fields in the vicinity of concentrated loads and macrogeometric features of the component must be included in the nominal stress. Both may cause significant redistribution of the membrane stresses across the section and significant shell bending stress may be generated as well. The secondary bending stress caused by axial or acceptable angular misalignment needs to be considered if the misalignment exceeds the amount already covered by the fatigue resistance S-N curve for the structural detail. This is done by the application of an additional stress magnification factor $k_{m,eff}$. Either the applied stress is multiplied by $k_{m,eff}$ or the fatigue resistance (stress) is divided by it. In simple components, the nominal stress can be determined using elementary linear-elastic behaviour. Nominal stress is the average stress in the weld throat or in the plate at the weld toe as indicated in the structural details. The stress σ_w or τ_w in weld throat a for a weld of length l_w and a force in the weld F becomes (Equation (72)):

$$\sigma = F / (a \cdot l_w) \quad (72)$$

Finite element method (FEM) modelling may be used in other situations. For example, for indeterminate structures and structural components incorporating macro geometric discontinuities, for which no analytical solutions are available. If the Finite Element Method is used, meshing can be simple and coarse (Figure 260).

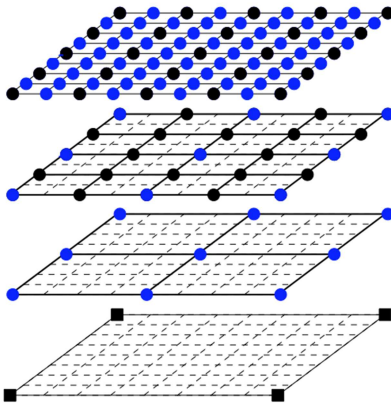


Figure 260. Different mesh accuracy.

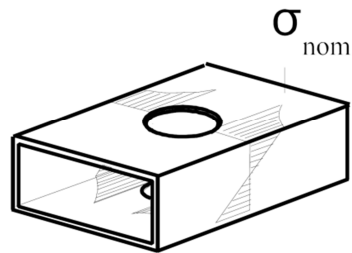


Figure 261. Modified nominal stress.

Care must be taken to ensure that all stress concentration effects from the structural detail of the welded joint are excluded when calculating the modified (local) nominal stress (Figure 261). Modified nominal stresses are nominal stress including macro-geometric effects, concentrated load effects and misalignments, ignoring the stress raising effects of the welded joint itself. If nominal stresses are calculated for fillet welds by coarse finite element meshes, nodal forces rather than element stresses should be used in a section through the weld in order to avoid stress underestimation. The fatigue resistance S-N curves of classified structural details are based on nominal stress excluding the stress or strain concentration due to the corresponding discontinuity. Thus, the stress check must be carried out outside the stress concentration field of the welded joint.

9.1.2 Structural (or geometric) stress: hot spot method

A hot spot is a point in a structure where a fatigue crack may initiate due to the combined effect of structural stress fluctuation (σ_{hs}) and the weld geometry or a similar notch. The structural or geometric stress (σ_{hs}) at the hot spot includes all stress raising effects of a structural detail excluding the non-linear peak stress σ_{nlp} caused by the local weld toe notch (Figure 262). The structural stress is dependent on the loading parameters and global dimensional of the component near the joint. It is determined on the surface at the hot spot of the plate, shell or tubular components.

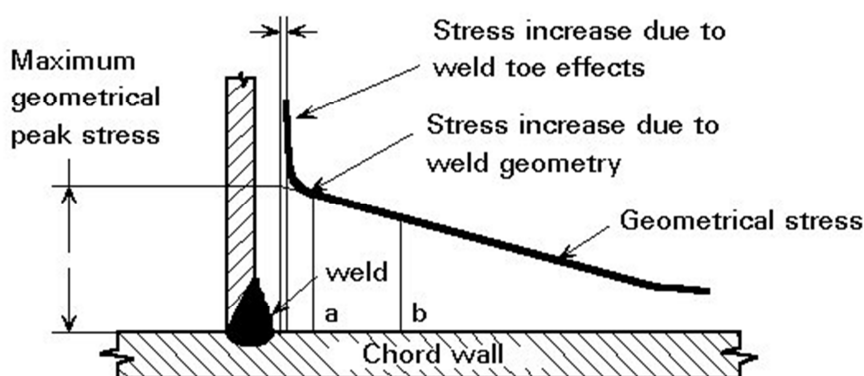


Figure 262. Structural stress at weld toe.

The structural hot spot stress approach is typically used where the structural discontinuity is not comparable to a classified structural detail or where no clearly defined nominal stress in complicated geometries is present. The structural hot-spot stress can be determined using reference points by extrapolation to the weld toe under consideration from stresses at reference points. The approach may be extended to assess potential fatigue crack initiation sites including the weld root. The S-N curves or the Stress Concentration Factors (SCF: the ratio of hot spot stress to local or modified nominal stress) used for verification in such cases depend on the geometric, dimensional parameters and are only valid in specified range. The Hot Spot Method may use specific S-N curves or standard Nominal stress curves. For the second option SCF correlates the nominal stress to structural stress (Equation (73)):

$$\sigma_{structural} = \sigma_{nominal} * SCF$$

(73)

In biaxial stress state at the plate surface (Figure 263), it is recommended to use the principal stress (Figure 264) that acts approximately in line with the perpendicular to the weld toe (within $\pm 60^\circ$). If necessary, the other principal stress may need to be analyzed using the welds parallel fatigue class in the nominal stress approach.

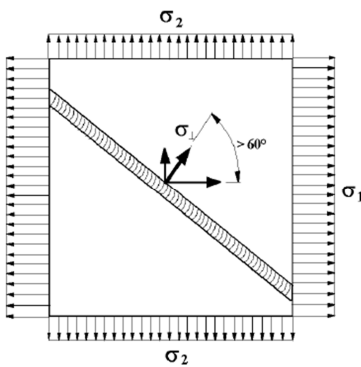


Figure 263. Stress discontinuities and stress orientation.

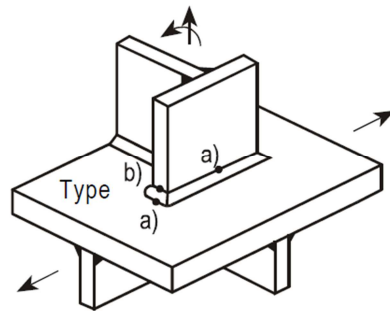


Figure 264. Hot spot types.

According to their location on the plate, their orientation in respect to the weld toe and their extrapolation direction two types of hot spots are defined. Hot spot *Type a* is located at the weld toe on plate surface moreover *Type b* near weld toe at plate edge. Measurement or calculation can determine the structural hot spot stress. The linearization of the stress through the plate thickness or stress extrapolation at the surface to the weld toe eliminate the non-linear peak stress. First operation is to establish the reference points and subsequently determine the structural hot spot stress by extrapolation to the weld toe from the stresses of those reference points. There are two or three reference points depending on the method used. Established the reference points, the non-linear peak stress is eliminated by linearization of the stress through the plate thickness. In a plate or shell element model 8-node elements (Figure 265) are recommended particularly in regions of steep stress gradients.

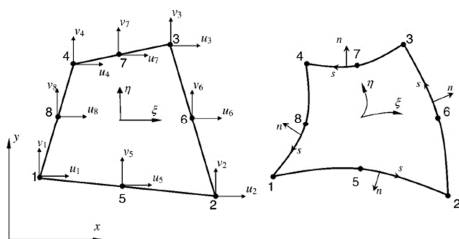


Figure 265. 8-nodes element.

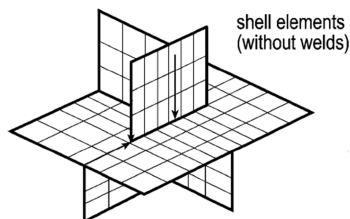


Figure 266. Component modelling.

In simplified models, the welds are not modeled (Figure 266), except for cases where the results are affected by local bending. In this case, the welds may be included by introducing constraint equations or rigid links or by vertical or inclined plate elements having appropriate stiffness. Thin-shell elements naturally provide a linear stress distribution through the shell thickness, suppressing the notch stress at weld toes. For “type a” (Figure 267) the structural hot spot stress σ_{hs} is determined using the reference points, referring to the plate thickness the extrapolation equations as given below:

1. fine mesh with element length not more than **0.4 t** at the hot spot: evaluation of nodal stresses at two reference points **0.4 t** and **1.0 t**, and linear extrapolation (Equation (74))

$$\sigma_{hs(a)} = 1,67\sigma_{0,4t} - 0,67\sigma_{1,0t} \quad (74)$$

2. fine mesh with element length not more than **0.4 t** at the hot spot: evaluation of nodal stresses at three reference points **0.4 t**, **0.9 t** and **1.4 t**, and quadratic extrapolation recommended for cases of pronounced non-linear structural stress increases towards the hot spot, at sharp changes of direction of the applied force or for thick walled structures (Equation (75)).

$$\sigma_{hs(a)} = 2,52\sigma_{0,4t} - 2,24\sigma_{0,9t} + 0,72\sigma_{1,4t} \quad (75)$$

3. coarse mesh with higher-order elements having lengths equal to plate thickness at the hot spot: Evaluation of stresses at mid-side points or

surface centers respectively, i.e. at two reference points $0.5 t$ and $1.5 t$, and linear extrapolation (Equation (76)):

$$\sigma_{hs(a)} = 1,50\sigma_{0,5t} - 0,50\sigma_{1,5t} \quad (76)$$

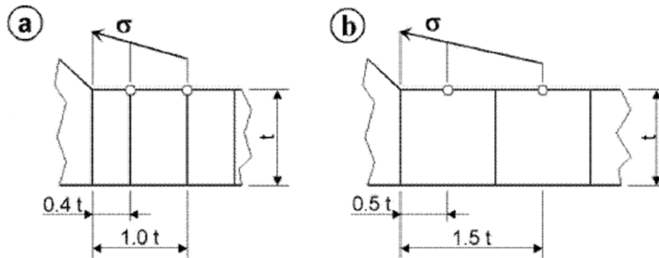


Figure 267. Type a. (a): relatively fine mesh; (b): relatively coarse mesh.

The influence of plate thickness on fatigue strength should be taken into account for weld toe. The fatigue resistance values refer to a wall thickness up to 25 mm. The lower fatigue strength for thicker members is taken into consideration by multiplying the FAT class of the structural detail by the thickness reduction factor $f(t)$ (Equation (77)):

$$f(t) = \left(\frac{25mm}{t_{eff}} \right)^n \quad (77)$$

For the determination of t_{eff} , the following cases have to be distinguished (Figure 268):

if $L/t > 2$ then $t_{eff} = t$

if $L/t \leq 2$ then $t_{eff} = 0.5 \cdot L$ or $t_{eff} = t$ whichever is the larger

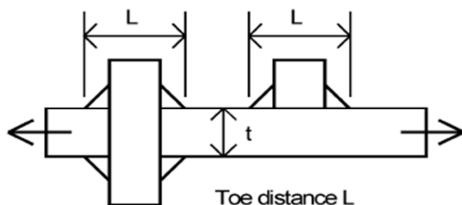


Figure 268. Toe distance.

The thickness correction exponent n is dependent on the effective thickness t_{eff} and the joint category (Figure 269):

Joint category	Condition	n
Cruciform joints, transverse T-joints, plates with transverse attachments, ends of longitudinal stiffeners	as-welded	0.3
Cruciform joints, transverse T-joints, plates with transverse attachments, Ends of longitudinal stiffeners	toe ground	0.2
Transverse butt welds	as-welded	0.2
Butt welds ground flush, base material, longitudinal welds or attachments to plate edges	any	0.1

Figure 269. Thickness correction exponents

Otherwise, for “type b” hot spot (Figure 270), the stress distribution is not dependent on plate thickness. Therefore, the reference points are given at absolute distances from the weld toe.

Fine mesh with element length of not more than 4 mm at the hot spot: evaluation of nodal stresses at three reference points 4 mm, 8 mm and 12 mm and quadratic extrapolation (Equation (78)).

$$\sigma_{hs(b)} = 3\sigma_{4\text{ mm}} - 3\sigma_{8\text{ mm}} + \sigma_{12\text{ mm}} \quad (78)$$

Coarse mesh with higher-order elements having length of 10 mm at the hot spot: evaluation of stresses at the mid-side points of the first two elements and linear extrapolation (Equation (79))

$$\sigma_{hs(b)} = 1,5\sigma_{5\text{ mm}} - 0,5\sigma_{15\text{ mm}} \quad (79)$$

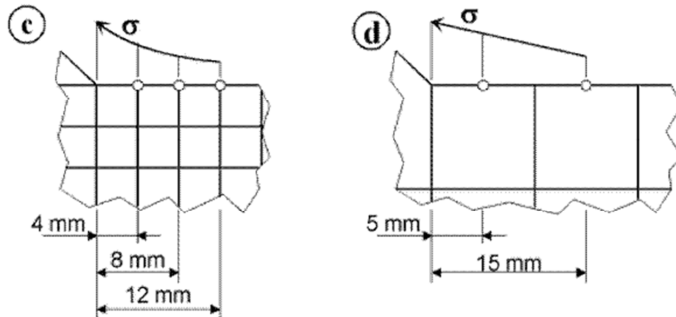


Figure 270. Type b. (c): relatively fine mesh; (d): relatively coarse mesh.

Type of model and weld toe	Relatively coarse model		Relative fine model	
	Type a	Type b	Type a	Type b
Shell size	t*t; max t*w/2	10*10 mm	≤0,4t*t or ≤0,4t*w/2	≤4*4 mm
Extrapolation points	0,5*t and 1,5*t mid-side points	5 and 15 mm mid-side points	0,4 and 1,0 t nodal points	4,8 and 12 mm nodal points

Table 42. Meshing extrapolation. "w" = longitudinal attachment thickness + 2 weld leg lengths; "mid-side points": surface centre at transverse welds, if the weld below the plate is not modelled.

9.1.2.1 Hot spot S-N curves

The S-N curves for assessing the fatigue resistance of a detail on the basis of structural hot spot stress are given in the table below (Figure 272). The resistance values consider:

- as-welded condition (unless stated otherwise);
- the effects of high tensile residual stress;
- only small effects of misalignment;
- design value of the structural hot spot stress range $\Delta\sigma_{hs}$ shall not exceed $2f_y$;
- fatigue resistance of a welded joint is limited by the fatigue resistance of the base material;
- the weld shape should be similar to the following (Figure 271 and Figure 272):

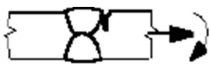
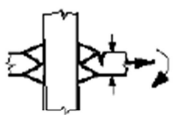
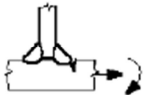
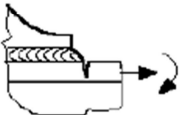

No	Structural detail	Description	Requirements	FAT Steel
1		Butt joint	As welded, NDT	100
2		Cruciform or T-joint with full penetration K-butt welds	K-butt welds, no lamellar tearing	100
3		Non load-carrying fillet welds	Transverse non-load carrying attachment, not thicker than main plate, as welded	100
4		Bracket ends, ends of longitudinal stiffeners	Fillet welds welded around or not, as welded	100
5		Cover plate ends and similar joints	As welded	100

Figure 271. Structural details.

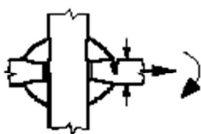



6		Cruciform joints with load-carrying fillet welds	Fillet welds, as welded	90
7		Lap joint with load carrying fillet welds	Fillet welds, as welded	90
8	$L \leq 100 \text{ mm}$ 	Type "b" joint with short attachment	Fillet or full penetration weld, as welded	100
9	$L \geq 100 \text{ mm}$ 	Type "b" joint with long attachment	Fillet or full penetration weld, as welded	90

Figure 272 Structural details.

Fatigue data from other sources that refer to a comparable detail, may be used. The reference detail should be chosen as similar as possible to the detail assessed. The procedure starts by selecting a reference detail with known fatigue resistance, which is as similar as possible to the detail being assessed with respect to geometric and loading parameters. Subsequently identify the type of stress (usually nominal stress) in which the fatigue resistance is expressed and establish a FEM model of the reference detail and the detail to be assessed with the same type of meshing and elements following the recommendations. After this, load the reference detail and the detail to be assessed with the stress identified above. Then determine the structural hot spot stress $\sigma_{hs,ref}$ of the reference detail and the structural hot spot stress $\sigma_{hs,assess}$ of the detail to be assessed. In conclusion, the fatigue resistance for 2E6 cycles of the detail to be assessed FAT_{assess} is then calculated from fatigue class of the reference detail FAT_{ref} using (Equation (80)):

$$FAT_{assess} = \frac{\sigma_{hs,ref}}{\sigma_{hs,assess}} FAT_{ref} \quad (80)$$

9.1.2.2 Strain gauge position

The classified structural details and their fatigue resistance S-N curves are based on Nominal Stress. The stress concentrations due to the welded joint are therefore ignored. Consequently, the sensors must exclude the stress or strain concentration field due to the corresponding discontinuity in the welded structural component (Figure 273). It may be necessary first to evaluate the extent and the stress gradient of the field of stress concentration due to the welded joint. After this, simple strain gauge application outside this field is sufficient. The recommended number and placement of strain gauges depends on the extent of plate bending stresses, the type of structural stress and the wall thickness. The center point of the first gauge, whose gauge length should not exceed $0.2 t$, is located at a distance of $0.4 t$ from the weld toe. If this is not possible for a small plate thickness, the leading edge of the gauge should be placed at a distance of $0.3 t$ from the weld toe. For *type "a"* hot spots the following extrapolation procedures are recommended:

4. Two gauges at reference points **0.4 t** and **1.0 t** and linear extrapolation (Equation (81)):

$$\varepsilon_{hs(a)} = 1,67\varepsilon_{0,4 t} - 0,67\varepsilon_{1,0 t} \quad (81)$$

5. Three gauges at reference points **0.4 t**, **0.9 t** and **1.4 t**, and quadratic extrapolation (pronounced non-linear structural stress increase towards the hot spot) (Equation (82)):

$$\varepsilon_{hs(a)} = 2,52\varepsilon_{0,4 t} - 2,24\varepsilon_{0,9 t} + 0,72\varepsilon_{1,4 t} \quad (82)$$

6. For *"b"* type three gauges are attached to the plate edge at reference points 4, 8 and 12 mm distant from the weld toe (Equation (83)):

$$\varepsilon_{hs(b)} = 3\varepsilon_{4 mm} - 3\varepsilon_{8 mm} + \varepsilon_{12 mm} \quad (83)$$

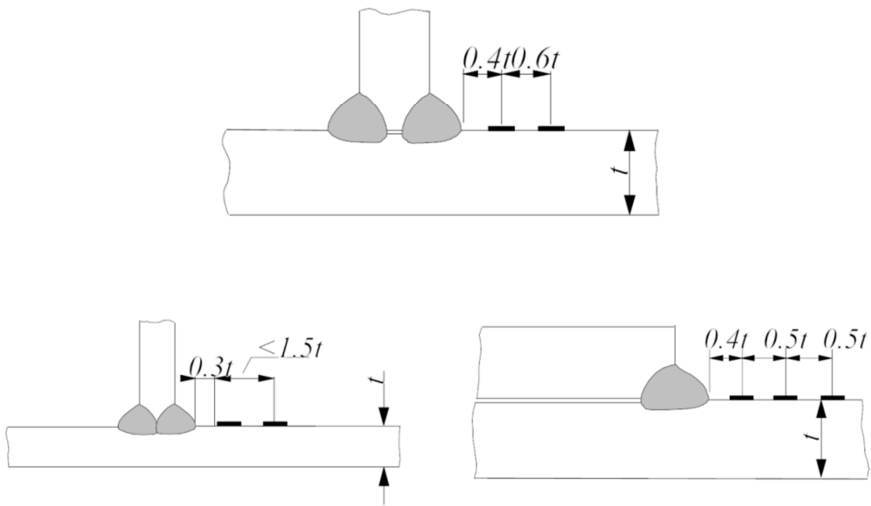


Figure 273. Example of strain gauges.

If the stress state is close to uniaxial, the approximation to the structural hot spot stress is (Equation (84)):

$$\sigma_{hs} = E \varepsilon_{hs} \quad (84)$$

For biaxial stress states, the use of rosette strain gauges is recommended. If the ratio of longitudinal to transversal strains is available (FEM) the structural hot spot stress, assuming the principal stress approximately perpendicular to the weld toe, can be resolved from (Equation (85)):

$$\sigma_{hs} = E \varepsilon_x \frac{1 + \nu \varepsilon_y / \varepsilon_x}{1 - \nu^2} \quad (85)$$

9.1.2.3 Stress determination

The notch stress distribution over the plate thickness (Figure 274) is non-linear and three stresses component must be considered. The stress components can be separated analytically for a given through thickness stress distribution $\sigma(x)$ from $x=0$ at the surface to $x=t$ at the edge.

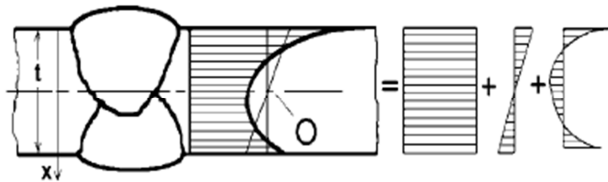


Figure 274. Non-linear stress distribution.

The stress components of the notch stress (σ_{ns}) are divided (Equation (86)) into membrane stress (σ_m), shell bending stress(σ_b) and non-linear stress peak (σ_{nl}). The constant membrane stress σ_m (Equation (87)) is equal to the average stress calculated through the thickness of the plate. The shell bending stress σ_b (Equation (88)) is linearly distributed, pass through the membrane mid plane and the gradient is chosen so that that the remaining non-linearly distributed component can reach a state of equilibrium. The non-linear stress peak σ_{nlis} (Equation (89)) is:

$$\sigma_{ns} = \sigma_m + \sigma_b + \sigma_{nl} \quad (86)$$

$$\sigma_m = 1/t \int_{x=0}^{x=t} \sigma(x) dx \quad (87)$$

$$\sigma_b = 6/t^2 \int_{x=0}^{x=t} [\sigma(x) - \sigma_m] [t/2 - x] dx \quad (88)$$

$$\sigma_{nl}(x) = \sigma(x) - \sigma_m - (1 - 2x/t)\sigma_b \quad (89)$$

9.2 Laboratory equipment

A specific steel frame (Figure 275) has been designed and realized in order to test San Stino's elements. A specific steel equipment is necessary for carrying out fatigue tests. As seen in §6.1 the cross girder bridge is 1600 mm high. Besides the usual structural and buckling analysis a detailed fatigue design has been executed due to the high number of cycles that the frame will endure. The goal was to design a fatigue resistant frame (or up to 10^7 cycles with maximum force applicable) conveniently designed for repeated loads. The frame must be more rigid than the transversal bridge girders and able to limit the relative displacement up to about 1/10 mm. The concept has been turned into a four anchored columns frame with a steel plate supporting the oil-dynamic actuator.

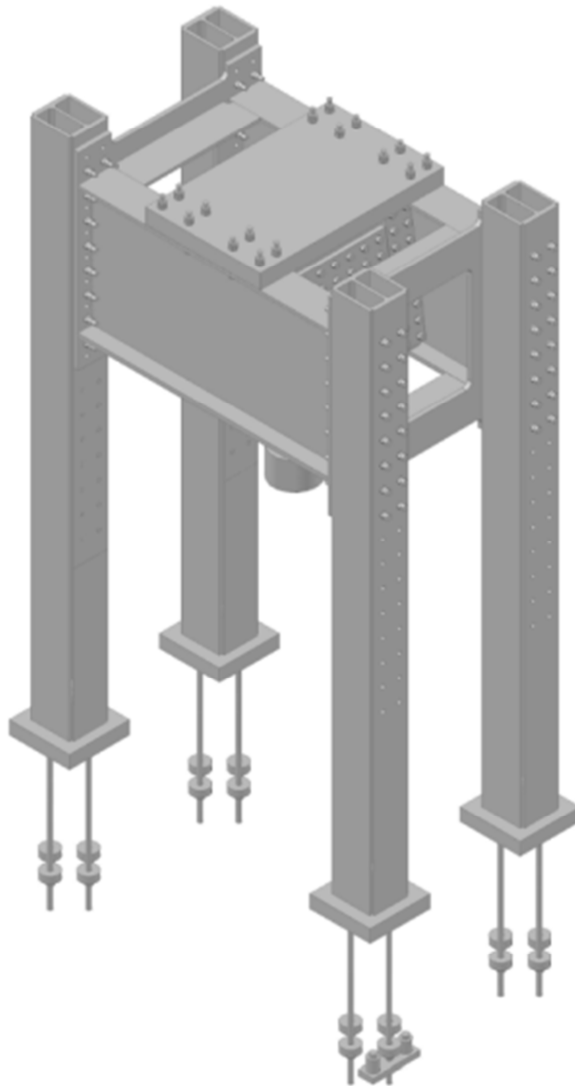
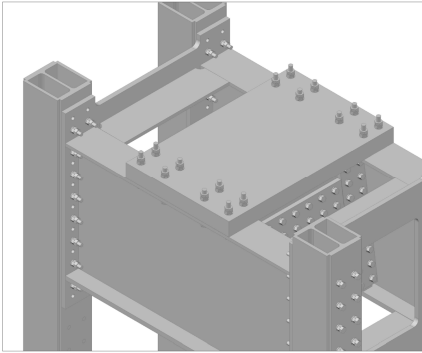


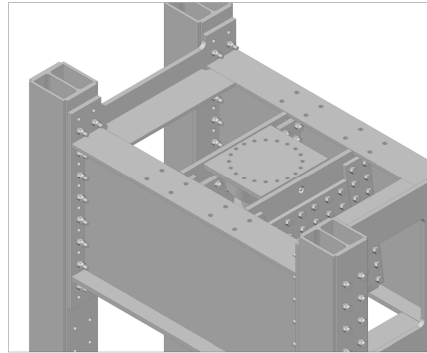
Figure 275. Steel frame.

The frame weight is about 160 kN moreover the Moog actuator is able to perform 1500 kN force. Four column 5 m high realized with HEM 360 and reinforced by 25 mm thickness plates compose the structure. This kind of solution allow an optimization for buckling problems and axial rigidity. The frame is supported by a strong concrete floor 1 m thick. The columns are connected to the floor with preloaded bars with the intention of performing force positive and negative tests. HEM 360 profiles are connected together by two short beams about 1200 mm high.

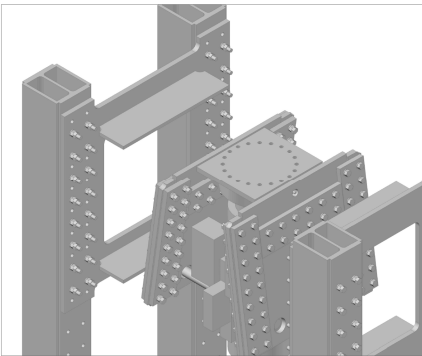
A thick steel plate 140 mm thick and reinforced by 40 mm thick plates supports the actuator. All the connections are realized using pre-stressed bolts with the purpose of avoid any type of stress concentrations. The welds are mostly V-groove type and well tapered. Moreover, Moog actuator needs an adjustable frame in order to work with different specimen heights: the columns and the box have dedicated holes. The structure is very sophisticated and a high accuracy 3D model has been realized. In the sequence below (Figure 277), some layer has been removed with the intention of showing the internal components. In 1 the entire structure is shown, in 2 the rectangular plates have been hidden; in 3 the deep beam has been hidden and in 4 the bolted joint has been hidden. Number 5 shows the actuator located in the middle of the steel box. Number 6 and 7 show the high precision assembly and the particular focus dedicated to the servo - valve and for the (electric, oil and data) cables. Finally, Number 8, discloses the assembly perfectly succeeded.



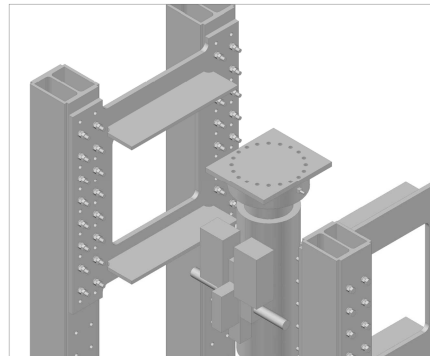
1. Entire structure.



2. Contrast plate hidden.

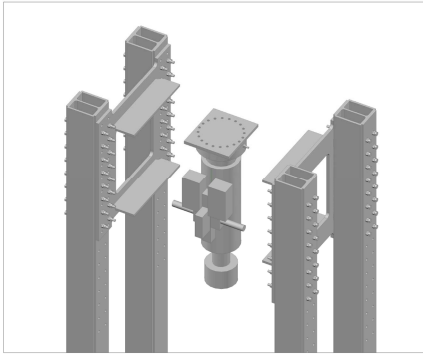


3. Deep beams hidden.

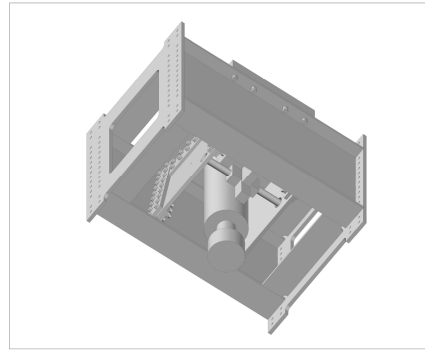


4. Joints hidden.

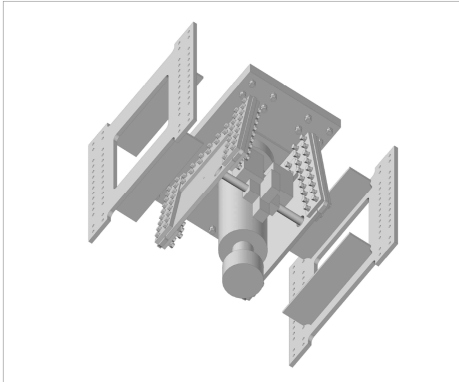
Figure 276. High precision 3D model: 1-4. 3D design.



5. Columns and actuator.



6. Box.



7. Plates and actuator.



8. Oil and data cables.

Figure 277. High precision 3D model: 5-7. 3D design, 8. Calibrated assembly.

9.2.1 Servo actuator

The hydraulic actuator consists of a cylinder that uses oil for moving specimen. Pressure is applied on each side of the piston; the actuator is double acting. Any difference in pressure between the two sides of the piston moves the piston to one side or the other. The actuator is produced by Moog and the maximum force applicable is ± 1500 kN at 0,5 Hz. See Table 43 for more details:

Stroke	240	mm
Stroke (effective)	200	mm
ϕ cylinder	340	mm
ϕ rod	210	Mm
Test pressure	420	bar
Mass	4200	kg
Load cell	1500	kN
Max speed	80	mm/s
Max frequency	10	Hz

Table 43

The length varies from 3000 mm (closed) up to 3240 mm (open). The system is composed by:

- actuator (Figure 278, Figure 279 and Figure 282),
- servo valve,
- position transducer SSI Temposonic,
- accumulator 2x5 l up to 190 bar,
- load cell up to 1500kN.

The hydraulic system has:

- 400+60 l/min at 280 bar flow,
- manifold 1x400l/min - 2x200 l/min (Figure 280),
- bench accumulator 8x50 liters.

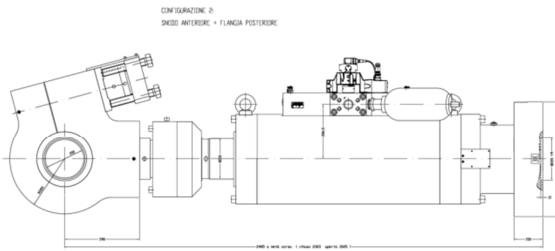


Figure 278. Lateral view.

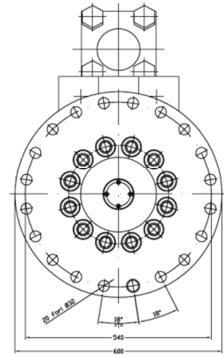


Figure 279. Front view.

A ball joint connects the control arms to the specimen connector and it is essential to compensate the misalignments. A specific electrohydraulic servo valve controls oil. The entire system is software controlled (Figure 281).



Figure 280. Manifold.



Figure 281. Test controller.

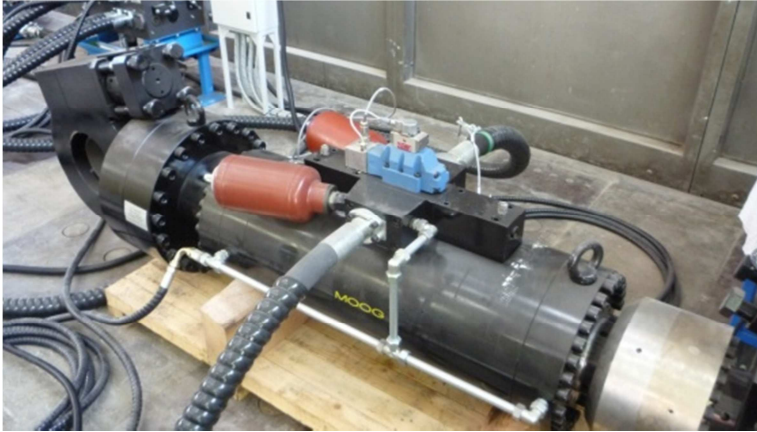


Figure 282. Servo actuator.

The equipment provides a very large possibility for fatigue testing due to high force applicable, for positive and negative specimen deflection and for the high frequency value.

9.2.2 Design

Following the recommendations described in [38] and [39], the frame has been designed introducing the mass, the actuator mass and the actuator active force. The frame complexity induces to model only a fourth part of the structure (Figure 283) due to the double geometric and load symmetry. Non - Liner FEM software has been used [29].

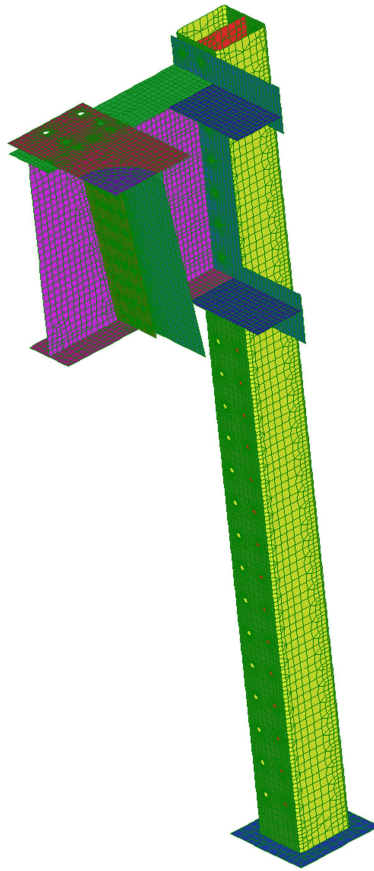
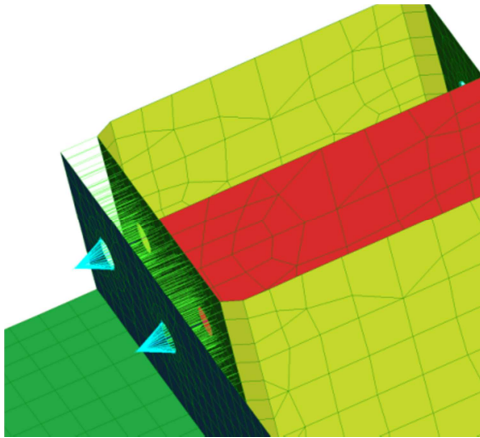


Figure 283. 1/4 Fem model.

The friction is essential to avoid stress concentration on the holes perimeter. Fem simulation is possible using "point contact" elements that introduces a nonlinear solution. The normal contact element is capable of generating a compressive axial force within itself, but not a tension. It can also generate a lateral friction force when it is in compression. An "only compression" element has been introduced with initial rigidity and a friction coefficient both vertical and horizontal direction (Figure 284).



Type	Normal
Stiffness (N/mm)	10^6
Friction (x)	0,45
Friction (y)	0,45

Figure 284. Point contact.

Sandblasting has been expected in contact surfaces moreover the friction coefficient established will be reached easily. The structure is realized in S355J2 with the following characteristics (Table 44, see [40]), :

Thickness (mm)	<3	<150
F_{yield} (fyk) [MPa]	355	295
$F_{ultimate}$ [MPa]	510	450
Kv (-20°) [J]	27	27

Table 44

This steel has been chosen for its fatigue behaviour. The bolts are pre stressed in 10.9 class (Table 45) moreover, the threaded bars are in S355J2.

$R_{traction}$ (MPa)	1000
HV (Vickers)	320
R_{yield} (MPa)	900
KU (J)	20

Table 45

For more detail about geometry and components used, see §11 and [41].



Figure 285. Profiles manufacturing.

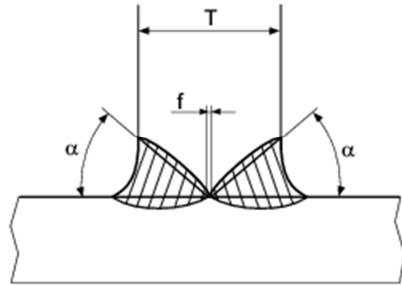
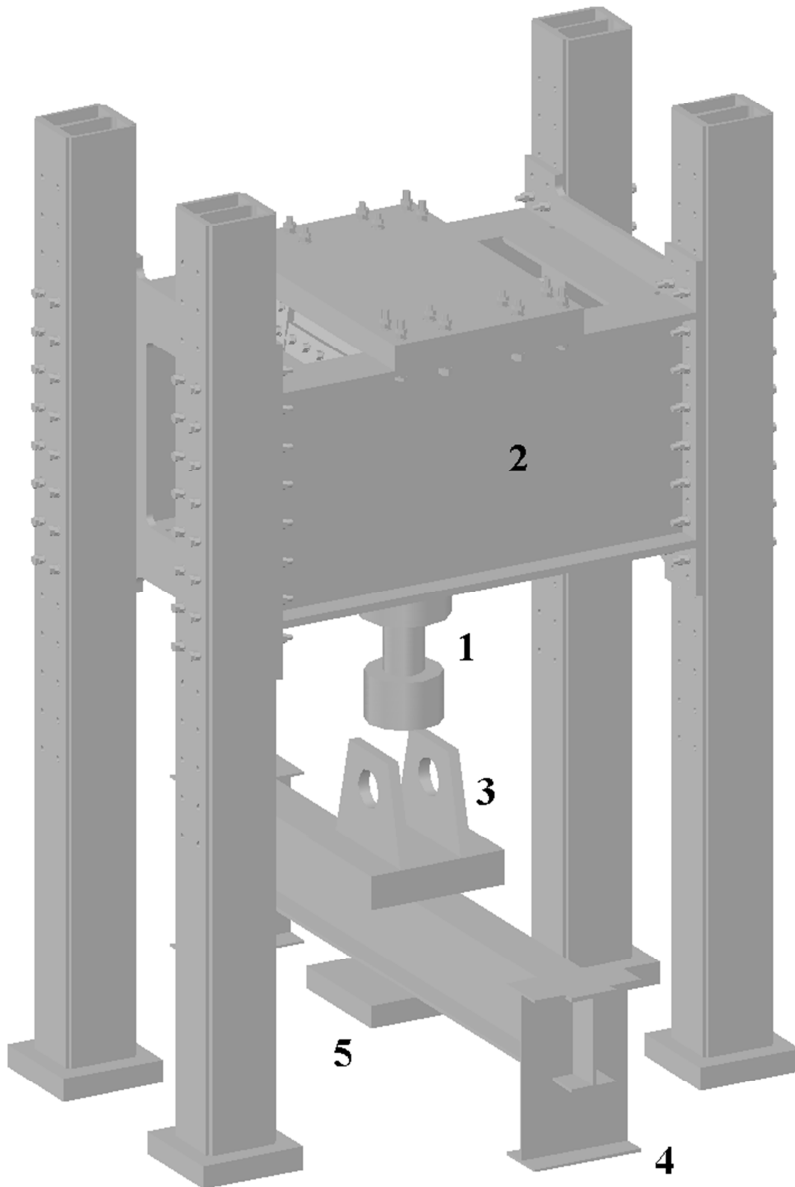


Figure 286. Full penetration weld.

Full penetration welds have been adopted with the intention of avoiding stress concentration and enhance fatigue life. The welds have 30° bevel angle and this kind of weld allows the structural continuity (Figure 285 and Figure 286).

9.2.2.1 Tests set up

The frame has been designed with the intention of realize tensile and compressive fatigue tests. Figure 287 shown the frame, the rail bearer and the connection elements. The frame contrasts the force introduced by the actuator, the connection element end the fastening element connect the structure to the rail bearer. Other setups with different specimen are available setting the steel box.



*Figure 287. Rail bearer test. 1: Actuator 2. Frame
3. Connection element 4. Rail bearer 5. Fastening element.*

9.2.3 Analysis

9.2.3.1 Global behavior

The maximum displacement occurs in the central plate directly linked to the actuator (Figure 288). At the maximum force applied (1500 kN) the displacement is about 0,44 mm (Figure 289). The HEM 360 profile has been used adding plates in order to create a rigid box beam. The tensions are very low according to the fatigue design. The bolt preload generates the highest stress concentration in the frame: more than 30 MPa (Figure 290).

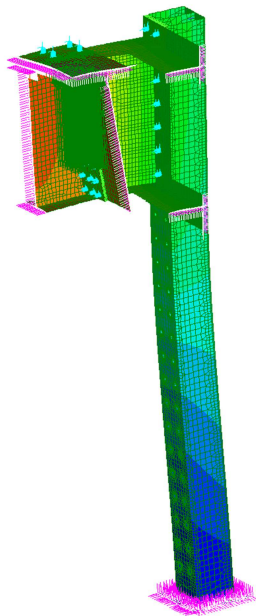


Figure 288. Plate displacement (DZ).

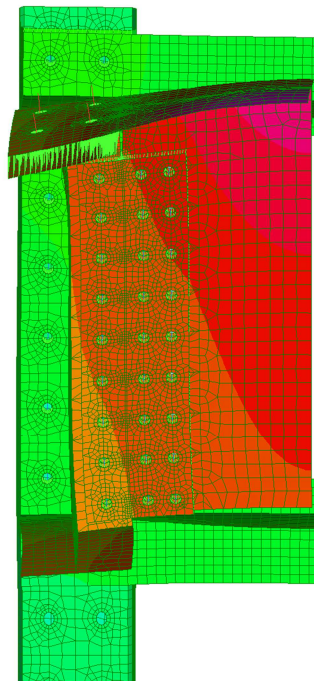


Figure 289. Maximum displacement: 0,44 mm (displacement scale increased).

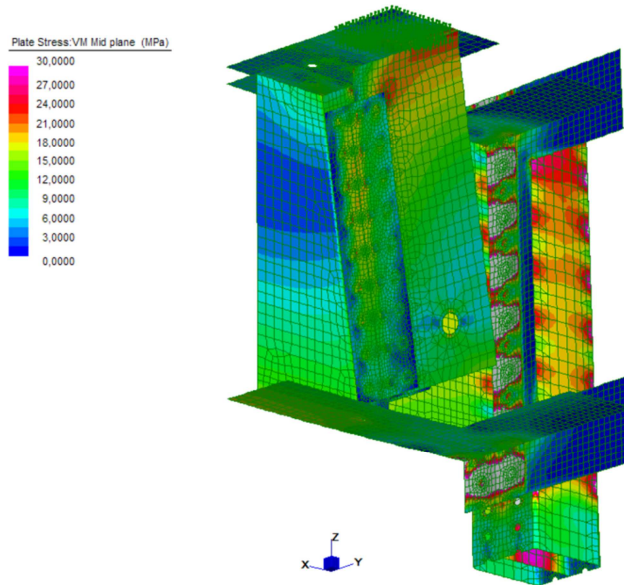


Figure 290. Plate stress.

The buckling force (Euler theory) for the entire structure is about 236000 kN. No buckling problems are present. With the intention of avoiding the resonance effect the frame frequency is about 116 Hz: more than 10 times of the actuator maximum frequency (10 Hz).

9.2.3.2 Columns

In the following, the columns design is presented. The HEM 360 profile (Figure 291) is in Class 1 (Figure 293, see [39]) and it is 5000 mm high. The additional plates, merged with round edge to allow weld operations, guarantee more stability. A sandblasting treatment has been carried out in order to achieve the requested friction coefficient (Figure 292).

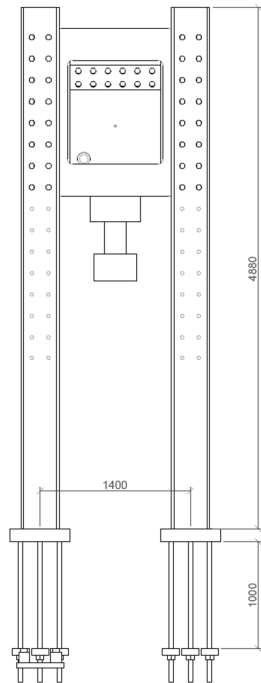


Figure 291. Columns.



Figure 292. Sandblasting.

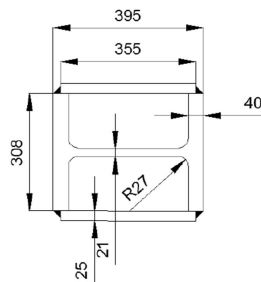


Figure 293. HEM360M + gusset plates.

No safety factor has been introduced in load combination because any uncertainties are present. With the purpose of taking in consideration some assembly imperfections, 15 kN of horizontal force has been introduced. Following the indication of [39] the maximum Von Mises tension is (Equation (90)):

$$\sigma_{max} \cong 18 \text{ MPa} < \frac{f_{yk}}{\gamma_{M0}} = 338 \text{ MPa} \quad (90)$$

The verification is (§4 [39], Equation (91)):

$$\frac{S_{Ed}}{S_{Rd}} \leq 1 \quad (91)$$

where S_{Ed} is the stress and S_{Rd} is the strength. Equation ((91)) gives:

$$SR = \text{active/resistant} = 5\% \quad (92)$$

where γ_{M0} is the safety factor and SR (Equation (92)) is the safety ratio. The buckling is verified with safety ratio of 7% (see [39]). Fatigue verification is (§C4.2.4.1.4.6.1 [39]) (Equation (93)):

$$\Delta\sigma_{max} \leq \Delta\sigma_D \quad (93)$$

where the first term is the stress and the second term is the fatigue resistance. Fatigue assessment refer to the following fatigue categories (see [5]):

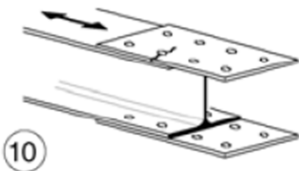
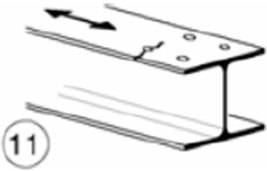

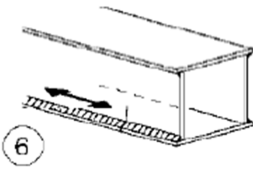
Detail class ($\Delta\sigma_c$)	Details
90	
	
100	
	

Table 46

The fatigue verification for weld (detail 6) gives (Equation (94))

$$\Delta\sigma_{sd} \cong 21 \text{ MPa} \leq \frac{\Delta\sigma_D}{\gamma_{Mf}} \rightarrow SR = 42\% \quad (94)$$

where SR is the safety ratio, $\Delta\sigma_D$ is the design stress and γ_{Mf} is the safety factor.

The fatigue verification for the entire section (detail 11) gives (Equation (95)):

$$\Delta\sigma_{sd} \cong 21 \text{ MPa} \leq \frac{\Delta\sigma_D}{\gamma_{Mf}} \rightarrow SR = 38\% \quad (95)$$

where SR is the safety ratio, $\Delta\sigma_D$ is the design stress and γ_{Mf} is the safety factor. The columns have a low stress range and consequently the fatigue verifications are fully accepted.

9.2.3.3 Deep beam and gusset plates

In the following, the deep beam and gusset plates design is presented. Girders (Figure 294) are 2400 mm length and 1235 mm high (Figure 295) and do not respect de Saint Venant theory (Figure 296).

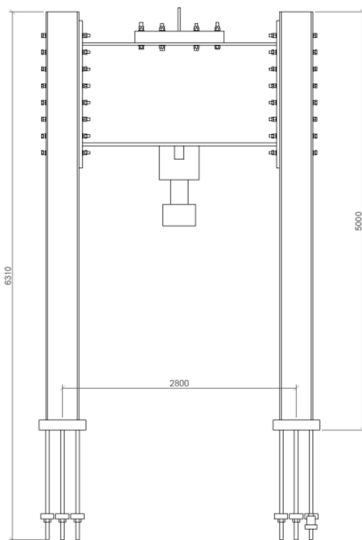


Figure 294. Deep beam (design).

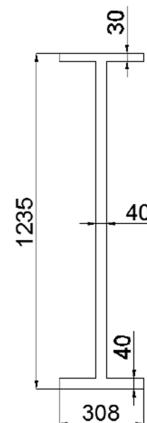


Figure 295. Section.



Figure 296. Deep beam.

The beam theory stress gives about 38 MPa at the middle of the beam. No instability problem has been observed. For welds fatigue verifications the following details has been used (Table 47):

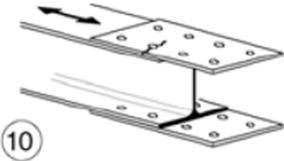
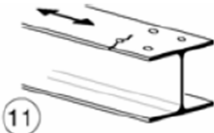
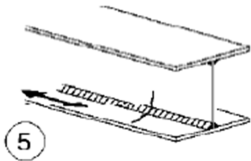
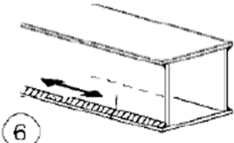
Detail class ($\Delta\sigma_c$)	Details
90	
	
100	
	

Table 47

For the intersection between flange and web the fatigue verification gives (Equation (96)):

$$SR = 68\% \tag{96}$$

and verification is satisfied. For the upper flange the fatigue verification gives (Equation (97)):

SR = 96%

(97)

Due to the elements complexity and for the Nominal Stress Method restrictions, some advanced verifications have been carried out. For the weld joints the following details have been used (Table 48):


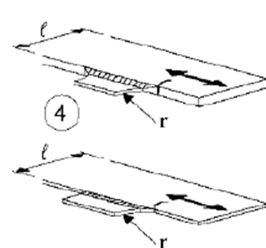
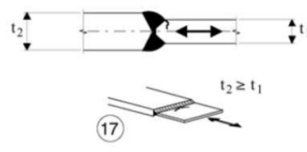
Detail class ($\Delta\sigma_c$)	Details
40	
90 (a) 71 (b) 50 (c)	
71	

Table 48

Referring to the gusset plate (1092 mm length, 300 mm wide and 30 or 40 mm thick) the following fatigue verifications have been carried out. Transversal and longitudinal stress direction have been considered. The welds stress (detail 5) is about 3 MPa moreover the verification is satisfied with (Equation (98)):

$$SR = 8\% \tag{98}$$

and verification is satisfied. For detail 17 (Equation (98)):

$$SR = 10\% \tag{99}$$

and verification is satisfied. Figure 297 show the Fem model adopted.

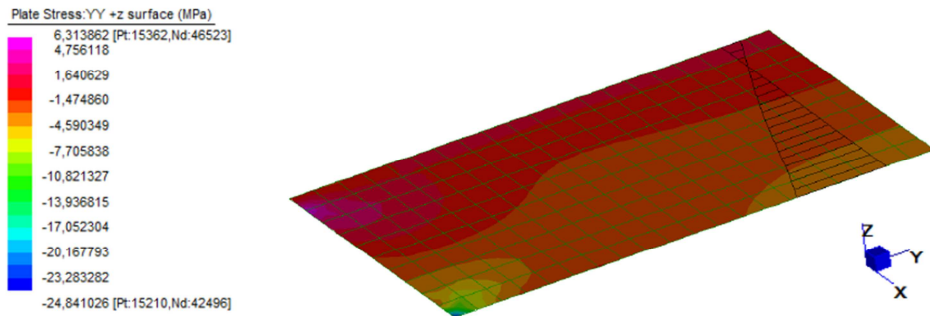


Figure 297. Fem model.

A specific radius of curvature has been designed with the intention of avoiding the stress concentration in the plate corner (Figure 298).



Figure 298. Removed corner.

9.2.3.4 Opposed plate and gusset plates

The actuator is restrained by 20 $\phi 32$ bolts connected to 140 mm thick plate. The horizontal plate has two gusset plates 40 mm thick in order to stiffen the structure and involve the deep beams into the global resistance (Figure 301).

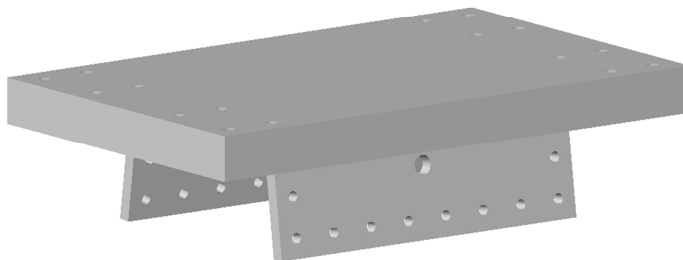


Figure 299. Opposed plate and gusset plates.

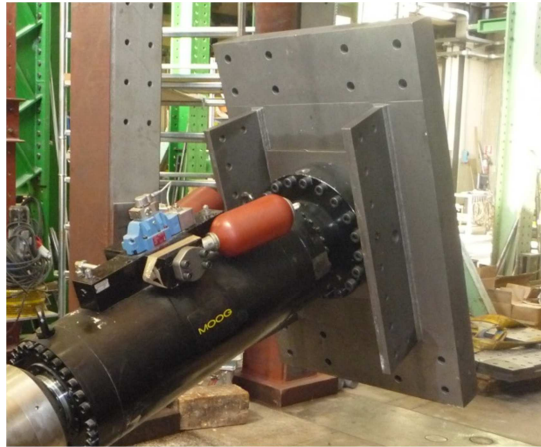


Figure 300. Opposed plate during assembly phases.

In this particular element, the fatigue verifications, cannot be conducted following the [5]. No details satisfy the geometric and stress requirement provided by the Nominal Stress approach. Starting from steel base resistance and introducing the correction factors, the fatigue resistance has been evaluated. For more details see [42]. The threshold stress is (Equation (100)):

$$\sigma_{a,\infty}^* = \frac{0,5 * \sigma_{ultimate}}{k_d k_f k_t k_v} \cong 26MPa \quad (100)$$

where k_d is the coefficient that synthesizes the effect of element dimension ($k_d=1,39$), k_l is the coefficient that synthesizes the superficial treatments ($k_l=1,4$), k_f is the coefficient that synthesizes the shape ($k_f=4,99$) and k_t is given by Peterson [42]. The element is subjected to about 23,5 MPa stress. The fatigue verification gives (Equation (101)):

$$SR = 90\% \quad (101)$$

Due to the high stress level, a 40 mm thick transition plate has been introduced. The additional plate smooths the stress and enhances the fatigue behavior. After the plate introduction the stress is about 15,5 MPa and SR is equal to 60%. The Nominal Stress Method has been used to check the gusset plates. Both cases in

which opposed plates or gusset plates are the main element has been considered. Moreover, both welds direction (x and y) have been taken into account. Table 49 show the fatigue detail category.

Detail class ($\Delta\sigma_c$)	Details
56 (d)	
125	

Table 49

Figure 302 shows the fem model. For (1-d) detail the verification gives (Equation (102)):

$$SR = 12\% \tag{ 102 }$$

For (1) detail the verification gives (Equation (103)):

$$SR = 33\% \tag{ 103 }$$



Figure 301. Bolted joints during the assembly phases.

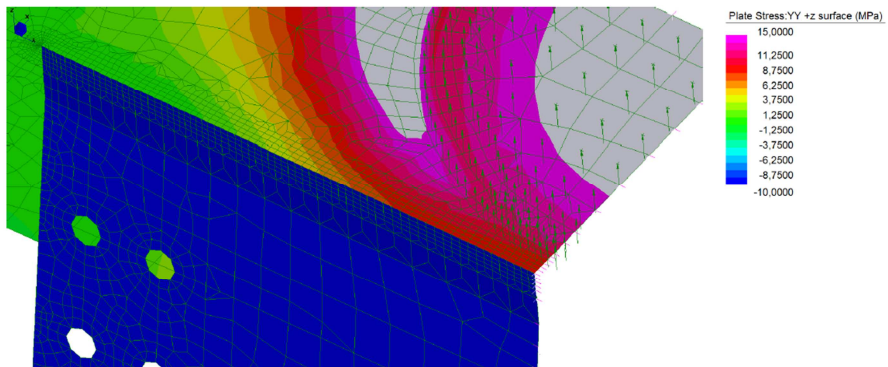


Figure 302. Fem model, y direction.

The fatigue verifications are largely satisfied. Considering the x direction, Table 50, show the fatigue class details.

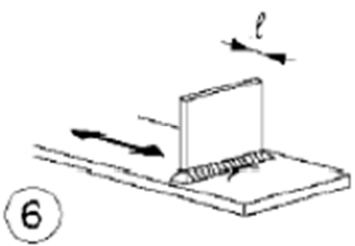
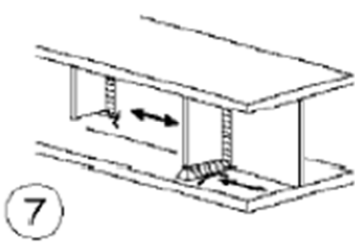
Detail class ($\Delta\sigma_c$)	Details
80 (a)	
80 (a)	

Table 50

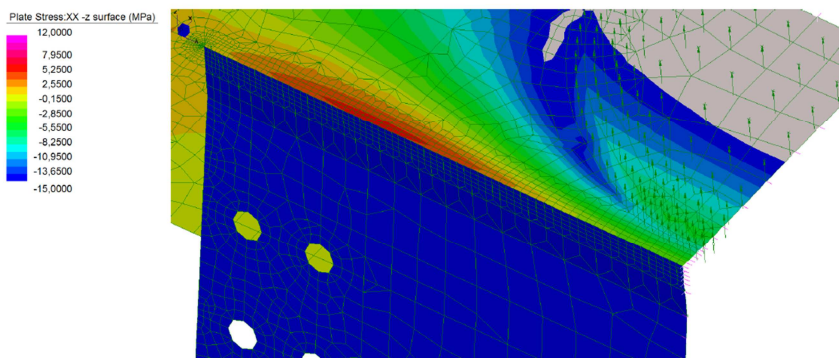


Figure 303. Fem model, x direction.

Figure 303 shows the fem model. For (6-a) detail the verification gives (Equation (104)):

$$SR = 16\% \tag{104}$$

For (7-a) detail the verification gives (Equation (105)):

$$SR = 13\% \tag{105}$$

Considering the gusset plates as the fundamental elements, the verifications are synthesized below. Considering the z direction, Table 51, shows the fatigue class details.

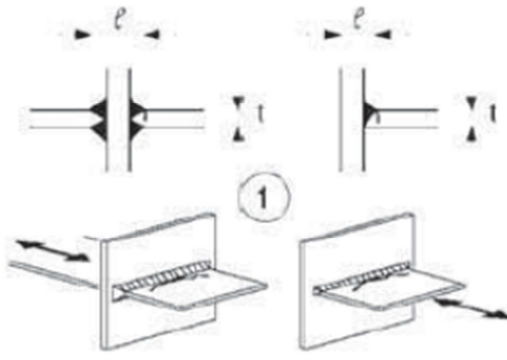

Detail class ($\Delta\sigma_c$)	Details
50 (e)	
50 (e)	

Table 51

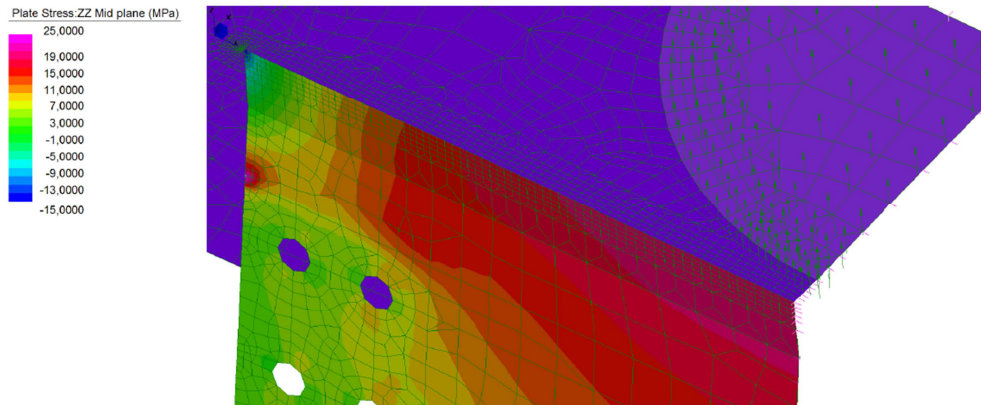


Figure 304. Fem model, z direction.

Figure 304 shows the fem model. For (1-e) detail the verification gives (Equation (106)):

$$SR = 96\% \quad (106)$$

For (2-e) detail the verification gives (Equation (107)):

$$SR = 88\% \quad (107)$$

using safety coefficient 1,15 instead of 1,35 (see [39]). The verifications are satisfied. In the follow, an advanced *Hot Spot analysis* has been carried out. The following procedure has been adopted:

- selection of Hot Spot detail (considering geometry and load type);
- selection of *type a* or *type b* Hot Spot due to the Fem modeling;
- calculation of Hot Spot stress $\Delta\sigma_{hs}$;
- evaluation of: $\Delta\sigma_{hs} < \Delta\sigma_c * 0,737 / \gamma_{Mf}$.

Following the recommendation of [37], the fatigue Hot spot stress design value is $\Delta\sigma_{hs} < 2 * f_y$. Moreover, the recommended category for this detail is FAT100 (Figure 305).

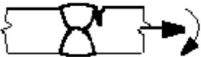
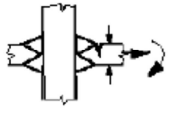
No	Structural detail	Description	Requirements	FAT Steel
1		Butt joint	As welded, NDT	100
2		Cruciform or T-joint with full penetration K-butt welds	K-butt welds, no lamellar tearing	100

Figure 305. Hot Spot detail.

Type a Hot Spot stress (σ_y) is measured along the gusset plate projection on the opposite plate (Figure 306 and Figure 307). It is noted that the stress gradient compromise the Hot Spot method reliability. For more detail about design of this element and for other specifications see [43].

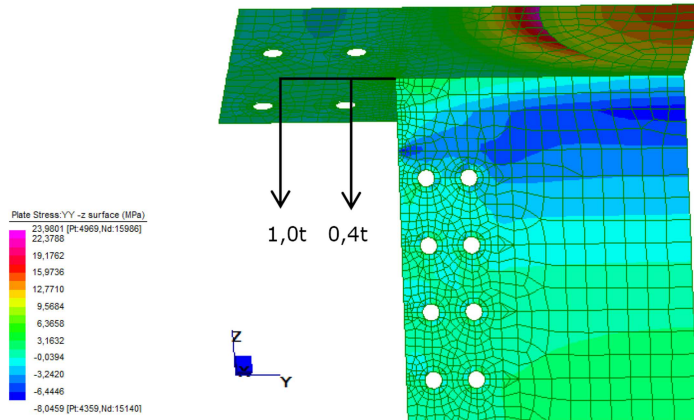


Figure 306. Type a Hot Spot.

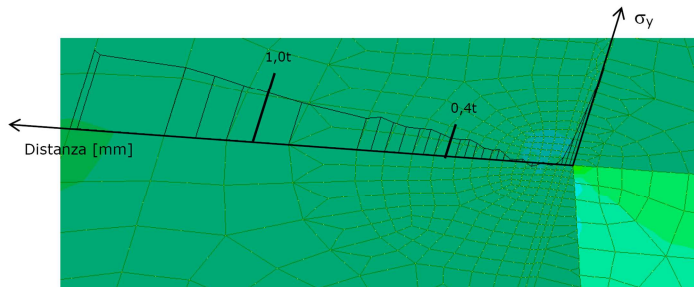


Figure 307. Detail: type a Hot Spot.

Type b Hot Spot stress (σ_z) is measured along the gusset plate edge. Figure 308 and Figure 309 show the Fem simulation:

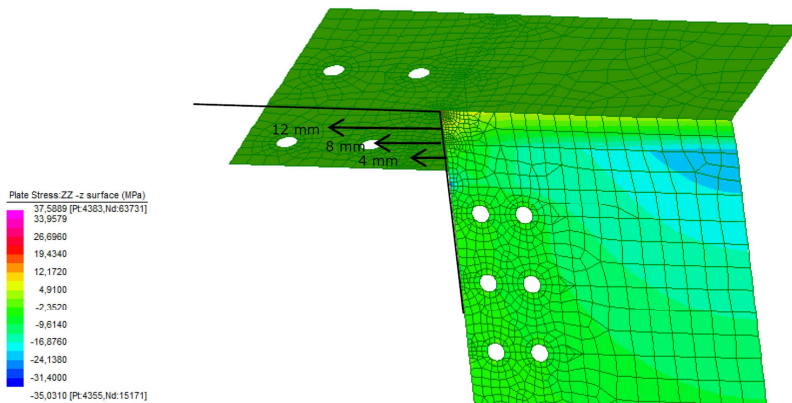


Figure 308. Type b Hot Spot.

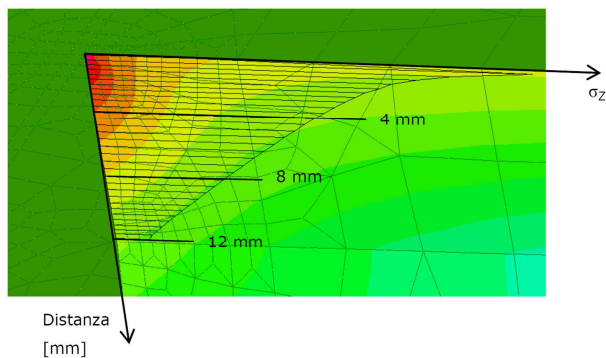


Figure 309 Detail: type b Hot Spot.

The Hot Spot interpolation is (Equation (108)):

$$\sigma_{hs} = 3 * \sigma_{4mm} - 3 * \sigma_{8mm} + \sigma_{12mm} = 3 * 16,4 - 3 * 9,3 + 5,21 = 26,51 \text{ MPa} \quad (108)$$

The stress range and the verification is (Equation (109)):

$$\Delta\sigma_{hs} = 2 * \sigma_{hs} = 53MPa < 100MPa/\gamma_{Mf} = 73MPa \quad (109)$$

9.2.3.5 Bolted joint

Figure 310 shows the bolted joint (Figure 312). These plates connect the opponent plate, the gusset plates and the deep beams. M30 10,9 pre-stressed bolts have been used. The static and the fatigue verification taking into account shear forces (V_{Ed}), pre-loaded forces, tensile forces ($P_{t,Ed}$) and frictions have been carried out (Figure 311).

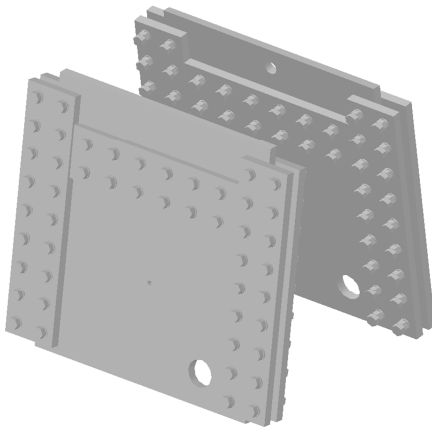


Figure 310. Bolted joint (design).

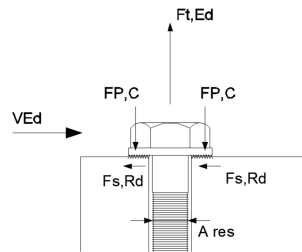


Figure 311. Bolt forces.



Figure 312. Bolted joint.

The fatigue class is FAT50 and the detail is number 14 ([39]), see Table 52.

Detail class ($\Delta\sigma_c$)	Details
50	A technical drawing showing two cross-sectional views of a bolted joint. The left view shows a bolt with a nut and a washer, with a vertical double-headed arrow indicating stress concentration at the top of the bolt. The right view shows a similar joint with a vertical double-headed arrow indicating stress concentration at the bottom of the bolt. A circled number '14' is placed between the two views.

Table 52

The fem analysis is shown in Figure 313. The bolts have been pre-stressed with about 2 kN*m torque. This moment guarantees an adequate joint friction behavior and the stress inside each bolt is about 500 MPa.

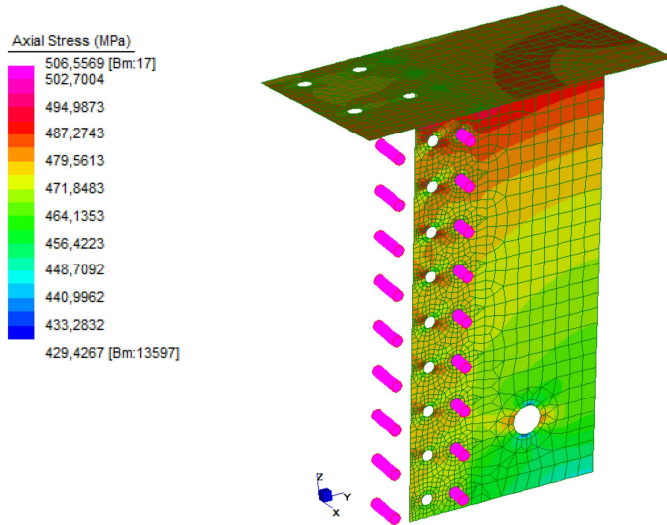


Figure 313. Fem simulation.

The fatigue shear behavior is referred to FAT100 class and the detail is number 15. Table 53 shows the fatigue detail.

Detail class ($\Delta\sigma_c$)	Details
100	

Table 53

The fatigue verification, considering $\Delta\tau_{sd} = 30MPa$, gives (Equation (110));

$$SR = 86\% \quad (110)$$

The verification is satisfied.

9.2.3.6 Columns/deep beam joint

Figure 315 shows the bolted joint. These plates connect the columns with the deep beams. $\phi 30$ pre-stressed bars have been used (Figure 316). The static and the fatigue verification taking into account shear forces, pre-loaded forces, tensile forces and frictions have been carried out. The fem analysis is shown in Figure 314. The bolts have been pre-stressed with about 2 kN*m torque. This moment guarantees an adequate joint friction behavior, moreover, the stress inside each bolt is about 440 MPa.

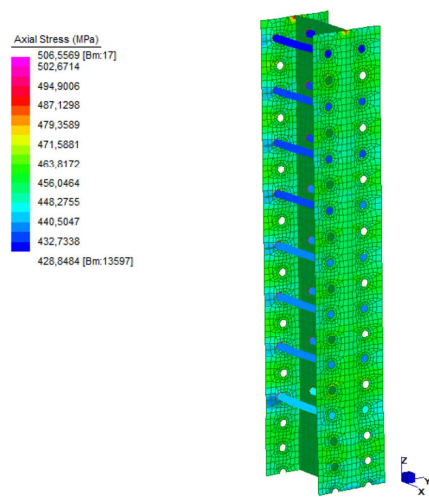


Figure 314. Fem simulation.

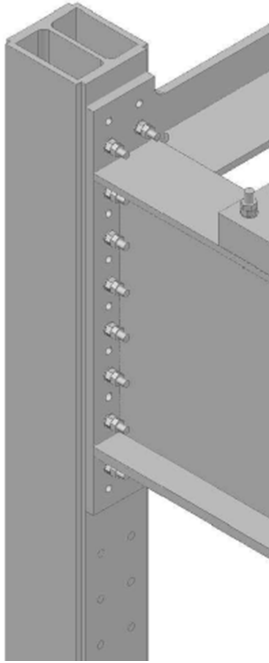


Figure 315. Bolted joint (design).



Figure 316. Joint.

The fatigue verification, considering $\Delta\tau_{sd} = 42MPa$, gives (Table 54 and Equation (110));

Detail class ($\Delta\sigma_c$)	Details
100	

Table 54

$SR > 100\%$

(111)

The verification is not satisfied. The fatigue stress on the shank weakens the bolts resistance. It is to be noted, however, that the pre-stress and the relative friction avoid the shear behavior of the bolts. A lock-nut is prescribed for every bolt in order to ensure the pre-stress even after a high number of cycles.

9.2.3.7 Floor anchoring and connection plates

For each column, four steel bars (S355) connect the structure to the strength floor. The bars have been threaded and the bolts have been screwed. The floor, 1000 mm high, guarantees a rigid connection. Tensile and compressive tests are available with this set up. The bar diameter is 42 mm as a result of the structural optimization performed taking into account the steel bars and floor stiffness.

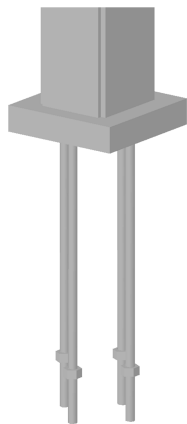


Figure 317. Floor bars.

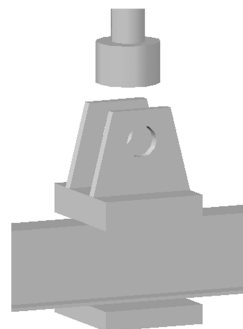


Figure 318. Connection plates.

A special element has been realized with the intention of connecting the servo actuator with the specimen. As shown in Figure 318, the element has two gusset plates and a steel hub. A non-linear fem model (Figure 319) has been realized in order to evaluate the stress distribution in the gusset plates (Figure 320). The hub

creates a localized force that could lead to fatigue failure. Following the Hertz theory, the plates have been modeled and fatigue verification has been carried out (Figure 321).

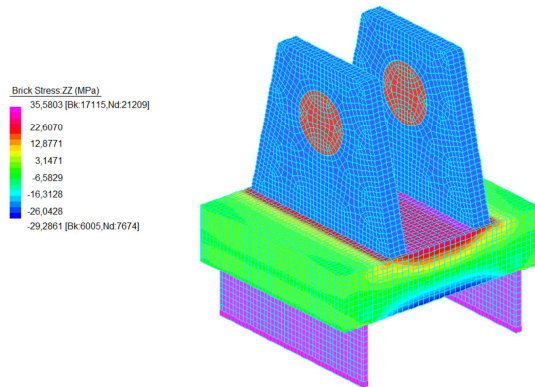


Figure 319. Brick model.



Figure 320. Connection plates.

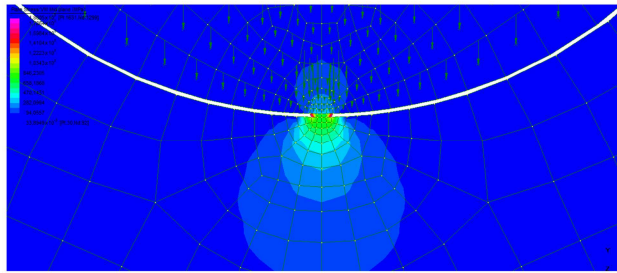


Figure 321. Contact element.

The fatigue verification, considering $\Delta\sigma_{sd} = 64MPa$ and considering category detail 80MPa, gives (Equation (112));

$$SR > 100\% \tag{ 112 }$$

The verification is not satisfied. The fatigue stress on the plates weakens the resistance around the hole. It is to be noted, however, that the fatigue problem could rise only if the actuator works at maximum force. For more details about the connection plates see [36].

9.3 Real scale fatigue test

The realized setup allows testing a large number and different typologies of elements. Depending on the specimen height, the steel box can be regulated in different configurations (Figure 322 and Figure 323). In these first analyses, fatigue test on rail bearer in real scale has been carried out.



Figure 322. High configuration.



Figure 323. Mid configuration.

The rail bearer "A" has been positioned under the frame for three point tests. The test has been conducted respecting the static setup configuration. Figure 324 and Figure 325 show the controller and the test setup. A preliminary fatigue test has been conducted with 300 kN force applied in the middle of span and at 1/3. For more detail about sensor and fem model see § 8.3. These tests are only preparations to the future experimentations. The system composed by the frame and the specimen is very complex. Nevertheless, the fatigue analysis needs a very accurate force control.

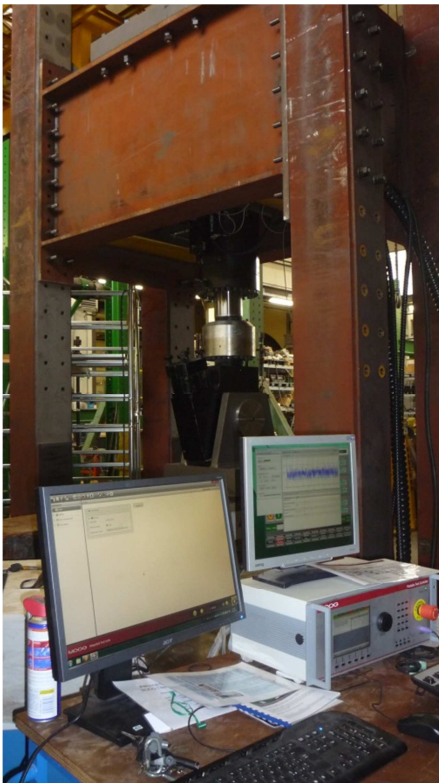


Figure 324. Test controller.



Figure 325. Fatigue test.

Preliminary tests have been conducted in order to corroborate the design assumptions. The controller provides different waves typologies with different load ramps (Figure 326).

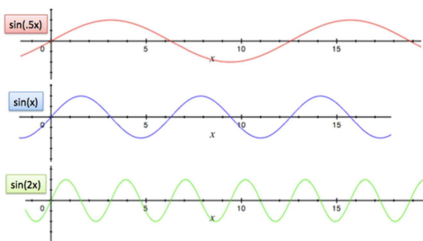


Figure 326. Different load waves.

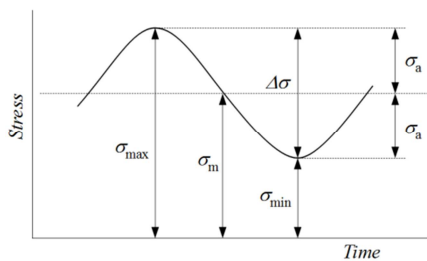


Figure 327. Stress wave.

The pumps and the chiller unit guarantee the system functioning. In these first tests, the oil pressure has been increased up to 280 bar in order to have sufficient energy to carry out the cycles. The oil temperature is set at about 50 °C in order to achieve the best performance. The frame reacts to the actuator force according the design evaluations: deformation is negligible and friction is activated. The test provides a pulsating force acting from about 5 kN up to 300 kN. The stress level is relatively low: the web stress is about 30 MPa whereas the flange stress is about 50 MPa.

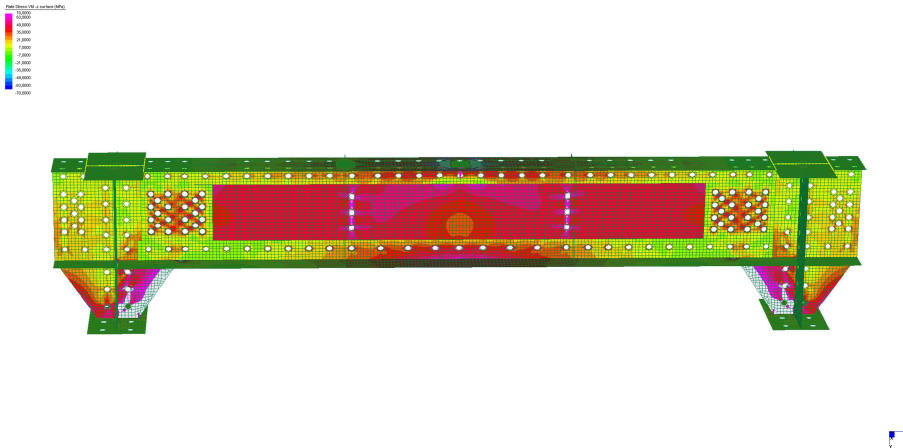


Figure 328. Laboratory stress distribution.

As mentioned in §8.2 the stress distribution (Figure 328) changes radically from in-site condition to laboratory condition. In order to test the equipment, the test has been carried out with 1 Hz frequency. Future tests will be executed with higher frequency with the intention of reducing the test duration. The test has been aimed to follow the previous full scale tests (Figure 329) in which stress is lower than 130 MPa. For more detail about other authors see [4]. Referring to § 8.2, the fatigue class and the consequently nominal stress for riveted structure is 71 MPa.

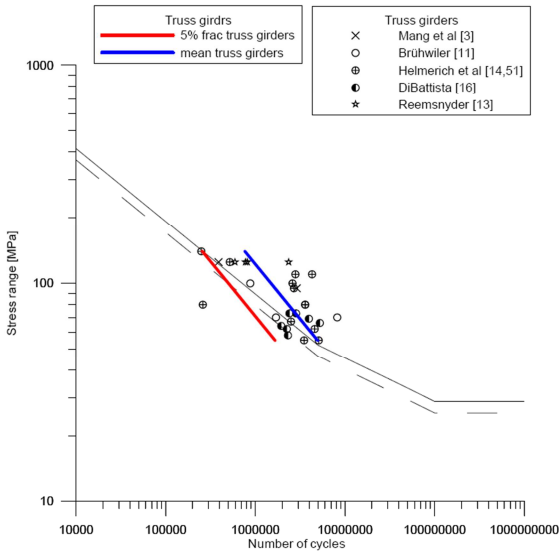


Figure 37. Truss girders plotted with detail category $C = 71$ and $C = 63$. The net stress range is plotted for the tests < 130 MPa.

Figure 329. Full scale tests: FAT 71.

The first test data output is summarized in Figure 330. The cycles envelope indicates the hysteresis loop. A linear behaviour is observed with maximum force 300 kN and maximum displacement 1,27 mm.

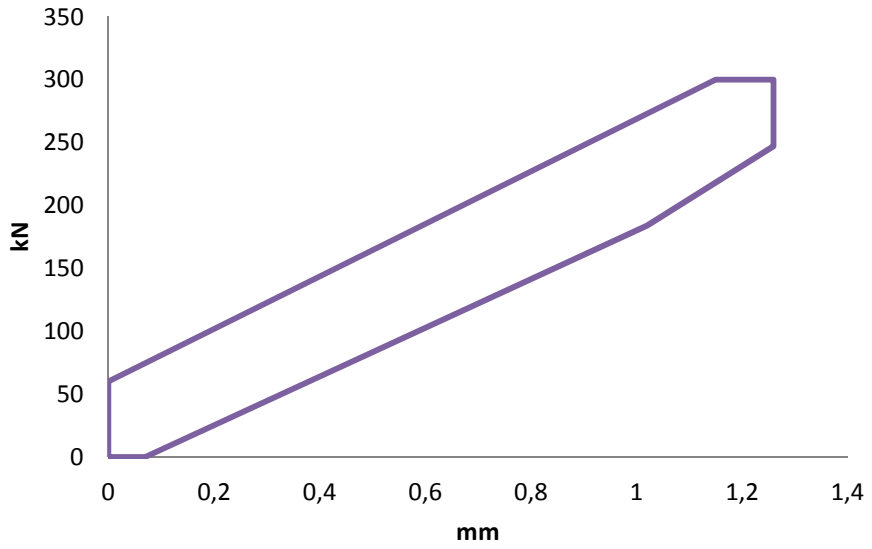


Figure 330. Fatigue cycles.



Figure 331. Real scale fatigue test.

The fatigue tests (Figure 331) are ongoing and the results will be illustrated in next publications. This first test has shown that the assumptions of elastic behaviour and friction involvement were correct. The applied cyclic force is spread into the rail bearer by the multilayer plates. The rivets bring together the plates involving the friction. Fatigue crack may occur indiscriminately into the web, into the flanges or near the rivet holes. The test will give information about the load history of rail bearer and verify the standard rivet fatigue class of 71 MPa. Other calibrations are necessary in order to improving the test output data. Different rail bearer supports and actuator settings are reassessing with the intention of carry out a representative fatigue test.

9.4 Final considerations

The real scale fatigue tests are essential for the understanding of the real structural behaviour. A specific metallic frame has been designed with the intention to test until 1,8 m high elements under 1500 kN force. The standard fatigue design is not accepted in the metallic frame due to the complexity of its details. For complex welded components, the nominal stress can be difficult to define even if the stress distribution is very well described with FEM. Modern approach, such as structural hot spot stress, is typically used where the structural discontinuity is not comparable to a classified structural detail. The goal is to realize a fatigue resistant frame conveniently designed for repeated loads. The concept has been translated into a four anchored columns frame with a steel plate supporting the oil-dynamic actuator. The frame weight is about 160 kN; moreover, the Moog actuator is able to perform 1500 kN force. All the connections are realized using pre-stressed bolts with the purpose of avoiding any type of stress concentrations. The welds are mostly V-groove type and well tapered. The structure is very sophisticated and a high accuracy 3D model has been realized. The actuator is produced by Moog and the maximum force applicable is ± 1500 kN at 0,5 Hz. The frame has been designed using a non - Liner FEM solution. The frame is adjustable with the intention of realizing tensile and compressive fatigue tests. A preliminary fatigue test has been conducted with 300 kN force applied in the middle of span and at 1/3. The test has been carried out on rail bearer in real scale. The stress level is relatively low: the web stress is about 30 MPa whereas the flange stress is about 50 MPa. The cycles envelope indicates the hysteresis loop. A linear behaviour is observed with maximum force 300 kN and maximum displacement 1,27 mm. Fatigue crack may

occur indiscriminately into the web, into the flanges or near the rivet holes. The fatigue tests are ongoing and the results will be illustrated in next publications.

10 CONCLUSIONS AND DEVELOPMENTS

The bridge is 34,4 m long, belongs to the Italian State Railways and it has been operational for about a century. San Stino's bridge was assembled using rivets and its simple supported reticular bridge had 5300 mm width and 3500 mm high. San Stino's bridge was designed and constructed before the standardisation and the widespread use of design codes. In July 2011, some elements were taken in order to test their static and fatigue behaviour. The reticular longitudinal elements were composed by overlapping a different number of plates in order to follow the bridge bending moment. The extracted elements have some damages like as WWII machine gun holes or corrosion degradation. In first approximation the rail bearer static scheme is considered fixed to the cross girder. A preliminary Fem analysis model is carried out in order to estimate the global and local structural behaviour. In a previous identification, carried out in July 2011, the dynamic response of the bridge was recorded using piezoelectric acceleration transducers. A good correlation between the Fem simulation and the acceleration registered by the sensors has been observed. In order to acquire sufficient information about the characteristics of the bridge, some steel samples were extracted and some tests were carried out. The traction test shows that San Stino's steel is comparable to Mild Steel (Yield point: 240 MPa, $E=190'000$ MPa). Some other physical and chemical tests confirm the consideration regarding the modern steel manufacture. A simple three points bending test has been carried out with the intention of investigating the fatigue behaviour. Different specimens have been subjected to different stress amplitude but for each individual item, the amplitude will never be varied. A short-life test has been performed; moreover, the steel stress has been modelled with a non-linear fem simulation. Preliminaries evaluations suggest a good fatigue behaviour for San Stino's steel. The pure material, subjected to bending moment, seem indicate a Fatigue Class 130. Despite the age of the bridge, the steel quality and the manufacture process guarantee a sufficient safety factor. The static and fatigue behaviour of rail bearers is correlated with the rivets clamping force. The clamping force are essential aspects of the construction process that can affect the strength and the lifetime of old riveted structures. Referring to the age of bridge construction, the clamping force is about 100 kN. Nevertheless, the clamping force decreases due to thermal load, vibrations, electric flows and other effects. The

evaluation of clamping force is usually carried out by destructive tests or simply referring to the initial steel yield stress. With the purpose of estimating the actual clamping force with an improved precision, a specific and innovative test has been conceived. A non-destructive test is recommended with the intention of extending this investigation campaign to other in-service bridges. The idea is to evaluate the clamping force by means of torsion test (TCT) on rivets. The applied torsional moment is proportional to the force generated by the frictional ring area of the rivet head subjected to clamping force. The clamping force has been calculated analytically and by software. A non-linear fem simulation has been carried out with the intention of validating the analytical estimates. Approximately, the same behaviour for each test series is observed. Moreover, the fem simulation gives a good validation of analytical results. The rivet manufacturing process has compromised the rivet regularity thus a variability in clamping force is observed. Experimental results show an average value of about 60 kN i.e. about 2/3 of original clamping force. In the lack of a more extended test campaign and analysing "small displacement" results, it is conceivable that a considerable amount of clamping force is lost. In conclusion, San Stino's elements have currently a significant amount of clamping force. A complete overview of rail bearers has been introduced. The element, as well as the entire structure, is brought together by rivets. The main elements composing the beam are the web, the flanges and riveted cover plates. Near the node, a triangular gusset plate connects the rail bearer to the transversal. A series of non-destructive tests has been performed with the intention of revealing the original structure. The beam is a plate composite section. Although the structure was slightly corroded and, except for the WWII damages, well preserved. A precise estimation of rivets dimensions and positions is carried out. The rivet section highlights a good head and shank regularity; moreover, the plates have a sufficient contact between themselves. Rivets have good head regularity, independently of any horizontal or vertical direction, and the average head diameter is 42 mm. The diameter variation is between 2 and 6% proving the good manufacturing level. Some holes have been inspected and their average diameter is about 26 mm. The shank diameter is 25 mm and a 1 mm gap is present. A brief overview on the in-service beam condition has been reported. The static schemes in-service condition and during the test campaign are substantially different. For about a century the San Stino's rail bearers have worked fixed between crossbeams; moreover, the consecutive fatigue test will operate in simple supported static scheme. A detailed load history is not available due to the bridge age. The train moving effect is sophisticated due to the continuous changing in static scheme. Considering the various train typologies, a typical fatigue verification

is carried out for rail bearers. The constraints simulate the cross girder effects (fixed at both ends). The maximum stress range is focused in the web, under the forces application area, and it is about 37 MPa (Von Mises criteria). Moreover, 20 MPa has been observed in the flanges. The preliminary analysis shows that the fatigue life of the rail bearer is ending rapidly due to the greater traffic and greater loads. In first analysis the fatigue verification is satisfied. Nevertheless, the stress distribution is completely different compared to the laboratory condition and it is not replicable due to the cross girder cut. A fatigue identification test has been carried out with the intention of predicting the fracture behaviour. A multi channels acquisition has been used intending to gain the entire beam structural behaviour. The static scheme is very simple although the beam deformation is very complex: many geometric imperfections are present and the element is composed by several different plates bound together by rivets. The test has been carried out performing different load steps in order to check the structural integrity during the experiment. In force – displacement graph the rise line is straight and this indicates an elastic behaviour. Each load increment traces the previous curve proving the elastic state. Analogically to the symmetric test and maintaining the same acquisition configuration, an asymmetric test has been carried out. An elastic behaviour is observed. In asymmetric configuration, an additional test has been performed: accurate sensors have been placed on the plates and on the rivets. The deformation and the relative displacements between web and cover plates and between rivets have been gained. An elastic behaviour is observed. The friction is still active and the rivets shank does not transfer shear force to the plates. The collected information regarding rail bearers allow modelling the beam accurately. The elastic Fem recreates the tests situation disregarding the friction and the local plasticization. The simple linear elastic model prevents a deep understanding behaviour of the rail bearers. A nonlinear solution allows to take into consideration different aspects: the nonlinear material constitutive law has been considered, the joint friction and the rivet clamping have been added. The element has been modelled as a composition of various plates. The model follows the experimental deformation with a good approximation. Moreover, there is a good correlation between the fem model and the plates – to - plates displacements. Starting from this considerations, a real scale fatigue test has been carried out. The real scale fatigue tests are essential for the understanding of the real structural behaviour. A specific metallic frame has been designed with the intention to test until 1,8 m high elements under 1500 kN force. The standard fatigue design is not accepted in the metallic frame due to the complexity of its details. For complex welded components, the nominal stress can be difficult to define even if the stress distribution is very well

described with FEM. Modern approach, such as structural hot spot stress, is typically used where the structural discontinuity is not comparable to a classified structural detail. The goal is to realize a fatigue resistant frame conveniently designed for repeated loads. The concept has been translated into a four anchored columns frame with a steel plate supporting the oil-dynamic actuator. The frame weight is about 160 kN; moreover, the Moog actuator is able to perform 1500 kN force. All the connections are realized using pre-stressed bolts with the purpose of avoiding any type of stress concentrations. The welds are mostly V-groove type and well tapered. The structure is very sophisticated and a high accuracy 3D model has been realized. The actuator is produced by Moog and the maximum force applicable is ± 1500 kN at 0,5 Hz. The frame has been designed using a non - Liner FEM solution. The frame is adjustable with the intention of realizing tensile and compressive fatigue tests. A preliminary fatigue test has been conducted with 300 kN force applied in the middle of span and at 1/3. The test has been carried out on rail bearer in real scale. The stress level is relatively low: the web stress is about 30 MPa whereas the flange stress is about 50 MPa. The cycles envelope indicates the hysteresis loop. A linear behaviour is observed with maximum force 300 kN and maximum displacement 1,27 mm. Fatigue crack may occur indiscriminately into the web, into the flanges or near the rivet holes. The fatigue tests are on-going and the results will be illustrated in next publications.

10.1 Further developments

For San Stino Bridge some other tests are scheduled. More information about steel will be collected. The characterization of material imposes a large number of tests in order to achieve a statistical validation. Many traction tests, impact tests, Vicker test and chemical analysis are scheduled. On the same way, the fatigue material characterization will continue taking in consideration some other levels of forces and cycles. The information exposed in this work refers principally to a one-rail bearer. Its characteristics are comparable to the others San Stino elements. Nevertheless, each element is unique due to its manufacturing and history condition. For this purpose, another rail bearer will be tested retracing the experimental campaign shown in this thesis. Analogically, the same procedure will be adopted for the two transversal beam elements. A bigger actuator force and enhanced oil vigour will be necessary with the intention to simulate the in-field conditions. For both rail bearers and transversal beams, a Torsional Clamping Test

CONCLUSIONS AND DEVELOPMENTS

campaign will be activated in order to increase the comprehension on the clamping force. The TCT test will be made in different specimens and for different joints. This test campaign is a part of a bigger project aimed to evaluate the rivets functionality on existing structures. In the follow, some pictures of San Donà Bridge (Venice): a similar riveted bridge dismantled in 2012. An experimental campaign on this bridge has been started and the results will be exposed in future works.



San Donà (VE) before 2012.



Dismantling (October 2012).



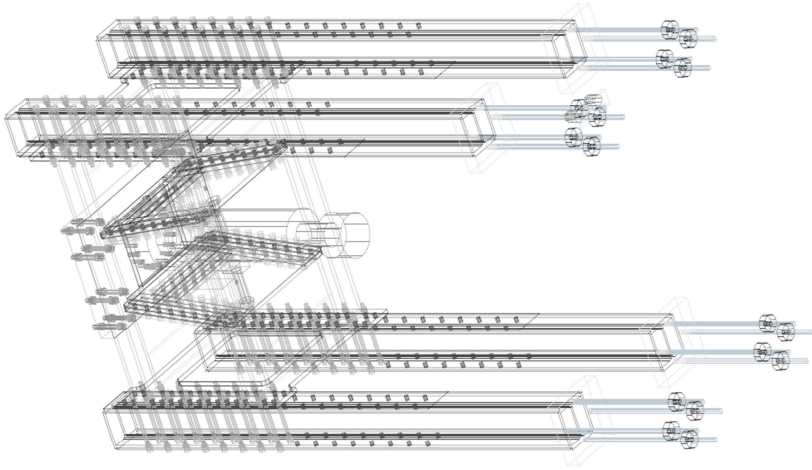
Rail bear (San Donà).

The non-destructive character and the cheapness of TCT will allow an extensive test campaign. The fatigue test on rail bearer is on-going and the specimen behaviour is carefully monitored. The results will show the fatigue crack zones and will be correlated with the Fem simulations. A better comprehension of frame-

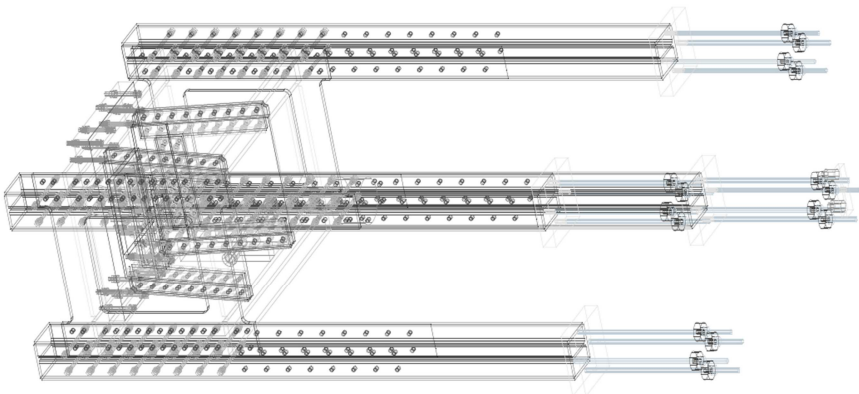
specimen system is essential in order to guarantee the adequacy of fatigue tests. An accurate monitoring system has been hypothesized for the fatigue metallic frame. The strain gauge sensors will be positioned in the hot spots verifying the design assumptions. The frame is able to test other samples typologies and will be used for different fatigue tests. Furthermore, a fatigue monitoring system is scheduled on in-service structures in order to gather information that is essential to laboratory practice. Referring to [44], the fatigue fragility curves for riveted structures will be created. Vulnerability analysis estimates the structure probability to be damaged over time. The study is conducted in probabilistic terms, and the structural consequences will be expressed in a probabilistic point of view as well. The methodology identifies the structure for different classes of vulnerabilities and each class defines more precisely the relationship between the input and the damage. This procedure allows to identify a combined fatigue-clamping failure probability for each specific train-load and relative number of cycles considered, configuring it as a valuable tool for the assessment, prevention and management of the existing steel bridges. It will be necessary a complete clamping force and fatigue degradation knowledge in order to predict statistically the structures failure. Furthermore, more specific tests on riveted joints are necessary for a better understanding of the slip between the plates and the eventual rivet shank involvement. The fatigue cracks of riveted structures are very hard to predict; further studies will enhance the knowledge of the problem.

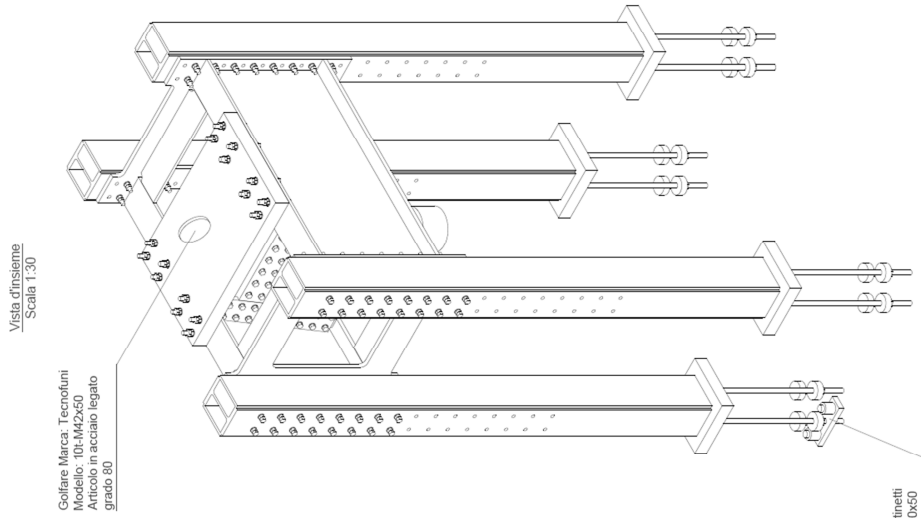
11 ATTACHED TABLES

Vista d'insieme
Scala 1:30

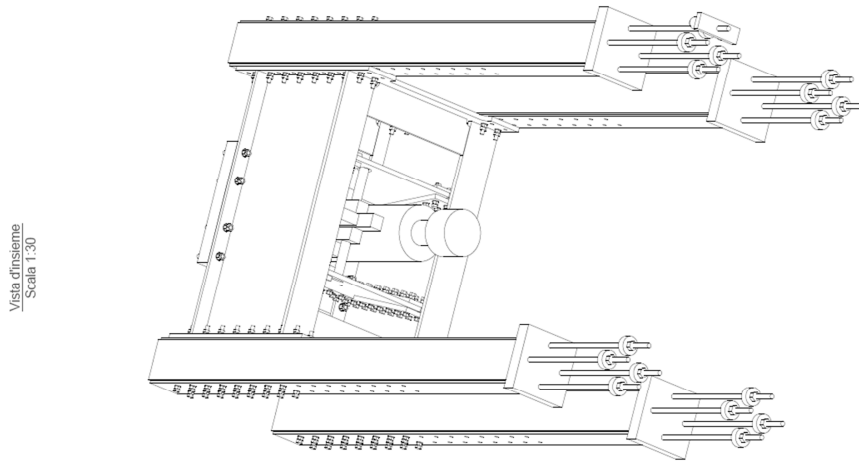


Vista d'insieme
Scala 1:30



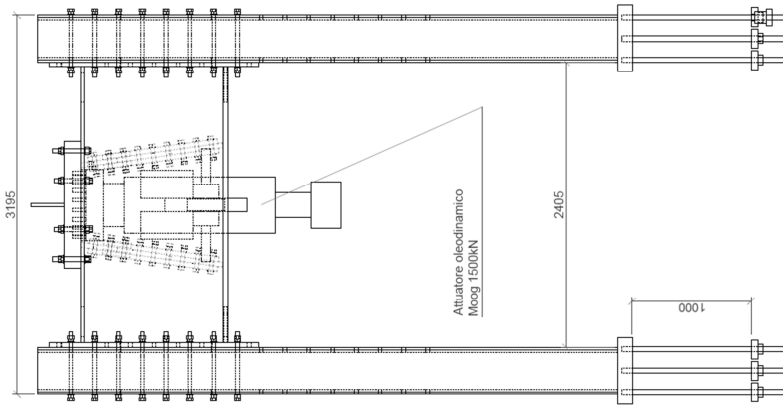


Piastra per martinetti
(bxbxh) 440x140x50

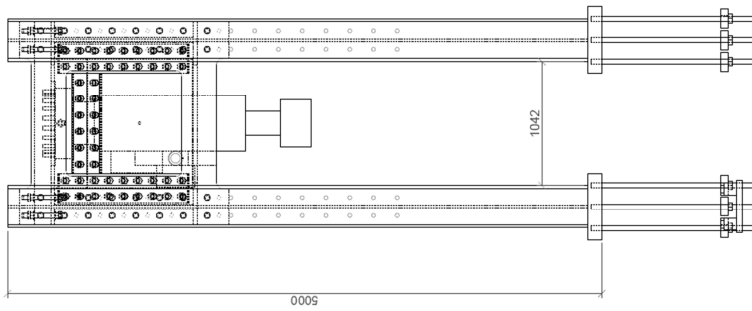


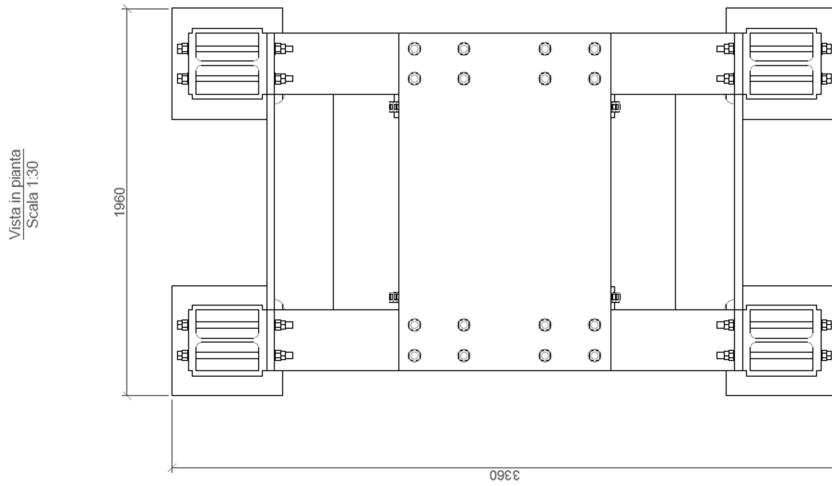
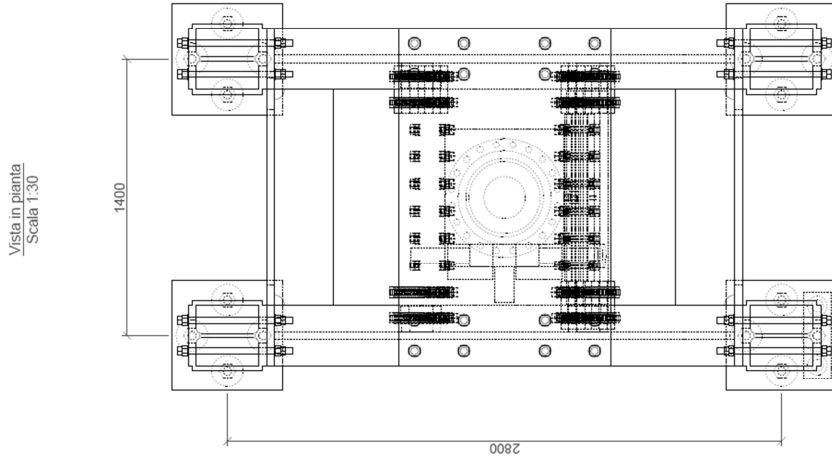
ATTACHED TABLES

Prospetto lato lungo
Scala 1:30



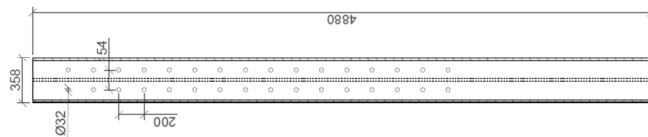
Prospetto lato corto
Scala 1:30



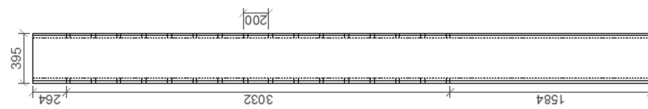


COLONNE (4 elementi)

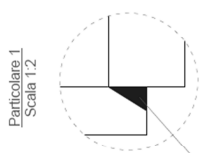
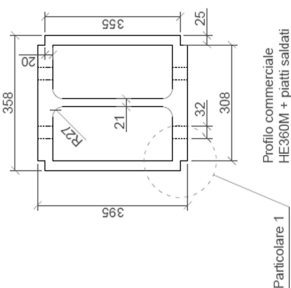
Vista frontale pitreilla
Scala 1:30



Vista laterale pitreilla
Scala 1:30

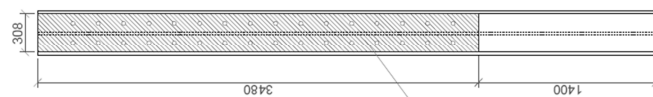


Pianta pitreilla
Scala 1:30



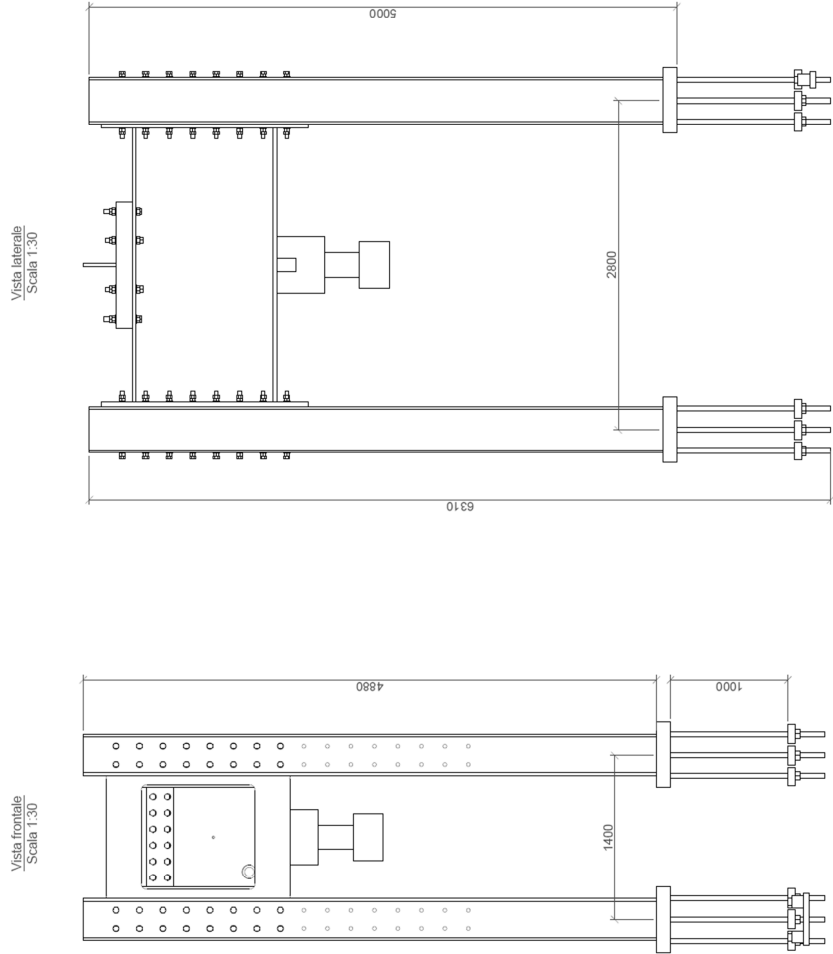
Saldature a V di I
Classe: S-20; lunghezza totale 4880 mm con spianatura del cordone.
Angolo di rifinitura 30°

Dettaglio lavorazioni
Scala 1:30

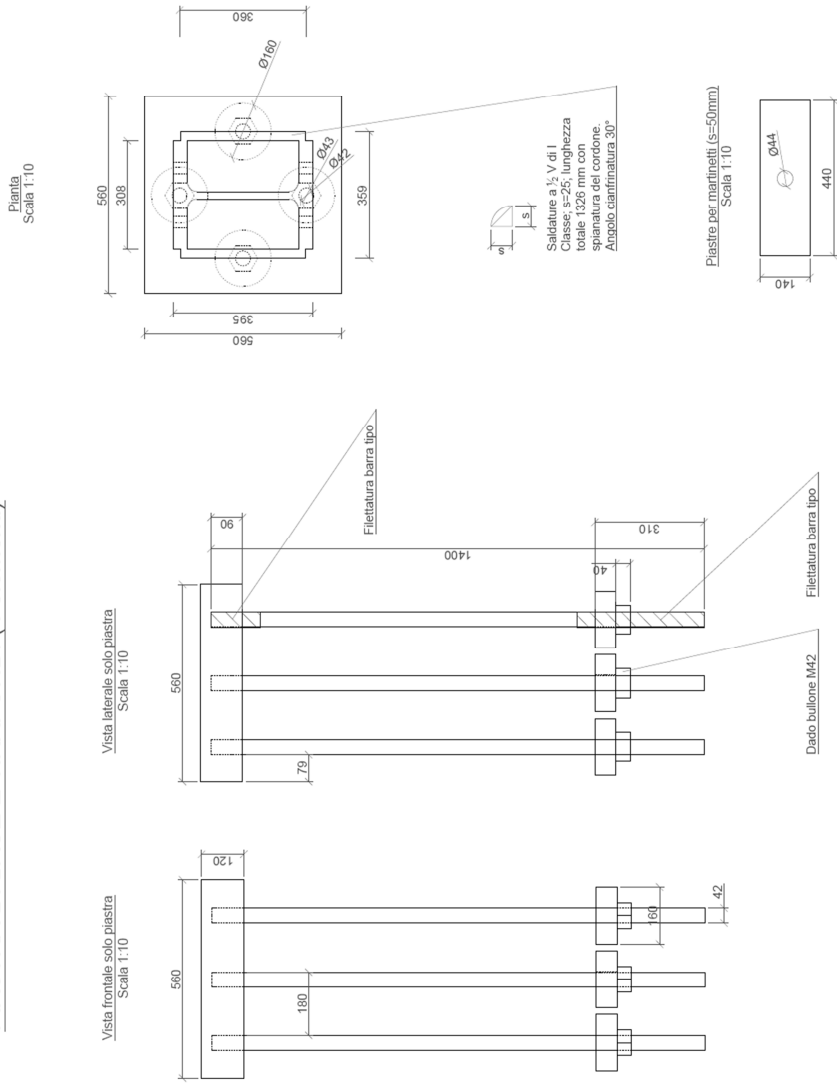


Superficie da rettificare e sabbiare (lato interno portale)

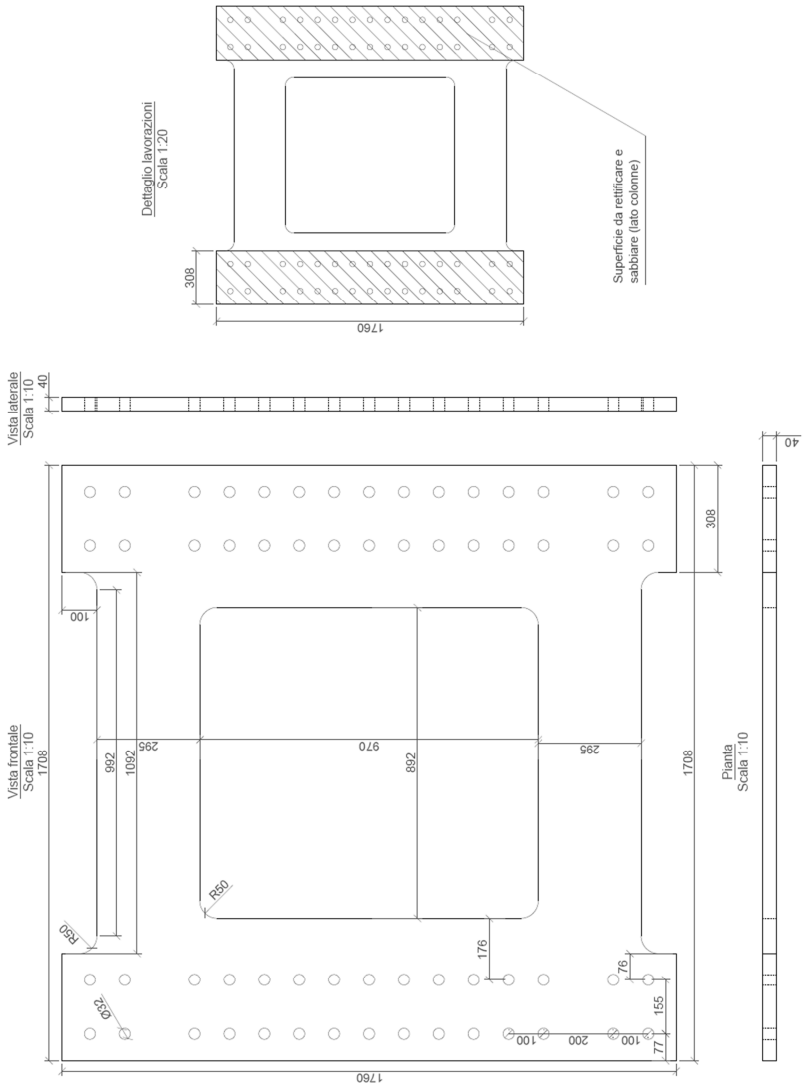
COLONNE E PIASTRE SALDATE



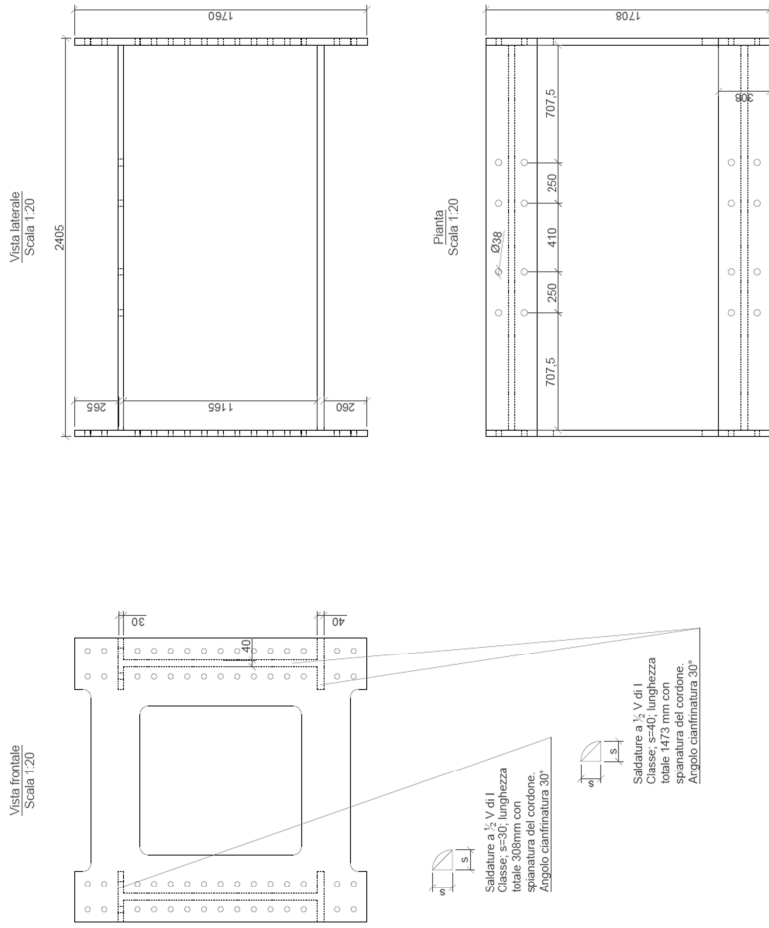
PIASTRA DI BASE E TIRAFONDI (4 elementi)



PIASTRONE FORATO (2 elementi)



PIASTRONE FORATO E TRAVI SALDATE



12 BIBLIOGRAPHY

- [1] J. A. Bannantine, J. J. Comer, and J. L. Handrock, *Fundamentals of metal fatigue analysis*. Prentis-Hall, Inc., 1990.
- [2] M. Al-Emrani and R. Kliger, "Fatigue prone details in steel bridges," pp. 112–119, 2009.
- [3] S. Suresh, *Fatigue of Materials*, Second Edi. Cambridge Univeristy Press, 1998.
- [4] L. C. Cremona, A. Patron, L. B. Johansson, T. Larsson, R. B. Eichler, S. Höhler, and P. A. B. Kühn, "SB 4.6 - Improved Assessment Methods for Static and Fatigue Final draft," pp. 1–218, 2007.
- [5] Eurocode3, "Design of steel structures Part 1-9: Fatigue," 2005.
- [6] F. B., "Utmattningshållfasthet hos äldre konstruktionsstål med korrosionsskador," Division of Steel Structures Luleå University of Technology, 1993.
- [7] G. L. Kulak, J. W. Fisher, and J. H. A. Struik, *Rivets: Guide to design criteria for bolted and riveted joints*. 2001.
- [8] Q. Collette, "Riveted connections in historical metal structures (1840-1940). Hot-driven rivets: technology, design and experiments," 2014.
- [9] C. Batho and E. H. Bateman, "Investigations on Bolts and Bolted Joints," London, 1934.
- [10] W. Participants, "SB 4.2 Guideline for Load and Resistance Assessment of Existing European Railway Bridges: Advices on the use of advanced methods.," *Sustain. Bridg.*
- [11] W. H. Munse and H. C. Cox, "The Static Strength of Rivets Subjected to Combined Tension and Shear," 1956.
- [12] UNI EN, "EN 1993-1-8:2005 - Eurocode 3: Design of steel structures - Part 1-8: Design of joints," *Eurocode 3*, vol. 8, no. 2005, p. 135, 2005.
- [13] B. Åkesson, *Fatigue Life of Riveted Steel Bridges*. 2010.

BIBLIOGRAPHY

- [14] I. Fernlund, "A Method to Calculate the Pressure Between Bolted or Riveted References Plates," 1961.
- [15] W. M. Wilson and F. P. Thomas, "Fatigue Tests on Riveted Joints," 1938.
- [16] T. R. Higgins and W. H. Munse, "How Much Combined Stress Can a Rivet Take?," *Eng. News-Record*, vol. 149, 1952.
- [17] P. Liechti, P., Josi, G., Kunz, "Ermüdungsversuche an genieteten Vollwandträgern," *Constr. Métallique*, 1997.
- [18] "Railtrack Line Code of Practice RT/CE/C/025." The Structural Assessment of Underbridges, 2003.
- [19] R. A. Hechtman, D. R. Young, A. G. Chin, and R. Savikko, "Slip Joints Under Static Loads." Transactions ASCE, p. Vol. 120, 1955, pp. 1335—1352, 1955.
- [20] A. Kuperus, "The Ratio Between the Slip Factor of Fe 52 and Fe 37." C.E.A.C.M. X-6-27, Stevin Laboratory, Department of Civil Engineering, Delft University of Technology, Delft, the Netherlands, 1966.
- [21] J. H. Lee, C. O'Connor, and J. W. Fisher, "Effect of Surface Coatings and Exposure on Slip." Journal of the Structural Division, ASCE, 1969.
- [22] D. D. Vasarhelyi and K. C. Chiang, "Coefficient of Friction in Joints of Various Steels." Journal of the Structural Division, ASCE, Vol. 93, ST4, 1969.
- [23] R. N. Allan and J. W. Fisher, "Bolted Joints with Oversize and Slotted Holes." Journal of the Structural Division, ASCE, Vol. 94, ST9, 1968.
- [24] G. H. Sterling and J. W. Fisher, "A440 Steel Joints Connected by A490 Bolts No Title." Journal of the Structural Division, ASCE. Vol. 92, ST3, 1966.
- [25] O. Steinhardt and K. Möhler, "Versuche zur Anwendung Vorgespannter Schrauben Stahlbau." Teil II, Bericht des Deutschen Ausschusses für Stahlbau, Stahlbau-Verlag GmbH, Cologne, Germany, 1959.
- [26] J. W. Fisher and J. L. Rumpf, "Analysis of Bolted Butt Joints." Journal of the Structural Division, ASCE, Vol. 91, ST5, 1965.
- [27] K. L. Johnson and J. J. O'Connor, "Mechanics of Fretting." Proceedings of the Institution of Mechanical Engineers, Vol. 178, Part 3J, London, 1963.
- [28] J. W. Carter, K. H. Lenzen and L. T. Wyly, "Fatigue in Riveted and Bolted Single-Lap Joints." Transactions ASCE, Vol. 120, 1955.

- [29] G+DComputing, "Straus7." Release 2.4.
- [30] K. Islami, "Enhanced system identification and automatic SHM of bridge structures," University of Padua, Italy, 2013.
- [31] A. Vendraminelli, "Caratterizzazione strutturale ed identificazione dinamica di un ponte ferroviario in acciaio e di un ponte stradale in cemento armato," University of Padua, Italy, 2011.
- [32] EN_10002-1, "Metallic materials Tensile testing Part 1: method of test at ambient temperature," *Eur. Comm. Stand.*, 2001.
- [33] EN_10045-1, "European Standard: Metallic materials Charpy impact test Part 1 : Test method," no. March. pp. 1–9, 1990.
- [34] UNI_EN_ISO_6507-1, "Metallic materials Vickers hardness test Part 1: Test method." 2006.
- [35] ASTM_A370-03a, "Standard Test Methods and Definitions for Mechanical Testing of Steel Products." 2003.
- [36] F. Zanin, "Non linear analysis of mechanical devices for fatigue experimental tests of bending elements," *Thesis*, 2013.
- [37] A. Hobbacher, "Recommendations for fatigue design of welded joints and components," *IIV Doc. 1823-07*, 2008.
- [38] Eurocode3, "Design of steel structures." 1993.
- [39] Italian Minister of Construction, "Norme Tecniche per le Costruzioni," *Off. Gaz.*, 2008.
- [40] European standards, "EN10025." 2004.
- [41] L. Michielutti, "Studio dell'attrezzatura per l'esecuzione di prove sperimentali su elementi soggetti a fatica e a carichi dinamici," University of Padua, 2013.
- [42] B. Atzori, "Appunti Di Costruzione Di Macchine." Edizioni Libreria Cortina, Padova, p. 347, 2000.
- [43] M. Colussi, "Studio dell'attrezzatura per l'esecuzione di prove sperimentali mediante metodi avanzati di progettazione a fatica," University of Padua, 2014.
- [44] F. P. Marchesini, R. Morbin, C. Pellegrino, and C. Modena, "Fatigue vulnerability analysis of a historical railway steel bridge," in *7th International*

BIBLIOGRAPHY

Conference on Bridge Maintenance, Safety and Management (IABMAS 2014), 2014, pp. 2237–2244.